Technical Physics, Vol. 47, No. 10, 2002, pp. 1205–1213. Translated from Zhurnal Tekhnicheskoĭ Fiziki, Vol. 72, No. 10, 2002, pp. 1–9.

THEORETICAL AND MATHEMATICAL PHYSICS

Electrophysical Characteristics of 2D Three-Component Regular Structures

B. Ya. Balagurov and V. A. Kashin

Emanuel Institute of Biochemical Physics, Russian Academy of Sciences, ul. Kosygina 4, Moscow, 119991 Russia
e-mail: balagurov@deom.chph.ras.ru

Received February 19, 2002

Abstract—Electrophysical characteristics of two 2D double-periodic three component systems (models) are studied analytically and numerically. For a number of model parameters, the effective conductivity, the partial electric field strength moments of second order, and the effective Hall coefficient for both models are calculated and graphically tabulated. © *2002 MAIK "Nauka/Interperiodica".*

INTRODUCTION

To date, considerable progress has been made toward studying electrophysical properties of double-component media (specifically, composites), especially of those representing 2D regular structures. For example, the analytical solution to the conductivity problem as applied to a number of double-periodic models (involving insulating or perfectly conducting inclusions) is given in [1–3]. For the most interesting case, when both components have a finite nonzero conductivity, the closed solution to the problem has been obtained for a staggered structure [1]. A more realistic model, a 2D system with regularly arranged circular inclusions was considered even by Rayleigh [4]. He found the first several terms of the virial expansion for effective conductivity. The solution to the problem of conductivity (and other effective parameters) for the Rayleigh model that is applicable for any concentration was reported in [5, 6]. Finally, the general method for computing electrophysical characteristics of regularly structured double-component systems is presented in [7].

As for investigation into multicomponent media, which have much more varied properties than double-component ones, the situation is different. Although multicomponent systems are of great scientific and applied interest, the theory of finding their properties is still in its infancy. Therefore, it is natural to begin with regular three-component systems, which are relatively simple to analyze. A step forward in this direction has been made in [8], where the conductivity of a 2D double-sublattice system (Fig. 1), which is a generalization of the Rayleigh model (an isotropic matrix with staggered circular inclusions of two types having different radii and conductivities), was considered. However, the approximate method employed in [8] is applicable only if the concentration of the inclusions is small. The solution to the problem of conductivity (and other effective parameters) of a double-sublattice model that is valid for any concentration was obtained in [9] with the method elaborated in [5].

In this work, we numerically analyze general formulas [9] throughout the range of concentrations studied for a fixed ratio of the inclusion radii and several ratios σ_i/σ_1 ($i = 2, 3$), where σ_i is the conductivity of the inclusions and σ_1 is that of the matrix. The effective conductivity of the model, partial rms electric field strengths, as well as functions entering into an expression for the effective Hall coefficient in a weak magnetic field, are calculated and graphically tabulated.

We also analyze another three-component model, an isotropic 2D matrix with double-layer circular inclusions forming a square lattice (Fig. 2). The core and sheath of the inclusions are a concentric circle and a ring

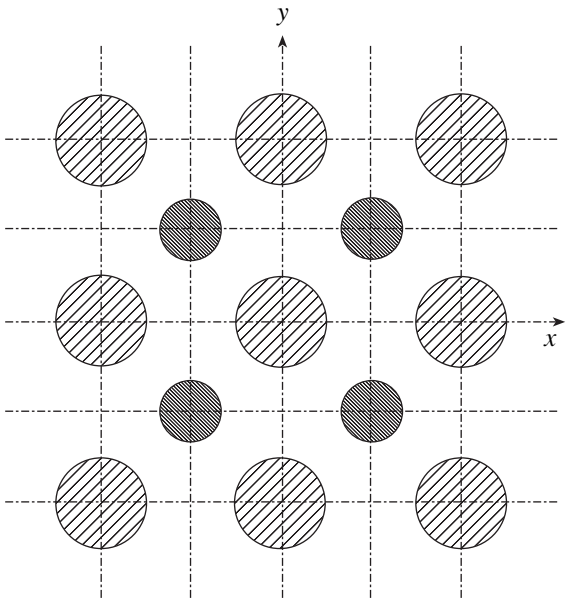

Fig. 1.

1063-7842/02/4710-1205$22.00

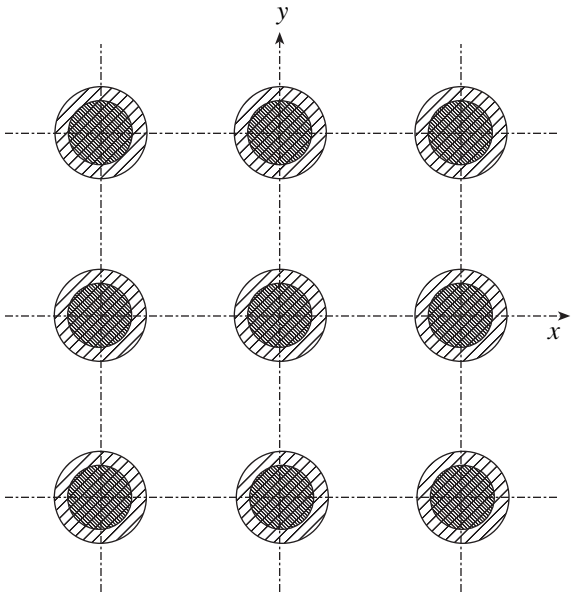

Fig. 2.

of different conductivity. This system is a generalization of the Rayleigh model [4] for the case when an inclusion is covered, e.g., by an oxide film. For this model, an analytical solution to the problem of conductivity and other effective parameters is found. Formulas derived are analyzed numerically, and the same electrophysical parameters as for the double-sublattice model are tabulated for a number of fixed problem parameters.

DOUBLE-SUBLATTICE MODEL

(1) Electric field in the medium. The model under consideration represents a 2D isotropic matrix of conductivity σ_1 with staggered circular inclusions of two types (Fig. 1). The inclusions of the first type (of conductivity σ_2 and radius R) form a square lattice with a period $2a$. The other inclusions (of conductivity σ_3 and radius ρ) form a similar lattice shifted by the half-period along the x and y axes.

Let the mean electric field strength $\langle \mathbf{E} \rangle$ be aligned with the x axis. Then, for the complex potential of the matrix, we have [9]

$$\Phi_1(z) = \beta\left\{z + \sum_{n=0}^{\infty} B_{2n}\zeta^{(2n)}(z) + \sum_{n=0}^{\infty} D_{2n}\zeta^{(2n)}(z - z_0)\right\}. \quad (1)$$

Here, $z = x + iy$, $z_0 = (1 + i)a$, $\zeta(z)$ is the Weierstrass zeta function [10], and $\zeta^{(2n)}(z)$ is the $2n$th derivative of $\zeta(z)$. The constants β, B_2, and D_{2n} are real for the direction of $\langle \mathbf{E} \rangle$ selected. The coefficients B_{2n} and D_{2n} satisfy an infinite set of algebraic equations. If B_{2n} and D_{2n} are replaced by "variables" ξ_n and η_n as

$$B_{2n} = \frac{R^{2n+2}\delta_{21}}{\sqrt{(2n)!(2n+1)!}}\xi_n, \quad (2)$$

$$D_{2n} = \frac{\rho^{2n+2}\delta_{31}}{\sqrt{(2n)!(2n+1)!}}\eta_n, \quad (3)$$

where

$$\delta_{ij} = \frac{1 - h_{ij}}{1 + h_{ij}}, \quad h_{ij} = \frac{\sigma_i}{\sigma_j}, \quad (4)$$

the above-mentioned set of equations takes the form [9]

$$\xi_n + \sum_{m=0}^{\infty}(M_{nm}\xi_m + P_{nm}\eta_m) = \delta_{n0}, \quad (5)$$

$$\eta_n + \sum_{m=0}^{\infty}(Q_{nm}\xi_m + N_{nm}\eta_m) = \delta_{n0}. \quad (6)$$

Here, δ_{n0} is the Kronecker symbol. In (5) and (6),

$$M_{nm} = G_{nm}R^{2(n+m+1)}c_{n+m+1}\delta_{21}, \quad (7)$$

$$P_{nm} = G_{nm}R^{2n}\rho^{2m+2}d_{n+m+1}\delta_{31}, \quad (8)$$

$$Q_{nm} = G_{nm}\rho^{2n}R^{2m+2}d_{n+m+1}\delta_{21}, \quad (9)$$

$$N_{nm} = G_{nm}\rho^{2(n+m+1)}c_{n+m+1}\delta_{31}, \quad (10)$$

$$G_{nm} = \frac{(2n+2m)!}{\sqrt{(2n)!(2n+1)!(2m)!(2m+1)!}}. \quad (11)$$

In (7) and (10), c_k are the coefficients in the expansion of the zeta function in the vicinity of $z = 0$ [10]:

$$\zeta(z) = \frac{1}{z} - \sum_{k=2}^{\infty}\frac{c_k}{2k-1}z^{2k-1}, \quad (12)$$

where

$$c_2 = \frac{g_2}{20}, \quad g_2 = \frac{1}{a^4}[K(1/\sqrt{2})]^4, \quad (13)$$

$$c_4 = \frac{1}{3}c_2^2, \quad c_6 = \frac{2}{3\times 13}c_2^3, \quad c_8 = \frac{5}{3\times 13\times 17}c_2^4, \ldots.$$

In (13), $K(1/\sqrt{2}) = 1.85407\ldots$ is the complete elliptic integral of the first kind $K(k)$ with a module $k = 1/\sqrt{2}$. Accordingly, d_k is the coefficient in the expansion of the zeta function near the point $z = z_0$ [10]:

$$\xi(z) = \xi(z_0) - \sum_{k=2}^{\infty}\frac{d_k}{2k-1}(z - z_0)^{2k-1}, \quad (14)$$

where

$$d_2 = -\frac{g_2}{4}, \quad d_4 = \frac{1}{5}d_2^2,$$
$$d_6 = \frac{2}{75}d_2^3, \quad d_8 = \frac{1}{325}d_2^4, \ldots. \tag{15}$$

In (14), $z_0 = (1 + i)a$ and $\xi(z_0) = \pi(1 - i)/(4a)$. The values of c_{2k} can be sequentially found from the recurrent relationship [10]

$$c_{2k} = \frac{3}{(4k+1)(2k-3)}\sum_{m=1}^{k-1} c_{2m}c_{2k-2m}, \quad k \geq 2. \tag{16}$$

In turn, d_{2k} is expressed through c_{2k} as [9]

$$d_{2k} = [(-4)^k - 1]c_{2k}. \tag{17}$$

The coefficients c_n and d_n with odd subscripts vanish in the square lattice under consideration (the so-called lemniscatic case [10]). Therefore, the matrices M_{nm}, P_{nm}, Q_{nm}, and N_{nm} in (7)–(10) are other than zero only if the subscripts n and m are of different parity.

(2) Effective characteristics. The dimensionless effective conductivity $f = \sigma_e/\sigma_1$ is expressed through the quantities ξ_0 and η_0 as [9]

$$f = \frac{1 - \xi_0 p_2 \delta_{21} - \eta_0 p_3 \delta_{31}}{1 + \xi_0 p_2 \delta_{21} + \eta_0 p_3 \delta_{31}}, \tag{18}$$

where $p_2 = \pi R^2/(2a)^2$ and $p_3 = \pi\rho^2/(2a)^2$ are the concentrations of the second and third components, respectively.

The effective conductivity σ_e is directly related to the partial rms characteristics of the electric field strength $\mathbf{E}(\mathbf{r})$ (see, e.g., [9]):

$$\psi_i \equiv \langle \mathbf{e}^2 \rangle^{(i)} = \frac{\partial \sigma_e}{\partial \sigma_i}; \quad \mathbf{e}(\mathbf{r}) = \mathbf{E}(\mathbf{r})/|\langle \mathbf{E}(\mathbf{r}) \rangle|. \tag{19}$$

Here, $\langle \ldots \rangle^{(i)}$ is the integral over the volume (surface in the 2D case) occupied by the ith component ($i = 1, 2, 3$) divided by the volume (surface area) V of the sample. For our two-sublattice model, we have [9]

$$\psi_i = \frac{4}{(1 + h_{i1})^2}\frac{p_i J_i}{\Delta^2}; \quad i = 2, 3; \tag{20}$$

$$J_2 = \sum_{n=0}^{\infty} \xi_n^2, \quad J_3 = \sum_{n=0}^{\infty} \eta_n^2, \tag{21}$$

where

$$\Delta = 1 + \xi_0 p_2 \delta_{21} + \eta_0 p_3 \delta_{31}. \tag{22}$$

For an N-component medium, the quantities ψ_i and f from (18) are related as [9]

$$\sum_{i=1}^{N} h_{i1}\psi_i = f. \tag{23}$$

Hence, for a three-component system, we find

$$\psi_1 = f - h_{21}\psi_2 - h_{31}\psi_3, \tag{24}$$

which means that there is no need for directly calculating ψ_1 with (19) in our model.

For a weak magnetic field $\mathbf{H}$, the effective Hall coefficient R_e is expressed through the off-diagonal (Hall) component σ_{ae} of the tensor $\hat{\sigma}_e$ as follows:

$$R_e = \frac{1}{H}\frac{\sigma_{ae}}{\sigma_e^2}. \tag{25}$$

According to [9], in the approximation linear in $\mathbf{H}$, we have for an N-component system

$$\sigma_{ae} = \sum_{i=1}^{N} \sigma_{ai}\varphi_{ai}, \tag{26}$$

$$\varphi_{ai} = \frac{\langle E_x^{(x)}E_y^{(y)} - E_y^{(x)}E_x^{(y)} \rangle^{(i)}}{\langle E_x^{(x)} \rangle \langle E_y^{(y)} \rangle}, \tag{27}$$

where $\langle \ldots \rangle^{(i)}$ is the same as in (19), $\mathbf{E}^{(v)} = \mathbf{E}^{(v)}(\mathbf{r})$ is the electric field strength at $\mathbf{H} = 0$, and the superscript v means that $\langle \mathbf{E}^{(v)} \rangle$ is aligned with the v axis.

For an N-component system, the functions φ_{ai} obey the rule of sum [9]

$$\sum_{i=1}^{N} \varphi_{ai} = 1. \tag{28}$$

Eliminating φ_{a1} with (28), we find from (26) for a three-component medium

$$\sigma_{ae} = \sigma_{a1} + (\sigma_{a2} - \sigma_{a1})\varphi_{a2} + (\sigma_{a3} - \sigma_a)\varphi_{a3}. \tag{29}$$

In the 2D case, there is one more relationship between φ_{ai} and effective conductivity σ_e [9]:

$$\sum_{i=1}^{N} \sigma_i^2 \varphi_{ai} = \sigma_e^2. \tag{30}$$

After eliminating φ_{a1} with (28), we find from (30) for a three-component system

$$1 - (1 - h_{21}^2)\varphi_{a2} - (1 - h_{31}^2)\varphi_{a3} = f^2. \tag{31}$$

Relationship (31) allows one to calculate only one of the functions φ_{ai}, for example, φ_{a2}, for the 2D case. On the other hand, the fulfillment of (31) means that the numerical solution to the system of Eqs. (5) and (6) is correct.

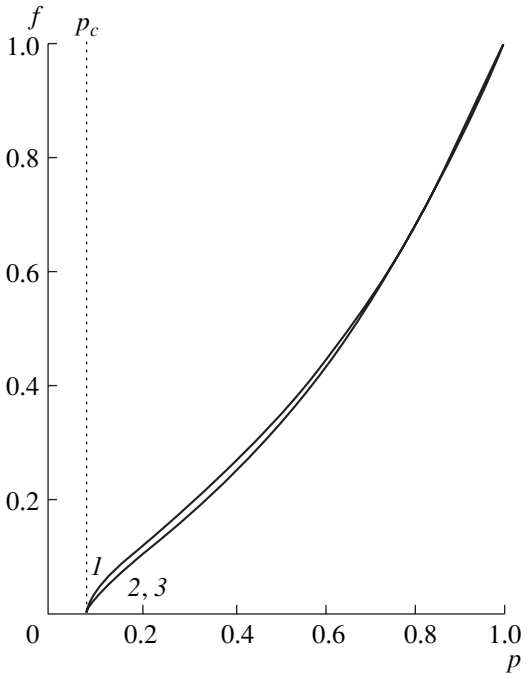

Fig. 3.

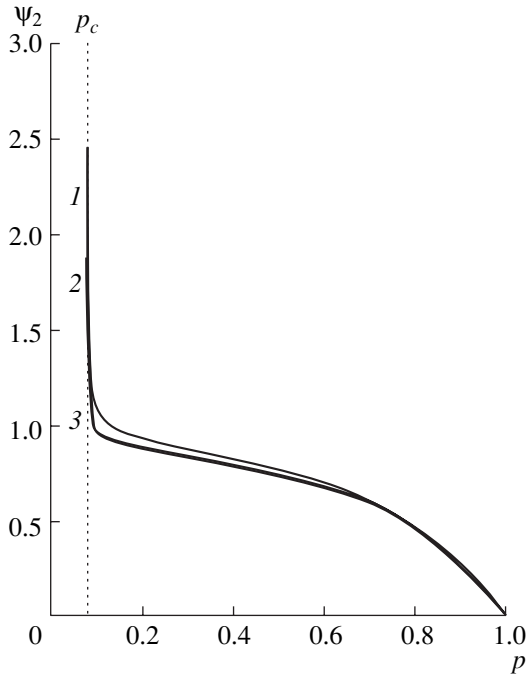

Fig. 4.

The determination of the functions φ_{a2} and φ_{a3} with (27) gives for our model [9]

$$\varphi_{ai} = \frac{4}{(1 + h_{i1})^2}\frac{p_i I_i}{\Delta^2}; \quad i = 2, 3, \tag{32}$$

$$I_2 = \sum_{n=0}^{\infty}(-1)^n\xi_n^2, \quad I_3 = \sum_{n=0}^{\infty}(-1)^n\eta_n^2 \tag{33}$$

with Δ from (22). In [9], it was shown that expressions (18), (32), and (33) convert relationship (31) into the identity.

In this work, the effective characteristics of the double-sublattice model were calculated for $\sigma_2 = 0$ and the parameter $h_{31} = \sigma_3/\sigma_1$, 10^{-1}, 10^{-2}, and 10^{-3} (curves *1–3*, respectively, in Figs. 3–7). The radius R was varied between 0 and a; ρ, by the law $\rho = (\sqrt{2} - 1)R$. To find the coefficients ξ_n and η_n from the infinite systems of Eqs. (5) and (6), a finite system of 80 equations was separated out. The effective values of f, ψ_2, ψ_3, φ_{a2}, and φ_{a3} as functions of the concentration p of the first component are demonstrated in Figs. 3–7.

DOUBLE-LAYER MODEL

(1) Electric field in a medium. The model under consideration represents a 2D isotropic matrix of conductivity σ_i with double-layer circular inclusions, forming a square lattice with a period $2a$ (Fig. 2). The core of the inclusion has a radius ρ and a conductivity σ_3. The sheath is a ring of an outer radius R, an inner radius ρ ($R > \rho$), and a conductivity σ_2.

Let the mean electric field strength $\langle \mathbf{E} \rangle$ be aligned with the x axis. Then, for the complex potentials of the matrix, sheath, and core, we have, respectively,

$$\Phi_1(z) = \beta\left\{z + \sum_{n=0}^{\infty} B_{2n}\zeta^{(2n)}(z)\right\}, \tag{34}$$

$$\rho < |z| < R\colon \Phi_2(z) = \beta\sum_{n=0}^{\infty}\left\{C_{2n+1}z^{2n+1} + \frac{D_{2n+1}}{z^{2n+1}}\right\}, \tag{35}$$

$$|z| < \rho\colon \Phi_3(z) = \beta\sum_{n=0}^{\infty} A_{2n+1}z^{2n+1}. \tag{36}$$

Here, $\zeta^{(2n)}(z)$ are, as in (1), the $2n$th derivatives of the Weierstrass zeta function $\zeta(z)$. The coefficients β, B_{2n}, C_{2n+1}, D_{2n+1}, and A_{2n+1} are real.

The electric potentials $\varphi_2(\mathbf{r}) = \mathrm{Re}\,\Phi_2(z)$ and $\varphi_3(\mathbf{r}) = \mathrm{Re}\,\Phi_3(z)$ must satisfy the standard conditions at the core–sheath interface:

$$r = \rho\colon \varphi_2 = \varphi_3,$$
$$\frac{\partial\varphi_2}{\partial r} = h_{32}\frac{\partial\varphi_3}{\partial r}; \quad h_{32} = \frac{\sigma_3}{\sigma_2}. \tag{37}$$

From (37), we express the coefficients C_{2n+1} and

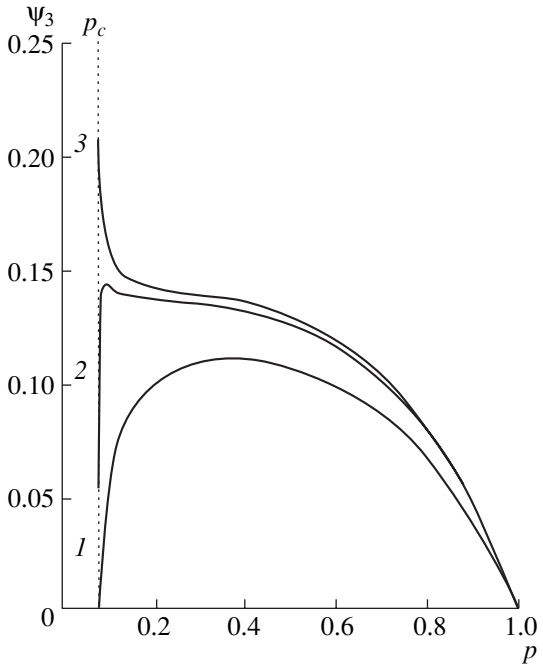

Fig. 5.

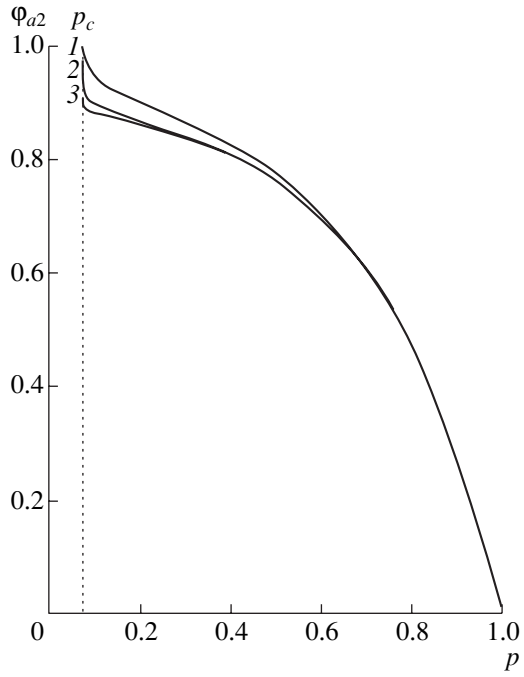

Fig. 6.

D_{2n+1} through A_{2n+1}:

$$C_{2n+1} = \frac{1}{2}(1+h_{32})A_{2n+1},$$
$$D_{2n+1} = \frac{1}{2}(1-h_{32})\rho^{4n+2}A_{2n+1}. \tag{38}$$

In turn, the potentials $\varphi_1(\mathbf{r}) = \mathrm{Re}\Phi_1(z)$ and $\varphi_2(\mathbf{r}) = \mathrm{Re}\Phi_2(z)$ must satisfy the conditions

$$t = R\colon \varphi_1 = \varphi_2,$$
$$\frac{\partial\varphi_1}{\partial r} = h_{21}\frac{\partial\varphi_2}{\partial r}, \quad h_{21} = \frac{\sigma_2}{\sigma_1}. \tag{39}$$

Expansion (12) is usually applied to the function $\zeta(z)$. As a result, for the coefficients B_{2n}, we obtain the infinite set of algebraic equations

$$B_{2n} + w_n\frac{1-h_{21}}{1+h_{21}}\sum_{m=0}^{\infty}B_{2m}\frac{(2n+2m)!}{(2n)!(2n+1)!}c_{n+m+1}R^{4n+2} = \frac{1-h_{21}}{1+h_{21}}R^2w_0\delta_{n0}, \tag{40}$$

where

$$w_n = \left[1+\frac{\delta_{32}}{\delta_{21}}\left(\frac{\rho}{R}\right)^{4n+2}\right]\Big/\left[1+\delta_{32}\delta_{21}\left(\frac{\rho}{R}\right)^{4n+2}\right]. \tag{41}$$

The quantities δ_{ij} are defined by (4). The coefficients A_{2n+1} are expressed through B_{2n} as

$$A_{2n+1} = B_{2n}\frac{4}{(1+h_{21})(1+h_{32})}\frac{(2n)!}{R^{4n+2}} \times\left[\delta_{21}+\delta_{32}\left(\frac{\rho}{R}\right)^{4n+2}\right]^{-1}. \tag{42}$$

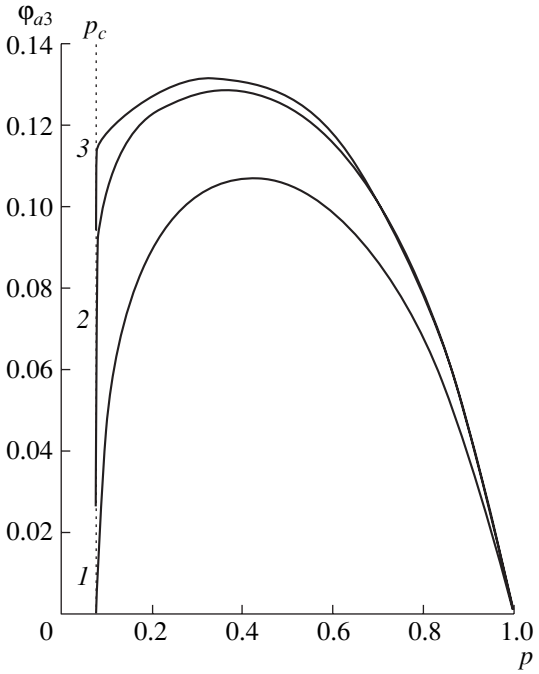

Fig. 7.

Note that Eqs. (40) can be derived from general formulas in [7]. For a circular double-layer inclusion, the multipole polarizability matrix [7] has the form

$$\Lambda_{nm} = \Lambda_n \delta_{nm}, \tag{43}$$

where

$$\Lambda_m = R^{2n} \frac{\delta_{21} + \delta_{32}(\rho/R)^{2n}}{1 + \delta_{21}\delta_{32}(\rho/R)^{2n}}. \tag{44}$$

In (43), δ_{nm} is the Kronecker symbol. Substituting (43) and (44) into formulas (19), (28), and (33) from [7] yields the set of Eqs. (40) for the coefficients B_{2n}.

If variables ξ_n are substituted for B_{2n},

$$B_{2n} = \frac{R^{2n+2}\delta_{21}}{\sqrt{(2n)!(2n+1)!}}\xi_n. \tag{45}$$

Eq. (40) will take the form

$$w_n^{-1}\xi_n + \sum_{m=0}^{\infty} S_{nm}\xi_m = \delta_{n0}, \tag{46}$$

where

$$S_{nm} = G_{nm} c_{n+m+1} R^{2(n+m+1)} \delta_{21} \tag{47}$$

with G_{nm} from (11). The matrix $\hat{S}$ is symmetric: $S_{nm} = S_{mn}$. The even-subscript ($n + m + 1 = 2k$) coefficients c_{n+m+1} are defined by (13) and (16); the odd-subscript coefficients c_{n+m+1} vanish. Therefore, the matrix S_{nm} is other than zero only if the subscript m and n are of different parity.

Now, let us direct $\langle \mathbf{E} \rangle$ along the y axis (associated values have bars). For the complex potentials of the matrix, sheath, and core, we have, respectively,

$$\bar{\Phi}_1(z) = -i\bar{\beta}\left\{ z - \sum_{n=0}^{\infty} \bar{B}_{2n}\zeta^{(2n)}(z) \right\}, \tag{48}$$

$$\rho < |z| < R:$$

$$\bar{\Phi}_2(z) = -i\bar{\beta}\sum_{n=0}^{\infty}\left\{ \bar{C}_{2n+1} z^{2n+1} - \frac{\bar{D}_{2n+1}}{z^{2n+1}} \right\}, \tag{49}$$

$$|z| < \rho: \bar{\Phi}_3(z) = -i\bar{\beta}\sum_{n=0}^{\infty} \bar{A}_{2n+1} z^{2n+1}. \tag{50}$$

The quantities $\bar{\beta}$, $\bar{B}_{2n}$, $\bar{C}_{2n+1}$, $\bar{D}_{2n+1}$, and $\bar{A}_{2n+1}$ are real.

From the boundary conditions for $r = \rho$ and $r = R$, we find a relationship between $\bar{C}_{2n+1}$, $\bar{D}_{2n+1}$, and $\bar{A}_{2n+1}$ like (38) and between $\bar{A}_{2n+1}$ and $\bar{B}_{2n}$ like (42), as well as a set of equations for the coefficients $\bar{B}_{2n}$. Introducing the variables $\bar{\xi}_n$ as in (45),

$$\bar{B}_{2n} = \frac{R^{2n+2}\delta_{21}}{\sqrt{(2n)!(2n+1)!}}\bar{\xi}_n, \tag{51}$$

we arrive at the set of equations for $\bar{\xi}_n$

$$w_n^{-1}\bar{\xi} - \sum_{m=0}^{\infty} S_{nm}\bar{\xi}_m = \delta_{n0} \tag{52}$$

with the matrix S_{nm} from (47) and w_n from (41).

For the quantities ξ_n, a number of useful relationships (rules of sum) can be derived. Multiplying (46) by $\bar{\xi}_n$ and (52) by ξ_n, adding the results, and summing over all n, we come, in view of (62), to

$$\sum_{n=0}^{\infty} (-1)^n w_n^{-1}\xi_n^2 = \xi_0. \tag{53}$$

Now, consider the same structure but with other conductivities of the components: κ_1, κ_2, and κ_3, respectively. Associates quantities will be marked by a tilde. Then, instead of (46), we have

$$\tilde{w}_n^{-1}\tilde{\xi}_n + \sum_{m=0}^{\infty} \tilde{S}_{nm}\tilde{\xi}_m = \delta_{n0}. \tag{54}$$

Now, we multiply (46) by $\tilde{\bar{\xi}}_n$ and (54) by ξ_n, subtract the results, and sum over all n to come, with regard for the symmetry of the matrix S_{mn}, to

$$\sum_{n=0}^{\infty} (w_n^{-1} - \tilde{w}_n^{-1})\xi_n\tilde{\xi}_n + \sum_{n=0}^{\infty}\sum_{m=0}^{\infty} (S_{nm} - \tilde{S}_{nm})\xi_n\tilde{\xi}_m = \tilde{\xi}_0 - \xi_0. \tag{55}$$

Let us put in (55) $\kappa_1 = \sigma_1$ and $\kappa_3 = \sigma_3$ and pass to the limit $\kappa_2 \longrightarrow \sigma_2$. Then, from (55), it follows the equality

$$\sum_{n=0}^{\infty} \xi_n^2 \frac{\partial}{\partial\sigma_2} w_n^{-1} + \sum_{n=0}^{\infty}\sum_{m=0}^{\infty} \xi_n\xi_m \frac{\partial}{\partial\sigma_2} S_{nm} = -\frac{\partial\xi_0}{\partial\sigma_2}. \tag{56}$$

Since

$$\frac{\partial}{\partial\sigma_2} S_{nm} = \frac{1}{\delta_{21}}\frac{\partial\delta_{21}}{\partial\sigma_2} S_{nm}, \tag{57}$$

we substitute (57) into (56) and eliminate $\sum_m S_{nm}\xi_m$ with Eq. (46) to obtain

$$\sum_{n=0}^{\infty} \xi_n^2 w_n^{-2} \frac{\partial}{\partial\sigma_2}(w_n\delta_{21}) = \frac{\partial}{\partial\sigma_2}(\xi_0\delta_{21}). \tag{58}$$

Similarly, putting in (55) $\kappa_1 = \sigma_1$ and $\kappa_2 = \sigma_2$ and passing to the limit $\kappa_3 \longrightarrow \sigma_3$, we find

$$\sum_{n=0}^{\infty} \xi_n^2 \frac{\partial}{\partial \sigma_3} w_n^{-1} = -\frac{\partial \xi_0}{\partial \sigma_3}. \tag{59}$$

(2) Effective characteristics. Calculating, as in [5], the voltage drop across an elementary cell and the total current, we obtain for the dimensionless effective conductivity $f = \sigma_e/\sigma_1$

$$f = \left(\alpha - \frac{\pi R^2}{4a^2}\delta_{21}\right)\left(\alpha + \frac{\pi R^2}{4a^2}\delta_{21}\right)^{-1}; \quad \alpha = \xi_0^{-1}, \tag{60}$$

therefore, finding the quantity ξ_0 (i.e., the coefficient B_0) will suffice to determine f.

If the concentration of the inclusions is small ($R \ll a$), the set of Eqs. (46) can be solved by iterations, that is, by expanding in powers of $w_n S_{nm}$:

$$\xi_n = w_0\left\{\delta_{n0} - w_n\left[S_{n0} - \sum_{m=0}^{\infty} S_{nm} w_m S_{m0} + \sum_{l=0}^{\infty}\sum_{m=0}^{\infty} S_{nl} w_l S_{lm} w_m S_{m0} - \ldots\right]\right\}. \tag{61}$$

Comparing with a similar expansion for $\bar{\xi}_n$ following from (52) shows that

$$\bar{\xi}_n = (-1)^n \xi_n. \tag{62}$$

From (61), we come to a virial expansion (in powers of R/a) for the quantities ξ_n, including ξ_0. It is, however, more convenient to find the associated expansion for $\alpha = 1/\xi_0$. From (46) at $n = 0$, we have

$$\xi_0 = w_0\left\{1 - \sum_{m\neq 0} S_{0m}\xi_m\right\}. \tag{63}$$

If $n \neq 0$,

$$\xi_n = -w_n S_{n0}\xi_0 - w_n \sum_{m\neq 0} S_{nm}\xi_m. \tag{64}$$

Solving Eq. (64) by iterations yields

$$n \neq 0: \xi_n = -\xi_0 w_n\left\{S_{n0} - \sum_{m\neq 0} S_{nm} w_m S_{m0} + \sum_{l\neq 0}\sum_{m\neq 0} S_{nl} w_l S_{lm} w_m S_{m0} - \ldots\right\}. \tag{65}$$

Substituting (65) into (63), we arrive at

$$\alpha = \xi_0^{-1} = w_0^{-1}\left\{1 - w_0\sum_{k\neq 0} S_{0k} w_k S_{k0} - w_0\sum_{k\neq 0}\sum_{l\neq 0}\sum_{m\neq 0} S_{0k} w_k S_{kl} w_l S_{lm} w_m S_{m0} - \ldots\right\}. \tag{66}$$

Using the explicit form of the matrix $\hat{S}$ [see (47)], one can find from (66) the expansion of α in powers of R/a. Up to terms $\sim(R/a)^{24}$, we have

$$\alpha = w_0^{-1}\left\{1 - \frac{1}{3}w_0 w_1 (gR^4)^2\delta_{21}^2 - \frac{1}{63}w_0 w_3 (gR^4)^4\delta_{21}^2 - \frac{5}{9}\left(w_0 w_1^2 w_2\delta_{21}^2 + \frac{4}{5\times 11\times 13^2}w_0 w_5\right)(gR^4)^6\delta_{21}^2 - \ldots\right\}, \tag{67}$$

where $g = g_2/20$; g_2 is defined by (13).

In our model, the reciprocity condition (see, e.g., [9]), which relates the effective conductivities of the initial and reciprocal systems (the latter is obtained from the former by making the change $h_{ij} \longrightarrow h_{ji}$) must be fulfilled:

$$f(h_{21}, h_{31})\, f(h_{12}, h_{13}) = 1. \tag{68}$$

Note that the change $h_{ij} \longrightarrow h_{ji}$ (the transition to the reciprocal system) is equivalent to the change $\delta_{ij} \longrightarrow \delta_{ji}$. In this case, $w_{n\to w_m}$, $S_{nm} \longrightarrow S_{mn}$, and ξ_0 remains unchanged. Hence, as follows from (60), $f \longrightarrow 1/f$ and reciprocity condition (68) is fulfilled automatically.

For the functions ψ_1 and ψ_3 defined by (19), we find

$$\psi_2 = \frac{\pi}{(4a)^2}\frac{(1+h_{32})^2}{\left(1 + B_0\frac{\pi}{4a^2}\right)^2}\sum_{n=0}^{\infty}(2n+1)R^{4n+2}(A_{2n+1})^2 \times\left[1 + \delta_{32}^2\left(\frac{\rho}{R}\right)^{4n+2}\right]\left[1 - \left(\frac{\rho}{R}\right)^{4n+2}\right]. \tag{69}$$

$$\psi_3 = \frac{\pi}{(2a)^2}\frac{1}{\left(1 + B_0\frac{\pi}{4a^2}\right)^2} \times \sum_{n=0}^{\infty}(2n+1)\rho^{4n+2}(A_{2n+1})^2. \tag{70}$$

The value of ψ_1 can be found from (24).

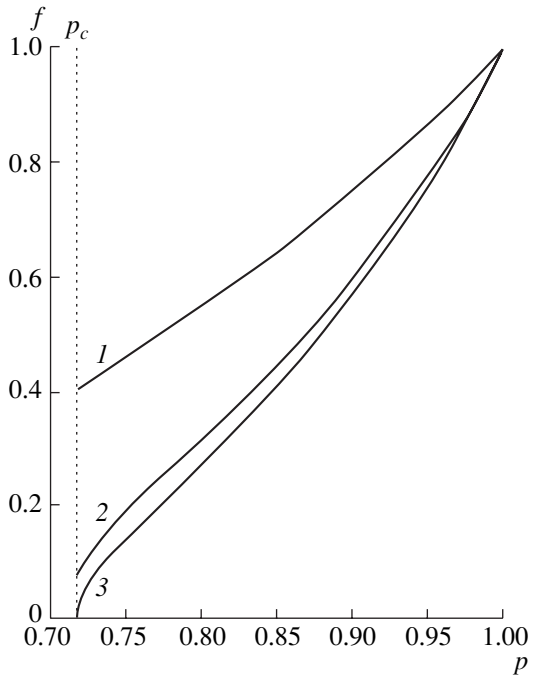

Fig. 8.

From (60), we find for the derivative $\partial\sigma_e/\partial\sigma_2$

$$\frac{\partial\sigma_e}{\partial\sigma_2} = -\frac{2\sigma_1}{\left(1+\xi_0\dfrac{\pi R^2}{4a^2}\delta_{21}\right)^2}\frac{\pi R^2}{4a^2}\frac{\partial}{\partial\sigma_2}(\xi_0\sigma_{21}). \quad (71)$$

On the other hand, substituting (42) and (45) into (69) yields

$$\psi_2 = -\frac{2\sigma_1}{\left(1+\xi_0\dfrac{\pi R^2}{4a^2}\delta_{21}\right)^2}\frac{\pi R^2}{4a^2} \times \sum_{n=0}^{\infty}\xi_n^2 w_n^{-2}\frac{\partial}{\partial\sigma_2}(w_n\delta_{21}). \quad (72)$$

Comparing (72) [in view of identity (58)] with (71) leads us to the equality

$$\psi_2 = \frac{\partial\sigma_e}{\partial\sigma_2}. \quad (73)$$

which is consistent with (19).

Similarly, from (60) and (70), we find

$$\frac{\partial\sigma_e}{\partial\sigma_3} = -\frac{2\sigma_1}{\left(1+\xi_0\dfrac{\pi R^2}{4a^2}\delta_{21}\right)^2}\frac{\pi R^2}{4a^2}\delta_{21}\frac{\partial\xi_0}{\partial\sigma_3}, \quad (74)$$

$$\psi_3 = \frac{2\sigma_1}{\left(1+\xi_0\dfrac{\pi R^2}{4a^2}\delta_{21}\right)^2}\frac{\pi R^2}{4a^2}\delta_{21}\sum_{n=0}^{\infty}\xi_n^2\frac{\partial}{\partial\sigma_3}w_n^{-1}. \quad (75)$$

Comparing (75) [in view of (59)] with (74) leads us to the equality

$$\psi_3 = \frac{\partial\sigma_e}{\partial\sigma_3}, \quad (76)$$

which also agrees with (19).

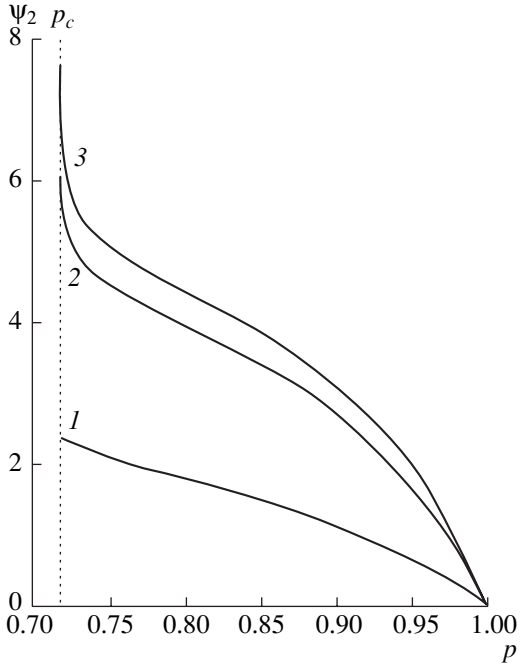

Fig. 9.

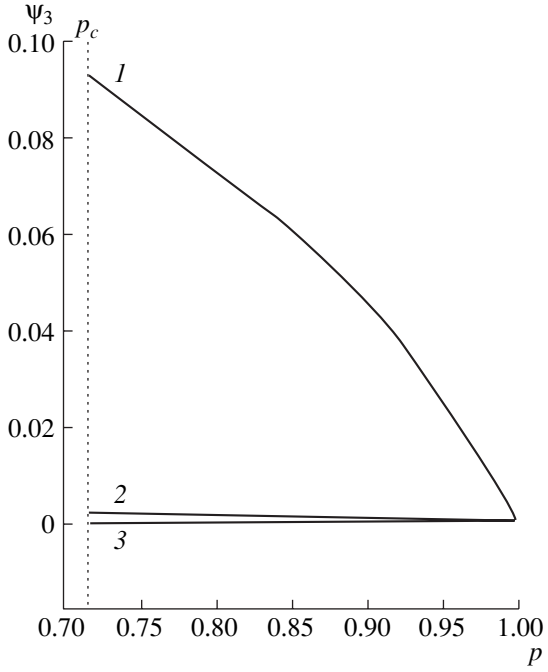

Fig. 10.

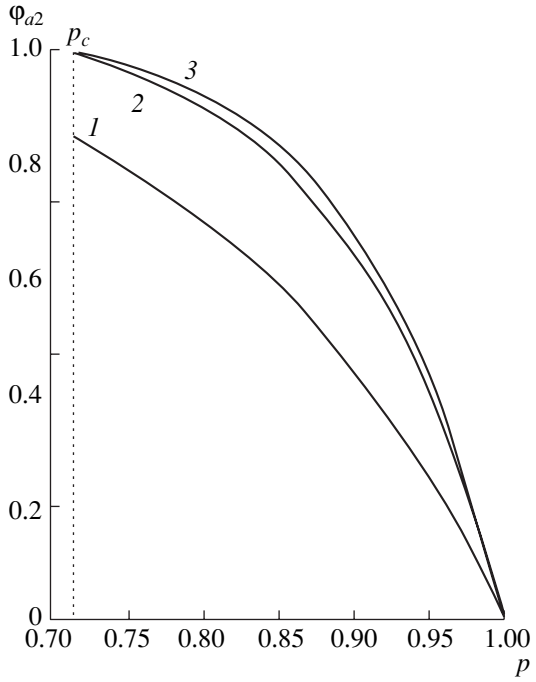

Fig. 11.

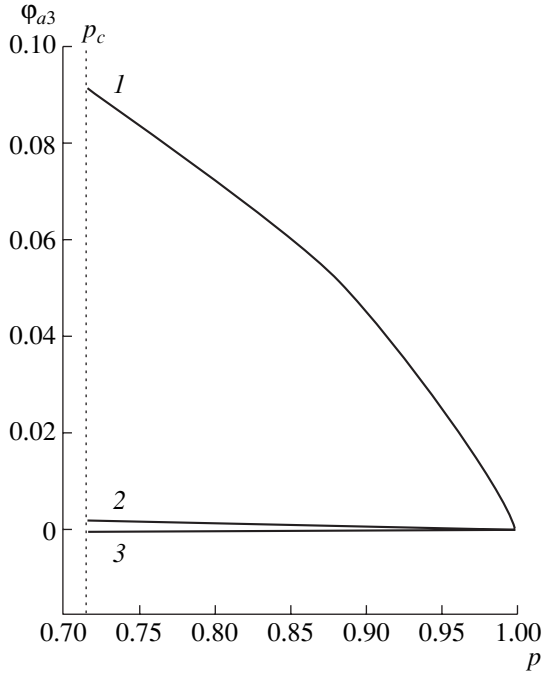

Fig. 12.

The Hall coefficient is given by expressions (25)–(29). Finding the strengths $\mathbf{E}^{(x)}$ and $\mathbf{E}^{(y)}$ from (35), (36) and (49), (50) and calculating the integrals appearing in the formulas for φ_{a2} and φ_{a3} [see (27)], we arrive at

$$\varphi_{a2} = \frac{\pi}{(4a)^2}\frac{(1+h_{32})^2}{\left(1+B_0\frac{\pi}{4a^2}\right)^2}\sum_{n=0}^{\infty}(-1)^n(2n+1)R^{4n+2} \times (A_{2n+1})^2\left[1-\delta_{32}^2\left(\frac{\rho}{R}\right)^{4n+2}\right]\left[1-\left(\frac{\rho}{R}\right)^{4n+2}\right], \quad (77)$$

$$\varphi_{a3} = \frac{\pi}{(2a)^2}\frac{1}{\left(1+B_0\frac{\pi}{4a^2}\right)^2} \times \sum_{n=0}^{\infty}(-1)^n(2n+1)\rho^{4n+2}(A_{2n+1})^2. \quad (78)$$

With expressions (77) and (78) and equalities (42) and (45), it is easy to check that

$$(1-h_{21}^2)\varphi_{a2} + (1-h_{31}^2)\varphi_{a3} = \frac{\pi R^2}{a^2}\frac{\delta_{21}}{\left(1+\xi_0\frac{\pi R^2}{4a^2}\delta_{21}\right)^2}\sum_{n=0}^{\infty}(-1)^n w_n^{-1}\xi_n^2. \quad (79)$$

Substituting (53) into (79), one can ensure that the right-hand-side of (79) equals $1-f^2$, so that relationship (31) is identically met with expressions (77) and (78).

The numerical analysis of set (46) was performed for a subset of 40 equations for $\sigma_3 = \sigma_1$, $\rho/R = 0.8$, and $h_{21} = \sigma_2/\sigma_1 = 10^{-1}$, 10^{-2}, and 10^{-3} (curves *1–3*, respectively, in Figs. 8–12). Figures 8–12 plot f, ψ_2, ψ_3, φ_{a2}, and φ_{a3} vs. the concentration p of the first component.

REFERENCES

1. Yu. P. Emets, *Electrical Properties of Composites with Regular Structure* (Naukova Dumka, Kiev, 1986).
2. B. Ya. Balagurov, Zh. Éksp. Teor. Fiz. **79**, 1561 (1980) [Sov. Phys. JETP **52**, 787 (1980)].
3. B. Ya. Balagurov, Zh. Tekh. Fiz. **51**, 1146 (1981) [Sov. Phys. Tech. Phys. **26**, 651 (1981)].
4. Lord Rayleigh, Philos. Mag. **34**, 481 (1892).
5. B. Ya. Balagurov and V. A. Kashin, Zh. Éksp. Teor. Fiz. **117**, 978 (2000) [JETP **90**, 850 (2000)].
6. B. Ya. Balagurov and V. A. Kashin, Zh. Tekh. Fiz. **71** (1), 106 (2001) [Tech. Phys. **46**, 101 (2001)].
7. B. Ya. Balagurov, Zh. Éksp. Teor. Fiz. **120**, 668 (2001) [JETP **93**, 586 (2001)].
8. Yu. P. Emets, Zh. Éksp. Teor. Fiz. **114**, 1121 (1998) [JETP **87**, 612 (1998)].
9. B. Ya. Balagurov, Zh. Éksp. Teor. Fiz. **119**, 142 (2001) [JETP **92**, 123 (2001)].
10. *Handbook of Mathematical Functions*, Ed. by M. Abramowitz and I. A. Stegun (National Bureau of Standards, Washington, 1964; Nauka, Moscow, 1979).

Translated by V. Isaakyan

Technical Physics, Vol. 47, No. 10, 2002, pp. 1214–1218. Translated from Zhurnal Tekhnicheskoĭ Fiziki, Vol. 72, No. 10, 2002, pp. 10–14.

THEORETICAL AND MATHEMATICAL PHYSICS

On the Polarization Interaction between Two Closely Spaced Conducting Spheres in a Uniform Electrostatic Field

V. A. Koromyslov and A. I. Grigor'ev

Yaroslavl State University, Sovetskaya ul. 14, Yaroslavl, 150000 Russia

e-mail: grig@uniyar.ac.ru

Received April 4, 2002

Abstract—An electrostatic interaction between two separate, grounded, uncharged, perfectly conducting spheres of different radii in a uniform electrostatic field is investigated. It is shown that at a small center-to-center distance of the spheres, the force of the polarization interaction between the spheres depends appreciably more weakly on that distance in comparison to the force of the electrostatic interaction of two elementary dipoles as it should be in view of the interaction between two like polarization charges. © *2002 MAIK "Nauka/Interperiodica".*

INTRODUCTION

An investigation of an electrostatic interaction between two closely spaced conducting particles (drops) in an external electrostatic field is of interest both in connection with calculations of coagulation rates in natural or artificial air-dispersed systems and the decay law for drops that are unstable against the polarization surface charge [1–5]. It is obvious that widely separated uncharged drops of a conducting liquid (for example, water) polarized in an external electrostatic field interact like dipoles with a force inversely proportional to the fourth power of the distance between their centers [6]. When the drops approach each other at small distances (typical for coagulation and decay), the charges induced by the dipoles of the approaching drop start to exert an appreciable influence on the coagulation and decay processes, and, simultaneously, a nonuniformity in the spatial distribution of the polarization charges starts to manifest itself. For example, according to calculations [7, 8], in a particular case of approaching conducting charged spheres in the absence of external electrostatic field, the interaction force between the spheres as a function of the center-to-center distance differs noticeably from the Coulomb law because of the considerable contribution of the polarization interaction.

It is worth noting that analytical solutions of the problem of the electrostatic interaction of two charged conducting spheres in both the absence and presence of a uniform external electrostatic field were obtained long ago (see, e.g., [1, 6, 9, 10]). Nevertheless, because of rather awkward mathematical forms of the solutions found (in the form of infinite series in linear combinations of exponents), a possibility for practical usage of these solutions has appeared only recently due to a convenient mathematical substitution [7] allowing one to sum determining series effectively, as well as owing to the development of contemporary software for analytical calculations (like Mathematica).

(1) We shall describe an electrostatic field in the vicinity of two separate grounded, perfectly conducting spheres with radii R_1 and R_2 placed in a medium with a permittivity ε at a distance h from each other and exposed to an external uniform electrostatic field $\mathbf{E}_0$ parallel to the symmetry axis (see Fig. 1). The *OZ* axis coincides with the symmetry axis.

It is obvious that the potential Φ of the total electrostatic field in the space outside the spheres satisfies the Laplace equation

$$\Delta\Phi = 0 \tag{1}$$

with natural boundary conditions

$$r = R_j: \Phi = 0 \ (j = 1, 2). \tag{2}$$

$$r \longrightarrow \infty: \mathbf{E} \longrightarrow \mathbf{E}_0. \tag{3}$$

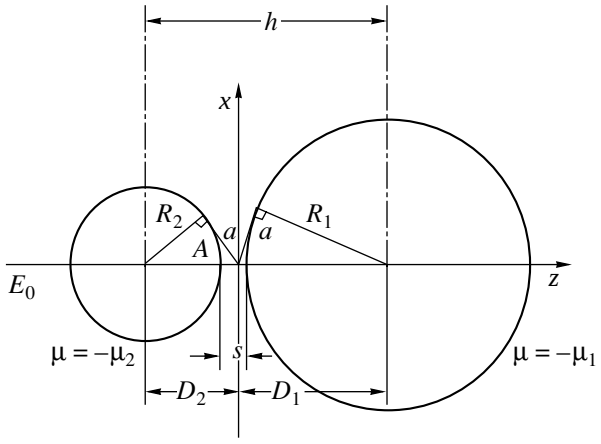

Fig. 1. A system of two spheres with radii R_1 and R_2 in a uniform electrostatic field $\mathbf{E}_0$ directed along the *z* axis.

1063-7842/02/4710-1214$22.00

R_j is the radius of the jth sphere in a bispherical coordinate system, $j = 1, 2$.

The vector **E** of the electric field strength is normal to the surfaces of the spheres. In the vicinity of the jth sphere, it is defined by the expression

$$r = R_j: \mathbf{E}^{(j)} = \mathbf{E}_n^{(j)} = -\frac{\partial\Phi}{\partial n_j}\mathbf{n}_j \ (j = 1, 2).$$

The force of interaction between the spheres is easily calculated in the form [1]

$$\mathbf{F}\mathbf{n}_z = \frac{\varepsilon}{8\pi}\oint_{S_j}\left(\frac{\partial\Phi}{\partial n}\right)^2 \mathbf{n}_z\mathbf{n}_j dS_j, \tag{4}$$

where $\mathbf{n}_z$ is the unit vector of the OZ axis and $\mathbf{n}_j$ is a unit vector normal to the surface element dS_j.

Let us present potential Φ in the space outside the spheres as the sum of the potential Φ_0 of the external uniform electrostatic field and the potential Ψ produced by charges induced at the sphere surfaces ($\Phi = \Psi + \Phi_0$). Both potentials satisfy the Laplace equations

$$\Delta\Psi = 0, \tag{1a}$$

$$\Delta\Psi_0 = 0. \tag{1b}$$

The solution of Eq. (1b) satisfying condition (3) in a spherical coordinate system with the origin at the axis (see Fig. 1) has the simple form

$$\Phi_0 = -\mathbf{E}_0\mathbf{r}. \tag{5}$$

(2) It is reasonable to seek an analytical solution of Eq. (1a) in bispherical coordinates μ, η, and φ that are related to the Cartesian coordinates by the well-known relationships [9, 10]

$$x = \frac{a\sin(\eta)\cos(\eta)}{\cosh(\mu) - \cos(\eta)},$$

$$y = \frac{a\sin(\eta)\sin(\varphi)}{\cosh(\mu) - \cos(\eta)}, \quad z = \frac{a\sinh(\mu)}{\cosh(\mu) - \cos(\eta)}, \tag{6}$$

$$-\infty < \mu < +\infty, \quad 0 < \eta < \pi, \quad 0 < \varphi < 2\pi.$$

In bispherical coordinates, the surfaces S_1 and S_2 of the spheres are described by the equations [9]

$$\mu = \mu_1, \quad \mu = -\mu_2,$$

$$\mu_1 = \ln\left(\frac{D_1 + a}{R_1}\right), \quad \mu_2 = \ln\left(\frac{D_2 + a}{R_2}\right), \tag{7}$$

where a is defined by

$$a = (D_1^2 - R_1^2)^{1/2} = (D_2 - R_2^2)^{1/2}. \tag{8}$$

Here, D_1 and D_2 are the distances between the origin of coordinates and the centers of the spheres, respectively,

$$D_1 = \frac{1}{2h}(h^2 + R_1^2 - R_2^2), \quad D_2 = \frac{1}{2h}(h^2 + R_2^2 - R_1^2), \tag{9}$$

where h is the distance between the centers of the spheres, calculated as

$$h = R_1 + R_2 + s = D_1 + D_2, \tag{10}$$

and s is the separation between the surfaces of the spheres (see Fig. 1).

Taking into account (6), one can obtain an expression for the surface area elements of both spheres and for the cosine of the polar angle Θ. For the second sphere, these expressions have the form

$$dS_2 = \frac{a^2\sin(\eta)d\eta d\varphi}{(\cosh(\mu_2) - \cos(\eta))^2},$$
$$\cos(\Theta) = \frac{1 - \cosh(\mu_2)\cos(\eta)}{\cosh(\mu_2) - \cos(\eta)}. \tag{11}$$

Potential Ψ of the electric field produced by the induced charges distributed over the surfaces of the spheres satisfies Eq. (1a), which in bispherical coordinates has the form [9]

$$\Delta\Psi = \frac{\partial}{\partial\mu}\left(\frac{a\sin(\eta)}{\cosh(\mu) - \cos(\eta)}\frac{\partial\Psi}{\partial\mu}\right)$$
$$+ \frac{\partial}{\partial\eta}\left(\frac{a\sin(\eta)}{\cosh(\mu) - \cos(\eta)}\frac{\partial\Psi}{\partial\eta}\right) \tag{12}$$
$$+ \frac{1}{\sin(\eta)(\cosh(\mu) - \cos(\eta))}\frac{\partial^2\Psi}{\partial\varphi^2} = 0.$$

The solution of Eq. (12) subject to boundary conditions (2) and (3) can easily be written as

$$\Psi = \sqrt{\cosh(\mu) - \cos(\eta)}\sum_{n=0}^{\infty}\left(A_n\exp\left[\left(n + \frac{1}{2}\right)\mu\right]\right.$$
$$\left.\times P_n(\cos(\eta)) + B_n\exp\left[-\left(n + \frac{1}{2}\right)\mu\right]\right)P_n(\cos(\eta)), \tag{13}$$

where A_n and B_n are constants.

In view of (5) and (12), the expression for the total potential Φ takes the form

$$\Phi = \sqrt{\cosh(\mu) - \cos(\eta)}\sum_{n=0}^{\infty}\left(A_n\exp\left[\left(n + \frac{1}{2}\right)\mu\right]\right.$$
$$\left. + B_n\exp\left[-\left(n + \frac{1}{2}\right)\mu\right]\right)P_n(\cos(\eta)) - E_0 z. \tag{14}$$

Let us expand z in this formula in the Legendre polynomials. According to [6],

$$\frac{1}{\sqrt{\cosh(\mu) - \cos(\eta)}}$$
$$= \sqrt{2}\sum_{n=0}^{\infty}\exp\left[-\left(n + \frac{1}{2}\right)|\mu|\right]P_n(\cos(\eta)). \tag{15}$$

Differentiating (15) with respect to μ and taking into account (7), we find the expression for z [6]:

$$|z| = \sqrt{2a}\sqrt{\cosh(\mu)-\cos(\eta)}\sum_{n=0}^{\infty}(2n+1) \times \exp\left[-\left(n+\frac{1}{2}\right)|\mu|\right]P_n(\cos(\eta)). \quad (16)$$

Using boundary condition (3) and substituting expression (16) into (14), we find the expansion coefficients in the expression for the potential of the induced field:

$$A_n = \frac{\sqrt{2}a(2n+1)E_0(\exp[(2n+1)\mu_2]+1)}{\exp[(2n+1)(\mu_1+\mu_2)]-1},$$
$$B_n = -\frac{\sqrt{2}a(2n+1)E_0(\exp[(2n+1)\mu_2]+1)}{\exp[(2n+1)(\mu_1+\mu_2)]-1}. \quad (17)$$

(3) To find the force of interaction between the spheres, let us take into account that the electric field strength in a point A located at the surface of the second sphere (see Fig. 1) is equal to the sum of the electric field strengths of both spheres,

$$E_A = E_A^{(1)} + E_A^{(2)},$$

and the field strength of each sphere is determined by the normal derivative of potential Φ.

The operator of the normal derivative to the surface of the second sphere in bispherical coordinates [9] is

$$\frac{\partial}{\partial n} \equiv -\frac{1}{a}\sqrt{\cosh(\mu_2)-\cos(\eta)}\frac{\partial}{\partial\mu}. \quad (18)$$

Then, the expression for the electric field strength of the second sphere in point A takes the form

$$\mu = -\mu_2: E_A^{(2)} = -\left(\frac{\partial\Phi}{\partial n}\right) = \frac{1}{a}(\cosh(\mu_2)-\cos(\eta))^{3/2} \times \sum_{n=0}^{\infty}\frac{\sqrt{2}a(2n+1)E_0(\exp[(2n+1)\mu_1]+1)}{\exp[(2n+1)(\mu_1+\mu_2)]-1} \times P_n(\cos(\eta))\exp\left[\left(n+\frac{1}{2}\right)\mu_2\right], \quad (19)$$

and for the first sphere,

$$\mu = \mu_1: E_A^{(1)} = -\left(\frac{\partial\Phi}{\partial n}\right) = -\frac{1}{a}(\cosh(\mu_1)-\cos(\eta))^{3/2} \times \sum_{n=0}^{\infty}\frac{\sqrt{2}a(2n+1)E_0(\exp[(2n+1)\mu_2]+1)}{\exp[(2n+1)(\mu_1+\mu_2)]-1} \times P_n(\cos(\eta))\exp\left[\left(n+\frac{1}{2}\right)\mu_1\right]. \quad (20)$$

In order to simplify (19) and (20), we introduce the following notation:

$$Y_n = \sqrt{2}(2n+1)\exp\left[\left(n+\frac{1}{2}\right)\mu_2\right] \times \frac{(2n+1)(\exp[(2n+1)\mu_1]+1)}{\exp[(2n+1)(\mu_1+\mu_2)]-1}, \quad (21)$$

$$Z_n = \sqrt{2}(2n+1)\exp\left[\left(n+\frac{1}{2}\right)\mu_1\right] \times \frac{(2n+1)(\exp[(2n+1)\mu_2]+1)}{\exp[(2n+1)(\mu_1+\mu_2)]-1}. \quad (22)$$

Substituting (21) and (22) into (19) and (20), we find

$$\mu = -\mu_2: E_A^{(2)} = -\left(\frac{\partial\Phi}{\partial n}\right) = E_0(\cosh(\mu_2) - \cos(\eta))^{3/2}\sum_{n=0}^{\infty}Y_nP_n(\cos(\eta)), \quad (23)$$

$$\mu = \mu_1: E_A^{(1)} = -\left(\frac{\partial\Phi}{\partial n}\right) = E_0(\cosh(\mu_1) - \cos(\eta))^{3/2}\sum_{n=0}^{\infty}Z_nP_n(\cos(\eta)). \quad (24)$$

Taking into account that $\cos(\pi) = -1$ and $P_n(-1) = (-1)^n$, we finally obtain an expression for the strength of the electric field produced by the second sphere in point A:

$$\mu = -\mu_2; \quad \eta = \pi: E_A^{(2)} = -\left(\frac{\partial\Phi}{\partial n}\right) = E_0(\cosh(\mu_2) - \cos(\eta))^{3/2}\sum_{n=0}^{\infty}(-1)^nY_n. \quad (25)$$

Similarly for the first sphere

$$\mu = -\mu_1; \quad \eta = \pi: E_A^{(1)} = -\left(\frac{\partial\Phi}{\partial n}\right) = E_0(\cosh(\mu_1) - \cos(\eta))^{3/2}\sum_{n=0}^{\infty}(-1)^nZ_n. \quad (26)$$

In order to describe the interaction between the spheres, it is sufficient to calculate the force acting on either sphere. Then, the force acting on the other sphere is determined by Newton's third law. In the case when an external electric field is directed along the z axis, expression (4) is transformed into the form

$$F = \frac{\varepsilon}{8\pi}\oint_{S_j}\left(\frac{\partial\Phi}{\partial n}\right)^2\cos(\Theta)dS_j. \quad (27)$$

Then, the relationship for the force acting on the second sphere takes the form

$$\mu = -\mu_2: F^{(2)} = \frac{\varepsilon}{8\pi}\int_{S_2}\left(\frac{\partial\Phi}{\partial n}\right)^2\cos(\Theta)dS_2. \quad (28)$$

From (11), (25), and (28), we find

$$F^{(2)} = \frac{\varepsilon}{4}a^2E_0^2\left[\sum_{n=0}^{\infty}Y_n^2\int_0^{\pi}P_n^2(\cos(\eta))(\sin(\eta))d\eta - \cosh(\mu_2)\sum_{n=0}^{\infty}(Y_nP_n(\cos(\Theta)))^2\cos(\eta)\sin(\eta)d\eta\right]. \quad (29)$$

Using the orthogonality of the Legendre polynomials, we obtain

$$\int_0^{\pi}\sum_{n=0}^{\infty}Y_n^2P_n^2(\cos(\eta))\sin(\eta)d\eta = \sum_{n=0}^{\infty}\frac{2}{2n+1}Y_n^2, \quad (30)$$

$$\int_0^{\pi}\sum_{n=0}^{\infty}(Y_nP_n(\cos(\eta)))^2\cos(\eta)\sin(\eta)d\eta = \sum_{n=0}^{\infty}Y_{n-1}Y_n\frac{n}{2n-1}\frac{2}{2n+1} + \sum_{n=0}^{\infty}Y_{n+1}Y_n\frac{n+1}{2n+3}\frac{2}{2n+1}. \quad (31)$$

In view of (30) and (31), (29) yields the force acting on the second sphere:

$$F^{(2)} = \frac{\varepsilon}{4}a^2E_0^2\sum_{n=0}^{\infty}\frac{2}{2n+1} \times Y_n\left[Y_n - \cosh(\mu_2)\left(Y_{n+1}\frac{n+1}{2n+3} + Y_{n-1}\frac{n}{2n-1}\right)\right]. \quad (32)$$

Taking into account (7), we find

$$\exp(\alpha\mu_2) = \exp\left[\alpha\ln\left(\frac{D_2+a}{R_2}\right)\right] = \left(\frac{D_2+a}{R_2}\right)^{\alpha},$$
$$\exp(\alpha\mu_1) = \exp\left[\alpha\ln\left(\frac{D_1+a}{R_1}\right)\right] = \left(\frac{D_1+a}{R_1}\right)^{\alpha}. \quad (33)$$

Substituting the expression for $\cosh(\mu_2)$ in terms of exponents (33) into (32), we arrive at an equation for the force $F^{(2)}$ acting on the second sphere in the form

$$F^{(2)} = \frac{\varepsilon}{4}a^2E_0^2\sum_{n=0}^{\infty}\frac{2}{2n+1}Y_n\left[Y_n - \frac{1}{2}\left(\frac{D_2+a}{R_2} + \frac{R_2}{D_2+a}\right)\left(Y_{n+1}\frac{n+1}{2n+3} + Y_{n-1}\frac{n}{2n-1}\right)\right], \quad (34)$$

$$Y_n = \sqrt{2}(2n+1)\left(\frac{D_2+a}{R_2}\right)^{(n+1/2)} \times\left\{\frac{(2n+1)\left[\left(\frac{D_1+a}{R_1}\right)^{(2n+1)}+1\right]}{\left[\left(\frac{D_1+a}{R_1}\right)\left(\frac{D_2+a}{R_2}\right)\right]^{(2n+1)}-1}\right\}. \quad (35)$$

(4) To simplify the numerical calculation, we represent the expression for the force component in dimensionless form by introducing the dimensionless variables $\gamma = R_1/R_2$ and $r = s/R_2$. Finally, we find

$$F^{(2)} = \frac{\varepsilon}{4}R_2^2\left\{\left[\frac{(\gamma+1+r)^2-\gamma^2+1}{2(\gamma+1+r)}\right]^{-1}-1\right\} \times E_0^2\sum_{n=0}^{\infty}\frac{2}{2n+1}Y_n\left[Y_n - \frac{1}{2}\left(G+\frac{1}{G}\right)\times\left(\frac{n+1}{2n+3}Y_{n+1} + \frac{n}{2n-1}Y_{n-1}\right)\right], \quad (36)$$

$$Y_n = \sqrt{2}(2n+1)G^{(n+1/2)}\left[\frac{(2n+1)(H^{(2n+1)}+1)}{H^{(2n+1)}G^{(2n+1)}-1}\right]. \quad (37)$$

Eventually, expression (36) for the dimensionless force of interaction between the spheres in terms of $R_2^2E_0^2\varepsilon$ takes the form

$$f = \frac{1}{4}\left\{\left[\frac{(\gamma+1+r)^2-\gamma^2+1}{2(\gamma+1+r)}\right]^{-1}-1\right\} \times\sum_{n=0}^{\infty}\frac{2}{2n+1}Y_n\left[Y_n - \frac{1}{2}\left(G+\frac{1}{G}\right)\times\left(\frac{n+1}{2n+3}Y_{n+1} + \frac{n}{2n-1}Y_{n-1}\right)\right]. \quad (38)$$

(5) Figure 2 shows a surface describing the dependence of the dimensionless force of interaction [calculated using (38) in view of (37)] on both the ratio γ of their radii and dimensionless distance r between the centers of the spheres in the space of parameters r and γ.

For a more detailed analysis, Fig. 3 shows the dependence of the dimensionless force f as a function

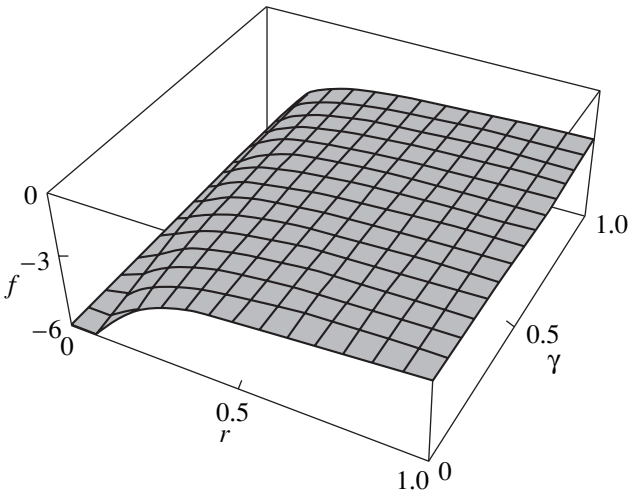

Fig. 2. Dependence of the dimensionless force acting on one of the spheres on the ratio of the sphere radii and the dimensionless distance between the spheres.

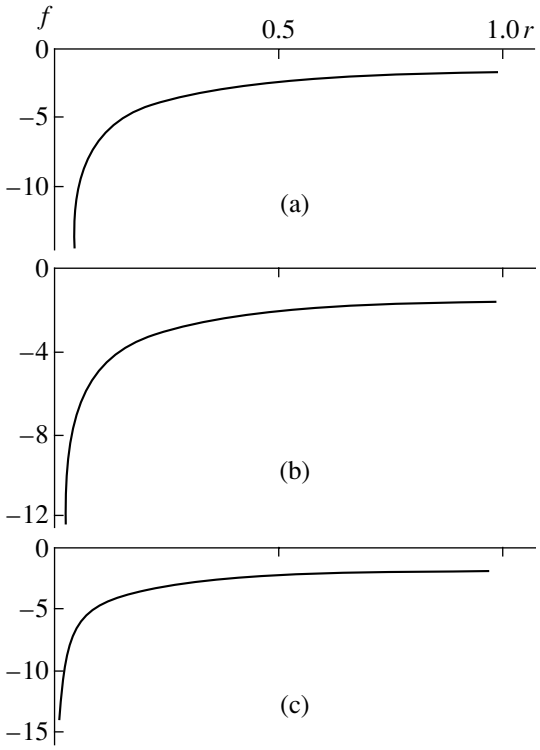

Fig. 3. Dimensionless force f as a function of the dimensionless distance r at different ratios of the sphere radii. γ: (a) 0.1, (b) 0.5, and (c) 1.0.

of the dimensionless distance r at different magnitudes of the ratios of the spheres' radii $\gamma = R_1/R_2$. It is seen that the force of attraction between the spheres increases rather slowly with decreasing distance between their centers approximately as $f \sim r^{-\alpha}$, where $\alpha \approx 1$, whereas this dependence would be much stronger ($\alpha = 4$) for an electrostatic interaction between elementary dipoles [6].

It is worth noting that the reasons presented are also applicable, in general, to nongrounded separate spheres of the same radii.

The pressure of an electric field on the surfaces of the spheres reaches its peak at points of the surface located at the *OZ* axis opposite to each other. In a real situation of spherical drops in clouds at small distances between them, the electrostatic pressure may become high and two situations are possible: (a) if the pressure of electric field in regions with the highest surface density of the induced charge is less than the Laplace pressure, then the drops coalesce into a single one, or (b) if the pressure of electric field exceeds the Laplace pressure, then an instability may take place; i.e., the drops eject toward each other jets of finely dispersed, highly charged daughter droplets [2].

CONCLUSION

Two separate grounded, perfectly conducting spheres of different radii placed in an external uniform electrostatic field directed along the axis passing through the centers of the spheres always attract each other. However, the dependence of the attraction force on the distance between the centers of the spheres, which has the form $f \sim r^{-n}$ (the power n is a function of r), turns out to be very weak at small distances (at a dimensionless distance $r \leq 1$). In this case, the power n is small: $n \approx 1$, whereas $n = 4$ for the interaction between two elementary dipoles.

REFERENCES

1. M. H. Davis, Q. J. Mech. Appl. Math. **176**, 499 (1964).
2. A. I. Grigor'ev and S. O. Shiryaeva, J. Phys. D **23**, 1361 (1990).
3. E. I. Mukhina and A. I. Grigor'ev, Zh. Tekh. Fiz. **62** (2), 18 (1992) [Sov. Phys. Tech. Phys. **37**, 122 (1992)].
4. V. A. Koromyslov, A. I. Grigor'ev, and S. O. Shiryaeva, Zh. Tekh. Fiz. **68** (8), 31 (1998) [Tech. Phys. **43**, 904 (1998)].
5. I. E. Mazets, Zh. Tekh. Fiz. **70** (10), 8 (2000) [Tech. Phys. **45**, 1238 (2000)].
6. W. R. Smythe, *Static and Dynamic Electricity* (McGraw-Hill, New York, 1950; Inostrannaya Literatura, Moscow, 1954).
7. V. A. Saranin, Usp. Fiz. Nauk **169**, 453 (1999).
8. E. A. Shcherba, A. I. Grigor'ev, and V. A. Koromyslov, Zh. Tekh. Fiz. **72** (1), 15 (2002) [Tech. Phys. **47**, 13 (2002)].
9. H. Buchholz, *Elektrische und magnetische Potentialfelder* (Springer-Verlag, Berlin, 1957; Inostrannaya Literatura, Moscow, 1961).
10. G. M. Panchenkov and L. K. Tsabek, *Behavior of Emulsions at External Electric Field* (Khimiya, Moscow, 1969).

Translated by N. Mende

Technical Physics, Vol. 47, No. 10, 2002, pp. 1219–1225. Translated from Zhurnal Tekhnicheskoĭ Fiziki, Vol. 72, No. 10, 2002, pp. 15–21.

GASES AND LIQUIDS

Analytical Calculation of the Velocity of a Rarefied Gas Sliding around a Solid Cylindrical Surface

V. N. Popov

Lomonosov Pomor State University, Arkhangelsk, 163006 Russia
e-mail: popov.vasily@pomorsu.ru

Received March 13, 2002

Abstract—An analytical method for solving the half-space boundary problem of a nonuniform (in both temperature and mass flow rate) rarefied gas flow along a solid cylindrical surface is developed in the framework of the inhomogeneous kinetic Boltzmann equation with the collision operator in the ellipsoidal–statistical model. In the linear approximation in the Knudsen number, the corrections to the coefficients of thermal and isothermal slidings are found in view of the interface curvature. A comparison with the literature data is presented. © *2002 MAIK "Nauka/Interperiodica".*

INTRODUCTION

The set of boundary conditions in a rarefied gas flow along an arbitrary smooth surface was found in [1] by the Bhatnagar–Gross–Krook (BGK) model of the kinetic Boltzmann equation. Later, this problem was solved in the case of a solid spherical surface by moment methods for the linearized Boltzmann equation with the collision operator in both the Boltzmann form [2] and ellipsoidal–statistical (ES) model [3, 4]. In [5], an exact analytical expression for the coefficient β_R was found in a closed form using the method of elementary solutions (Keis method) [6] on the basis of the ES model. This expression makes it possible to take into account the dependence of the thermal sliding coefficient on the radius of curvature for a solid surface flowed around by a rarefied gas. The value of the coefficient β_R found in [5] by numerically integrating final expressions is in good agreement with the results obtained in [2, 7, 8].

The aim of this paper is to calculate the velocity of a rarefied gas sliding around a solid cylindrical surface by the method developed in [5] in view of the interface curvature influence on the coefficients of thermal and isothermal slidings.

PROBLEM STATEMENT: DERIVATION OF BASIC EQUATIONS

Consider a temperature nonuniform stream of a rarefied gas flowing around a solid cylindrical surface at low deviations from an equilibrium state. The gas flow dynamics will be described by the Boltzmann kinetic equation with a linearized collision operator in the ES model [9, 10] expressed in a cylindrical coordinate system with the *Oz* axis coinciding with the cylinder axis. We assume that the temperature gradient is perpendicular to the surface at large distances from it.

Let us linearize the distribution function describing the gas state with respect to a locally equilibrium distribution function in the Chapman–Enskog approximation [11]. Expanding function $Y(\rho, \varphi, C_i)$, implying the deviation of the gas molecule velocity and coordinate distribution function in the Knudsen layer from that in the gas volume, in the small parameter $1/R$,

$$Y(\rho, \varphi, C_i) = Y^{(1)}(\rho, \varphi, C_i) + R^{-1}Y^{(2)}(\rho, \varphi, C_i) + \ldots, \quad (1)$$

we arrive at the set of one-dimensional integrodifferential equations

$$C_\rho \frac{\partial Y^{(1)}}{\partial \rho} + Y^{(1)}(\rho, \varphi, C_i) = \pi^{-3/2}\int \exp(-C'^2) \times K(\mathbf{C}, \mathbf{C}')Y^{(1)}(\rho, \varphi, C_i')d^3C_i', \quad (2)$$

$$C_\rho \frac{\partial Y^{(2)}}{\partial \rho} + Y^{(2)}(\rho, \varphi, C_i) = \pi^{-3/2}\int \exp(-C'^2) \times K(\mathbf{C}, \mathbf{C}')Y^{(2)}(\rho, \varphi, C_i')d^3C_i' - C_\varphi^2 \frac{\partial Y^{(1)}}{\partial C_\rho} + C_\rho C_\varphi \frac{\partial Y^{(1)}}{\partial C_\varphi} - C_\varphi \frac{\partial Y^{(1)}}{\partial \varphi} \quad (3)$$

with the boundary conditions

$$Y^{(1)}(R, \varphi, C_i) = -2C_\varphi U_\varphi^{(1)}\big|_S + C_\varphi\left(C^2 - \frac{5}{2}\right)k, \quad C_\rho > 0,$$

$$Y^{(2)}(R, \varphi, C_i) = -2C_\varphi U_\varphi^{(2)}\big|_S, \quad C_\rho > 0,$$

$$Y^{(1)}(\infty, \varphi, C_i) = 0, \quad Y^{(2)}(\infty, \varphi, C_i) = 0,$$

yielding first two terms of the expansion (1). Here, $\rho(3\mu_g/2p)\beta$ is a dimensional radius vector; βU_i, the components of the gas mass velocity; βC_i, the components of the gas molecule velocity; μ_g, the gas dynamic viscosity; $\beta = (2k_BT_S/m)^{1/2}$; p, the static pressure; R and S, the radius and surface of the cylinder, respectively;

$$k = \frac{1}{T_S}\frac{\partial T}{R\partial\varphi}\bigg|_S,$$

and

$$K(\mathbf{C}, \mathbf{C}') = 1 + 2\mathbf{C}\mathbf{C}' + \frac{2}{3}\left(C^2 - \frac{3}{2}\right)\left(C'^2 - \frac{3}{2}\right) - 2C_iC_j\left(C_i'C_j' - \frac{1}{3}\delta_{ij}C'^2\right).$$

Equation (2) describes the processes taking place at the boundary of a solid plane surface. Equation (3) allows one to take into account the interface curvature.

Let us seek a solution of (2) in the form of an expansion in two orthogonal polynomials:

$$Y^{(1)}(\rho, \varphi, C_i) = C_\varphi Y_a^{(1)}(\rho, \varphi, C_\rho) + C_\varphi(C_\varphi^2 + C_z^2 - 2)Y_b^{(1)}(\rho, \varphi, C_\rho). \quad (4)$$

Note that the orthogonality is understood here in terms of the scalar product

$$(f, g) = \int_{-\infty}^{+\infty} f(\rho, \varphi, C_i)g(\rho, \varphi, C_i)\exp(-C^2)d^3C_i.$$

We will look for a solution of (3) in the form

$$Y^{(2)}(\rho, \varphi, C_i) = C_\varphi Y_a^{(2)}(\rho, \varphi, C_\rho). \quad (5)$$

Denote $\mu = C_\mu$. Then, substituting expansions (4) and (5) into (3), multiplying the resulting equation by $C_\varphi\exp(-C_\varphi^2 - C_z^2)$ and integrating with respect to C_φ and C_z between $-\infty$ and $+\infty$, we find the equation for the function $Y_a^{(2)}(\rho, \varphi, \mu)$:

$$\mu\frac{\partial Y_n^{(2)}}{\partial\rho} + Y_a^{(2)}(\rho, \varphi, \mu) = \frac{1}{\sqrt{\pi}}\int_{-\infty}^{\infty} Y_a^{(2)}(\rho, \varphi, \mu')\exp(-\mu'^2)d\mu - \frac{\mu}{\sqrt{\pi}}\int_{-\infty}^{\infty}\mu' Y_a^{(2)}(\rho, \varphi, \mu')\exp(-\mu'^2)d\mu' \quad (6)$$

$$+ \mu Y_a^{(1)}(\rho, \varphi, \mu) - \frac{3}{2}\frac{\partial Y_a^{(1)}}{\partial\mu} + 3\mu Y_b^{(1)}(\rho, \varphi, \mu) - \frac{3}{2}\frac{\partial Y_b^{(1)}}{\partial\mu}$$

with the boundary conditions

$$Y_a^{(2)}(R, \varphi, \mu) = -2U_\varphi^{(2)}\big|_S, \quad \mu > 0, \qquad Y_a^{(2)}(\infty, \varphi, \mu) = 0. \quad (7)$$

In view of the fact that in the case of a rarefied gas sliding along a solid plane surface, the results found on the basis of the ES and BGK models of the Boltzmann kinetic equation coincide, we have [6]

$$Y_a^{(1)}(\rho, \varphi, \mu) = \int_0^\infty a(\eta, \varphi)F(\eta, \mu)\exp(-x/\eta)d\eta,$$

$$x = \rho - R,$$

$$Y_b^{(1)}(\rho, \varphi, \mu) = k\int_0^\infty \exp(-x/\eta)\delta(\eta - \mu)d\eta, \quad (8)$$

$$F(\eta, \mu) = \frac{1}{\sqrt{\pi}}\eta P\frac{1}{\eta - \mu} + \exp(\eta^2)\lambda(\eta)\delta(\eta - \mu),$$

$$\lambda(z) = 1 + \frac{1}{\sqrt{\pi}}z\int_{-\infty}^{\infty}\frac{\exp(-\mu^2)}{\mu - z}d\mu,$$

$$a(\eta, \varphi) = \frac{\eta(\eta - Q_1)\exp(-\eta^2)X(-\eta)}{2|\lambda^+(\eta)|^2}k,$$

$$\lambda^\pm(\eta) = \lambda(\eta) \pm \sqrt{\pi}i\eta\exp(-\eta^2),$$

$$X(z) = \frac{1}{z}\exp\left\{\frac{1}{\pi}\int_0^\infty\frac{\Theta(\tau) - \pi}{\tau - z}d\tau\right\}, \quad (9)$$

$$\Theta(\tau) - \pi = -\pi/2 - \arctan\frac{\lambda(\tau)}{\sqrt{\pi}\tau\exp(-\tau^2)}.$$

Here, $\lambda(z)$ is the Cercignani dispersion function; Px^{-1}, the distribution of the principal integral value in the integration of x^{-1}; $\delta(x)$, the Dirac delta function; and $\Theta(\tau)$, a single-valued regular branch of the function argument $\lambda^+(\tau)$ determined by the condition $\Theta(0) = 0$.

Thus, the problem reduces to solving Eq. (6) with boundary conditions (7).

INFLUENCE OF THE SURFACE CURVATURE ON THE COEFFICIENT OF THERMAL SLIDING

The substitution

$$Y^{(2)}_{a\eta}(\rho, \varphi, \mu) = \psi(\eta, \varphi, \mu)\exp(-x/\eta)$$

turns (6) into the nonuniform characteristic equation

$$\left(1-\frac{\mu}{\eta}\right)\psi(\eta, \varphi, \mu) = \frac{1}{\sqrt{\pi}}\int_{-\infty}^{\infty}\psi(\eta, \varphi, \mu')\exp(-\mu'^2)d\mu' - \frac{1}{\sqrt{\pi}}\mu\int_{-\infty}^{\infty}\mu'\psi(\eta, \varphi, \mu')\exp(-\mu'^2)d\mu' + Z(\eta, \varphi, \mu), \quad (10)$$

$$Z(\eta, \varphi, \mu) = \mu a(\eta, \varphi)F(\eta, \mu) - \frac{3}{2}a(\eta, \varphi)\frac{\partial F}{\partial \mu} + 3\mu k\delta(\eta-\mu) - \frac{3k}{2}\frac{\partial}{\partial\mu}\delta(\eta-\mu). \quad (11)$$

Multiplying (10) by $\exp(-\mu^2)$ and integrating with respect to μ between the limits from $-\infty$ to ∞, we find

$$\int_{-\infty}^{\infty}\mu\psi(\eta, \varphi, \mu)\exp(-\mu^2)d\mu = -\eta\int_{-\infty}^{\infty}Z(\eta, \varphi, \mu)\exp(-\mu^2)d\mu.$$

Let us rewrite (10) in view of the fact that the value of the second integral is equal to zero [5]:

$$(\eta-\mu)\psi(\eta, \varphi, \mu) = \frac{1}{\sqrt{\pi}}\eta m(\eta, \varphi) + \eta Z(\eta, \varphi, \mu), \quad (12)$$

$$m(\eta, \varphi) = \int_{-\infty}^{\infty}\psi(\eta, \varphi, \mu)\exp(-\mu^2)d\mu. \quad (13)$$

The general solution of Eq. (12) in the space of generalized functions has the form [12]

$$\psi(\eta, \varphi, \mu) = \eta P\frac{1}{\eta-\mu}\left[\frac{1}{\sqrt{\pi}}m(\eta, \varphi) + Z(\eta, \varphi, \mu)\right] + g(\eta, \varphi)\delta(\eta-\mu).$$

We find the explicit form of the function $g(\eta, \varphi)$ substituting $\psi(\eta, \varphi, \mu)$ into (13)

$$g(\eta, \varphi) = \left[m(\eta, \varphi)\lambda(\eta) - \eta\int_{-\infty}^{\infty}P\frac{1}{\eta-\mu}Z(\eta, \varphi, \mu)\exp(-\mu^2)d\mu\right]\exp(\eta^2).$$

In [5], it is shown that

$$\int_{-\infty}^{\infty}P\frac{1}{\eta-\mu}\mu F(\eta, \mu)\exp(-\mu^2)d\mu = -1,$$

$$\int_{-\infty}^{\infty}P\frac{1}{\eta-\mu}(F(\eta, \mu))'_\mu\exp(-\mu^2)d\mu = -1,$$

$$\int_{-\infty}^{\infty}P\frac{1}{\eta-\mu}\mu\delta(\eta-\mu)\exp(-\mu^2)d\mu = 2\exp(-\eta^2)\left(\eta^2-\frac{1}{2}\right),$$

$$\int_{-\infty}^{\infty}P\frac{1}{\eta-\mu}(\delta(\eta-\mu))'_\mu\exp(-\mu^2)d\mu = 2\exp(-\eta^2)\left(\eta^2-\frac{1}{2}\right).$$

Taking (11) into account, we find

$$\int_{-\infty}^{\infty}P\frac{1}{\eta-\mu}Z(\eta, \varphi, \mu)\exp(-\mu^2)d\mu = \frac{1}{2}a(\eta, \varphi) + 3k\exp(-\eta^2)\left(\eta^2-\frac{1}{2}\right).$$

In view of results found, the solution of Eq. (6) has the form

$$Y^{(2)}_a(\rho, \varphi, \mu) = \int_0^{\infty}\psi(\eta, \varphi, \mu)\exp(-x/\eta)d\eta,$$

$$\psi(\eta, \varphi, \mu) = \eta P\frac{1}{\eta-\mu}\left[\frac{1}{\sqrt{\pi}}m(\eta, \varphi) + Z(\eta, \varphi, \mu)\right] + \left[m(\eta, \varphi)\exp(\eta^2)\lambda(\eta) - \frac{1}{2}\eta a(\eta, \varphi)\exp(\eta^2) - 3k\eta\left(\eta^2-\frac{1}{2}\right)\right]\delta(\eta-\mu). \quad (14)$$

Allowing for (7), we turn from (14) to a singular integral equation with a Cauchy kernel

$$-2U^{(2)}_\varphi\big|_S = \frac{1}{\sqrt{\pi}}\int_0^{\infty}\frac{\eta m(\eta, \varphi)}{\eta-\mu}d\eta + \int_0^{\infty}nZ(\eta, \varphi, \mu)\frac{d\eta}{\eta-\mu} + m(\mu, \varphi)\exp(\mu^2)\lambda(\mu) \quad (15)$$

$$-\frac{1}{2}\mu a(\mu, \varphi)\exp(\mu^2) - 3k\mu\left(\mu^2 - \frac{1}{2}\right), \quad \mu > 0.$$

In [5], it is shown that

$$\int_0^\infty \eta P\frac{1}{\eta - \mu}a(\eta, \varphi)F(\eta, \mu)d\eta = (\mu Y_a^{(1)}(R, \varphi, \mu))'_\mu,$$

$$\int_0^\infty \eta P\frac{1}{\eta - \mu}(a(\eta, \varphi)F(\eta, \mu))'_\mu d\eta = \frac{1}{2}(\mu Y_a^{(1)}(R, \varphi, \mu))''_{\mu\mu},$$

$$\int_0^\infty \eta P\frac{1}{\eta - \mu}\delta(\eta - \mu)d\eta = 1,$$

$$\int_0^\infty \eta P\frac{1}{\eta - \mu}(\delta(\eta - \mu))'_\mu d\mu = 0.$$

Taking into consideration that

$$Y_a^{(1)}(R, \varphi, \eta) = (\eta^2 + Q_2)k,$$

we find

$$\int_0^\infty \eta Z(\eta, \varphi, \mu)\frac{d\eta}{\eta - \mu} = \left(3\mu^3 + Q_2\mu - \frac{3}{2}\mu\right)k.$$

Here, Q_n denotes the Loyalka integrals [13]

$$Q_n = \frac{2}{\sqrt{\pi}}\int_0^\infty \frac{t^{n+1}\exp(-t^2)dt}{X(-t)}.$$

Using the results found, let us rewrite (15) in the form

$$f(\mu, \varphi) = m(\mu, \varphi)\exp(\mu^2)\lambda(\mu) + \frac{1}{\sqrt{\pi}}\int_0^\infty \frac{\eta m(\eta, \varphi)}{\eta - \mu}d\eta, \quad \mu > 0, \tag{16}$$

$$f(\mu, \varphi) = -2U_\varphi^2\big|_S - Q_2\mu + \frac{1}{2}a(\eta, \varphi)\exp(\eta^2). \tag{17}$$

Introduce the auxiliary function

$$M(z, \varphi) = \frac{1}{2\pi i}\int_0^\infty \frac{\eta m(\eta, \varphi)}{\eta - z}d\eta$$

and reduce (16) to the Riemann boundary value problem in a half-space [14]:

$$M^+(\mu, \varphi)\lambda^+(\mu) - M^-(\mu, \varphi)\lambda^-(\mu) = \mu f(\mu, \varphi)\exp(-\mu^2), \quad \mu > 0. \tag{18}$$

The coefficient of boundary value problem (18) coincides with that for a gas sliding along a solid plane surface [5]. Therefore, (18) can be reduced to the problem with a jump [14]

$$M^+(\mu, \varphi)X^+(\mu) - M^-(\mu, \varphi)X^-(\mu) = \mu f(\mu, \varphi)\exp(-\mu^2)\frac{X^-(\mu)}{\lambda^-(\mu)}, \quad \mu > 0,$$

which has a solution vanishing at infinity if the condition

$$\frac{2}{\sqrt{\pi}}\int_0^\infty \frac{f(t, \varphi)}{X(-t)}t\exp(-t^2)dt = 0 \tag{19}$$

is satisfied [15].

Substituting (17) into (19), in view of (9), we have

$$U_\varphi^{(2)}\big|_S = \frac{k}{2}\left[Q_1Q_2 - \frac{1}{2\sqrt{\pi}}\int_0^\infty \frac{t^2(t - Q_1)}{|\lambda^+(t)|^2}\exp(-t^2)dt\right].$$

Since

$$\frac{1}{\sqrt{\pi}}\int_0^\infty \frac{t^2(t - Q_1)}{|\lambda^+(t)|^2}\exp(-t^2)dt = -3Q_3 - Q_1Q_2, \tag{20}$$

we find

$$U_\varphi^{(2)}\big|_S = \frac{3k}{4}[Q_3 + Q_1Q_2].$$

Substituting the values of the Loyalka integrals [13] $Q_1 = -1.01619$, $Q_2 = -1.26663$, and $Q_3 = -1.8207$ into the expression found, we have $U_\varphi^{(2)}\big|_S = -0.40017k$.

Allowing for (1), this yields the velocity of thermal sliding of a rarefied gas around a solid cylindrical surface

$$U_\varphi\big|_S = U_\varphi^{(1)}\big|_S + R^{-1}U_\varphi^{(2)}\big|_S = (0.38332 - 0.40017R^{-1})k. \tag{21}$$

Since, according to a standard method to make physical quantities dimensionless, $R^{-1} = (3/\sqrt{\pi})\,\mathrm{Kn}$, returning to dimensional quantities in (21), we obtain

$$U_\varphi\big|_S = 1.14995\nu(1 - 1.7684\mathrm{Kn})\frac{1}{T_S}\frac{\partial T}{R\partial\varphi}\bigg|_S.$$

Thus, $\beta_{R\perp} = 1.7684$ in the case of a rarefied gas flow around a solid cylindrical surface.

INFLUENCE OF THE SURFACE CURVATURE ON THE COEFFICIENT OF ISOTHERMAL SLIDING

Assume that the mass velocity component tangent to a surface is not constant but varies along the direction

of the normal to a surface; i.e.,

$$k_1 = \left.\frac{\partial U_\varphi}{\partial \rho}\right|_S$$

is nonzero.

In this case, we seek a solution of (2) and (3) in the form [6]

$$Y^{(j)}(\rho, \varphi, C_i) = C_\varphi Y_a^{(j)}(\rho, \varphi, C_\rho); \quad j = 1, 2. \quad (22)$$

Substituting expansions (22) into (3), multiplying the resulting equation by $C_\varphi \exp(-C_\varphi^2 - C_z^2)$, and integrating with respect to C_φ and C_z from $-\infty$ to $+\infty$, we find the equation for the function $Y_a^{(2)}(\rho, \varphi, \mu)$:

$$\mu\frac{\partial Y_a^{(2)}}{\partial \rho} + Y_a^{(2)}(\rho, \varphi, \mu)$$
$$= \frac{1}{\sqrt{\pi}}\int_{-\infty}^{\infty} Y_a^{(2)}(\rho, \varphi, \mu')\exp(-\mu'^2)d\mu'$$
$$-\frac{\mu}{\sqrt{\pi}}\int_{-\infty}^{\infty}\mu' Y_a^{(2)}(\rho, \varphi, \mu')\exp(-\mu'^2)d\mu'$$
$$+\mu Y_a^{(1)}(\rho, \varphi, \mu) - \frac{3}{2}\frac{\partial Y_a^{(1)}}{\partial \mu}$$

with boundary conditions (7). Here, $Y_a^{(1)}(\rho, \varphi, \mu)$ is determined by relationship (8):

$$a(\eta, \varphi) = \frac{2\exp(-\eta^2)X(-\eta)}{3|\lambda^+(\eta)|^2}k_1,$$

$$Y_a^{(1)}(R, \varphi, \eta) = \frac{4}{3}(\eta + Q_1)k_1.$$

In the case under consideration,

$$Z(\eta, \varphi, \mu) = \mu a(\eta, \varphi)F(\eta, \mu) - \frac{3}{2}a(\eta, \varphi)\frac{\partial F}{\partial \mu},$$

$$\int_{-\infty}^{\infty} P\frac{1}{\eta - \mu}Z(\eta, \varphi, \mu)\exp(-\mu^2)d\mu = \frac{1}{2}a(\eta, \varphi),$$

$$\int_{-\infty}^{\infty}\eta Z(\eta, \varphi, \mu)\frac{d\eta}{\eta - \mu} = \frac{2}{3}(4\mu^2 + 2Q_1\mu - 3)k_1,$$

$$f(\mu, \varphi) = -2U_\varphi^{(2)}\big|_S - \frac{2}{3}(4\mu^2 + 2Q_1\mu - 3)k_1$$
$$+\frac{1}{2}a(\mu, \varphi)\exp(\mu^2),$$

$$U_\varphi^{(2)}\big|_S = \frac{k_1}{3}\left[4Q_2 + 2Q_1 - 3Q_0\right.$$
$$\left. - \frac{1}{\sqrt{\pi}}\int_0^{\infty}\frac{t^2}{|\lambda^+(t)|^2}\exp(-t^2)dt\right].$$

Taking into account that

$$\frac{1}{\sqrt{\pi}}\int_0^{\infty}\frac{t^2}{|\lambda^+(t)|^2}\exp(-t^2)dt = \frac{3}{2},$$
$$2Q_2 + Q_1^2 = -\frac{3}{2}, \quad (23)$$

we find

$$U_\varphi^{(2)}\big|_S = -\frac{1}{2}k_1.$$

In view of (1), the velocity of a rarefied gas isothermally sliding around a solid cylindrical surface is

$$U_\varphi|_S = U_\varphi^{(1)}\big|_S + R^{-1}U_\varphi^{(2)}\big|_S$$
$$= (0.67746 - 0.50000R^{-1})k_1. \quad (24)$$

Turning to dimensional quantities in (24), we obtain

$$U_\varphi|_S = 1.14665\lambda(1 - 1.24922\mathrm{Kn})\left.\frac{\partial U_\varphi}{\partial \rho}\right|_S.$$

Thus, $C_{m\perp}^{(1)} = 1.24922$.

LONGITUDINAL FLOW AROUND A CYLINDRICAL SURFACE (THERMAL SLIDING)

Assume that the temperature gradient is directed along the cylinder axis at large distances from its surface. Let us denote

$$k_2 = \left.\frac{1}{T_S}\frac{\partial T}{\partial z}\right|_S.$$

We will look for a solution of (2) and (3) in the form

$$Y^{(1)}(\rho, C_i) = C_z Y_a^{(1)}(\rho, C_\rho)$$
$$+ C_z(C_\varphi^2 + C_z^2 - 2)Y_b^{(1)}(\rho, C_\rho), \quad (25)$$

$$Y^{(2)}(\rho, C_i) = C_z Y_a^{(2)}(\rho, C_\rho). \quad (26)$$

Substituting expansions (25) and (26) into (3), multiplying the resulting equation by $C_z\exp(-C_\varphi^2 - C_z^2)$, and integrating with respect to C_φ and C_z between $-\infty$

and +∞, we find the equation for the function $Y_a^{(2)}(\rho, \mu)$:

$$\mu\frac{\partial Y_a^{(2)}}{\partial\rho} + Y_a^{(2)}(\rho,\mu) = \frac{1}{\sqrt{\pi}}\int_{-\infty}^{\infty} Y_a^{(2)}(\rho,\mu')\exp(-\mu'^2)d\mu'$$
$$-\frac{\mu}{\sqrt{\pi}}\int_{-\infty}^{\infty}\mu' Y_a^{(2)}(\rho,\mu')\exp(-\mu'^2)d\mu'$$
$$-\frac{1}{2}\frac{\partial Y_a^{(1)}}{\partial\mu} + \mu Y_b^{(1)}(\rho,\mu) - \frac{1}{2}\frac{\partial Y_b^{(1)}}{\partial\mu}$$

with the boundary conditions

$$Y_a^{(2)}(R,\mu) = -2U_z^{(2)}\big|_S, \quad \mu > 0,$$
$$Y_a^{(2)}(\infty,\mu) = 0. \tag{27}$$

Here,

$$Y_a^{(1)}(\rho,\mu) = \int_0^{\infty} a(\eta)F(\eta,\mu)\exp(-x/\eta)d\eta,$$
$$x = \rho - R,$$
$$Y_b^{(1)}(\rho,\mu) = k_2\int_0^{\infty}\exp(-x/\eta)\delta(\eta-\mu)d\eta,$$
$$a(\eta) = \frac{\eta(\eta - Q_1)\exp(-\eta^2)X(-\eta)}{2|\lambda^+(\eta)|^2}k_2, \tag{28}$$
$$Y_a^{(1)}(R,\mu) = (\mu^2 + Q_2)k_2.$$

In the case under consideration,

$$Z(\eta,\mu) = -\frac{1}{2}a(\eta)\frac{\partial F}{\partial\mu} + \mu k_2\delta(\eta-\mu) - \frac{k_2}{2}\frac{\partial}{\partial\mu}\delta(\eta-\mu),$$
$$\int_{-\infty}^{\infty} P\frac{1}{\eta-\mu}Z(\eta,\mu)\exp(-\mu^2)d\mu$$
$$= \frac{1}{2}a(\eta) + k_2\exp(-\eta^2)\left(\eta^2 - \frac{1}{2}\right),$$
$$\int_0^{\infty} nZ(\eta,\mu)\frac{d\eta}{\eta-\mu} = -\frac{1}{3}\mu k_2,$$
$$f(\mu) = -2U_z^{(2)}\big|_S + \frac{1}{2}a(\mu)\exp(\mu^2) + \mu^3 k_2,$$
$$U_z^{(2)}\big|_S = -\frac{k_2}{2}\left[Q_3 + \frac{1}{2\sqrt{\pi}}\int_0^{\infty}\frac{t^2(t-Q_1)}{|\lambda^+(t)|^2}\exp(-t^2)dt\right].$$

In view of (20) and (1), we find

$$U_z^{(2)}\big|_S = \frac{1}{4}(Q_3 + Q_1Q_2)k_2,$$
$$U_z\big|_S = U_z^{(1)}\big|_S + R^{-1}U_z^{(2)}\big|_S \tag{29}$$
$$= (0.38332 - 0.13339R^{-1})k_2$$

or, in terms of dimensional quantities,

$$U_z\big|_S = 1.14995\nu(1 - 0.589495\mathrm{Kn})\frac{1}{T_S}\frac{\partial T}{\partial z}\bigg|_S.$$

Thus, $\beta_{R\|} = 0.589495$.

LONGITUDINAL FLOW AROUND A CYLINDRICAL SURFACE (ISOTHERMAL SLIDING)

We assume that

$$k_3 = \frac{\partial U_z}{\partial\rho}\bigg|_S$$

is nonzero.

We represent the solution of (2) and (3) in the form

$$Y^{(j)}(\rho, C_i) = C_z Y_a^{(j)}(\rho, C_\rho); \quad j = 1, 2. \tag{30}$$

Substituting expansions (30) into (3), multiplying the resulting equation by $C_z\exp(-C_\varphi^2 - C_z^2)$, and integrating with respect to C_φ and C_z between –∞ and +∞, we find the equation for the function $Y_a^{(2)}(\rho, \mu)$:

$$\mu\frac{\partial Y_a^{(2)}}{\partial\rho} + Y_a^{(2)}(\rho,\mu) = \frac{1}{\sqrt{\pi}}\int_{-\infty}^{\infty} Y_a^{(2)}(\rho,\mu')\exp(-\mu'^2)d\mu'$$
$$-\frac{\mu}{\sqrt{\pi}}\int_{-\infty}^{\infty}\mu' Y_a^{(2)}(\rho,\mu')\exp(-\mu'^2)d\mu' - \frac{1}{2}\frac{\partial Y_a^{(1)}}{\partial\mu}$$

with boundary conditions (27). Here, $Y_a^{(1)}(\rho, \mu)$ is determined by relationship (28):

$$a(\eta) = \frac{2\exp(-\eta^2)X(-\eta)}{3|\lambda^+(\eta)|^2}k_3,$$
$$Y_a^{(1)}(R,\mu) = \frac{4}{3}(\mu + Q_1)k_3.$$

In this case,

$$Z(\eta,\mu) = -\frac{1}{2}a(\eta)\frac{\partial F}{\partial\mu},$$
$$\int_{-\infty}^{\infty} P\frac{1}{\eta-\mu}Z(\eta,\mu)\exp(-\mu^2)d\mu = \frac{1}{2}a(\eta),$$

$$\int_0^\infty \eta Z(\eta,\mu)\frac{d\eta}{\eta-\mu} = \frac{2}{3}k_3,$$

$$f(\mu) = -2U_z^{(2)}\big|_S + \frac{2}{3}k_3 + \frac{1}{2}a(\mu)\exp(\mu^2),$$

$$U_z^{(2)}\big|_S = \frac{k_3}{3}\left[1 - \frac{1}{\sqrt{\pi}}\int_0^\infty \frac{t^2}{|\lambda^+(t)|^2}\exp(-t^2)dt\right].$$

Using (24), we find

$$U_z^{(2)}\big|_S = -\frac{1}{6}k_3.$$

Thus, in the case of the longitudinal flow of a rarefied gas that is nonuniform in mass velocity around a cylindrical surface,

$$\begin{aligned} U_z\big|_S &= U_z^{(1)}\big|_S + R^{-1}U_z^{(2)}\big|_S \\ &= (0.67746 - 0.166667R^{-1})k_3 \end{aligned} \qquad (31)$$

or, in dimensional form,

$$U_z\big|_S = 1.14665\lambda(1 - 0.415407\mathrm{Kn})\frac{\partial U_z}{\partial \rho}\bigg|_S.$$

Thus, $C_{m\|}^{(1)} = 0.415407$.

CONCLUSIONS

The sliding velocities of a rarefied gas that is nonuniform in temperature and mass velocity flowing around a solid cylindrical surface are found from the solution of the ES model of the Boltzmann kinetic equation in the Knudsen layer. The dependences of the coefficients of thermal and isothermal slidings on the radius of curvature found in the linear approximation with respect to the Knudsen number have the same form as in [1]. In the case of longitudinal flow around a cylindrical surface, the thermal sliding velocities (29) coincide with the corresponding result in [1].

In view of the fact that the BGK model yields isothermal sliding velocities one and a half times greater than those of the ES model, (31) is written as

$$\begin{aligned} U_z\big|_S &= U_z^{(1)}\big|_S + R^{-1}U_z^{(2)}\big|_S \\ &= (1.01619 - 0.25000R^{-1})k_3. \end{aligned}$$

Thus, in the case of the longitudinal flow of a rarefied gas around a solid cylindrical surface, the isothermal sliding velocity also coincides with the corresponding result in [1].

REFERENCES

1. Y. Sone, *Rarefied Gas Dynamics* (Academic, New York, 1969), Vol. 1, pp. 243–253.
2. E. G. Mayasov, A. A. Yushkanov, and Yu. I. Yalamov, Pis'ma Zh. Tekh. Fiz. **14**, 498 (1988) [Sov. Tech. Phys. Lett. **14**, 220 (1988)].
3. A. B. Poddoskin, A. A. Yushkanov, and Yu. I. Yalamov, Zh. Tekh. Fiz. **52**, 2253 (1982) [Sov. Phys. Tech. Phys. **27**, 1383 (1982)].
4. Yu. I. Yalamov, A. A. Poddoskin, and A. A. Yushkanov, Dokl. Akad. Nauk SSSR **254**, 343 (1980) [Sov. Phys. Dokl. **25**, 734 (1980)].
5. M. N. Gaĭdukov and V. N. Popov, Izv. Akad. Nauk, Mekh. Zhidk. Gaza, No. 2, 165 (1998).
6. C. Cercignani, *Mathematical Methods in Kinetic Theory* (Plenum, New York, 1969; Mir, Moscow, 1973).
7. V. I. Roldugin, Kolloidn. Zh. **49**, 45 (1987).
8. S. P. Bakanov, V. V. Vysotskiĭ, and A. N. Nekrasov, Kolloidn. Zh. **48**, 851 (1986).
9. L. H. Holway, Phys. Fluids **3**, 1658 (1966).
10. C. Cercignani and G. Tironi, Nuovo Cimento B **43**, 64 (1966).
11. S. Chapman and T. G. Cowling, *Mathematical Theory of Non-Uniform Gases* (Cambridge Univ. Press, Cambridge, 1952; Inostrannaya Literatura, Moscow, 1960).
12. V. S. Vladimirov, *Equations of Mathematical Physics* (Nauka, Moscow, 1988; Marcel Dekker, New York, 1971).
13. S. K. Loyalka, Transp. Theory Stat. Phys. **4**, 55 (1975).
14. F. D. Gakhov, *Boundary Value Problems* (Nauka, Moscow, 1977; Addison-Wesley, Reading, 1966).
15. C. Cercignani, Ann. Phys. **20**, 219 (1962).

Translated by M. Fofanov

Technical Physics, Vol. 47, No. 10, 2002, pp. 1226–1236. Translated from Zhurnal Tekhnicheskoĭ Fiziki, Vol. 72, No. 10, 2002, pp. 22–32.

GASES AND LIQUIDS

Capillary Disintegration of a Suspended Filamentary Drop of a Viscous Magnetic Fluid in a Longitudinal Magnetic Field

V. M. Korovin

Research Institute of Mechanics, Moscow State University, Michurinskiĭ pr. 1, Moscow, 119899 Russia

e-mail: korovin@imec.msu.ru

Received July 10, 2001; in final form, March 25, 2002

Abstract—A differential equation that describes the axisymmetric motion of two immiscible magnetic fluids of the same density and viscosity is derived. It includes in explicit form the contribution of capillary forces localized at the interface between the fluids, which has the form of a weakly distorted cylindrical surface. With this equation, a dispersion relation for the problem of capillary instability of an extended axisymmetric drop placed in a uniform longitudinal magnetic field is obtained. The effect of magnetic forces on the capillary disintegration of the drop for the extreme cases (large and small Ohnesorge numbers) is analyzed. © *2002 MAIK "Nauka/Interperiodica".*

INTRODUCTION

From numerous experiments (see, e.g., [1–3] and Refs. therein), it is known that the free surfaces of magnetic fluids, as well as the interfaces between immiscible magnetic and nonmagnetic fluids, respond, as a rule, to external magnetic fields. The associated effects to a great extent depend on the field orientation relative to the surface. When subjected to sufficiently high orthogonal fields, the initially flat free surfaces of magnetic fluids become unstable with the formation of various periodic surface structures [1–6]. Conversely, tangential fields stabilize the free surfaces, suppressing wave disturbances caused by any external reasons. The stabilizing effect of tangential magnetic fields has been observed in many experiments studying fingering instability in porous media [1], capillary disintegration of a cylindrical layer [1, 2] and a thin cylindrical jet of a magnetic fluid [7], and Rayleigh–Taylor instability [8]. Systems consisting of thin magnetic-fluid and nonmagnetic-fluid layers in contact that are placed between solid walls respond to switching and growth of the magnetic field in a most unusual way [1–3].

The pioneer experiment on the capillary disintegration of a heavily extended thin cylindrical drop of a high-viscosity fluid was performed by Taylor [9]. In his experiment, a specially configured fluid jet flowed around an initially spherical drop to form an extended drop, the jet and the drop having the same density. Subsequently, such an approach to form filamentary drops was widely used in similar experiments [10–12]. Experimental equipment employed in later experiments is described in [13].

Theoretically, the capillary instability of a cylindrical thread of a viscous nonmagnetic fluid at rest in air was first considered by Rayleigh [14]. An example of such a system was a natural object, an as-woven spider's web. The dispersion relation obtained by Rayleigh and its analysis as applied to the evolution of instability under conditions when viscous forces dominate over inertial forces gave an insight into the disintegration of a thin cylindrical thread into regularly arranged droplets (see Fig. 37 in [15]). This figure shows that coarser drops are separated by finer droplets (satellites), which form by nonlinear hydrodynamic processes.

In the general case of a fluid thread surrounded by a viscous fluid, a dispersion relation is usually derived by equating the fourth-order determinant to zero, the elements of the determinant being expressed through Bessel functions [16]. A dispersion relation thus obtained is awkward; therefore, analytical expressions for its roots were long known only for the case studied by Rayleigh [16–18], as well as for the capillary instability of a thin cylinder of a nonviscous fluid under conditions when viscous forces dominate over inertial forces in the surrounding viscous fluid [16, 18]. Recently, a new formula applicable to contacting fluids of the same viscosity has been obtained by Stone and Brenner [19]. They used the quasi-stationary Stokes equation involving surface tension forces localized at the interface and applied the Hankel integral transformation to find the dependence $\sigma = \sigma(k)$ that allows one to trace the effect of the wave number k on the time evolution of harmonics in the form $\exp(\sigma t)\sin kz$ and $\exp(\sigma t)\cos kz$.

In this work, we generalize the differential equation for fluid motion [19] to the case of immiscible magnetic fluids placed in a magnetic field. The effect of volume magnetic forces on the capillary disintegration of a filamentary drop subjected to a longitudinal magnetic field is studied in terms of equations of ferrohydrodynamics and the equation derived in this work.

1063-7842/02/4710-1226$22.00

STATEMENT OF THE PROBLEM

Let a thin axisymmetric magnetic-fluid drop of length (measured along the axis) exceeding its characteristic cross size by several tens of times be placed into an infinite volume of another magnetic fluid. In many experiments with nonmagnetic fluids, drops of an extended shape were produced with special devices similar to Taylor's device by principle of operation [9, 13]. When studying the effect of a longitudinal magnetic field on the disintegration of such a drop, we neglect effects due to the axial components of magnetic forces at the drop edges and approximate the drop by a straight cylindrical thread of radius a.

Let us introduce the cylindrical coordinate system (r, ϑ, z) in such a way that the interface in hydrostatic equilibrium is described by the equation $r = a$. It is assumed that both fluids are Newtonian and have the same density ρ and dynamic viscosity coefficient η. In addition, their absolute permeabilities μ_1 (in the domain $r < a$) and μ_2 (in the domain $r > a$) depend only on the magnitude of the magnetic field vector $\mathbf{H}$ with $\mu_1(H) \neq \mu_2(H)$. Unlike the problem of capillary instability of a jet of a magnetic fluid in air, in our configuration both the cases $\mu_1 > \mu_2$ and $\mu_2 > \mu_1$ are possible. In the presence of a longitudinal uniform magnetic field $\mathbf{H} = (0, 0, H_0)$, the magnetic induction $\mathbf{B}_{j0} = \mu_j \mathbf{H}_0$ and magnetization $\mathbf{M}_{j0} = \chi_j \mathbf{H}_0$ of either of the media are uniform and the density of the mass force $\mathbf{F}_{\mathrm{m}0}^{(j)} = \mu_0 M_{j0} \operatorname{grad} H_0 \equiv 0$. Hereafter, $j = 1, 2$; $\chi_j = \mu_j/\mu_0 - 1$ is the magnetic susceptibility; and $\mu_0 = 4\pi \times 10^{-7}$ H/m is the magnetic constant.

Let us state the problem of axisymmetric motion of the fluids in the linear approximation, where the shape of the interface is represented by the equation $r = r_s(z, t)$. We put $r_s(z, t) = a + \zeta(z, t)$, where $\zeta(z, t)$ is a small perturbation of the initial radius of the thread ($|\zeta(z, t)| \ll a$) and t is time. A distortion of the interface causes a perturbation of the magnetic field $\mathbf{H}_j - \mathbf{H}_0 = \operatorname{grad}\varphi_j(r, z, t)$, magnetic induction $\mathbf{B}_j - \mathbf{B}_{j0} = \mathbf{b}_j(r, z, t)$, and magnetization $\mathbf{M}_j - \mathbf{M}_{j0} = \mathbf{m}_j(r, z, t)$, and generates volume magnetic forces of density $\mathbf{f}_{\mathrm{m}}^{(j)}(r, z, t)$, which affect the dynamics of the fluids. Up to first-order infinitesimals, we have

$$H_j - H_0 = \frac{\partial \varphi_j}{\partial z}, \quad M_j - M_{j0} = m_{jz},$$
$$\mathbf{m}_j = \frac{1}{\mu_0}\mathbf{b}_j - \operatorname{grad}\varphi_j,$$
$$\mathbf{b}_j = \mu_j(H_0)\frac{\partial \varphi_j}{\partial r}\mathbf{e}_r + \mu_{tj}(H_0)\frac{\partial \varphi_j}{\partial z}\mathbf{e}_z, \tag{1}$$
$$\mathbf{f}_{\mathrm{m}}^{(j)} = \mu_0 M_{j0} \operatorname{grad}\frac{\partial \varphi_j}{\partial z},$$

where $\mathbf{e}_r$ and $\mathbf{e}_z$ are the basis vectors corresponding to the coordinate lines r and z and $\mu_{tj} = dB_j/dH_j$ is the differential permeability.

In view of (1), the equation of magnetostatics $\operatorname{div}\mathbf{B}_j = 0$ implies that the perturbations of the magnetic field potential in either of the contacting magnetic fluids are described by the equations

$$\frac{\partial^2 \varphi_j}{\partial r^2} + \frac{1}{r}\frac{\partial \varphi_j}{\partial r} + \beta_j^2 \frac{\partial^2 \varphi_j}{\partial z^2} = 0, \quad \beta_j = \sqrt{\frac{\mu_{tj}(H_0)}{\mu_j(H_0)}}. \tag{2}$$

In the linear approximation, the continuity equations for the tangential components of the magnetic field and for the normal component of the induction at the interface (for $r = a$) have the form

$$\varphi_1 = \varphi_2, \quad \mu_{r1}\frac{\partial \varphi_1}{\partial r} - \mu_{r2}\frac{\partial \varphi_2}{\partial r} = (M_{10} - M_{20})\frac{\partial \zeta}{\partial z}, \tag{3}$$
$$\mu_{rj} = \frac{\mu_j(H_0)}{\mu_0}.$$

In stating the hydrodynamic problem, we do away with the common approach used in the statement of the magnetostatic problem given by (2) and (3). This approach requires that solutions to hydrodynamics equations be constructed separately for each domain where motion parameters and fluid states vary continuously with the subsequent joining of them via kinematic and dynamic conditions at the interface. Specifically, it is necessary that the normal and tangential components of the velocity vector $\mathbf{u}(r, z, t) = (u_r, 0, u_z)$ be continuous at the interface and also that the tangential component of the surface force density $\mathbf{p}_{n\tau}$ be continuous. Recall that, in the common approach, the dynamic condition relating the normal components p_{nn} of surface forces on both sides of the interface between immiscible fluids includes a discontinuity due to the surface tension effect. It should be noted that if the dynamic viscosity coefficients of the fluids are the same, it follows from the continuity equation and the continuity conditions for $\mathbf{u}$ and $\mathbf{p}_{n\tau}$ that $\partial u_r/\partial r$, $\partial u_r/\partial z$, $\partial u_z/\partial r$, and $\partial u_z/\partial z$ are also continuous at the interface.

Now, we formulate hydrodynamic equations, assuming that the fluids constitute a single medium where the pressure $p(r, \vartheta, z, t)$ experiences a jump at the interface $r = a + \zeta(z, t)$. The amount of the jump depends on the surface tension coefficient α and the mean curvature K of the interface. Consider an arbitrary individual (i.e., covering similar particles of the medium) volume $V(t)$ and imagine that it is arbitrarily divided into two parts by a segment of the interface.

Following the conventional concepts of the continuity of the vector field $\mathbf{u}$ and its derivatives with respect to coordinates and bearing in mind the derivation [20] of the continuity equation that relies on the law of conservation of mass for any individual volume, we naturally come to the solenoidal condition for the velocity field:

$$\operatorname{div}\mathbf{u} = 0. \tag{4}$$

When deriving a differential equation of motion, we will proceed from the integral form (A9) of the law of conservation of momentum for the individual volume. In the linear approximation, the convective time derivative of the velocity, the term $(\mathbf{u}\cdot\nabla)\mathbf{u}$ on the left of (A9), and a magnetic pressure jump on the right-hand side of (A9) are certainly rejected because of their smallness.

Note that in our approximation, an element of the weakly distorted $[(\partial\zeta/\partial z)^2 \ll 1]$ interface is written as $d\sigma = ad\vartheta dz$ and the mean curvature is calculated by the formula

$$K = \frac{1}{2}\left(\frac{1}{a} - \frac{\zeta}{a^2} - \frac{\partial^2\zeta}{\partial z^2}\right).$$

We will neglect the deviation of the normal vector $\mathbf{n}$ to the interface from the radial direction, which is directed toward the symmetry axis of the surface, and put $\mathbf{n} = -\mathbf{e}_r$. Then, the integral over the part of the interface lying inside the individual volume [see (A9)] can easily be transformed into the integral over the individual volume:

$$\int_s K\mathbf{n}d\sigma = \int_V \mathbf{e}_r\delta(r-a)\left(\frac{\zeta}{a^2} + \frac{\partial^2\zeta}{\partial z^2} - \frac{1}{a}\right)dV, \qquad (5)$$

where $\delta(r-a)$ is the Dirac delta function of the argument $(r-a)$ and $dV = rdrd\vartheta dz$.

In view of (5) and formulas (1) for the magnetic force perturbation $\mathbf{f}_m$,

$$\mathbf{f}_m = \begin{cases} \mathbf{f}_m^{(1)} & \text{for} \quad r < r_s,\ 0 \le \vartheta \le 2\pi,\ -\infty < z < \infty \\ \mathbf{f}_m^{(2)} & \text{for} \quad r > r_s,\ 0 \le \vartheta \le 2\pi,\ -\infty < z < \infty, \end{cases}$$

we recast (A9) in the form

$$\int_V \left[\rho\frac{\partial\mathbf{u}}{\partial t} + \operatorname{grad} p - \eta\Delta\mathbf{u} - \rho\mathbf{g} - \mathbf{f}_m + \mathbf{e}_r\alpha\delta(r-a)\left(\frac{1}{a} - \frac{\zeta}{a^2} - \frac{\partial^2\zeta}{\partial z^2}\right)\right]dV = 0,$$

where Δ is Laplacian.

Recall that this integral equality applies (in terms of the linear statement) to an arbitrary individual volume. Certainly, it is fulfilled if the integrand vanishes. Leaving aside the question of how rigorous the transition from the integral equality to the differential equation obtained by equating the integrand to zero is, we will use the equation of motion

$$\rho\frac{\partial\mathbf{u}}{\partial t} = -\operatorname{grad} p + \eta\Delta\mathbf{u} + \rho\mathbf{g} + \mu_0 M_{10}[1-\Theta(r-a)]\operatorname{grad}\frac{\partial\varphi_1}{\partial z} + \mu_0 M_{20}\Theta(r-a)\operatorname{grad}\frac{\partial\varphi_2}{\partial z} - \mathbf{e}_r\alpha\delta(r-a)\left(\frac{1}{a} - \frac{\xi}{a^2} - \frac{\partial^2\zeta}{\partial z^2}\right), \qquad (6)$$

where

$$\Theta(r-a) = \begin{cases} 0 & \text{for} \quad r < a \\ 1 & \text{for} \quad r > a \end{cases}$$

is the Heaviside function.

At the interface ($r = a$ in the linear approximation), a solution to system (4), (6) must satisfy the kinematic condition

$$\frac{\partial\zeta}{\partial t} = u_r, \qquad (7)$$

which means that the interface consists of the same particles.

Certainly, the functions $\mathbf{u}$ and p limited at $r = 0$ have a physical meaning and $\mathbf{u} \longrightarrow 0$ at $r \longrightarrow \infty$.

To simplify the subsequent mathematics, we rearrange equation of motion (6). In hydrodynamics, an important kinematic parameter of the velocity field is the velocity vortex vector $\omega_c = (1/2)\operatorname{curl}\mathbf{u}$. In the case being considered, only the azimuth component of the vortex vector is other than zero; therefore, vortex lines in each of the planes $z = \text{const}$ represent a family of concentric circles. Applying the curl operator to Eq. (6), we obtain

$$\frac{\partial\omega_c}{\partial t} - \nu\Delta\omega_c = \mathbf{e}_\vartheta\frac{\delta(r-a)}{2\rho}\left[\alpha\left(\frac{1}{a^2}\frac{\partial\zeta}{\partial z} + \frac{\partial^3\zeta}{\partial z^3}\right) + \mu_0\left(M_{10}\frac{\partial^2\varphi_1}{\partial z^2} - M_{20}\frac{\partial^2\varphi_2}{\partial z^2}\right)\right], \quad \nu = \frac{\eta}{\rho}. \qquad (8)$$

Such a vector equation is common in theoretical physics. As follows from the right-hand side of (8), if the motion of the fluids is nonstationary, capillary forces localized at the interface and the discontinuity in the axial component of the magnetic force density $\mathbf{f}_m$ at the interface generate vortices in liquid particles forming the interface. According to (8), the vortices in the fluids propagate on both sides of the interface by diffusion, with the diffusion coefficient being equal to the kinematic viscosity coefficient ν of the fluids. From Eq. (8), one can easily estimate the characteristic time τ_d of vortex diffusion across a liquid cylindrical thread of characteristic radius a. Indeed, equating terms of the same order of magnitude on the left-hand side of (8), we find $\tau_d = a^2/\nu$; hence, τ_d grows as the viscosity coefficient decreases. In the limiting case of nonviscous flu-

ids ($\nu = 0$), it follows from Eq. (8) that

$$\omega_c = \mathbf{e}_\vartheta \frac{\delta(r-a)}{2\rho}\int_0^t\left[\alpha\left(\frac{1}{a^2}\frac{\partial\zeta}{\partial z}+\frac{\partial^3\zeta}{\partial z^3}\right)\right.$$
$$\left.+\mu_0\left(M_{10}\frac{\partial^2\varphi_1}{\partial z^2}-M_{20}\frac{\partial^2\varphi_2}{\partial z^2}\right)\right]dt.$$

This means that the vortices do not leave the site of origin.

Using continuity equation (4), we introduce the stream function $\psi(r, z, t)$ such that

$$u_r = \frac{1}{r}\frac{\partial\psi}{\partial z}, \quad u_z = -\frac{1}{r}\frac{\partial\psi}{\partial r}$$

then,

$$\omega_c = \mathbf{e}_\vartheta\frac{1}{2r}L\psi, \quad \Delta\omega_c = \mathbf{e}_\vartheta\frac{1}{2r}LL\psi,$$
$$L = \frac{\partial^2}{\partial r^2}-\frac{1}{r}\frac{\partial}{\partial r}+\frac{\partial^2}{\partial z^2}.$$

With these expressions, Eq. (8) takes the form

$$\left(L-\frac{1}{\nu}\frac{\partial}{\partial t}\right)L\psi = \frac{r\delta(r-a)}{\eta}$$
$$\times\left[\mu_0\left(M_{20}\frac{\partial^2\varphi_2}{\partial z^2}-M_{10}\frac{\partial^2\varphi_1}{\partial z^2}\right)-\alpha\left(\frac{1}{a^2}\frac{\partial\zeta}{\partial z}+\frac{\partial^3}{\partial z^3}\right)\right]. \quad (9)$$

Kinematic condition (7) is recast to the form

$$\frac{\partial\zeta}{\partial t} = \frac{1}{a}\frac{\partial\psi}{\partial z} \quad \text{for} \quad r = a. \quad (10)$$

Thus, the functions $\zeta(z, t)$, $\varphi_j(r, z, t)$, and $\psi(r, z, t)$ are found from the solution to the problem stated by (2), (3), (9), and (10).

DISPERSION RELATION AND ITS ANALYSIS

To investigate the time evolution of the interface, let us trace the time behavior of partial solutions (harmonics) to the linear problem, which have the form

$$\zeta_k\exp[i(kz-\omega t)], \quad \Phi_k^{(j)}(r)\exp[i(kz-\omega t)],$$
$$\Psi_k(r)\exp[i(kz-\omega t)], \quad i = \sqrt{-1}. \quad (11)$$

Here, ζ_k, $\Phi_k^{(j)}(r)$, and $\Psi_k(r)$ are the Fourier transforms of the desired functions $\zeta(z, t)$, $\varphi_j(r, z, t)$, and $\psi(r, z, t)$ (taken at the initial time instant) with respect to the variable z.

In expressions (11), the appearance of the exponential $\exp(-i\omega t)$ and the associated separation of variables stem from the fact that the coefficients of linear homogeneous partial differential equations (2) and (9) are time independent. Because of this, our problem admits partial solutions like (11) at any value of the wave number k provided that the relation between ω and k (dispersion relation) imposed by the equations and boundary conditions is met. With the dispersion relation, one can find wave number ranges where the harmonics grow or decay with time, the wave number of the fastest growing harmonic, and some other valuable information.

Substituting (11) into (2), (3), (9), and (10) yields

$$\frac{d^2\Phi_k^{(j)}}{dr^2}+\frac{1}{r}\frac{d\Phi_k^{(j)}}{dr}-(\beta_j k)^2\Phi_k^{(j)} = 0, \quad (12)$$
$$\Phi_k^{(1)} = \Phi_k^{(2)},$$

at $r = a$, and

$$\mu_{r1}\frac{d\Phi_k^{(1)}}{dr}-\mu_{r2}\frac{d\Phi_k^{(2)}}{dr} = ik\zeta_k(M_{10}-M_{20}), \quad (13)$$

$$L_1L_2\Psi_k = \frac{r\delta(r-a)}{\eta}\left[\mu_0k^2(M_{10}\Phi_k^{(1)}-M_{20}\Phi_k^{(2)})\right.$$
$$\left.-i\alpha\zeta_k k\left(\frac{1}{a^2}-k^2\right)\right], \quad (14)$$

$$\omega a\zeta_k + k\Psi_k = 0, \quad (15)$$

at $r = a$.

Here,

$$L_1 = \frac{d^2}{dr^2}-\frac{1}{r}\frac{d}{dr}-k^2, \quad L_2 = \frac{d^2}{dr^2}-\frac{1}{r}\frac{d}{dr}-m^2,$$
$$m = \sqrt{k^2-i\frac{\omega}{\nu}}, \quad \mathrm{Re}\,m > 0.$$

Solutions to the problem of magnetostatics stated as (12) and (13) that have derivatives limited at $r = 0$ and $r \longrightarrow \infty$ are written as

$$\Phi_k^{(1)} = \frac{i\zeta_k}{c}(M_{10}-M_{20})K_0(\beta_2 ka)I_0(\beta_1 kr),$$
$$\Phi_k^{(2)} = \frac{i\zeta_k}{c}(M_{10}-M_{20})I_0(\beta_1 ka)K_0(\beta_2 kr), \quad (16)$$
$$c = \beta_1\mu_{r1}I_1(\beta_1 ka)K_0(\beta_2 ka)+\beta_2\mu_{r2}I_0(\beta_1 ka)K_1(\beta_2 ka),$$

where $I_l(x)$ and $K_l(x)$ ($l = 0, 1$) are the modified Bessel functions of the first and second kind.

Substituting expressions (16) into Eq. (14) yields

$$L_1L_2\Psi_k = \delta(r-a)T(r), \quad (17)$$

where

$$T(r) = \frac{i\alpha\zeta_k kr}{\eta a^2}\left\{\frac{\mu_0 ka^2}{\alpha c}(M_{10} - M_{20})[M_{10}K_0(\beta_2 ka)I_0(\beta_1 kr) - M_{20}I_0(\beta_1 ka)K_0(\beta_2 kr)] + (ka)^2 - 1\right\}.$$

It is easy to write a fundamental set of homogeneous equations corresponding to fourth-order linear inhomogeneous equation (17):

$$\Psi_{k1} = rI_1(kr), \quad \Psi_{k2} = rK_1(kr), \quad \Psi_{k3} = rI_1(mr), \quad \Psi_{k4} = rK_1(mr). \tag{18}$$

Using (18), we apply the method of variation of constants to find a partial solution to Eq. (17) that has continuous first- and second-order derivatives at the point $r = a$ satisfying the condition of velocity boundedness at $r \longrightarrow 0$ and $r \longrightarrow \infty$:

$$\Psi_k = \frac{i\alpha}{\eta a}\frac{k\zeta_k}{m^2 - k^2}(\kappa^2 + \kappa N\Lambda - 1)R(r), \tag{19}$$

where

$$R(r) = r[K_1(\kappa)I_1(kr) - K_1(ma)I_1(mr)] \text{ for } r \le a,$$

$$R(r) = r[I_1(\kappa)K_1(kr) - I_1(ma)K_1(mr)] \text{ for } r \ge a,$$

$$\Lambda = \frac{(\mu_{r1} - \mu_{r2})^2 I_0(\beta_1\kappa)K_0(\beta_2\kappa)}{\beta_1\mu_{r1}I_1(\beta_1\kappa)K_0(\beta_2\kappa) + \beta_2\mu_{r2}I_0(\beta_2\kappa)K_1(\beta_2\kappa)},$$

$$N = \frac{a\mu_0}{\alpha}H_0^2, \quad \kappa = ka.$$

(Note that this procedure is similar to that used to construct a solution to inhomogeneous second-order equation (7.2.48) in [21], which involves a shifted delta function on the right-hand side.)

Substituting expressions (11) and (19) into kinematic condition (15) at the interface, we arrive at the dispersion relation

$$\frac{\rho a^3}{\alpha}\omega^2 = \kappa^2(1 - \kappa N\Lambda - \kappa^2) \times [I_1(q)K_1(q) - I_1(\kappa)K_1(\kappa)], \tag{20}$$

where

$$q = \sqrt{\kappa^2 - i\omega\tau_d}, \quad \mathrm{Re}\, q > 0.$$

Since all the quantities on the right of (20) are dimensionless, the problem has, along with τ_d, the characteristic time scale $\tau_i = \sqrt{\rho a^3/\alpha}$, as follows from the left of (20). The physical meaning of τ_i can be elucidated by considering the dispersion relation for the problem of stability of cylindrical interface between nonviscous fluids at rest. In experiments, we certainly deal with low-viscosity fluids, where the effect of viscosity forces on the capillary-force-induced macroscopic flow of the fluids is small in comparison with the effect of inertial and magnetic forces. In this case, $\tau_d \longrightarrow \infty$ and expression (20) takes the form

$$(\omega\tau_i)^2 = \kappa^2 I_1(\kappa)K_1(\kappa)(\kappa^2 + \kappa N\Lambda - 1). \tag{21}$$

Since $I_1(\kappa)K_1(\kappa) > 0$ for $\kappa > 0$, it follows from (21) that the frequency ω is a real-valued function of the dimensionless wave number κ in the absence of the magnetic field (at $N = 0$) for $\kappa > 1$. For the range $0 < \kappa < 1$, $\mathrm{Re}\,\omega = 0$, while $\mathrm{Im}\,\omega > 0$ and $\mathrm{Im}\,\omega < 0$ in the different branches of the double-valued function $\omega(\kappa)$. Since perturbation spectra in a real physical experiment contain any wave numbers, the conditions $\mathrm{Re}\,\omega = 0$ and $\mathrm{Im}\,\omega > 0$ imply that the configuration of fluids that are initially at rest is unstable, the instability having a monotonic character. Thus, the time evolution of a filamentary drop of a perfectly incompressible fluid that is initially at rest fundamentally differs from the behavior of a spherical drop [22] self-oscillating under the action of capillary forces.

Analysis shows that at $N \neq 0$ the magnetic field only narrows the wave number range where the drop is unstable without changing radically the character of the instability of harmonics. Since dispersion relations (20) and (21) describe the linear stage of the evolution of harmonics, the time scale τ_i also characterizes the linear stage of filamentary drop instability initiated by capillary forces when inertial forces dominate over viscous forces (the inertial condition of capillary disintegration).

Turning back to the behavior of a thread of viscous ferrofluids, we note that numerous experiments with nonmagnetic fluids have demonstrated that there exists a viscous regime of capillary disintegration of the thread, where the contribution of inertial forces to the force balance is small and the evolution of the thread shape is governed mainly by capillary and viscous forces acting on the fluid. Let τ_v be the time scale of the linear stage of capillary disintegration in the viscous regime. Based on the hydrodynamic part of the problem considered, it is easy to check that $\tau_v = \eta a/\alpha$ (similar estimates were made in [23]). In terms of the dimensionless criteria, the condition for the viscous regime of disintegration appears as $Z \gg 1$, where $Z = \eta/\sqrt{\rho\alpha a}$ is the Ohnesorge number. Since $\tau_i/\tau_v = Z^{-1}$ and $\tau_d/\tau_v = Z^{-2}$, we have $\tau_d \ll \tau_i \ll \tau_v$ for $Z \gg 1$. If $Z \ll 1$, $\tau_v \ll \tau_i \ll \tau_d$; this is precisely the case to which dispersion relation (21) corresponds.

Passing to the dimensionless function $\Omega = \omega\tau_v$ in (20), we come to

$$\varepsilon\Omega^2 = \kappa(1 - \kappa N\Lambda - \kappa^2)[I_1(q)K_1(q) - I_1(\kappa)K_1(\kappa)], \quad q = \sqrt{\kappa^2 - i\varepsilon\Omega}, \quad \varepsilon = Z^{-2}. \tag{22}$$

In the case considered, $\varepsilon \ll 1$; therefore, leaving the linear term in the expansion of the right-hand side of (22) in powers of ε, we find a root of the dispersion relation that describes the evolution of the capillary instability of the drop when viscous forces are much greater than inertial forces:

$$\omega\tau_v = i(1 - \kappa N\Lambda - \kappa^2) \times \left\{ I_1(\kappa)K_1(\kappa) + \frac{\kappa}{2}[I_1(\kappa)K_0(\kappa) - I_0(\kappa)K_1(\kappa)] \right\}. \quad (23)$$

As follows from (23), if κ is real, the principal term of the expansion of ω in powers of ε is purely imaginary. The numerical analysis indicates that the function in the braces is positive at any $\kappa > 0$, so that the sign of $\mathrm{Im}\omega$ coincides with the sign of the expression in the parentheses [the same is valid for one of the branches of the double-valued function $\omega(\kappa)$ in the case of a nonviscous fluid; see (21)]. It should be noted that, with the next term of expansion (23) included, $\mathrm{Re}\omega$ remains to be equal to zero: $\mathrm{Re}\omega = 0$. In the absence of the magnetic field (at $N = 0$), as well as if $\mu_{r1} = \mu_{r2}$, the form of root (23) coincides with the expression found in [19] up to notation.

When constructing plots illustrating the effect of the magnetic field on the capillary instability of a filamentary drop, we assumed that ferrofluids are magnetized according to a linear law ($\beta_1 = 1$, $\beta_2 = 1$). Figure 1 shows dispersion relation (23) for fixed μ_{r1} and μ_{r2} and various N. For a given N and any κ lying to the right of the point $\kappa_c = \kappa_c(\mu_{r1}, \mu_{r2}, N)$ where the corresponding curve crosses the abscissa axis, $\mathrm{Im}\omega < 0$; for κ lying to the left of κ_c, $\mathrm{Im}\omega > 0$. Thus, harmonics with dimensionless wave numbers $\kappa > \kappa_c$ are stable; those with $\kappa < \kappa_c$ are unstable. The points $\kappa = \kappa_c$ are the threshold values of the wave number. As follows from Fig. 1, in the presence of a discontinuity in the relative permeabilities ($\mu_{r1} - \mu_{r2} \neq 0$), the magnetic field stabilizes a number of harmonics (with wavelengths $\lambda > 2\pi a$) that are unstable without the field. As both N and $|\mu_{r1} - \mu_{r2}|$ increase, so does the characteristic time $(\mathrm{Im}\omega)_*^{-1}$ of emergence of the fastest growing harmonic (that is, the harmonic with the dimensionless wave number $\kappa_*(N, \mu_{r1}, \mu_{r2})$ responsible for the peak of the associated curve at given N, μ_{r1}, and μ_{r2}). Note that $(\mathrm{Im}\omega)_*^{-1}$ at $\mu_{r1} > \mu_{r2}$ is always greater than at $\mu_{r1} < \mu_{r2}$ for the same pair of fluids and a fixed N.

From expressions (21) and (23), it is easy to see that the threshold wave numbers κ_c for $Z \ll 1$ and $Z \gg 1$ equal each other for given N, μ_{r1}, and μ_{r2}. Figure 2 plots dispersion relations (21). From Figs. 1 and 2, it follows that viscosity considerably affects the characteristic times of emergence of the fastest growing harmonics: in high-viscosity fluids, they are one order of magnitude larger than in low-viscosity ones.

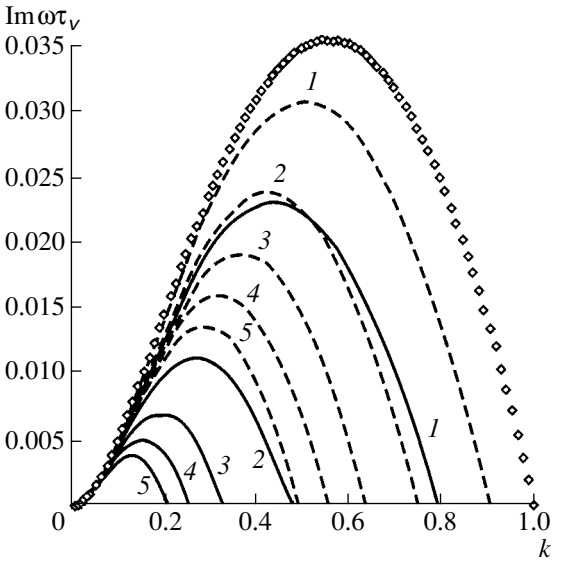

Fig. 1. Dispersion relation (23) for different N in the absence of the magnetic field ($N = 0$) (data points), in the presence of the field for the fluids with $\mu_{r1} = 5$ and $\mu_{r2} = 1$ (continuous curves), and in the presence of the field for the fluids with $\mu_{r1} = 1$ and $\mu_{r2} = 5$ (dashed curves). $N = 0.1$ (*1*), 0.3 (*2*), 0.5 (*3*), 0.7 (*4*), and 0.9 (*5*).

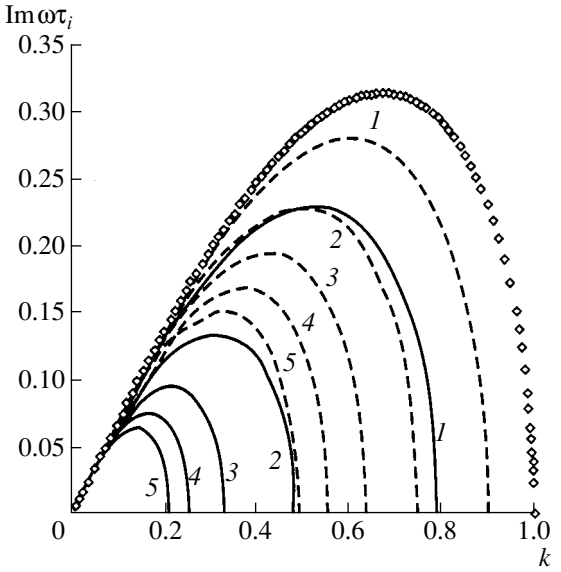

Fig. 2. Dispersion relation (21) for the same values of the parameters N, μ_{r1}, and μ_{r2} as in Fig. 1.

Dispersion relations (20) and (21) yield the same family of neutral stability curves, which depend on μ_{r1} and μ_{r2}:

$$N = \frac{1 - \kappa^2}{\kappa\Lambda}. \quad (24)$$

In the plane (κ, N), the condition $\mathrm{Im}\omega = 0$ is fulfilled along these curves. In essence, neutral stability curves

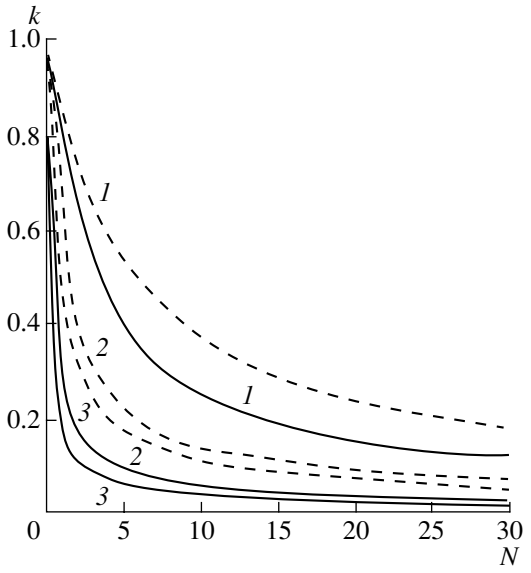

Fig. 3. Neutral stability curves. Continuous curves correspond to $\mu_{r2} = 1$ and $\mu_{r1} = 2$ (*1*), 4 (*2*), and 5 (*3*). Dashed curves correspond to $\mu_{r1} = 1$ and $\mu_{r2} = 2$ (*1*), 4 (*2*), and 5 (*3*).

are demarcation lines between domains of stability (everywhere $\mathrm{Im}\omega < 0$) and instability ($\mathrm{Im}\omega > 0$) in the band ($0 \le \kappa \le 1$, $N \ge 0$). It is more reasonable to construct the domains of stability and instability (Fig. 3) in the plane (N, κ), since N is a controllable parameter under experimental conditions, while a perturbation spectrum may have any wave numbers. The transition from the plane (κ, N) to the plane (N, κ) is accomplished by inverting function $N = N(\kappa)$ (24).

In Fig. 3, the domains of stability and instability are located above and below, respectively, the neutral stability curves for given μ_{r1} and μ_{r2}. It is also seen from Fig. 3 that the threshold wave number decreases with increasing both N and the discontinuity between the magnetic susceptibilities of the fluids. For the same pair of fluids, the threshold wave number κ_{c1} at $\mu_{r1} > \mu_{r2}$ is less than the threshold wave number κ_{c2} at $\mu_{r1} < \mu_{r2}$ for given a magnetic field strength and thread diameter. As a result, the range $\kappa_{c1} < \kappa < 1$ of harmonics stabilized by the magnetic field at $\mu_{r1} > \mu_{r2}$ is wider than the range $\kappa_{c2} < \kappa < 1$ of harmonics stabilized by the magnetic field at $\mu_{r1} < \mu_{r2}$. Thus, a magnetic field of a fixed strength stabilizes a drop of a ferrofluid suspended in a nonmagnetic fluid (configuration I) more effectively than a drop of a nonmagnetic fluid suspended in the same ferrofluid (configuration II).

From (20), it is easy to see that a family of lines (24) represents neutral stability curves at any Ohnesorge number. Therefore, the stability and instability domains depicted in Fig. 3 describe (for given N, κ, μ_{r1}, and μ_{r2}) the evolution of a harmonic for an arbitrary relation between inertial and viscous forces during the capillary disintegration of a ferrofluid thread exposed to a longitudinal magnetic field.

If the viscosity coefficients of nonmagnetic fluids are unequal, the wavelength λ_* of the fastest growing harmonic observed under the capillary disintegration of a filamentary drop when viscous forces dominate over inertial forces is in good agreement with experimental data found by measuring the diameters of droplets after the disintegration [11, 12, 16] (recall that λ_* was calculated in the linear approximation). Certainly, the forma-

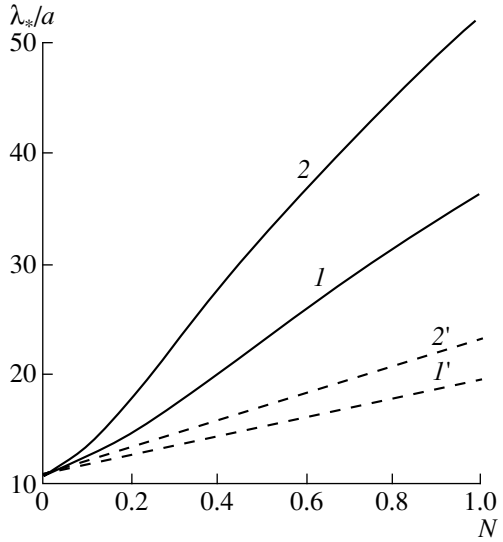

Fig. 4. Wavelength of the fastest growing harmonic vs. dimensionless magnetic field strength squared for $Z \gg 1$. Continuous curves correspond to $\mu_{r2} = 1$ and $\mu_{r1} = 4$ (*1*) and 5 (*2*). Dashed curves correspond to $\mu_{r1} = 1$ and $\mu_{r2} = 4$ (*1'*) and 5 (*2*').

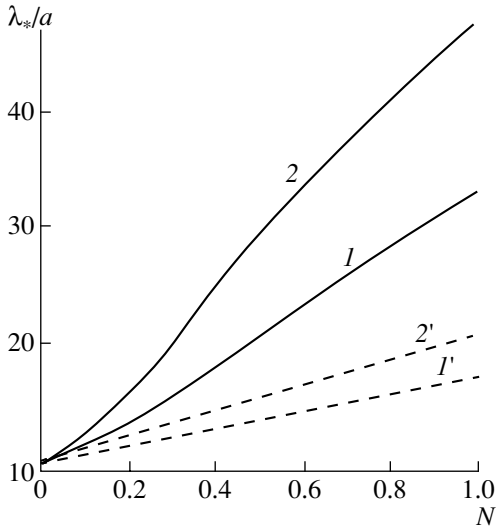

Fig. 5. The same as in Fig. 4 for $Z \ll 1$.

tion of satellites between regularly arranged coarser drops was not taken into account in this case.

Figure 4 shows the dependences of λ_* vs. N constructed with the root (23) of dispersion relation (20) for $Z \gg 1$, and Fig. 5 demonstrates similar dependences constructed with dispersion relation (21) corresponding to $Z \ll 1$. From these plots, we see that at both $Z \gg 1$ and $Z \ll 1$, the characteristic diameter of droplets appearing after the capillary disintegration grows with both magnetic field strength and discontinuity in the magnetic susceptibilities of the fluids in both configurations I and II (if the diameter of the initial thread is fixed). It is also seen that, at both $Z \gg 1$ and $Z \ll 1$, drops appearing after the disintegration are coarser in configuration I than in configuration II (for a fixed magnetic field strength).

From Figs. 4 and 5, it follows that the size of the droplets differ markedly at $Z \gg 1$ and $Z \ll 1$ for the same configuration and the same H_0 and a. In the viscous regime of capillary disintegration, the droplets are coarser than in the inertial regime. For example, $\lambda_*/a = 11.1896$ at $Z \gg 1$ and 9.2843 at $Z \ll 1$ without the magnetic field.

CONCLUSION

Based on the integral form of the law of conservation of momentum for a finite material volume consisting of two contacting immiscible magnetic fluids placed in a magnetic field, we derived a differential equation for the motion of the fluids. Along with mass forces, the equation includes also capillary forces localized at the interface. With this equation, it was easy to derive in explicit form a dispersion relation for the problem of capillary instability as applied to a suspended filamentary drop of a viscous ferrofluid subjected to a longitudinal magnetic field. The case when the density and viscosity of a fluid surrounded the drop are equal to those of the drop but the magnetic susceptibilities differ was considered.

The effect of the field on the disintegration of the filamentary drop was analyzed for the cases when (i) viscous forces are much greater than inertial forces (viscous regime of disintegration, the Ohnesorge number $Z \gg 1$) and (ii) inertial forces dominate over viscous forces (inertial regime, $Z \ll 1$). For both regimes of disintegration, if a drop of a ferrofluid is suspended in a nonmagnetic fluid (configuration I), the magnetic field of a given strength stabilizes a wider range of harmonics that are unstable in the absence of the field than when a drop of a nonmagnetic fluid is suspended in the same ferrofluid (configuration II), provided that the diameters of the filamentary drops are the same. Also, in both regimes ($Z \gg 1$ and $Z \ll 1$), the capillary disintegration of configuration I generates coarser droplets than the disintegration of configuration II. In the capillary disintegration of both configurations, as the magnetic field strength increases, so do (i) a range of field-stabilized harmonics, (ii) the characteristic time of developing the fastest growing harmonic, and (iii) the characteristic size of droplets after the disintegration of the initial filamentary drop.

Comparing the viscous and inertial regimes of capillary disintegration of ferrofluid filaments indicates that, under the same conditions, viscous forces affect mostly the characteristic times of developing the fastest growing harmonics (at $Z \gg 1$, these times are one order of magnitude greater than at $Z \ll 1$), while the difference in the sizes of droplets formed after the disintegration is much smaller.

APPENDIX

The basic dynamic equation postulated in continuum mechanics [20] is the momentum equation for a finite volume of a continuous medium. According to this equation written in the inertial coordinate system, the rate of change of the momentum $\mathbf{Q}$ in time for any individual (i.e., consisting of the same particles of a medium under consideration) volume $V(t)$ bounded by the surface $\Sigma(t)$ equals the resultant vector of external forces acting on the medium enclosed by this volume:

$$\frac{d\mathbf{Q}}{dt} = \int_V \rho \mathbf{F} dV + \int_\Sigma \mathbf{p}_n d\sigma, \quad \mathbf{Q} = \int_V \rho \mathbf{u} dV. \qquad \text{(A1)}$$

Here, ρ and $\mathbf{u}$ are, respectively, the density of the medium and the velocity field; $\mathbf{F}$ is the mass force density; $\mathbf{p}_n$ is the stress vector (density of surface forces) on a surface area $d\sigma$ with a normal $\mathbf{n}$; and dV is a volume element. In continuum mechanics, the normal $\mathbf{n}$ is always outer with respect to that part of the medium on which the surface force $\mathbf{p}_n d\sigma$ acts. If the volume V considered is subjected to forces (other than those distributed over the area Σ) concentrated on some surfaces inside V, the sum of these forces should be added to the right of (A1).

To simplify the mathematics, we will use the rectangular Cartesian coordinates (x_1, x_2, x_3) with the basis vectors $\mathbf{e}_1$, $\mathbf{e}_2$, and $\mathbf{e}_3$. In this coordinate system, $\mathbf{u} = u_i \mathbf{e}_i$, $\mathbf{n} = n_i \mathbf{e}_i$, and also $\mathbf{p}_n = \mathbf{p}^i n_i$ ($\mathbf{p}^i = p_{ki} \mathbf{e}_k$, where p_{ki} are the components of the stress tensor $P = p_{ki} \mathbf{e}_k \mathbf{e}_i$; $i, k = 1, 2, 3$). Hereafter, in all expressions including a pair of the same indices, independent summation over repeating indices is performed.

It should be emphasized that Eq. (A1) applies to both continuous and discontinuous motions of a continuum. If the states of a continuum, as well as the motion characteristics and their time and space derivatives, are continuous, it can be rigorously proved (specifically with the Gauss–Ostrogradsky formula applied to trans-

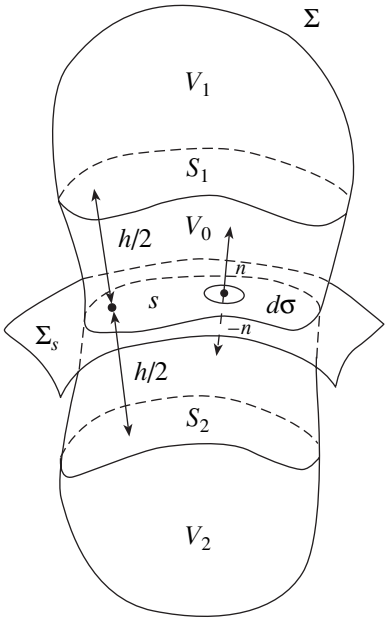

Fig. 6. On the derivation of integral equality (A4).

form the integral over the surface area Σ in (A1) into the integral over the Σ-bounded volume *V*) that the integral form of momentum Eq. (A1) is equivalent to the differential equation of continuum motion

$$\rho\left[\frac{\partial \mathbf{u}}{\partial t} + (\mathbf{u}\cdot\nabla)\mathbf{u}\right] = \rho\mathbf{F} + \frac{\partial \mathbf{p}^i}{\partial x_i}, \quad \nabla = \mathbf{e}_i\frac{\partial}{\partial x_i}. \quad \text{(A2)}$$

If the volume *V* has an inner isolated time-invariable surface Σ_s at which the parameters of the medium experience a discontinuity, Eq. (A1) makes it possible to establish one of the finite relationships between the parameters on the different sides of the surface Σ_s.

Let us transform Eq. (A1) for the case when the smooth surface of discontinuity Σ_s divides the individual volume *V* into two parts in either of which the motion of the continuum is continuous. As in the derivation of conditions on surfaces of discontinuity [20], we will introduce an auxiliary volume V_0 related to a part *s* of the surface Σ_s lying inside the volume *V* (Fig. 6). From each point of the domain *s* on both its sides, we pass normal segments of small length *h*/2 sideways from the surface Σ_s. Sets of the ends of these segments lying inside *V* produce surfaces S_1 and S_2 equidistant from Σ_s. These surfaces, along with the lateral surface Σ_l (a part of Σ) adjacent to them bound the volume V_0.

Let V_1 and V_2 be the volumes cut by the surfaces S_1 and S_2 from the initial volume $V = V_0 + V_1 + V_2$ and ∂V_0, ∂V_1, and ∂V_2 be surfaces bounding V_0, V_1, and V_2. Bearing in mind that the outer normals to ∂V_0 and ∂V_1 at points of the surface S_1 are oppositely directed (the same is true for the outer normals to ∂V_0 and ∂V_2 on S_2) and taking into account the equality $\mathbf{p}_n = -\mathbf{p}_{-n}$ fulfilled for the inner stresses on S_1 and S_2, we have

$$\int_\Sigma \mathbf{p}_n d\sigma = \int_{\partial V_1} \mathbf{p}_n d\sigma + \int_{\partial V_2} \mathbf{p}_n d\sigma + \int_{\partial V_0} \mathbf{p}_n d\sigma, \quad \text{(A3)}$$

since the integrals over the surfaces S_1 and S_2 between the volumes V_0, V_1 and V_0, V_2 cancel, each other on the right-hand side of (A3).

Having transformed the first two integrals on the right-hand side of (A3) into the integrals over the volumes V_1 and V_2 with the Gauss–Ostrogradsky formula, we pass to the limit $h \longrightarrow 0$. In this case, the lateral surface Σ_l, which bounds the volume V_0, tends to zero. Because of the finiteness of $\mathbf{p}_n$, the last integral on the right of (A3) transforms (in the limit) into the integral over the different sides of *s* with oppositely directed normals; hence, in view of the obvious equality $\lim_{h\to 0} V_0 = 0$, we arrive at

$$\lim_{h\to 0}\int_\Sigma \mathbf{p}_n d\sigma = \int_V \frac{\partial \mathbf{p}^i}{\partial x_i} dV + \int_s [\mathbf{p}_n] d\sigma, \quad [\mathbf{p}_n] = \mathbf{p}_n + \mathbf{p}_{-n}.$$

Eventually, Eq. (A1) takes the form

$$\int_V \left\{\rho\left[\frac{\partial \mathbf{u}}{\partial t} + (\mathbf{u}\cdot\nabla)\mathbf{u} - \mathbf{F}\right] - \frac{\partial \mathbf{p}^i}{\partial x_i}\right\} dV = \int_s [\mathbf{p}_n] d\sigma. \quad \text{(A4)}$$

Now, let Σ_s be the interface between two immiscible Newtonian magnetic fluids whose parameters (density ρ, dynamic viscosity coefficient η, and absolute permeability μ) differ on the different sides of Σ_s. For an incompressible Newtonian fluid,

$$p_{ki} = -p\delta_{ki} + \pi_{ki}, \quad \pi_{ki} = \eta\left(\frac{\partial u_k}{\partial x_i} + \frac{\partial u_i}{\partial x_k}\right),$$

$$\delta_{ki} = 1 \quad \text{for} \quad k = i, \quad \delta_{ki} = 0 \quad \text{for} \quad k \neq i,$$

where *p* is the pressure and π_{ki} is the viscous stress tensor.

In addition,

$$\frac{\partial \mathbf{p}^i}{\partial x_i} = -\nabla p + \eta\Delta\mathbf{u}, \quad \Delta = \nabla^2. \quad \text{(A5)}$$

It is assumed that the fluids are placed in a magnetic field **H** produced by external sources. According to the laws of magnetostatics, the magnetic field component normal to Σ_s, the tangential component of the induction vector $\mathbf{B} = \mu\mathbf{H}$, and the magnetization $\mathbf{M} = \mu_0^{-1}\mathbf{B} - \mathbf{H}$ experience a discontinuity on the surface Σ_s; here, $\mu_0 = 4\pi \times 10^{-7}$ H/m is the magnetic constant.

A magnetic fluid placed in a gradient magnetic field undergoes a mass gravity force with a density **g** (**g** is the gravitational acceleration) and a mass magnetic force.

Neglecting the dipole interaction between colloidal particles, we can write [1] the expression for the volume density of the magnetic force $\mathbf{F}_m = \mu_0 M \nabla H$. Then, the total density of the external mass force $\rho\mathbf{F}$ appearing in (A4) is given by

$$\rho\mathbf{F} = \rho\mathbf{g} + \mu_0 M \nabla H. \quad \text{(A6)}$$

Each point O of the smooth interface Σ_s radiates the normal vectors $\mathbf{n}$ and $-\mathbf{n}$ in opposite directions. These vectors specify the orientation of elementary areas $d\sigma_+$ and $d\sigma_-$ centered at the point O that represent on a local scale the opposite sides of the surface Σ_s. Hereafter, subscripts 1 and 2 designate the pressure, magnetization, and components of the viscous stress tensor on the areas $d\sigma_+$ and $d\sigma_-$. When immiscible ferrofluids move simultaneously, the dynamic condition [2]

$$(p_1 - p_2)n_k - (\pi_{ki}^{(1)} - \pi_{ki}^{(2)})n_i = \left\{2\alpha K + \frac{\mu_0}{2}[(M_i^{(2)}n_i)^2 - (M_i^{(1)}n_i)^2]\right\}n_k, \quad \text{(A7)}$$

$$K = \frac{1}{2}\left(\frac{1}{R_1} + \frac{1}{R_2}\right),$$

is fulfilled at any point of the interface. Here, α is the surface tension coefficient and R_1 and R_2 are the principal radii of curvature of the surface Σ_s at the point under consideration. This expression reflects the balance of surface forces acting on the opposite sides of the interface and is a generalization of the dynamic conditions used in hydrodynamics [22].

From physical considerations, it follows that the values of R_1 and R_2 have the same sign at any point of Σ_s. The sign is selected so that the hydrostatic pressure on the elementary areas $d\sigma_+$ and $d\sigma_-$ with the normals $\mathbf{n}$ and $-\mathbf{n}$, respectively, to the curved interface Σ_s is higher on the concave side of Σ_s.

Unlike the case of nonmagnetic liquids ($\mathbf{M}^{(1)} = 0$, $\mathbf{M}^{(2)} = 0$), the right-hand side of (A7) includes not only the surface pressure $2\alpha K$ due to capillary forces [22] but also a magnetic discontinuity of the pressure. This discontinuity, arising in the presence of a discontinuity in the normal component of the magnetization vector, does not depend on the interface curvature. If ferrofluids are at rest and have a flat interface, that of the areas $d\sigma_+$ and $d\sigma_-$ adjacent to the ferrofluid with a lesser value of $\mathbf{M} \cdot \mathbf{n}$ undergoes a higher pressure. For example, the pressure under the flat ferrofluid–air interface is less than atmospheric by a value of $\mu_0(\mathbf{M} \cdot \mathbf{n})/2$.

In a more compact vector form, dynamic condition (A7) is written as

$$\mathbf{p}_n + \mathbf{p}_{-n} = \left\{2\alpha K + \frac{\mu_0}{2}[(\mathbf{M}^{(2)} \cdot \mathbf{n})^2 - (\mathbf{M}^{(1)} \cdot \mathbf{n})^2]\mathbf{n}\right\}. \quad \text{(A8)}$$

Substituting (A5), (A6), and (A8) into (A4) yields

$$\int_V \left\{\rho\left[\frac{\partial \mathbf{u}}{\partial t} + (\mathbf{u} \cdot \nabla)\mathbf{u} - \mathbf{g}\right] + \nabla p - \eta\Delta\mathbf{u} - \mu_0 M \nabla H\right\} dv = \int_s \left\{2\alpha K + \frac{\mu_0}{2}[(\mathbf{M}^{(2)} \cdot \mathbf{n})^2 - (\mathbf{M}^{(1)} \cdot \mathbf{n})^2]\right\}\mathbf{n}\, d\sigma. \quad \text{(A9)}$$

In the basic text, this integral equality is written in the cylindrical coordinate system.

ACKNOWLEDGMENTS

This work was supported by the Russian Foundation for Basic Research (grant no. 99-01-01057).

REFERENCES

1. P. Rosensweig, *Ferrohydrodynamics* (Cambridge Univ. Press, Cambridge, 1985; Mir, Moscow, 1989).
2. B. M. Berkovskiĭ, V. F. Medvedev, and M. S. Krakov, *Magnetic Fluids* (Khimiya, Moscow, 1989).
3. É. Ya. Blum, M. M. Maĭorov, and A. O. Tsebers, *Magnetic Fluids* (Zinatne, Riga, 1989).
4. V. M. Korovin and A. A. Kubasov, Zh. Tekh. Fiz. **68** (1), 23 (1998) [Tech. Phys. **43**, 19 (1998)].
5. W. Luo, T. Du, and J. Huang, Phys. Rev. Lett. **82**, 4134 (1999).
6. H. C. Yang, I. J. Jang, H. E. Horng, *et al.*, J. Magn. Magn. Mater. **201**, 313 (1999).
7. V. G. Bashtovoĭ and M. S. Krakov, Prikl. Mekh. Tekh. Fiz., No. 4, 147 (1978).
8. V. M. Korovin and A. A. Kubasov, J. Magn. Magn. Mater. **202**, 547 (1999).
9. G. I. Taylor, Proc. R. Soc. London, Ser. A **146**, 501 (1934).
10. F. D. Rumscheidt and S. G. Mason, J. Colloid Sci. **17**, 260 (1962).
11. W.-K. Lee, K.-L. Yu, and R. W. Flumerfelt, Int. J. Multiphase Flow **7**, 385 (1981).
12. H. A. Stone, B. J. Bentley, and L. G. Leal, J. Fluid Mech. **173**, 131 (1986).
13. B. J. Bentley and L. G. Leal, J. Fluid Mech. **167**, 219 (1986).
14. Lord Rayleigh, Philos. Mag. **34**, 145 (1892).

15. Ch. V. Boys, *Soap Bubbles and the Forces Which Mould Them* (Society for Promoting Christian Knowledge, London, 1990; Nauchnoe Knigoizdatel'stvo, Petrograd, 1919).
16. S. Tomotika, Proc. R. Soc. London, Ser. A **150**, 322 (1935).
17. S. Chandrasekhar, *Hydrodynamic and Hydromagnetic Stability* (Clarendon, Oxford, 1961).
18. W.-K. Lee and R. W. Flumerfelt, Int. J. Multiphase Flow **7**, 363 (1981).
19. H. A. Stone and M. P. Brenner, J. Fluid Mech. **318**, 373 (1996).
20. L. I. Sedov, *A Course in Continuum Mechanics* (Nauka, Moscow, 1983; Wolters-Noordhoff, Groningen, 1971), Vol. 1.
21. P. M. Morse and H. Feshbach, *Methods of Theoretical Physics* (McGraw-Hill, New York, 1953; Inostrannaya Literatura, Moscow, 1958), Vol. 1.
22. L. D. Landau and E. M. Lifshitz, *Course of Theoretical Physics*, Vol. 6: *Fluid Mechanics* (Nauka, Moscow, 1988; Pergamon, New York, 1987).
23. V. M. Korovin, Zh. Tekh. Fiz. **71** (12), 16 (2001) [Tech. Phys. **46**, 1504 (2001)].

Translated by V. Isaakyan

Technical Physics, Vol. 47, No. 10, 2002, pp. 1237–1245. Translated from Zhurnal Tekhnicheskoĭ Fiziki, Vol. 72, No. 10, 2002, pp. 33–40.

GASES AND LIQUIDS

Formation and Dispersion of an Electrolyte Film on an Ice Electrode Melting as a Result of Joule Heat Evolution

A. I. Grigor'ev, V. V. Morozov, and S. O. Shiryaeva

Demidov State University, Sovetskaya ul. 14, Yaroslavl, 150000 Russia

e-mail: grig@uniyar.ac.ru

Received April 4, 2002

Abstract—The thickness of a liquid film (≈3.6 μm) forming on an ice electrode is determined by solving the Stefan problem. The electrode melts as a result of Joule heat evolution when the current passes through it. The temperature distributions in the film and ice substrate are found. The radius of curvature of emitting asperities formed as a result of film instability against the surface charge is found to be ≈40 nm. This value provides the intense field evaporation of individual ions and ionic clusters from the top of the asperities at a potential difference of ≈100 V. © *2002 MAIK "Nauka/Interperiodica".*

In mass spectrometry of nonvolatile and thermally unstable organic (biological) materials, their solutions in weak electrolytes are usually electrodynamically dispersed at the early stage of ion beam formation [1–4]. According to today's concepts, a liquid surface that is unstable against the surface charge emits heavily charged drops and solution clusters that have several molecules of interest from the emitting asperities that form at the final stage of instability development. Subsequently, the emitted drops and clusters lose the excess charge either because they become unstable against the self-charge or by field evaporation of tiny ionic clusters [2, 4–6]. The charged clusters may also be emitted directly from the emitting asperities on the free surface of the solution if their curvature is sufficiently large [7, 8]. The curvature of the asperity top also specifies the size of the drops emitted because of instability and, hence, their evolution. Depending on its radius and viscosity, the initial drop may disintegrate either through the emission of many fine heavily charged droplets (of radius $R \le 0.1$ μm) or by dividing into two parts comparable in size [4, 9]. Because of this, of interest are conditions under which emitting asperities form in low-temperature mass spectrometers, where water solutions freeze on the top of a capillary feeding the solution to the discharge chamber. Here, the drops and clusters leave the surface of a thin solution film arising on the ice substrate because of the Joule heat evolution due to current passage. Naturally, the thickness of this film has an effect on the height and top curvature of emitting asperities that form when electrohydrodynamic instability develops [10, 11].

In this work, in terms of an idealized model, we study the formation of a liquid film on the ice surface when the current passing through the melt generates Joule heat.

(1) Let a plate of ice (a frozen water solution of NaCl) of length a, width b, and thickness h be in contact with a thermostat kept at a temperature T_0. At the initial time instant $t = 0$, a current source (with an internal resistance r) is connected to the upper surface of the plate covered by a thin electrolyte film of initial thickness $\xi_{in} \ll h$. The emf ε of the current source acts in the direction of the x axis (Fig. 1). When the current passes through the electrolyte, the latter heats up according to the Joule law and the Joule heat Q evolves in a unit volume of the film per unit time. The effect of the current on the ice substrate is considered to be negligible. The heat evolved in the liquid film is spent on radiative heat exchange between the free surface of the film and the environment (the Stefan–Boltzmann law), is removed

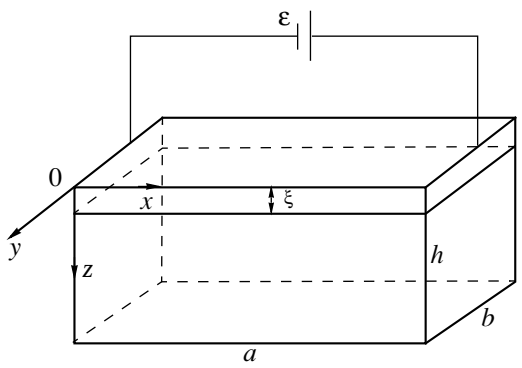

Fig. 1. Idealized model of an ice plate melting under the action of Joule heat.

1063-7842/02/4710-1237$22.00 © 2002 MAIK "Nauka/Interperiodica"

into the ice substrate due to heat conduction, and melts the ice (the melting point of ice is T_*).

Let us find the time dependence of the electrolyte film thickness $\xi = \xi(t)$ and the steady-state value of the film thickness $\xi_{ss} = \xi(\infty) = \lim_{t\to\infty}\xi(t)$, assuming that the electrophysical and thermal properties of the electrolyte and ice remain constant and the heat of phase transition κ is known. We will also find the steady-state spatial dependence of the temperature in the electrolyte and ice.

The analysis will be performed in the Cartesian coordinates with the $x0y$ plane coincident with the free surface of the film and the z axis directed downward (Fig. 1).

We will also assume that the thickness of the electrolyte film is much less than all other characteristic linear sizes of the system ($\xi \ll a, b, h$); hence, the heat transfer process in the space is one-dimensional.

(2) Mathematically, our process can be represented as the Stefan boundary-value problem:

$$\frac{\partial T_e}{\partial t} = \alpha_e\frac{\partial^2 T_e}{\partial z^2} + Q, \quad t>0, \quad 0<z<\xi(t);$$

$$\frac{\partial T_\mathrm{i}}{\partial t} = \alpha_\mathrm{i}\frac{\partial^2 T_\mathrm{i}}{\partial z^2}, \quad t>0, \quad \xi(t)<z<h;$$

$$z = 0\text{: } \lambda_e\frac{\partial T_e(0,t)}{\partial z} = \sigma T_e^4(0,t);$$

$$z = \xi\text{: } T_\mathrm{i}(\xi,t) = T_e(\xi,t) = T_*;$$

$$z = \xi(t)\text{: } \lambda_\mathrm{i}\frac{\partial T_\mathrm{i}}{\partial z} - \lambda_e\frac{\partial T_e}{\partial z} = \rho_\mathrm{i}\kappa\frac{d\xi}{dt};$$

$$z = h\text{: } T_\mathrm{i}(h,t) = T_0; \quad \xi(0) = \xi_\mathrm{in};$$

$$Q = \frac{\gamma\varepsilon^2}{a^2 c_e\rho_e}\frac{1}{\left(\gamma\dfrac{b}{a} + r\xi\right)^2}.$$

Here, Q is the rate of heat evolution in a unit electrolyte volume (an associated expression is easy to derive from general physical considerations [12]); γ is the resistivity of the electrolyte in the liquid state; $T_\mathrm{i}(z, t)$ and $T_e(z, t)$ are the desired temperature fields in the ice substrate and in the liquid electrolyte film, respectively; $\alpha_\mathrm{i} = \lambda_\mathrm{i}/c_\mathrm{i}\rho_\mathrm{i}$ and $\alpha_e = \lambda_e/c_e\rho_e$ are the thermal diffusivities of the ice and electrolyte, respectively; ρ_i and ρ_e are the respective volume densities; λ_i and λ_e are the respective thermal conductivities; c_i and c_e are the respective specific heats; $d\xi/dt$ is the rate of change of the electrolyte film thickness; and σ is the Stefan–Boltzmann constant.

In dimensionless form, this boundary-value problem can be written as follows:

$$\beta_e\frac{\partial\Theta_e}{\partial\tau} = \frac{\partial^2\Theta_e}{\partial Z^2} + \frac{A}{(1+\xi)^2}, \quad \tau>0, \quad 0<Z<\zeta(\tau); \quad (1)$$

$$\beta_\mathrm{i}\frac{\partial\Theta_\mathrm{i}}{\partial\tau} = \frac{\partial^2\Theta_\mathrm{i}}{\partial Z^2}, \quad \tau>0, \quad \zeta(\tau)<Z<H; \quad (2)$$

$$z = 0\text{: } B\frac{\partial\Theta_e(0,\tau)}{\partial Z} = \Theta_e^4(0,\tau); \quad (3)$$

$$Z = \zeta\text{: } \Theta_\mathrm{i}(\zeta,\tau) = \Theta_e(\zeta,\tau) = 1; \quad (4)$$

$$Z = \zeta(\tau)\text{: } D_1\frac{\partial\Theta_\mathrm{i}}{\partial Z} - D_2\frac{\partial\Theta_e}{\partial Z} = \frac{d\zeta}{d\tau}; \quad (5)$$

$$Z = H\text{: } \Theta_\mathrm{i}(H,\tau) = \frac{T_0}{T_*}; \quad (6)$$

$$\zeta(0) = \zeta_\mathrm{in}; \quad (7)$$

$$\tau = t/t_c; \quad \Theta_e = T_e/T_c, \quad \Theta_a = T_\mathrm{i}/T_c;$$

$$Z = z/\xi_c, \quad \zeta = \xi/\xi_c, \quad \zeta_\mathrm{in} = \xi_\mathrm{in}/\xi_c, \quad H = h/\xi_c.$$

Here, $T_c = T_*$, $\xi_c = \gamma b/ar$, and t_c are the characteristic temperature, length, and transition time of the heat exchange process;

$$A = \frac{\varepsilon^2\gamma}{T_* a^2\lambda_e r^2}; \quad B = \frac{\lambda ar}{T_*^\mathrm{i}\sigma\gamma b}; \quad D_1 = \lambda_\mathrm{i}\frac{T_* a^2 r^2 t_c}{\rho_\mathrm{i}\kappa\gamma^2 b^2};$$

$$D_2 = \lambda_e\frac{T_* a^2 r^2 t_c}{\rho_\mathrm{i}\kappa\gamma^2 b^2}; \quad \beta_\mathrm{i} = \frac{1}{\alpha_\mathrm{i}}\frac{\gamma^2 b^2}{a^2 r^2 t_c}; \quad \beta_e = \frac{1}{\alpha_e}\frac{\gamma^2 b^2}{a^2 r^2 t_c}.$$

(3) Boundary-value problem (1)–(7) will be solved by expanding in the small dimensionless parameters β_i and β_e, which are the ratio of the rate of temperature equalizing (when the system tends to the steady state) to the thermal diffusivity of the film (ice) times the squared resistance of the electrolyte film. For the electrolyte–ice system, β_i and β_e are of the same order of smallness ($\sim 10^{-2}$). The desired temperature fields will be sought in the form of expansions

$$\Theta_e(Z,\tau,\beta_e) = \Theta_{e0}(Z) + \beta_e\Theta_{e1}(Z,\tau) + O(\beta_e^2); \quad (8)$$

$$\Theta_\mathrm{i}(Z,\tau,\beta_\mathrm{i}) = \Theta_{\mathrm{i}0}(Z) + \beta_\mathrm{i}\Theta_{\mathrm{i}1}(Z,\tau) + O(\beta_\mathrm{i}^2), \quad (9)$$

where $\theta_{e0}(Z)$ and $\theta_{\mathrm{i}0}(Z)$ are the temperature fields in the electrolyte and ice in the steady state (i.e., when the temperature at each point of the system and the phase transition position are time independent).

Bearing in mind that the electrolyte temperature differs little from the ice melting point, we linearize boundary condition (3):

$$\Theta_e = \Theta_* + \Delta\Theta, \quad \Delta\Theta = \Theta_e - \Theta_*;$$

$$(\Theta_* + \Delta\Theta)^4 \approx \Theta_*^4 + 4\Theta_*^3\Delta\Theta = 4\Theta_*^3\Theta_e - 3\Theta_*^4.$$

Since $Q_* = T_*/T_c \equiv 1$, $\Theta_e^4(0, \tau) \approx 4\Theta_e(0, \tau) - 3$. Hence,

$$Z = 0: B\frac{\partial\Theta_e(0,\tau)}{\partial Z} = 4\Theta_e(0,\tau) - 3. \quad (3a)$$

An expression for the electrolyte film thickness is represented as

$$\zeta(\tau, \beta_i) = \zeta_0(\tau) + \beta_i\zeta_1(\tau) = \zeta_0(\tau) + \frac{\alpha_e}{\alpha_i}\beta_e\zeta_1(\tau) + O(\beta_e^2). \quad (10)$$

Now, substituting solutions (8) and (9) into (1), (2), (3a), and (4)–(6) and expression (10) into (5) and (7) and equating the coefficients by the same powers of β_e and β_i, we come to the boundary-value problem (stated in the zeroth order of smallness in β_e and β_i for finding the desired temperature fields in the time dependences of the electrolyte film thickness:

$$\frac{\partial^2\Theta_{e0}}{\partial Z^2} = -\frac{A}{(1+\zeta_0)^2}, \quad 0 < Z < \zeta_0; \quad (11)$$

$$\frac{\partial^2\Theta_{i0}}{\partial Z^2} = 0, \quad \zeta_0 < Z < H; \quad (12)$$

$$Z = 0: B\frac{\partial\Theta_{e0}(0,\tau)}{\partial Z} = \Theta_{e0}(0,\tau) - 3; \quad (13)$$

$$Z = \zeta_0: \theta_{e0}(\zeta_0, \tau) = \theta_{i0}(\zeta_0, \tau) = 1; \quad (14)$$

$$Z = \zeta_0: D_1\frac{\partial\Theta_{i0}}{\partial Z} - D_2\frac{\partial\Theta_{e0}}{\partial Z} = \frac{d\zeta_0}{d\tau}; \quad (15)$$

$$Z = H: \Theta_{i0}(H, \tau) = \frac{T_0}{T_*}; \quad (16)$$

$$\zeta_0(0) = \zeta_{in}. \quad (17)$$

To find first-order corrections to the temperature fields, we must solve the boundary-value problem

$$\frac{\partial^2\Theta_{e1}}{\partial Z^2} = \frac{\partial\Theta_{e0}}{\partial\tau} + \frac{\alpha_e}{\alpha_i}\frac{2A\zeta_1}{(1+\zeta_0)^3}, \quad 0 < Z < \zeta; \quad (18)$$

$$\frac{\partial^2\Theta_{i1}}{\partial Z^2} = \frac{\partial\Theta_{i0}}{\partial\tau}, \quad \zeta < Z < H; \quad (19)$$

$$Z = 0: B\frac{\partial\Theta_{e1}(0,\tau)}{\partial Z} = 4\Theta_{e1}(0,\tau); \quad (20)$$

$$Z = \zeta: \Theta_{e1}(\zeta_0, \tau) = \Theta_{i1}(\zeta_0, \tau) = 0; \quad (21)$$

$$Z = \zeta: D_1\frac{\partial\Theta_{i1}}{\partial Z} - D_2\frac{\alpha_i}{\alpha_e}\frac{\partial\Theta_{e1}}{\partial Z} = \frac{d\zeta_1}{d\tau}; \quad (22)$$

$$Z = H: \Theta_{i1}(H, \tau) = 0; \quad (23)$$

$$\zeta_1(0) = 0, \quad (24)$$

where the electrolyte film thickness ζ is defined by (10).

(4) Let us solve the zeroth-order problem. In view of boundary conditions (13) and (14), we find from (11) the function describing the temperature distribution in the liquid film:

$$\Theta_{e0} = -\frac{AZ^2}{2(1+\zeta_0)^2} + \frac{3(\zeta_0 - Z)}{4\zeta_0 + B} + \frac{4Z + B}{4\zeta_0 + B}\left(1 + \frac{A\zeta_0^2}{2(1+\zeta_0)^2}\right). \quad (25)$$

Similarly, in view of boundary conditions (14) and (16), we find from (12) the temperature distribution in the ice plate:

$$\Theta_{i0} = 1 + \frac{T_0 - T_*}{T_*}\frac{Z - \zeta_0}{H - \zeta_0}. \quad (26)$$

To uniquely determine the temperature fields in the liquid film and in the ice plate, it is necessary to find the electrolyte film thickness in the zero approximation as a function of time: $\zeta_0(\tau)$. To find a determining differential equation, we substitute expressions (25) and (26) into boundary condition (15):

$$D_1\frac{T_0 - T_*}{T_*}\frac{1}{H - \zeta_0} + D_2\left[\frac{A\zeta_0}{(1+\zeta_0)^2} + \frac{3}{4\zeta_0 + B} - \frac{4}{4\zeta_0 + B}\left(1 + \frac{A\zeta_0^2}{2(1+\zeta_0)^2}\right)\right] = \frac{d\zeta_0}{d\tau}.$$

With actual values of the physical quantities defining the parameter B, the condition $B \gg 1$ is valid ($B \approx 8.6 \times 10^5$, $A \approx 0.15$, and $\zeta_0 \sim 1$); therefore, in the approximation used, this equation can be simplified by rejecting terms proportional to $\sim B^{-1}$:

$$\frac{d\zeta_0}{d\tau} \approx D_1\frac{T_0 - T_*}{T_*}\frac{1}{H - \zeta_0} + AD_2\frac{\zeta_0}{(1+\zeta_0)^2}. \quad (27)$$

Integrating this expression with regard for condition (17) yields

$$\tau = \frac{1}{L}\left[\frac{\zeta_{in}^2 - \zeta_0^2}{2} + W_1(\zeta_{in} - \zeta_0) + N_1\ln\left|\frac{\zeta_{in} - \eta_1}{\zeta_0 - \eta_1}\right| + N_2\ln\left|\frac{\xi_{in} - \eta_2}{\zeta_0 - \eta_2}\right|\right];$$

$$N_1 = \frac{W_3 + W_2\eta_1}{\eta_1 - \eta_2}; \quad N_2 = \frac{W_3 + W_2\eta_2}{\eta_1 - \eta_2};$$

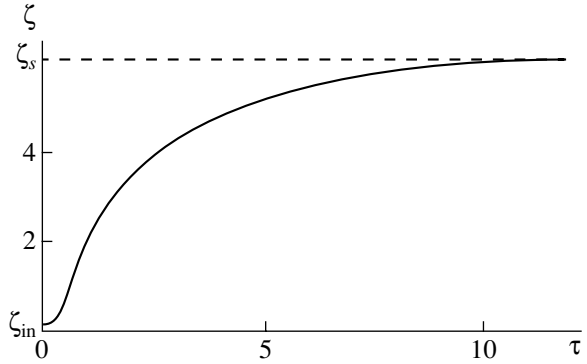

Fig. 2. Dimensionless thickness ζ of the liquid film vs. dimensionless time τ.

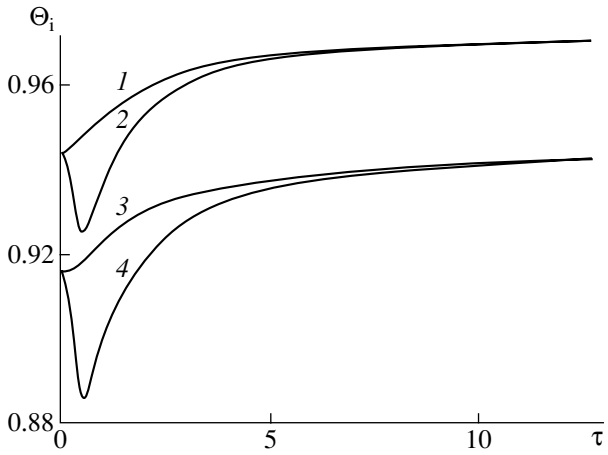

Fig. 3. Dimensionless temperature Θ_i of the ice plate vs. dimensionless time τ in the (*1*, *3*) zeroth and (*2*, *4*) first approximations calculated at various distances *Z* from the free surface: $Z = 2\zeta_9$ (*1*, *2*) and $3\zeta_9$ (*3*, *4*).

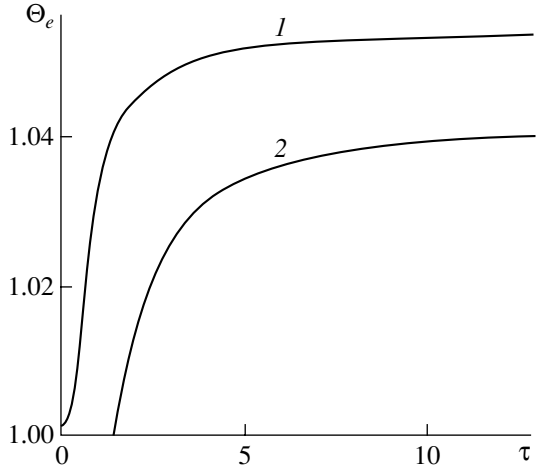

Fig. 4. Dimensionless temperature Θ_e of the liquid film vs. dimensionless time τ calculated at various distances *Z* from the free surface: $Z = 0$ (*1*) and $0.5\,\zeta_6$ (*2*).

$$W_1 = 2 - H - V_1; \quad W_2 = 1 - 2H - V_2 - V_1 W_1;$$

$$W_3 = -H - V_2 W_1; \quad V_1 = \frac{2K - AD_2 H}{L};$$

$$V_2 = \frac{K}{L}; \quad L = K - AD_2; \quad K = D_1 \frac{T_0 - T_*}{T_*},$$

where η_1 and η_2 are the roots of the equation

$$\zeta_0^2 + V_1 \zeta_0 + V_2 = 0.$$

The plot of the electrolyte film thickness vs. time constructed with (27) is given in Fig. 2.

The dependence $\zeta_0 = \zeta_0(\tau)$ defined by (27) cannot be written in explicit form; therefore, the functions describing the temperature fields in the film and ice are extremely awkward. It is convenient to write them in parametric form (through the parameters φ and ψ):

$$\Theta_{i0} = 1 + \frac{T_0 - T_*}{T_*} \frac{Z - \varphi}{H - \varphi};$$

$$\tau = -\frac{1}{L}\left[\frac{\varphi^2}{2} + W_1 \varphi + N_1 \ln|\varphi - \eta_1| + N_2 \ln|\varphi - \eta_2|\right] + \text{const};$$

$$\Theta_{e0} = -\frac{AZ^2}{2(1+\psi)^2} + \frac{3(\psi - Z)}{4\psi + B} + \frac{4Z + B}{4\psi + B}\left(1 + \frac{A\psi^2}{2(1+\psi)^2}\right);$$

$$\tau = -\frac{1}{L}\left[\frac{\psi^2}{2} + W_1 \psi + N_1 \ln|\psi - \eta_1| + N_2 \ln|\psi - \eta_2|\right] + \text{const};$$

$$\frac{1}{L}\left[\frac{\zeta_{in}^2}{2} + W_1 \zeta_{in} + N_1 \ln|\zeta_{in} - \eta_1| + N_2 \ln|\zeta_{in} - \eta_2|\right] = \text{const}.$$

The temperature distribution in the electrolyte film can also be simplified. Since $B \gg |\psi|$ (because $|\varphi|$ and $|\psi| \sim 1$), we have

$$\Theta_{e0} \approx 1 + \frac{A(\psi^2 - Z^2)}{2(1+\psi)^2}.$$

The time dependences of the temperature of the ice plate calculated in the zeroth approximation are presented in Fig. 3 by curves *1* and *3*. In Fig. 4, similar dependences are shown for the electrolyte film (curves *1*, *2*).

(5) Now, let us calculate the first-order corrections. Substituting (25) into Eq. (18) and integrating the resultant equation with boundary conditions (20) and (21), we arrive at the temperature field in the electrolyte film:

$$\Theta_{e1} = \frac{A\dot{\zeta}_0}{12(1+\zeta_0)^3}[Z^2(6\zeta_0+Z^2)-Z_0^2(6\zeta_0+\zeta_0^2)] + \frac{\alpha_e}{\alpha_i}\frac{A\zeta_1(Z^2-\zeta_0^2)}{12(1+\zeta_0)^3}; \quad (28)$$

$$\dot{\zeta}_0 \equiv \frac{d\zeta_0}{d\tau} = -L\left[\zeta_0 + W_1 + \frac{N_1}{\zeta_0-\eta_1} + \frac{N_2}{\zeta_0-\eta_2}\right]^{-1} \quad (29)$$

(here, it is taken into account that $B \gg \zeta_0$).

Similarly, substituting (26) into Eq. (19) and integrating the resultant equation with boundary conditions (21) and (23), we arrive at the temperature field in the ice plate:

$$\theta_{i1} = \frac{T_0-T_*}{T_*}\dot{\zeta}_0\left\{\frac{Z^3-3HZ^2+2H^2}{6(\zeta_0-H)^2} + (H-Z)\frac{\zeta_0^3-3H\zeta_0^2+2H^3}{6(\zeta_0-H)^3}\right\}. \quad (30)$$

Now, substituting functions (28) and (30) into phase-matching condition (22), we come to a differential equation for finding the time dependence of the electrolyte film thickness in the first approximation:

$$\frac{1}{3}D_1\frac{T_0-T_*}{T_*}\dot{\zeta}_0 - \frac{AD_2}{6}\frac{\zeta_0}{(1+\zeta_0)^3} \times\left\{2\frac{\alpha_e}{\alpha_i}\dot{\zeta}_0\zeta_0(3+\zeta_0)+\zeta_1\right\} = \frac{d\zeta_1}{d\tau}$$

or

$$\frac{d\zeta_1}{d\tau} + u(\tau)\zeta_1 = \nu(\tau);$$

$$u(\tau) = \frac{AD_2\zeta_0(\tau)}{6[1+\zeta_0(\tau)]^3};$$

$$\nu(\tau) = \frac{\dot{\zeta}_0}{3}\left\{K - \frac{\alpha_i}{\alpha_e}\frac{AD_2\zeta_0^2(\tau)[3+\zeta_0(\tau)]}{[1+\zeta_0(\tau)]^3}\right\},$$

where $\zeta_0(\tau)$ and $\dot{\zeta}_0$ are defined by (27) and (20), respectively.

The general solution of this first-order linear inhomogeneous differential equation is as follows (in view of initial condition (24)):

$$\zeta_1(\tau) = \exp\left(-\int_0^\tau u(\mu)d\mu\right) \times\left\{\int_0^\tau \nu(\nu)\exp\left(\int_0^\nu u(\mu)d\mu\right)d\nu\right\}. \quad (31)$$

Since the function $\zeta_0(\tau)$ is irreducible to explicit form, the function $\zeta_1(\tau)$ cannot be found analytically; however, it can be found by numerically integrating (31).

One can also roughly estimate the function $\zeta_1(\tau)$. Assuming that $\zeta_0 = \zeta_9$, where $\zeta_9 = \zeta_0(\infty)$, we obtain

$$u(\tau) = u_9 = \frac{AD_2\zeta_9}{6(1+\zeta_9)^3}; \quad \nu(\tau) = 0,$$

where

$$\zeta_1(\tau) = \exp(-u_9\tau). \quad (32)$$

The first-order spatial temperature distribution in the ice plate is demonstrated by curves *2* and *4* in Fig. 3. The slight decrease in the temperature at the early stage of Joule heat evolution is due to the fact that the interface, at which the solid electrolyte melts, serves as a heat sink. When it comes into effect, the temperature of the ice plate decreases for a time because the heat flux to the interface grows according to boundary condition (22). First-order corrections to the temperature distribution in the liquid film and to the time dependence of the film are insignificant and are not seen in Fig. 3.

To make numerical estimates, we put $a = b = h = 10^{-4}$ m, $T_* = 273$ K, $T_0 = 60$ K, $\gamma = 0.06$ Ω m, $\kappa = 3.35 \times 10^5$ J/kg, $\rho_i = 920$ kg/m^3, $r = 10^5$ Ω, $\alpha_i = 1.14 \times 10^{-6}$ m^2/s, $\alpha_e = 1.37 \times 10^{-7}$ m^2/s, $\lambda_i = 2.2$ W/(m K), $\lambda_e = 0.6$ W/(m K), $\varepsilon = 200$ V, and $\xi_{in} = 10^{-7}$ m. With such values of the parameters, we find two values of the dimensionless thickness of the film: $\eta_1 \approx 0.16$ and $\eta_2 \approx 6.06$. The former is meaningless since $\zeta_0 \longrightarrow \eta_1$ at $\tau \longrightarrow -\infty$ ($\eta_2 = \zeta_2$). Eventually, the thickness of the film tends to the steady-state value ≈3.6 μm for a characteristic time $t_c \approx 100$ μs.

(6) When the drop becomes unstable against the surface charge (in an external electrostatic field), emitting asperities form through the superposition of unstable short-wavelength modes [10, 13]. In experiments with an electric discharge initiated from the surface of a melting icicle in a nonuniform electrostatic field [10, 14], an emitting asperity in the form of a soliton was observed. The soliton formed in the domain of the weak field and propagated in the direction of field growth. Having reached the point of maximum field, the soliton stopped, and a discharge in the form of diffuse glow was initiated at its top. The height of the soliton was at least one order of magnitude greater than the thickness of the film.

In the case of a vacuum mass spectrometer, we also deal with a discharge from the surface of a small piece of ice (when a potential difference $\Delta\psi$ is applied normally to the surface of the liquid film, i.e., along the z axis in Fig. 1). Therefore, it might be expected that an emitting asperity on the ice surface will also have the form of a soliton. For our qualitative analysis, it is necessary to estimate the curvature of its top, which specifies the field strength near the site of discharge ignition. According to [15], the analytical expression for the shape of the soliton of height H in a liquid film of thickness h has the form

$$y = H\operatorname{sech}^2\left\{\sqrt{\frac{3H}{2h}}\frac{\delta}{h}\right\},$$

where $\delta = \zeta(x, t) = x - vt$ and v is a constant having the dimension of velocity.

The radius of curvature r of the soliton top is given by

$$r = \left[\sqrt{1+\left(\frac{dy}{d\delta}\right)^2}\Big/\frac{d^2y}{d\delta^2}\right]_{\delta=0} \equiv \left(\frac{d^2y}{d\delta^2}\right)^{-1}_{\delta=0} \equiv \frac{h^3}{3H^2}.$$

Assuming that $h/H \sim 0.1$, one can easily check that $r \sim 10^{-2}h$. As applied to the mass-spectrometric conditions, we find that $r \sim 40$ nm for $h \approx 4$ μm. This means that the field strength at the top of an emitting asperity may be as high as ≈2.5 V/nm even at $\Delta\psi = 100$ V. Hence, the field evaporation of individual ions and ionic clusters may take place [2, 5, 6]. We will consider the field evaporation of ions from electrolytic solutions.

(7) According to [16], the physical mechanism behind the field evaporation of ions and charged clusters from electrolytic solutions is assumed to be identical to the mechanism of the field evaporation of ions from the metal surface that was theoretically elaborated for field-ion microscopy [17] and liquid-metal ion sources [18] and involves the thermal activation of the process. For example, when the thermal activation exceeds the Schottky barrier (this barrier appears when the metal surface is subjected to an electric field of strength E), the rate constant K of metal evaporation by the electrolytic field is given by the Arrhenius law [17]:

$$K = \omega\exp\left[-\frac{Q-(z_q^9|q|^9E)^{1/2}}{kT}\right], \quad Q \equiv \Lambda + J - \varphi; \quad (33)$$

where k is the Boltzmann constant, T is absolute temperature, ω is the atom oscillation frequency, q is the ionic charge, and z_q is the charge number.

In the exponent, Q is the energy of activation of ion evaporation. In a virtual cycle of thermal ionization as applied to field-ion microscopy [17], this parameter is calculated as follows. An atom evaporates from the metal surface, absorbing the energy of sublimation Λ; the atom ionizes, consuming an energy J; and the electron being released returns to the metal, evolving an energy φ equal to the work function of an electron in the metal. The second term in the numerator of the exponent stands for a decrease in the energy of activation due to the Schottky effect.

To describe the field evaporation of ions and ionic clusters from electrolytic solutions, one can also use an expression like (33) [7, 16]. In this expression, ω is replaced by kT/h (in terms of the theory of absolute reaction rates), where h is the Planck constant, and the energy of activation of ion evaporation from the metal surface Q is replaced by ΔH_+, where ΔH_+ is the change in the enthalpy when an ion or an ionic cluster passes from the solution to a vacuum. The value of ΔH_+ is taken to be equal in magnitude but opposite in sign to ΔH_*, where ΔH_* is the change in the enthalpy upon the solvation of an ion or the complete solvation of an ionic cluster in the solution. It was shown [16, 19] that the ΔH_* as a function of n (n is the number of atoms in a cluster) for ionic clusters is nonmonotonic and reaches the minimum $\Delta H_* = 2.32$–2.73 eV at a certain $n = n_*$. Such a value of the energy of activation for the field evaporation of ionic clusters provides consistency with experimental data even at $E = 1$ V/nm. For individual ions, however, the energy of activation of their evaporation ΔH_* calculated from the energy of solvation is twice or three times as great as the values found [19, 20]. At first glance, this means that agreement between the theory and experiment requires electric field strengths at the surface of the solution to be one order of magnitude higher, i.e., the same as for the field evaporation of metal ions ($E \geq 10$ V/nm) [19, 21]). Such a conclusion, however, is somewhat premature because, in practice, a field strength $E \geq 10$ V/nm used in the field evaporation of ions from the surface of a solid or liquid metal is provided by preparing a special ion-emitting tip that has a radius of curvature of ≈1 μm. In mass spectrometers where the material to be analyzed is introduced into the discharge chamber electrohydrodynamically through a capillary of diameter ≈100 μm (the theory of which was developed in [7, 16, 19]), field

strengths on the order of 10 V/nm are unlikely to be reached. In addition, a number of possible channels for the field evaporation of ions from solutions were not considered in [7, 16, 19, 21].

In actual (nonideal) solutions, dissolved molecules do not all dissociate; the fraction of dissociated molecules depends on the concentrations of solution components, temperature, and intermolecular interaction [20]. Let us consider the field evaporation of a Na^+ positive ion from water solutions of NaI and NaCl salts. The energy of activation of Na^+ field evaporation from the solution surface will be calculated following a virtual cycle of thermal ionization for NaI and NaCl molecules, as is done for the field evaporation of ions from the metal surface [16]. However, unlike [16], we will consider the decomposition of a NaI or NaCl neutral molecule on the surface of the electrolytic solution (subjected to a strong electric field) into Na^+ and I^- (Cl^-) ions with the Na^+ ion passing to the gas phase, rather than the field extraction of an ion from the metal continuous surface. If Λ is the energy of sublimation of the molecule, D is the energy of molecule dissociation into two atoms (Na and I or Cl), J is the energy of Na atom ionization, L is the electron affinity to the I (Cl) atom, and φ is the electron work function in water, then the energy of activation for the field evaporation of the Na^+ ion from the electrolytic solution has the form

$$Q = \Lambda + D + J - \varphi - L. \tag{34}$$

In other words, a salt molecule sublimates from the solution and dissociates into two atoms; the Na atom ionizes; and the electron and the I (Cl) atom return to the solution, where the electron adheres to the I (Cl) atom with the formation of the negative ion. Recall that the entire thermochemical cycle is virtual and that here we are actually dealing with the field decomposition of a salt molecule into Na^+ and I^- (Cl^-) ions directly on the solution surface. According to [22], for a NaI molecule, $\Lambda = 2.08$ eV and $D = 3.76$ eV; for a NaCl molecule, $\Lambda = 2.39$ eV and $D = 4.22$ eV. In addition, according to [22, 23], the ionization potential for a Na atom is $J = 5.14$ eV, and the electron affinity to I and Cl atoms is $L = 3.06$ and 3.61 eV. The electron work function in water is $\varphi = 6.13$ eV [24]. Substituting these values into (34), we find the activation energy for the field evaporation of a Na^+ ion from NaI and NaCl aqueous electrolytes: $Q_{NaI} = 1.78$ eV and $Q_{NaCl} = 2.01$ eV. It is easy to check that in both cases the energy Q calculated from (34) is less than the energy of evaporation for an individual Na^+ ion, 4.18 eV [7], found from its hydration (solvation) energy in accordance with [2, 16]. One can also see that the calculated values of Q are close to the activation energies for the field evaporation of ionic clusters from the solution: 2.32–2.73 eV [16, 19].

To summarize, we note that the rate constant for the field evaporation of an ion from an electrolytic solution should be calculated by the formula

$$K = (kT/h)\exp\left[-\frac{Q - (z_q^9|q|^9E)^{1/2}}{kT}\right], \tag{35}$$
$$Q = \Lambda + D + J - \varphi - L.$$

In order to find the rate V of field evaporation of ions from the solution surface using the reaction rate constant defined by (35), it is necessary to multiply the reaction rate constant K by N, where N is the number of undissociated salt molecules on the solution surface subjected to a strong electric field: $V = KN$. The dimension of V is s^{-1} (the number of ions evaporated per second).

(8) Let us evaluate the rate of Na^+ field evaporation from a NaCl aqueous solution of concentration 10^{-3} M (as in experiments [19]) with a degree of molecule dissociation of 0.9. We assume (according to Section 6) that ions evaporate from the hemispherical top of an isolated soliton with a radius of the top $r = 40$ nm under an electric field $E = 2.5$ V/nm. It is easy to check that only a limited number N of undissociated NaCl molecules will remain on the hemispherical surface of the asperity in the region of the strong field. Assume also (according to Section 5) that the electrolyte surface temperature $T = 290$ K and (according to Section 7) that the activation energy of Na^+ field evaporation $Q_{NaCl} = 2.01$ eV. Then, according to (35), $K \approx 4 \times 10^{10}$ s^{-1} and the rate of Na^+ field evaporation $V \approx 4 \times 10^{11}$ s^{-1}, which corresponds to a current through the asperity of ~0.01 μA. Clearly, this estimate is rather crude and determines only the upper limit of possible currents, since at $N \sim 1$ the rate of ion field evaporation will be limited by the rate of NaCl molecule diffusion from the bulk of the solution to the emitting asperity surface in the region of a high electric field ($E \geq 1$ V/nm).

Obviously, according to Section 7, the field evaporation of individual ions will be accompanied by the evaporation of ionic clusters with activation energies between 2.32 and 2.73 eV [16, 19].

(9) The future of field-evaporated ions depends on their interaction with a cloud of neutral molecules of the solvent that evaporate from the electrolyte film. To perform a qualitative analysis, we will consider only the steady-state distribution of the water vapor molecule concentration near a spherical drop of radius R_0 (R_0 is on the order of the characteristic linear horizontal size of the electrolyte film; see. Sec. 1). This distribution is found by solving the initial problem

$$\mathrm{div}[D(c)\mathrm{grad}c] = 0; \tag{36}$$

$$r = r_0\colon -D(c)\mathrm{grad}c = J \equiv 0.25\chi V(c_0 - c_\infty); \quad c = c_0. \tag{37}$$

Here, χ is the evaporation coefficient, $D(c)$ is the diffusion coefficient of vapor molecules, V is the thermal velocity of the molecules, c_0 is the vapor molecule concentration near the drop, and c_∞ is the vapor molecule concentration away from the drop. An expression for the vapor flux from the surface of the drop in (37) is defined by the Hertz–Knudsen law [2]. The concentration dependence of the diffusion coefficient is taken in the form $D(c) = V/3cS$, where S is the molecule collision cross section.

A solution to the problem stated by (36) and (37) is

$$c(\mathbf{r}) = c_0 \exp[-0.75 c_0 S \chi R_0 (1 - R_0/r)], \qquad (38)$$

where r is a radial constant.

A field-evaporated Na^+ ion will move in the high electric field near the emitting asperity through a cloud of water vapor molecules. To estimate the number n of collisions between the ion and neutral molecules, one must integrate the product of its cross section S_* of collisions with molecules by the molecule concentration defined by (38) along the ion path (e.g., along the x axis):

$$n = \int_{R_0}^{\infty} S_* c(\mathbf{r}) dx. \qquad (39)$$

Let us assume that $\chi = 0.4$, c_0 equals the concentration of water vapor saturated at the electrolyte surface temperature ($c_0 \approx 4 \times 10^{17}$ cm^{-3}), and the cross sections of molecule–molecule and molecule–ion collisions depend only on the molecule and ion geometrical sizes. Then, it is easy to verify that the concentration $c(r)$ drops rapidly with distance from the liquid electrolyte surface: $c(r) \sim \exp[-22(1 - R_0/r)]$. The asymptotic value of integral (39) depends on its value in the neighborhood of the lower limit (i.e., at the point where the exponent of the exponential reaches a maximum) and is easy to take by one of the techniques commonly used in this situation (see, e.g., [25, Chap. 3]). As follows from the calculation, $n \approx 3$.

It is clear that the passage of high-energy ions (both individual and clustered) through a cloud of neutral vapor will cause the intense excitation and ionization of the molecules, as well as the intense decomposition of the clusters. Eventually, a cloud of weakly ionized plasma will form near an emitting asperity. This cloud will affect the motion and time evolution of ions evaporated, as occurs, e.g., in liquid-metal ion sources, which operate by a similar mechanism [18]. This phenomenon deserves special consideration.

It should be noted that, along with the field evaporation of individual ions and ionic clusters, the separation of drops from the top of an emitting asperity may take place. These drops have a characteristic size on the order of the radius of curvature of the asperity and bare a charge slightly exceeding the critical value in terms of Rayleigh stability [9, 26]. The future of these drops depends on their viscosity, which plays a crucial role for the tiny drops under consideration and provides a path for excess charge removal upon ion field evaporation [27].

CONCLUSION

Qualitative analysis of an ion emitter in a low-temperature mass spectrometer with electrohydrodynamic feed of the material to be studied allowed us to establish the essentials of individual and clustered ion emission from electrolytic solutions. The basic mechanism behind the formation of an ion–cluster beam in the mass spectrometer is the field evaporation of individual ions and ionic clusters and their subsequent interaction with neutral solvent vapor molecules, which form a cloud near the emitter top because of their thermal evaporation from the liquid electrolyte film.

ACKNOWLEDGMENTS

This work was supported by grant no. 00-15-9925 of the President of the Russian Federation.

REFERENCES

1. D. S. Simona, Int. J. Mass Spectrom. Ion Processes **15**, 291 (1974).
2. N. B. Zolotoĭ, G. V. Karpov, and V. E. Skurat, Zh. Tekh. Fiz. **58**, 315 (1988) [Sov. Phys. Tech. Phys. **33**, 193 (1988)].
3. J. B. Fenn, M. Mann, Chin Kai Meng, *et al.*, Science **246**, 64 (1989).
4. S. O. Shiryaeva and A. I. Grigor'ev, Zh. Tekh. Fiz. **63** (8), 162 (1993) [Tech. Phys. **38**, 715 (1993)].
5. A. I. Grigor'ev, Pis'ma Zh. Tekh. Fiz. **27** (4), 52 (2001) [Tech. Phys. Lett. **27**, 155 (2001)].
6. A. I. Grigor'ev, Pis'ma Zh. Tekh. Fiz. **27** (7), 89 (2001) [Tech. Phys. Lett. **27**, 305 (2001)].
7. N. B. Zolotoĭ, Zh. Tekh. Fiz. **65** (11), 159 (1995) [Tech. Phys. **40**, 1175 (1995)].
8. N. B. Zolotoĭ and G. V. Karpov, Dokl. Akad. Nauk **348**, 336 (1996).
9. N. B. Grigor'ev and S. O. Shiryaeva, Izv. Akad. Nauk, Mekh. Zhidk. Gaza, No. 3, 3 (1994).
10. A. I. Grigor'ev, I. D. Grigor'eva, and S. O. Shiryaeva, J. Sci. Exploration **5**, 163 (1991).
11. A. I. Grigor'ev, M. I. Munichev, and S. O. Shiryaeva, J. Colloid Interface Sci. **166**, 267 (1994).
12. A. I. Grigor'ev and V. V. Morozov, Pis'ma Zh. Tekh. Fiz. **28** (4), 12 (2002) [Tech. Phys. Lett. **28**, 131 (2002)].
13. D. F. Belonozhko, A. I. Grigor'ev, and S. O. Shiryaeva, Zh. Tekh. Fiz. **68** (10), 27 (1998) [Tech. Phys. **43**, 1160 (1998)].
14. A. I. Grigor'ev, Pis'ma Zh. Tekh. Fiz. **11** (16), 1004 (1985) [Sov. Tech. Phys. Lett. **11**, 415 (1985)].
15. E. N. Pelinovskiĭ, *Nonlinear Waves: Propagation and Interaction* (Nauka, Moscow, 1981), pp. 187–202.

16. J. V. Iribarne and B. A. Thomson, J. Chem. Phys. **64**, 2287 (1976).
17. E. W. Muller and T. T. Tsong, *Field Ion Microscopy: An Introduction to Principles, Experiments, and Applications* (Elsevier, New York, 1969; Metallurgiya, Moscow, 1972).
18. R. Gomer, Appl. Phys. **19**, 365 (1979).
19. B. A. Thomson and J. V. Iribarne, J. Chem. Phys. **71**, 4451 (1979).
20. N. A. Izmaĭlov, *Electrochemistry of Solutions* (Khimiya, Moscow, 1976).
21. N. B. Zolotoĭ and G. V. Karpov, Dokl. Akad. Nauk **348**, 336 (1996).
22. L. V. Gurvich, I. V. Veĭts, V. A. Medvedev, *et al.*, *Thermodynamic Properties of Substances: Reference Edition* (Nauka, Moscow, 1982), Vol. 4, Part 1.
23. L. V. Gurvich, I. V. Veĭts, V. A. Medvedev, *et al.*, *Thermodynamic Properties of Substances: Reference Edition* (Nauka, Moscow, 1982), Vol. 4, Part 1.
24. V. S. Fomenko, *Emission Properties of Materials: A Handbook* (Naukova Dumka, Kiev, 1981).
25. A. H. Nayfeh, *Introduction to Perturbation Techniques* (Wiley, New York, 1981; Mir, Moscow, 1984).
26. A. I. Grigor'ev and S. O. Shiryaeva, Inzh.-Fiz. Zh. **61**, 632 (1991).
27. A. I. Grigor'ev, Zh. Tekh. Fiz. **71** (10), 1 (2001) [Tech. Phys. **46**, 1205 (2001)].

Translated by V. Isaakyan

Technical Physics, Vol. 47, No. 10, 2002, pp. 1246–1249. Translated from Zhurnal Tekhnicheskoĭ Fiziki, Vol. 72, No. 10, 2002, pp. 41–44.

GAS DISCHARGES, PLASMA

Characteristic Features of Reactions Initiated by a Flash Corona Discharge

N. A. Aristova* and I. M. Piskarev**

** Nizhni Tagil Technological Institute, Ural State Technical University, Nizhni Tagil, Russia*

*** Skobeltsin Research Institute of Nuclear Physics, Moscow State University, Moscow, 119992 Russia*

Received January 28, 2002

Abstract—The oxidation of solutes in water under the action of a flash corona discharge between solid electrodes and the water surface is investigated. The dependences of the oxidation rate on the gas-phase volume, the electrode–liquid distance, the discharge current, and the number of electrodes are examined. These dependences should be taken into consideration when designing reactors. © *2002 MAIK "Nauka/Interperiodica".*

Chemical reactions of impurity decomposition in water under the action of an electric discharge have attracted great interest because they do not need expensive equipment and the energy expenditure is nearly the same as that required for other oxidation processes [1, 2]. At the same time, electric discharges are practically not used in treatment plants because these processes are still poorly understood. In [3], conditions for the initiation of oxidation reactions in liquids under the action of a certain type of pulsed electric discharge (namely, a flash corona discharge) were considered. Under certain conditions, the efficiency of these reactions turns out to be higher than the ozonization efficiency [4]. It is of interest to consider the features of oxidation kinetics in a reactor based on a flash corona electric discharge. In this paper, we study the decomposition rate of solutes in water under the action of a flash corona electric discharge as a function of the gas-phase volume and the dependence of the oxidation yield on the discharge current, the electrode–liquid distance, and the number of electrodes over the surface.

EXPERIMENTAL TECHNIQUE

The dependence of the reaction rate on the gas-phase volume was studied in a cylindrical glass vessel with a base area of 50 cm^2 and height of 20 cm. A 0.2-mm-diameter platinum electrode contacting the liquid was inserted through a hole in the cylinder bottom. A Teflon plug in the form of a piston with holes for introducing an aluminum discharge electrode and two glass pipes through which oxygen was blown was inserted into the cylinder. The height of the plug over the liquid surface determined the gas-phase volume. The distance between the contact electrode and the liquid surface was kept at 6 mm irrespective of the plug position. The vessel was filled up with 40 ml of an orange aniline dye solution (Orange-1, $C_{16}H_{12}O_4N_2S$) with a concentration of 4.5×10^{-4} mol/l. We used a commercial dye and distilled water. The dye solution was filtrated. The dye concentration was measured with a visible-light spectrophotometer. This allowed us to measure a decrease in the dye concentration to 0.5% of the initial one. We investigated how the dye decoloration time depended on the gas-phase volume. By decoloration we meant a decrease in the concentration to 1%, at which the dye color became invisible.

The dependence of the oxidation rate I^- on the electrode current (in the current range in which the discharge remained a flash corona) was studied in a cylindrical glass vessel with a base area of 100 cm^2 and volume of 500 ml. The vessel was filled up with 100 ml of a 0.01-M (1.66-g/l) KI solution. The electrode–liquid distance was 7.5 mm. The discharge current was varied from 7 to 125 μA by varying the high voltage across the discharge gap from 7 to 13.8 kV. The reaction time was 30 min.

The dependence of the oxidation rate I^- on the distance between the electrode and the liquid surface was studied in the same vessel and for the same solution. The discharge current was maintained at a constant level of 70 μA by controlling the high voltage. The distance was varied in the range 5.1–13.9 mm; in this case, the high voltage was varied from 9.2 to 15 kV. The treatment duration was 30 min for each distance.

The dependence of the reaction yield on the number of electrodes was investigated in a glass vessel with a base area of 150 cm^2 and volume of 2.5 l. The vessel was filled up with 100 ml of a solution. Twenty discharge electrodes were introduced through the holes in a Teflon plug. The contact electrode was located at the vessel bottom. A negative voltage of 10 kV was applied to each electrode through an individual 12-MΩ ballast resistor. The current through each electrode amounted to 70 μA. The distance from the electrodes to the liquid surface was chosen to be 6 mm. In the course of the experiment, the voltage was applied either to one electrode or to a group (from two to twenty) of the elec-

1063-7842/02/4710-1246$22.00

trodes. We treated 0.1-M KI and oxalic acid solutions. The oxalic acid concentration was determined by titrating with 0.05-M KI in an acid medium. In all cases, the amount of free iodine was determined by titrating with sodium thiosulfate.

RESULTS AND DISCUSSION

Figure 1 shows the dependence of the decoloration time of Orange-1 dye on the gas-phase volume. The dependence consists of two segments in which the time first decreases (segment *AB*) and then increases (segment *BC*). The minimum decoloration time was ~10.5 min (point *B*) and was obtained for a gas volume of 600 cm^3. The dependence observed can be explained as follows. The amount of active particles generated in the electric discharge depends on the design of electrodes, the discharge current, and the electric-field strength. These parameters were fixed under our experimental conditions. A change in the gas volume leads to a change in the concentration of active particles. The active particles generated under these conditions are OH radicals and ozone [5].

The OH radicals can interact with each other and with ozone via the reactions

$$OH + OH \longrightarrow H_2O_2 \quad (k_1 = 1.3 \times 10^{10}), \qquad (1)$$

$$OH + O_3 \longrightarrow HO_2 + O_2 \quad (k_2 = 4.0 \times 10^{7}), \qquad (2)$$

$$HO_2 + O_3 \longrightarrow OH + 2O_2 \quad (k_3 = 1.2 \times 10^{6}). \qquad (3)$$

In reaction (1), these radicals are lost. In reaction (2), they transform into HO_2 radicals, which interact with ozone and transform again into OH radicals via reaction (3). Calculations based on the full scheme of interactions between active particles, as well as the experiments of [5], give the steady-state concentration of ozone at a level of $(0.4–3.4) \times 10^{-4}$ mol/l, depending on the discharge current and the number of electrodes in the reaction chamber. At the same time, the steady-state concentration of OH radicals amounts to ~10^{-9} mol/l. [6]. Under these conditions, reaction (2) is prevailing and OH radicals, instead of being lost immediately in the region of their formation, spread over the entire volume.

At low ozone concentrations, when active particles are lost in second-order reaction (1), the decrease in the concentration of OH radicals is described by the expression [7]

$$[OH] = \frac{[OH]_0}{1 + k_1[OH]_0 t}.$$

In this case, for a small concentration of radicals [OH] ~ 10^{-9} mol/l, we have $k_1[OH]_0 \sim 10$; consequently, the radicals moving with thermal velocities have time to propagate through the entire volume. Hence, the entire concentration of active particles decreases with increasing volume.

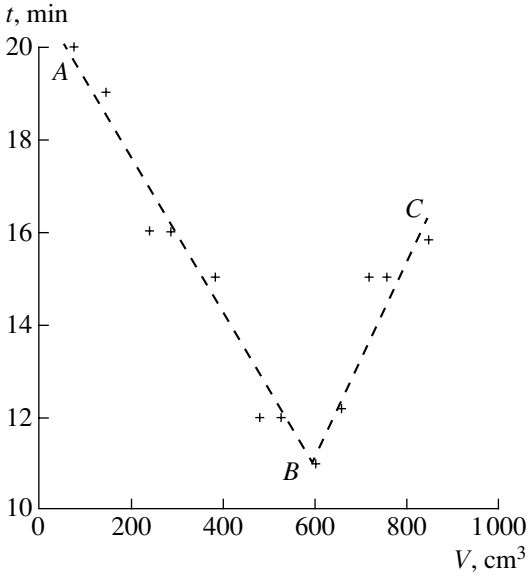

Fig. 1. Decoloration time *t* of an Orange-1 dye solution as a function of the gas-phase volume *V*.

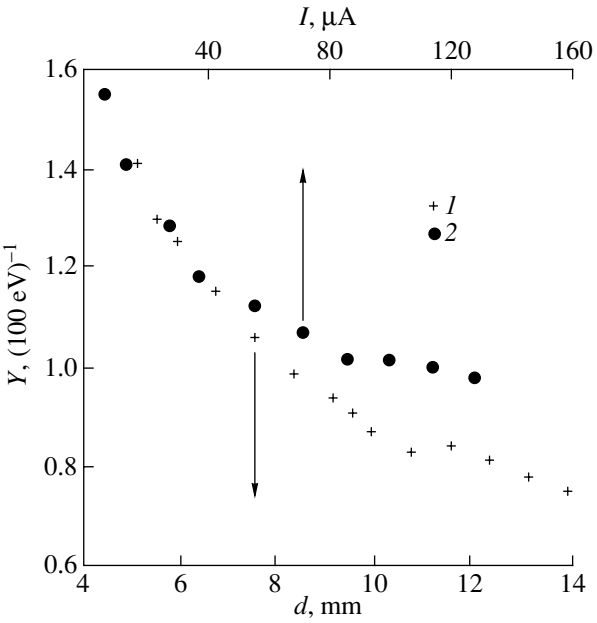

Fig. 2. Oxidation yield *Y* of iodine in a 0.01-M KI solution as a function of (*1*) the distance *d* between the electrode and the liquid surface, and (*2*) the discharge current *I*.

Active particles produced in a discharge are expended on oxidizing the impurity in water at the rate $w_A = k_A[OH][A]$ (where [*A*] is the impurity concentration) and, interacting with each other, are lost at the rate $w_{OH} = k_{OH}[OH]^2$. The ratio between these rates is

$$\frac{w_A}{w_{OH}} = \frac{k_A[A]}{k_{OH}[OH]} = \frac{k_A[A]V_g}{k_{OH}(OH)},$$

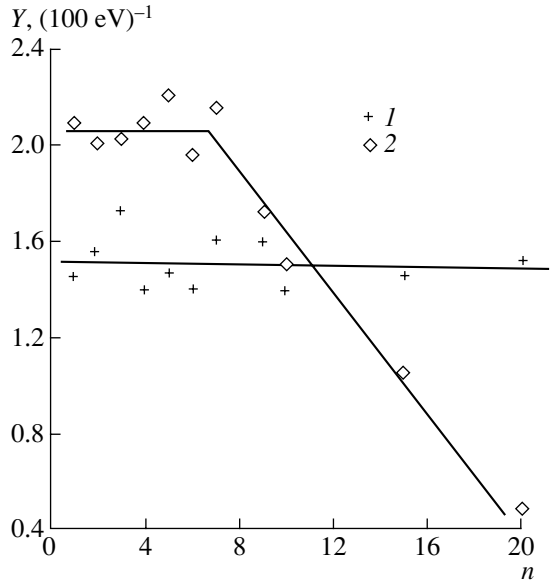

Fig. 3. The oxidation yield for a solute in water as a function of the number of electrodes in a reactor with a base area of 150 cm^2 and volume of 2.5 l: (*1*) 0.1-M KI solution and (*2*) 0.1-M oxalic acid solution ($Y \times 10$).The discharge current through each electrode is 70 μA.

where (OH) is the number of OH radicals generated per unit time (this ratio is determined by the discharge conditions and does not depend on the volume) and V_g is the gas-phase volume. It follows from here that the oxidation rate of the impurity in water increases and the decoloration time decreases with increasing gas-phase volume. The maximum decoloration rate and, accordingly, the minimum decoloration time are achieved when almost all of the active particles are expended on oxidizing the impurity. As the volume increases further and the radical concentration decreases, the oxidation rate falls and the decoloration time for a given amount of dye begins to increase.

Crosses in Fig. 2 show the yield of iodine oxidation in a 0.01-M KI solution as a function of the distance *d* between the electrode and the liquid surface at a discharge current of 70 μA. It is seen that the yield increases with decreasing *d*. This is explained by the increase in the electric field strength in the spark gap. Closed circles in Fig. 2 show the yield of iodine oxidation in a 0.01-M KI solution as a function of the electrode current at a distance between the electrode and the liquid surface of 7.5 mm. It is seen that the reaction yield per 100 eV of the expended energy increases with decreasing discharge current. This is explained by the fact that the fraction of active particles lost due to their interactions via reaction (1) decreases because the concentration of active particles decreases with decreasing discharge current.

Figure 3 shows the dependences of the oxidation yield on the number of electrodes for (*1*) a 0.1-M KI and (*2*) 0.1-M oxalic acid solutions. For a KI solution, all active particles are almost instantly absorbed and, thus, have no time to interact with each other, because the rate constants Γ for reactions with ozone and OH radicals are fairly high (higher than 10^9 l (mol s)$^{-1}$). For this reason, the reaction yield per 100 eV of the expended energy does not depend on the number of electrodes (or the number of active particles generated per unit time).

Oxalic acid is oxidized primarily by OH radicals, and the rate constant for its oxidation by ozone is small, ~0.01 l (mol s)$^{-1}$ [8, 9]. The absolute reaction yield is determined by the OH radical yield, which amounts to 0.32/(100 eV) under our experimental conditions [5]. According to the stoichiometric ratio, two OH radicals are required to oxidize one oxalic acid molecule. In addition, oxygen dissolved in water can contribute to the oxidation in the intermediate stage [9]. The experimental value of the yield of oxalic acid oxidation, Y = 0.22/(100 eV), at the number of electrodes $n \le 7$ (Fig. 3) means that all radicals produced are expended on oxidation. It follows from Fig. 3 that the yield of oxalic acid oxidation begins to fall when the number of electrodes is larger than 7. As in the previous cases, this can be attributed to the change in the concentration of active particles. The concentration of OH radicals increases as the number of electrodes increases. Starting from a certain concentration, the loss of radicals due to their interaction becomes appreciable; as the number of electrodes increases further, the fraction of lost radicals increases. For this reason, the yield of the oxalic acid oxidation decreases.

CONCLUSIONS

(i) There is an optimum gas-phase volume for which the reaction yield is maximum.

(ii) The reaction yield increases as the distance between the electrode and the liquid surface decreases. However, at short distances, the discharge becomes unstable and easily transforms from the corona to a spark discharge. In the spark regime, the reaction yield decreases [4, 10].

(iii) The reaction yield increases as the discharge current per one electrode decreases.

(iv) When ozone plays a significant role in the oxidation reaction and the reaction rates are high (~10^9–10^{10} l (mol s)$^{-1}$), almost all of the active particles are instantly absorbed in the region where they are produced. If ozone is of little importance and the rate constant for the reaction with radicals is ~10^7 l (mol s)$^{-1}$ or lower, there exists a critical number of electrodes per unit area of the liquid surface above which the reaction yield decreases.

Hence, the design of a reactor based on a flash corona discharge substantially affects the yield of impurity oxidation in water. We note that none of the effects described in this paper was observed previously in the widely known process usually referred to as electrolysis in a glow discharge [11].

REFERENCES

1. A. M. Kutepov, A. G. Zakharov, and A. I. Maksimov, Teor. Osn. Khim. Tekhnol. **34**, 76 (2000).
2. N. Karpel Vel Leitner, N. A. Aristova, T. S. Mokina, and I. M. Piskarev, Preprint No. MGU-2001-16/656 (Research Institute of Nuclear Physics, Moscow State University, Moscow, 2001).
3. I. M. Piskarev, Zh. Fiz. Khim. **72**, 1976 (1998).
4. I. M. Piskarev, Teor. Osn. Khim. Tekhnol. **34**, 333 (2000).
5. I. M. Piskarev, Zh. Fiz. Khim. **74**, 546 (2000).
6. I. M. Piskarev, Kinet. Katal. **40**, 505 (1999).
7. N. M. Emanuel' and D. G. Knorre, *Chemical Kinetics; Homogeneous Reactions* (Vysshaya Shkola, Moscow, 1962; Wiley, New York, 1973).
8. J. Hoigne and H. Bader, Water Res. **17**, 185 (1983).
9. N. Karpel Vel Leitner and M. Dore, Water Res. **31**, 1383 (1997).
10. I. M. Piskarev, A. E. Rylova, and A. I. Sevast'yanov, Élektrokhimiya **32**, 895 (1996).
11. A. Hickling, in *Modern Aspects of Electrochemistry* (Butterworths, London, 1971), Vol. 6, p. 329.

Translated by N. Larionova

Technical Physics, Vol. 47, No. 10, 2002, pp. 1250–1257. Translated from Zhurnal Tekhnicheskoĭ Fiziki, Vol. 72, No. 10, 2002, pp. 45–52.

GAS DISCHARGES, PLASMA

Transition Region between a Nonequilibrium Plasma and a Negative Electrode

V. Ya. Martens

North Caucasian State Technical University, Stavropol, 355038 Russia

e-mail: VMartens@yandex.ru

Received December 24, 2001

Abstract—A model is developed that describes the transition region between a quasineutral plasma and a planar negative electrode and in which the electron velocity distribution is represented as the sum of two Maxwellian distributions with different temperatures or as the sum of a Maxwellian distribution and distribution corresponding to an electron beam directed toward the electrode. Criteria for the formation of a sheath of positive space charge and a secondary plasma in the transition region are derived. An analysis is made of the dependence of the structure of the transition region on the parameters of the electron distribution, the space charge density distribution in the sheath, and the density of the ion current to the electrode. The criteria obtained are compared with the Bohm criterion. © *2002 MAIK "Nauka/Interperiodica".*

INTRODUCTION

The electric field of a negative electrode placed in a quasineutral plasma medium penetrates into the surrounding plasma and perturbs it, giving rise to a transition region between an unperturbed plasma and an electrode. The transition region is thought to consist of a sheath of positive space charge directly adjacent to the electrode and a presheath, i.e., a perturbed quasineutral plasma with a potential drop of a certain magnitude [1–5]. For a nonisothermal plasma with an equilibrium electron velocity distribution and a collisionless sheath, the potential drop across the presheath is determined by the Bohm criterion [6] and is equal to $0.5\ kT_e/e$. In this case, the potential distribution across the sheath of positive space charge relaxes to a monotonic one regardless of the magnitude of the electrode potential.

In some cases, the electron velocity distribution in a plasma can deviate substantially from equilibrium. The experimentally observed electron distributions often provide evidence for the existence of two electron populations with essentially different energies. For this reason, nonequilibrium electron distributions are approximated by the sum of two Maxwellian distributions with different temperatures or by the sum of a Maxwellian distribution and distribution corresponding to a directed electron beam [7–11]. Under these conditions, the sheath and presheath parameters [12, 13] differ from those in the above case of a nonisothermal plasma with an equilibrium electron velocity distribution. Moreover, the results obtained in [12, 13] indicate that, for certain parameters of the electron distribution, the structure of the transition region may also change. This problem, which is very important for some practical applications and thus requires more detailed examination, is the subject of the present paper.

MODEL OF THE TRANSITION REGION

In order to solve the problem, we consider the transition region between a semi-infinite quasineutral plasma with the potential φ_p in the unperturbed region and an infinite planar electrode whose potential is lower than the unperturbed plasma potential by the amount $\Delta\varphi_0$ (Fig. 1). The origin of the coordinate system is chosen to be located at the electrode surface. The plasma consists of ions with the temperature T_i, thermal electrons with the temperature T_{et} (such that $T_{et} \gg T_i$), and hot electrons described by a Maxwellian velocity distribution function with the temperature T_{eh} or a distribution function corresponding to an electrode-directed electron beam with the energy eU in the unperturbed plasma. It is assumed that $U > \Delta\varphi_0$, in which case the

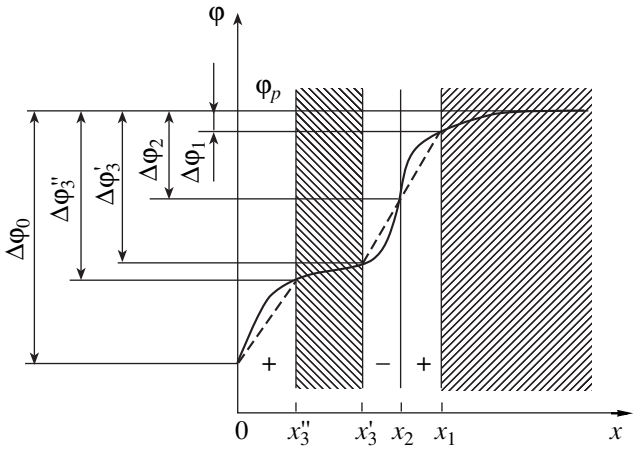

Fig. 1. Schematic potential distribution in the transition region between a nonequilibrium plasma and a negative electrode.

1063-7842/02/4710-1250$22.00

beam electrons (as well as ions) reach the electrode surface, and that the ion and electron beams in the transition region are scattered insignificantly. The potential distribution across the transition region is monotonic, $(d\varphi/dx) \geq 0$. Under the conditions just described, the electron densities in the transition region can be represented as the sum of two Boltzmann distributions or by the sum of a Boltzmann distribution and distribution corresponding to a directed electron beam.

We start by considering the case of two Boltzmann distributions. In a certain part of a transition region that is adjacent to the unperturbed plasma and is bounded by the plane $x = x_1$ (Fig. 1), the plasma is quasineutral, although there is a nonzero electric field. This part of the transition region, with the potential drop $\Delta\varphi_1$, is called a presheath. As the potential further decreases (i.e., $\Delta\varphi > \Delta\varphi_1$ in the region $x < x_1$, where $\Delta\varphi = \varphi_p - \varphi$ and φ is the plasma potential at the point x), the ion and electron densities deviate increasingly from one another, indicating the formation of a space-charge sheath in this part of the transition region. As will be clear later, the sign of the space charge in the sheath depends on the parameters of the model. The sheath–presheath system is stable if the layer adjacent to the sheath is dominated by a positive ion charge screening the electric field of the negative electrode so substantially that the electric fields in the quasineutral presheath are weak.

In order to derive a criterion for the formation of the sheath of positive space charge, it is necessary to take into account the ion density distribution in the transition region. Since the presheath plasma is quasineutral, the ion density distribution in the presheath coincides entirely with the electron density distribution and thus is determined by the laws described above. The ion density distribution in the sheath is determined from the assumption that all ions enter the sheath through the boundary $x = x_1$, at which the ion energy is $e\Delta\varphi_1$, and are then accelerated by the electric field of the sheath. In this case, the ion density distributions n_i along the x axis, as well as the electron density distributions n_e, have no breaks at the boundary $x = x_1$; i.e., the derivatives dn_i/dx and dn_e/dx of the densities with respect to x are continuous at the sheath–presheath boundary. Because of the continuity of the function $d\varphi/dx$, the functions $dn_i/d\varphi$ and $dn_e/d\varphi$ are also continuous in the transition region.

Here, by $\Delta\varphi_1$ is meant the potential drop such that, at the boundary $x = x_1$ of the presheath, the plasma is still quasineutral (i.e., the electron and ion densities, as well as their gradients, are the same) and, in the region $x < x_1$ (where $\Delta\varphi > \Delta\varphi_1$), the ion density gradient is smaller than the electron density gradient. This indicates the formation of a sheath of positive space charge in the layer adjacent to the presheath of the transition region.

The case of a Boltzmann distribution and distribution corresponding to an electron beam differs from the case of two Boltzmann distributions in that, as the electrode surface is approached, the electron density decreases only to a value corresponding to a certain potential drop, which will be denoted by $\Delta\varphi_4$. In the part of the transition region in which $\Delta\varphi < \Delta\varphi_4$, the decrease in the density of thermal electrons dominates over the increase in the density of beam electrons, and vice versa in the part where $\Delta\varphi > \Delta\varphi_4$. As in the previous case, the density of the ions accelerated in the sheath decreases toward the electrode surface. Consequently, the sheath of positive space charge can in principle form only when $\Delta\varphi_4 > \Delta\varphi_1$. The potential drop $\Delta\varphi_4$ can be found from the condition $(dn_e/dx) = 0$ or $(dn_e/d\varphi) = 0$.

CRITERIA FOR THE FORMATION OF A SHEATH OF POSITIVE SPACE CHARGE AND THEIR ANALYSIS

According to the above considerations, the criterion for the formation of a sheath of positive space charge in the case of two Boltzmann distributions can be formulated as follows:

$$n_i\big|_{\Delta\varphi = \Delta\varphi_1} = (n_{et} + n_{eh})\big|_{\Delta\varphi = \Delta\varphi_1}, \quad (1)$$

$$\left.\frac{dn_i}{d\varphi}\right|_{\Delta\varphi = \Delta\varphi_1} = \left.\frac{d(n_{et} + n_{eh})}{d\varphi}\right|_{\Delta\varphi = \Delta\varphi_1}, \quad (2)$$

$$\left.\frac{dn_i}{d\varphi}\right|_{\Delta\varphi > \Delta\varphi_1} < \left.\frac{d(n_{et} + n_{eh})}{d\varphi}\right|_{\Delta\varphi > \Delta\varphi_1}, \quad (3)$$

where n_{et} and n_{eh} are the densities of thermal and hot electrons, respectively. This criterion is stated in terms of the derivatives $dn/d\varphi$ rather than in terms of the density gradients dn/dx.

The distributions of the charged-particle densities in the sheath are determined by the expressions

$$n_i\big|_{\Delta\varphi > \Delta\varphi_1} = (\Delta\varphi_1/\Delta\varphi)^{1/2} n_i\big|_{\Delta\varphi = \Delta\varphi_1},$$

$$n_{et}\big|_{\Delta\varphi > \Delta\varphi_1} = \exp\left(\frac{e\Delta\varphi_1 - e\Delta\varphi}{kT_{et}}\right) n_{et}\big|_{\Delta\varphi = \Delta\varphi_1}, \quad (4)$$

$$n_{eh}\big|_{\Delta\varphi > \Delta\varphi_1} = \exp\left(\frac{e\Delta\varphi_1 - e\Delta\varphi}{kT_{eh}}\right) n_{eh}\big|_{\Delta\varphi = \Delta\varphi_1}.$$

Taking into account the continuity of the derivatives at the sheath–presheath boundary and the quasineutrality of the unperturbed plasma, we differentiate expressions (4) with respect to φ, substitute relationship (1) into relationships (2) and (3), switch to the charged-particle densities in the unperturbed plasma ($\Delta\varphi = 0$), and

introduce the notation

$$W = \frac{e\Delta\varphi}{kT_{et}}, \quad W_1 = \frac{e\Delta\varphi_1}{kT_{et}},$$
$$\beta = \frac{T_{et}}{T_{eh}}, \quad \alpha_h = \left(\frac{n_{eh}}{n_i}\right)\Big|_{\Delta\varphi = 0}. \tag{5}$$

As a result, we arrive at the following dimensionless criterion for the formation of a sheath of positive space charge in the case of two Boltzmann distributions:

$$(1-\alpha_h)\exp(-W_1)(1-2W_1) + \alpha_h\exp(-\beta W_1)(1-2\beta W_1) = 0, \tag{6}$$

$$(1-\alpha_h)\exp(-W_1)\left[1-2\frac{W^{3/2}}{W_1^{1/2}}\exp(W_1-W)\right] + \alpha_h\exp(-\beta W_1)\left[1-2\beta\frac{W^{3/2}}{W_1^{1/2}}\exp(\beta W_1-\beta W)\right] < 0. \tag{7}$$

An analogous criterion in the case of a Boltzmann distribution and distribution corresponding to an electron beam has the form

$$(1-\alpha_b)\exp(-W_1)(1-2W_1) + \alpha_b\left(\frac{E}{E-W_1}\right)^{3/2} = 0, \tag{8}$$

$$(1-\alpha_b)\exp(-W_1)\left[1-2\frac{W^{3/2}}{W_1^{1/2}}\exp(W_1-W)\right] + \alpha_b\left(\frac{E}{E-W_1}\right)^{3/2}\left[1-\frac{W_1}{E}+\left(\frac{E-W_1}{E-W}\right)^{3/2}\frac{W^{3/2}}{W_1^{1/2}E}\right] < 0, \tag{9}$$

where $E = eU/kT_{et}$, $a_b = (n_{eb}/n_i)|\Delta_{\varphi = 0}$, and n_{eb} is the electron beam density.

Moreover, recall that, in this case, the following necessary (but not sufficient) condition for the formation of the sheath of positive space charge should be satisfied:

$$W_1 < W_4, \tag{10}$$

where the quantity $W_4 = e\Delta\varphi_4/(kT_{et})$ can be determined from the relationship

$$2(1-\alpha_b)\exp(-W_4) - \alpha_b\frac{E^{1/2}}{(E-W_4)^{3/2}} = 0, \tag{11}$$

which is a consequence of the condition $[d(n_{et} + n_{eb})/d\varphi] = 0$.

In the absence of high-energy electrons ($\alpha_h = 0$ or $\beta = 1$ and $\alpha_b = 0$), criteria (6) and (8) pass over to the Bohm criterion $W_1 = 0.5$ and inequalities (7) and (9) hold for $0.5 < W < 3.356$, indicating that, in this range of W values, the ion density gradient in the sheath is smaller than the electron density gradient, and vice versa for $W > 3.356$. It is known that, in the case of the Bohm criterion, the space charge in the entire sheath is positive.

In the presence of high-energy electrons, the potential drop W_1 across the presheath can be determined from criterion (6) or (8), provided that inequality (7) or (9) is satisfied in the interval of W values that is bounded from below by W_1. In what follows, when speaking of whether or not inequalities (7) and (9) are satisfied, we will mean precisely this interval of W values. Note that an analysis of inequalities (7) and (9) shows that, depending on the particular circumstances, they can also hold in other intervals, in particular, in the intervals bounded from above by W_1 or bounded from below by a value larger than W_1.

Figure 2 illustrates how the potential drop W_1 depends on the parameters of the electron distribution. In the case of two Boltzmann distributions, an increase in α_h from 0 to 1 corresponds to the transition of plasma electrons from an equilibrium distribution with the temperature T_{et} to an equilibrium distribution with the temperature T_{eh} through nonequilibrium distributions corresponding to different relative contents of thermal and hot electrons. As β changes within the range $0 \le \beta \le 1$, W_1 increases from 0.5 at $\alpha_h = 0$ to $0.5/\beta$ at $\alpha_h = 1$. In this case, in the range $0.101 \le \beta \le 1$, Eq. (6) has one solution (Fig. 2; curves *1*, *2*), so that all W_1 values obtained from Eq. (6) can be treated as potential drops across the sheath because inequality (7) is satisfied under these conditions. For $0 \le \beta < 0.101$ and for a certain range of α_h values (which depends on the β value), Eq. (6) has three solutions (Fig. 2, curves *3*–*6*). Let us discuss this situation in more detail, using, as an example, curve *4*, which was calculated for $\beta = 5 \times 10^{-2}$. For W_1 values over the portion *BC* of curve *4*, inequality (7) fails to hold. This indicates that, under such conditions, the ion density gradient in the part of the sheath that is near the sheath–presheath boundary exceeds the electron density gradient; as a result, a sheath of negative space charge should form near the presheath boundary. However, as was noted above, such a system cannot be stable. For the two remaining solutions to Eq. (6), one of which is described by the portion *AB* of curve *4* and the other is described by the portion *CD*, inequality (7) is satisfied. Out of the two physically possible stable states corresponding to these two solutions, the state with a lower W_1 value actually occurs, because, when W is larger than W_1, the sheath of positive space charge that begins to form near the boundary of the presheath prevents the formation of a quasineutral presheath with a large W_1 value. An analysis of inequality (7) under conditions corresponding to the portion *AB* of curve *4* shows that, as α_h increases from zero to the critical value α_{hc} corresponding to point *B*, the interval over which inequality (7) is satisfied shrinks from the Bohm interval $0.5 < W < 3.356$ to zero, in which case the derivative $dW_1/d\alpha_h$ increases from a finite value to

infinity (Fig. 2). This indicates that, at $\alpha_h = \alpha_{hc}$, the sheath of positive space charge does not form near the boundary of the presheath; as a result, the potential drop in the presheath increases in a jumplike manner to the value W_1, which corresponds to point *D*. In the states corresponding to portion *DE*, the sheath of positive space charge again forms near the boundary of the presheath, because inequality (7) is satisfied for the W_1 value at point *D*, as well as for all W_1 values over portion *DE*. Calculations show (see also Fig. 2) that, as β decreases, the critical value α_{hc} decreases from 0.461 at $\beta = 0.101$ to 0.309 at $\beta = 0$, whereas the potential difference W_1 increases in a jumplike manner from zero to infinity as β changes in the same range.

In the case of a Boltzmann distribution and distribution corresponding to an electron beam (Fig. 2, curves *6–8*), Eq. (8) has two finite solutions in the interval $0 < \alpha_b < \alpha_{bc}$, where α_{bc} is the critical value of α_b at which $(dW_1/d\alpha_b) \longrightarrow \infty$. For $\alpha_{bc} < \alpha_b \le 1$, Eq. (8) has one solution, namely, $W_1 \longrightarrow \infty$. Out of the two finite solutions (see the solid and dashed-and-dotted portions of curves *6–8* in Fig. 2), inequality (9) holds only for the solution with smaller W_1 values. Moreover, this case is similar to that of two Boltzmann distributions: as α_b increases from zero to α_{bc}, the interval over which inequality (9) is satisfied shrinks from the Bohm interval to zero and the derivative $dW_1/d\alpha_b$ increases from a finite value to infinity. Accordingly, condition (10) holds for $0 \le \alpha_b < \alpha_{bc}$ and fails to hold for $\alpha_{bc} < \alpha_b \le 1$.

These results can be interpreted as follows. For $0 \le \alpha_b < \alpha_{bc}$, there exists a sheath of positive space charge in the transition region. The sheath is separated from the unperturbed plasma by a presheath. As α_b increases, the potential drop W_1 across the sheath becomes larger (see the solid portions of curves *6–8* in Fig. 2) and the sheath of positive space charge near the boundary of the presheath becomes thinner. As α_b reaches the critical value α_{bc}, the sheath of positive space charge disappears and the potential drop W_1 increases to infinity in a jumplike manner, so that condition (10) is violated. This indicates that, for $\alpha_{bc} \le \alpha_b \le 1$, the entire transition region is a quasineutral presheath for any electrode potential consistent with the above model assumptions; i.e., $0 < W_0 < E$, where $W_0 = e\Delta\varphi_0/(kT_{et})$. In this situation, however, the term "presheath" is physically meaningless because there is no sheath in the transition region. The critical value α_{bc} and the potential drop W_1 corresponding to it are maximum at $E = \infty$ and are equal to 0.309 and 1.5, respectively. It can be readily shown that the case of two Boltzmann distributions coincides with the case of a Boltzmann distribution and distribution corresponding to an electron beam when $\beta = 0$ and $E \longrightarrow \infty$ (Fig. 2, curve *6*).

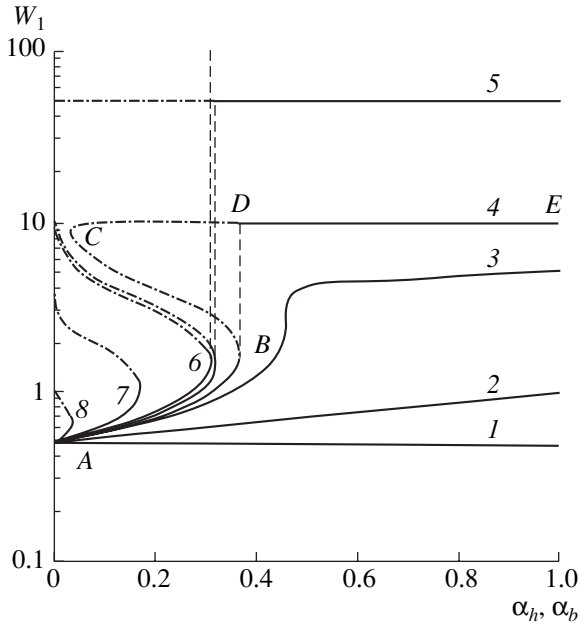

Fig. 2. Dependence of the potential drop across the presheath on the parameters of the electron distribution. The curves in the case of two Boltzmann distributions were obtained for β = (*1*) 1.0, (*2*) 0.5, (*3*) 0.1, (*4*) 5×10^{-2}, (*5*) 10^{-2}, and (*6*) 0. The curves in the case of a Boltzmann distribution and distribution corresponding to an electron beam were obtained for E = (*6*) ∞, (*7*) 3, and (*8*) 1.

CHARGE DENSITY DISTRIBUTION IN THE SHEATH

Above, it has been shown that, when α_h and α_b are nonzero and are smaller than their critical values, the interval of W values in which inequalities (7) and (9) are satisfied is shorter than the Bohm interval. This suggests that, under the conditions in question, a double layer of space charge can, in principle, exist in which the region near the boundary of the presheath is dominated by a positive ion charge and the region far from this boundary is dominated by a negative electron charge.

In the case of two Boltzmann distributions, the relative charge density ρ_h in the layer can be represented as

$$\rho_h = \frac{(n_i - n_{et} - n_{eh})|_{\Delta\varphi > \Delta\varphi_1}}{n_i|_{\Delta\varphi = 0}}. \qquad (12)$$

We substitute expressions (4) and relationship (1) into relationship (12), switch to the charged particle densities in an unperturbed quasineutral plasma, and take into account notation (5). As a result, we obtain

$$\rho_h = (1-\alpha_h)\exp(-W_1)\left[\left(\frac{W_1}{W}\right)^{1/2} - \exp(W_1 - W)\right] + \alpha_h \exp(-\beta W_1)\left[\left(\frac{W_1}{W}\right)^{1/2} - \exp(\beta W_1 - \beta W)\right]. \qquad (13)$$

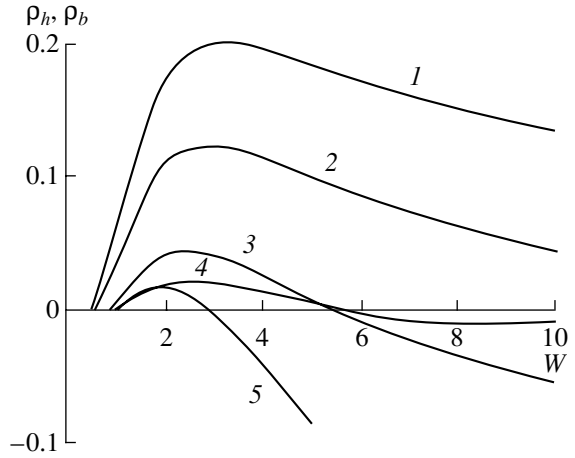

Fig. 3. Charge density distribution in the layer: (*1*) the Bohm case ($\alpha_h = 0$, or $\beta = 1$, or $\alpha_b = 0$); (*2*) the case $\beta = 0$ and $\alpha_h = 0.099$ or $E \longrightarrow \infty$ and $\alpha_b = 0.099$; (*3*) the case $\beta = 0$ and $\alpha_h = 0.212$ or $E \longrightarrow \infty$ and $\alpha_b = 0.212$; (*4*) the case $\beta = 5 \times 10^{-2}$ and $\alpha_h = 0.301$; and (*5*) the case $E = 10$ and $\alpha_b = 0.220$.

The expression for the relative charge density ρ_b in the layer in the case of a Boltzmann distribution and distribution corresponding to an electron beam can be derived in an analogous way:

$$\rho_b = (1-\alpha_b)\exp(-W_1)\left[\left(\frac{W_1}{W}\right)^{1/2} - \exp(W_1 - W)\right] + \alpha_b\left(\frac{E}{E-W_1}\right)^{1/2}\left[\left(\frac{W_1}{W}\right)^{1/2} - \left(\frac{E-W_1}{E-W}\right)^{1/2}\right], \quad (14)$$

where the relative charge density is defined as

$$\rho_b = \frac{(n_i - n_{et} - n_{eb})|_{\Delta\varphi > \Delta\varphi_1}}{n_i|_{\Delta\varphi = 0}}.$$

Expressions (13) and (14) made it possible to analyze the charge density distribution in the layer (see Fig. 3) and to prove that the double layer of space charge can actually form under the conditions adopted here (Fig. 3, curves *3–5*).

Equating the right-hand sides of expressions (13) and (14) to zero, we can determine the boundary values $W_2 = e\Delta\varphi_2/(kT_{et})$, where $\Delta\varphi_2$ is the potential difference between the unperturbed plasma and the boundary $x = x_2$, which separates the regions of positive and negative space charges in the double layer (Fig. 1). The dependence of W_2 on the parameters of the electron distribution is illustrated in Fig. 4.

CRITERIA FOR THE FORMATION OF THE SECONDARY QUASINEUTRAL PLASMA AND THE STRUCTURE OF THE TRANSITION REGION

Here, we analyze the potential distribution in the space-charge sheath. To do this, we use Poisson's equation. Since the electric field in the sheath, and, accordingly, at the boundary $x = x_1$, is weak, the integration of Poisson's equation with the boundary condition $(d\varphi/dx)|_{x = x_1} = 0$ in the case of two Boltzmann distributions yields

$$\left(\frac{d\varphi}{dx}\right)^2 = -\frac{2e}{\varepsilon_0}\left\{\Delta\varphi_1\left[1 - \left(\frac{\Delta\varphi}{\Delta\varphi_1}\right)^{1/2}\right]2n_i|_{x = x_1} + \frac{kT_{et}}{e}\left[1 - \exp\left(\frac{e\Delta\varphi_1 - e\Delta\varphi}{kT_{et}}\right)\right]n_{et}|_{x = x_1} + \frac{kT_{eh}}{e}\left[1 - \exp\left(\frac{e\Delta\varphi_1 - e\Delta\varphi}{kT_{eh}}\right)\right]n_{eh}|_{x = x_1}\right\}. \quad (15)$$

In the Bohm case, the right-hand side of Eq. (15) is positive over the entire range $\Delta\varphi_1 < \Delta\varphi < \infty$, indicating that the potential distribution in the space-charge sheath is monotonic for any magnitude of the electrode potential that satisfies the condition $\Delta\varphi_0 > \Delta\varphi_1$. In [13], it was shown that, in the presence of high-energy electrons, the potential gradient may vanish in a certain region $x < x_2$ of the sheath in which $\Delta\varphi > \Delta\varphi_2$ and the negative electron space charge dominates over the positive ion space charge. Let us assume that the potential gradient vanishes at the boundary $x = x_3$, the corresponding potential difference being $\Delta\varphi = \Delta\varphi_3$ (Fig. 1). The values of $\Delta\varphi_3$ can be determined by equating the right-hand side of Eq. (15) to zero. We perform the same manipulations with the expressions for the charged particle densities as those made in deriving expression (13). As a result, we arrive at the following condition for the dimensionless potential gradient to vanish in the case of two Boltzmann distributions:

$$(1-\alpha_h)\exp(-W_1)[1 - \exp(W_1 - W_3) + F] + \alpha_h \times \exp(-\beta W_1)\{[1 - \exp(\beta W_1 - \beta W_3)]/\beta + F\} = 0, \quad (16)$$

where $F = 2[W_1 - (W_1 W_3)^{1/2}]$ and $W_3 = e\Delta\varphi_3/(kT_{et})$.

In the case of a Boltzmann distribution and distribution corresponding to an electron beam, an analogous condition has the form

$$(1-\alpha_b)\exp(-W_1)[1 - \exp(W_1 - W_3) + F] + \alpha_b\left(\frac{E}{E-W_1}\right)^{1/2}\{2(E-W_1) \times \left[1 - \left(\frac{E-W_3}{E-W_1}\right)^{1/2}\right] + F\} = 0. \quad (17)$$

The dependence of W_3 on the parameters of the electron distribution is illustrated in Fig. 4. The characteristic feature of the case of two Boltzmann distributions is that Eq. (16) has, if ever, two (possibly coincident)

solutions, W_3' and W_3'' ($W_3' < W_3''$). In the intervals $W_1 < W < W_3'$ and $W_3'' < W < \infty$, the right-hand side of Eq. (15) is positive. This indicates that the corresponding parts of the transition region are space-charge sheaths with a monotonic potential distribution. In the interval $W_3' < W < W_3''$, the right-hand side of Eq. (15) is negative, so that $d\varphi/dx$ is an imaginary quantity. As a result, in the corresponding part of the transition region, the potential distribution is oscillatory [5, 12]. However, in [5] it was shown that, when the electric fields in this part are weak (at the boundaries of the interval, we have $(d\varphi/dx) = 0$)), even an insignificant ionization of the gas by plasma electrons and ions and rare collisions of plasma ions with other plasma particles in which the ions are decelerated and undergo charge exchange can restore the monotonic potential distribution. Also, the processes just mentioned promote the equalization of the ion and electron densities in this part of the transition region, thereby leading to the formation of the secondary plasma.

In the case of a Boltzmann distribution and distribution corresponding to an electron beam, Eq. (17) has only one solution W_3 (Figs. 4c, 4d). Similar considerations show that the secondary plasma is produced in the part of the transition region in which the potential drop W satisfies the condition $W_3 < W < E$ (the upper bound E is the boundary of applicability of the model used here).

In accordance with the above analysis, expressions (16) and (17) serve as criteria for the formation of the secondary plasma in the transition region. Earlier, the condition $(d\varphi/dx) = 0$, from which expressions (16) and (17) have been derived, was also used as a criterion for secondary plasma formation [14, 15].

Hence, the model developed here shows that, under certain conditions, the secondary quasineutral plasma can form in the transition region. The secondary plasma is separated from the main plasma by an electric double layer. At the boundary $x = x_3$ between the sheath and the secondary plasma, the electric field vanishes. In the secondary plasma, the potential decreases monotonically toward the electrode. In the case of two Boltzmann distributions, the secondary plasma can be bounded by space-charge sheaths on both sides; moreover, at both boundaries of the secondary plasma, the potential gradient vanishes.

Interestingly, using the formal assumption of an infinitely strong electric field at the plasma–sheath boundaries, Demirkhanov *et al.* [12] also arrived at the conclusion that, under the conditions in question, there can exist two plasma regions separated by an electric double layer. However, under such boundary conditions, a double layer with positive space charge cannot exist near the plasma region with a higher potential. The same is true of a double layer with negative space charge near the plasma region with a lower potential. In [12], the space-charge sheath was not considered, presumably because the model adopted in that paper was inappropriate for describing it.

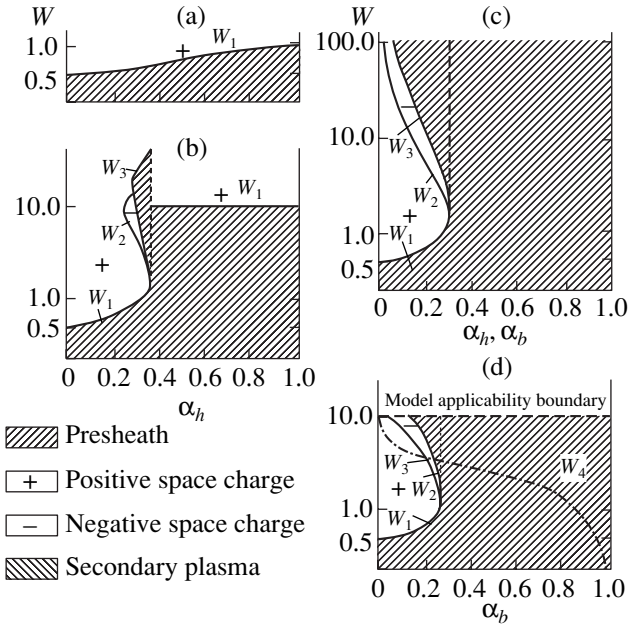

Fig. 4. Structure of the transition region between a nonequilibrium plasma and a negative electrode for different parameters of the electron distribution. The structures in the case of two Boltzmann distributions were obtained for β = (a) 0.5, (b) 5×10^{-2}, and (c) 0. The structures in the case of a Boltzmann distribution and distribution corresponding to an electron beam were obtained for E = (c) ∞ and (d) 10.

The results obtained above are illustrated in Fig. 4, which shows structural diagrams of the transition region between a plasma and a negative electrode. Using these diagrams, we can determine the structure of the transition region and the boundary values W_1, W_2, and W_3 for the required values of the parameters of the electron distribution (α_h and β or α_b and E) and the electrode potential W_0. The diagrams show the following possible structures of the transition region: (i) a quasineutral presheath; (ii) a quasineutral presheath and a space-charge sheath adjacent to the electrode [in this case, the sign of the space charge predominating in the sheath remains the same (positive) over the entire sheath, or changes from positive to negative as the electrode is approached (a double layer), or changes from positive to negative and then becomes positive again (a triple layer)]; (iii) a quasineutral presheath, a double layer, and a secondary plasma adjacent to the electrode; and (iv) the previous structure plus the second space-charge sheath between the secondary plasma and the electrode.

ION CURRENT TO THE ELECTRODE

The ion current to the electrode is carried, first, by the thermal ions that enter the transition region from the

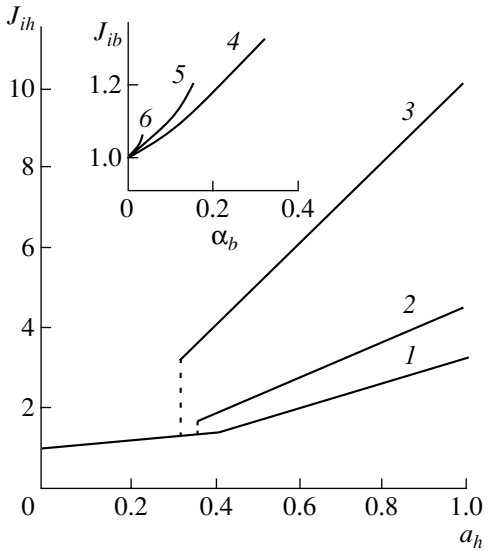

Fig. 5. Dependence of the ion current density at the sheath–presheath boundary. The curves in the case of two Boltzmann distributions were obtained for β = (*1*) 0.1, (*2*) 5×10^{-2}, and (*3*) 10^{-2}. The curves in the case of a Boltzmann distribution and distribution corresponding to an electron beam were obtained for E = (*4*) ∞, (*5*) 3, and (*6*) 1.

side of the unperturbed plasma and are accelerated there by the electric field and, second, by the ions that are produced as a result of gas ionization over the entire transition region.

If the parameters of the electron distribution and the electrode potential are such that no space-charge sheath forms in the transition region (so that the entire transition region is a perturbed quasineutral presheath), then the presheath becomes thicker and the density of the ion current to the electrode becomes higher as the potential difference between the unperturbed plasma and the negative electrode increases. In this case, the electrode-directed current density in an actual device can be bounded from above by the value corresponding to the electrode potential at which the plasma perturbation by the electric field of the negative electrode extends into the entire plasma volume and the presheath stops expanding.

If a sheath of positive space charge forms in the transition region, then it weakens the perturbing effect of the electric field of the negative electrode on the plasma. In this case, the thickness of the forming presheath and the potential drop across it are both independent of the electrode potential. The ion current density at the sheath–presheath boundary is equal to

$$j_i = e(n_i V_i)|_{\Delta\varphi = \Delta\varphi_1},$$

where $V_i|_{\Delta\varphi = \Delta\varphi_1} = (2e\Delta\varphi_1/m_i)^{1/2}$ and m_i is the mass of an ion.

Using condition (1), switching to the charged particle densities in an unperturbed plasma, and taking into account notation (5), we arrive at the following representation of the ion current density j_{ih} at the sheath–presheath boundary in the case of two Boltzmann distributions:

$$j_{ih} = [(1-\alpha_h)\exp(-W_1) + \alpha_h \exp(-\beta W_1)] \times (2e\Delta\varphi_1/m_i)^{1/2} en_i|_{\Delta\varphi = 0.}$$

In the Bohm case ($\alpha_h = 0$ or $\beta = 1$), for $W_1 = 0.5$, we have

$$j_i^* = \exp(-0.5)(kT_{et}/m_i)^{1/2} en_i|_{\Delta\varphi = 0}.$$

For convenience of further analysis, it is expedient to consider the ratio J_{ih} of the ion current densities in the case of two Boltzmann distributions and in the Bohm case at the same ion densities $n_i|_{\Delta\varphi = 0}$:

$$J_{ih} = j_{ih}/j_i^* = \exp(0.5)[(1-\alpha_h)\exp(-W_1) + \alpha_h \exp(-\beta W_1)](2W_1)^{1/2}. \quad (18)$$

For the case of a Boltzmann distribution and distribution corresponding to an electron beam, the analogous ratio has the form

$$J_{ib} = \exp(0.5)\left[(1-\alpha_b)\exp(-W_1) + \alpha_b\left(\frac{E}{E-W_1}\right)^{1/2}\right](2W_1)^{1/2}. \quad (19)$$

For a collisionless sheath, expressions (18) and (19) determine the ion current density not only at the sheath–presheath boundary but also at the electrode surface. An increase in the fraction α_h or α_b of high-energy electrons results in an increase in the ion current density (Fig. 5). In the case of two Boltzmann distributions, the ratio J_{ih} increases from 1 at $\alpha_h = 0$ to $\beta^{-1/2}$ at $\alpha_h = 1$. A jumplike change in J_{ih} at the critical value α_{hc} (Fig. 5, curves *1–3*) is associated with a jump in the potential drop W_1 in the sheath (Fig. 2, curves *3–5*). Curves *4–6* in Fig. 5 were obtained for the case of a Boltzmann distribution and distribution corresponding to an electron beam and are limited to the interval where the sheath of positive space charge exists ($0 \le \alpha_b \le \alpha_{bc}$). A certain contribution to the ion current densities in expressions (18) and (19) may come from the secondary plasma (when it forms in the transition region).

CONCLUSION

Some of the conclusions of this paper were experimentally confirmed by the author and the corresponding measurement results were described in [16]. Here, however, it is expedient to turn to the results of other experiments, namely, those reported in papers [17, 18], which were devoted to a comparison between different methods for processing the current–voltage character-

istics of the probes immersed in nonequilibrium plasmas. It was shown that the traditional processing of the ion portion of the probe characteristics by means of the Bohm criterion, in which high-energy electrons are neglected, overestimates the plasma density by more than an order of magnitude.

The approach proposed here for calculating the parameters of the transition region can also be applied to other nonequilibrium electron energy distributions, because any complicated distribution can be represented as a sum of distributions of several electron groups with their own temperatures or energies.

The physical situations analyzed in this paper may be encountered in tokamak physics (in wall plasmas), in plasma chemistry, and in plasma technologies. The effect of high-energy electrons on the current through a negative electrode in a plasma should be taken into account in probe measurements of the plasma parameters. Finally, the results obtained make it possible to suggest some ways of increasing the efficiency of ion sources, for instance, by choosing an appropriate type of gas discharge that generates plasmas with high-energy electrons (e.g., a reflex discharge [7] and a beam–plasma discharge [8, 9]).

REFERENCES

1. F. F. Chen, in *Plasma Diagnostic Techniques*, Ed. by R. H. Huddlestone and S. L. Leonard (Academic, New York, 1965; Mir, Moscow, 1967).
2. L. Schott, in *Plasma Diagnostics*, Ed. by W. Lochte-Holtgreven (Elsevier, New York, 1968; Mir, Moscow, 1971).
3. C. Lejeune, *Applied Charged Particle Optics*, Ed. by A. Septier (Academic, New York, 1983), Part C, pp. 207–293.
4. B. V. Alekseev and V. A. Kotel'nikov, *Probe Method of Plasma Diagnostics* (Énergoatomizdat, Moscow, 1988).
5. I. N. Morozov and A. F. Nastoyashchiĭ, Teplofiz. Vys. Temp. **33**, 179 (1995).
6. D. Bohm, P. H. E. Burhop, and H. S. M. Massey, *The Characteristics of Electrical Discharges in Magnetic Fields*, Ed. by A. Guthrie and R. K. Wakerling (McGraw-Hill, New York, 1949), pp. 360–366.
7. R. A. Demirkhanov, Yu. V. Kursanov, and L. P. Skripal', Zh. Tekh. Fiz. **39** (4), 666 (1969) [Sov. Phys. Tech. Phys. **14**, 500 (1969)].
8. R. A. Demirkhanov, Yu. V. Kursanov, and L. P. Skripal', Zh. Tekh. Fiz. **40**, 1351 (1970) [Sov. Phys. Tech. Phys. **15**, 1047 (1971)].
9. Yu. Ya. Volkolupov, A. Zh. Martinson, and P. I. Ryl'tsev, in *Proceedings of the 8th All-Union Conference on Emission Electronics* (Nauka, Moscow, 1981), pp. 262–263.
10. L. Sevarac, Nucl. Instrum. Methods **38**, 12 (1965).
11. A. I. Karchevskiĭ, V. G. Averin, and V. N. Bezmel'nitsyn, Zh. Éksp. Teor. Fiz. **58**, 1131 (1970) [Sov. Phys. JETP **31**, 605 (1970)].
12. R. A. Demirkhanov, Yu. V. Kursanov, and L. P. Skripal', Zh. Tekh. Fiz. **44**, 1424 (1974) [Sov. Phys. Tech. Phys. **19**, 891 (1974)].
13. V. Ya. Martens, Zh. Tekh. Fiz. **66** (5), 70 (1996) [Tech. Phys. **41**, 444 (1996)].
14. Yu. E. Kreĭndel', E. A. Litvinov, and E. Yu. Sadovskaya, Zh. Tekh. Fiz. **59** (10), 47 (1989) [Sov. Phys. Tech. Phys. **34**, 1119 (1989)].
15. M. Yu. Kreĭndel' and E. A. Litvinov, Zh. Tekh. Fiz. **62** (5), 159 (1992) [Sov. Phys. Tech. Phys. **37**, 570 (1992)].
16. V. Ya. Martens, Zh. Tekh. Fiz. **72** (11) (2002) (in press) [Tech. Phys. **47** (2002) (in press)].
17. A. S. Mustafaev, A. P. Mezentsev, V. Ya. Simonov, *et al.*, Zh. Tekh. Fiz. **54**, 2153 (1984) [Sov. Phys. Tech. Phys. **29**, 1263 (1984)].
18. V. I. Demidov and V. Ya. Simonov, in *Proceedings of 7th All-Union Conference on Physics of Low-Temperature Plasma, Tashkent, 1987*, Part 2, p. 210.

Translated by O. Khadin

Technical Physics, Vol. 47, No. 10, 2002, pp. 1258–1262. Translated from Zhurnal Tekhnicheskoĭ Fiziki, Vol. 72, No. 10, 2002, pp. 53–57.

GAS DISCHARGES, PLASMA

Propagation of Nonlinear Longitudinal Waves in a Solid with Regard to the Interaction between the Strain Field and the Field of Defects

F. Mirzoev

Institute for Problems of Laser and Information Technologies, Russian Academy of Sciences, Shatura, Moscow oblast, 140700 Russia

e-mail: mirzo@laser.nictl.msk.su

Received September 11, 2001; in final form, February 8, 2002

Abstract—A model of nonlinear longitudinal wave propagation in a solid with quadratic nonlinearity of an elastic continuum exposed to laser impulses is developed in view of the interaction between the strain field and the field of point defects. The influence of the generation and recombination of laser-induced defects on the propagation of an elastic strain wave is analyzed. The existence of a nonlinear elastic shock wave of low intensity is revealed in the system and its structure is studied. The estimations of the depth and velocity of the wave front are performed. The contributions due to the interaction of the strain field and the field of defects to both a linear elastic modulus and the dispersion parameters of a lattice are found. © *2002 MAIK "Nauka/Interperiodica".*

INTRODUCTION

Prominent features of the behavior of a solid under intense impulse exposures (in particular, under impulse laser-beam exposures) are the appearance and propagation of nonlinear strain waves (in particular, solitons) of various natures. This phenomenon is of considerable interest, and numerous theoretical and experimental papers [1–7] are devoted to it. In considering the evolution of nonlinear elastic waves in a crystal, the deviation of elastic lattice properties from Hooke's law is commonly considered as nonlinearity [1]. In exposed solids, various structural imperfections of a lattice, namely, point defects generated under external influences and resulting in a considerable strain of a medium, may be of essential importance. The strain of a medium is due to the difference in the covalent radii of lattice and defect atoms. The defect-strain interaction may occur via both the changing energy parameters of the subsystem of defects (the energy of the defect formation, the energy of their migration) and the appearance of the diffusion current (strain-induced drift). Under certain conditions, nonlinearities related to these interactions may become essential for the propagation of nonlinear elastic perturbations in solids and result in a renormalization of lattice parameters (both linear and nonlinear elastic moduli). The presence of point defects with a finite recombination velocity in a medium may induce the appearance of dissipative terms, which are absent in ordinary equations for nonlinear elastic waves. The wave dynamics may depend on dispersion due to the finiteness of either the lattice spacing [8] or specimen width [9] as well as dispersion related to nonequilibrium defects. The propagation of an elastic strain wave in such systems may occur in the form of shock waves. In this case, the influence of generation and recombination processes turns out to be similar to the dissipation of the elastic oscillation energy in a viscoelastic medium with aftereffect and relaxation. The formation of the shock front of an acoustic wave in insulators exposed to 0.15 μs laser pulses with energy up to 5 J was experimentally observed in [10]. The study of the wave dynamics in view of their interaction with structure defects is of certain theoretical and practical interest, in particular, in analyzing the mechanisms of an anomalous mass transfer detected in the laser and ion implantations of metal materials [11] and in studying the mechanical activation of components in solid-phase chemical reactions. Elastic wave propagation in a condensed medium carries information about the distortion of their shape and velocity, energy loss, defect structure, etc. This information is necessary to determine various parameters and the structure of solids.

In this paper, the possibility of the existence of shock waves in the propagation of a nonlinear longitudinal-strain wave in a medium with a quadratic nonlinearity of an elastic continuum exposed to laser pulses is studied in view of the generation of point defects (vacancies and interstitial sites). It is shown that generation and recombination processes in the defect subsystem result in dissipative effects and, hence, the appearance of elastic shock waves of low intensity. The renormalization is found of linear elastic moduli and parameters of dispersion due to defect-strain interaction.

1063-7842/02/4710-1258$22.00

BASIC EQUATIONS

Consider an isotropic solid with point defects induced by laser radiation. Let $n_j(x, t)$ be the volume density of defects ($j = v$ for vacancies, and $j = i$ for interstitial sites). In the propagation of longitudinal strain waves, the activation energy for the defect formation varies in the regions of compression and tension. The renormalized energy of point defect formation may be represented in the form $E = E_0 - \varphi \mathrm{div}\mathbf{u}$, where $\varepsilon - \mathrm{div}\mathbf{u}$ is the strain of a medium; $\mathbf{u}$, the vector of the displacement of a medium; φ, the strain potential; and E_0, the energy of defect formation in a strainless crystal. The variation of formation energy results in a corresponding variation of the defect source function and, consequently, in the spatial redistribution of defects [12]. In addition, defects may migrate over a crystal and recombine at various centers, e.g., dislocations, interstitial impurities, etc. In the framework of the aforementioned assumptions, the nonlinear dynamic equation describing the propagation of the longitudinal strain wave in a crystal in view of defect generation (in the one-dimensional case) may be written as

$$\frac{\partial^2 u}{\partial t^2} - c_s^2\frac{\partial^2 u}{\partial x^2} - \frac{\beta_N}{\rho}\frac{\partial^2 u}{\partial x^2}\frac{\partial u}{\partial x} - \alpha_1\frac{\partial^4 u}{\partial t^2 \partial x^4} + \alpha_2\frac{\partial^4 u}{\partial x^4} = -\frac{K\Omega_j}{\rho}\frac{\partial n_j}{\partial x}. \quad (1)$$

Here, $u(x, t)$ is the displacement of the medium; $c_s = ((3K + 4\mu)/3\rho)^{1/2}$, the longitudinal wave velocity in a crystal; K and μ, the bulk and rigidity moduli, respectively (linear elastic moduli); ρ, the density of the medium; α_1 and α_2, the dispersion parameters [13]; and Ω_j, the dilatation parameter describing the variation of the crystal volume in the result of point defect formation ($\Omega_j < 0$ for $j = v$, and $\Omega_j > 0$ for $j = i$). The nonlinearity coefficient [13] $\beta_N = 3\rho c_s^2 + 2(A + 3B + C)$, where A, B, and C are the third-order elastic moduli. For most solids (metals and a lot of polymers), $\beta_N < 0$. There are also metals in which the deviation of elastic lattice properties from Hooke's law is insignificant. In this case, $\beta_N > 0$. In (1), we restricted our consideration to a smooth strain disturbance and took into account the contributions of the elastic moduli to the spatial dispersion in the first nonvanishing approximation.

Equation (1) in the absence of elastic concentration stresses, which is called an equation with two dispersions (α_1, α_2), was studied in detail in [2–5]. The generalization of this equation to the case in which the elastic concentration stresses are present in a system is performed in [12] in the framework of the Hamiltonian approach.

The distribution of point defects determining the right side of Eq. (1) depends on the strains and stresses. Therefore, Eq. (1) should be supplemented by an equation for the defect density to completely describe the elastic wave propagation. If the basic processes determining the time behavior of defects are defect generation from the lattice sites and their recombination at the centers of various nature, the kinetic equation

$$\frac{\partial n_{1j}}{\partial t} = q_\varepsilon\frac{\partial u}{\partial x} - \beta_j n_{1j} \quad (2)$$

takes place for weak nonuniform density perturbations $n_{1j} = n_j - n_{j0}$ and $n_{1j} \ll n_{j0}$, where $n_{j0} = q_0\tau_j$ is a uniform stationary defect distribution. Here, q_0 is the rate of point defect generation in the absence of strain; the first term in the right-hand side of (2) corresponds to strain-induced generation ($\varepsilon = \partial u/\partial x$ is the strain of a medium); the second term, the defect decrease due to the recombination ($\beta_j = 1/\tau_j = \rho_j D_j$ is the recombination rate at sinks; ρ_j, the sink density; D_j, the diffusion coefficient for a defect of j type; and τ_j, the relaxation time); the bulk mutual recombination of dissimilar defects is neglected; and $q_\varepsilon = q_0(K\Omega_j/kT)$ for the thermal mechanism of the point defect generation.

Equations (1) and (2) make up a closed system. This system completely describes the distribution of one-dimensional strain perturbations in a solid due to nonstationary and nonlinear distributions of a point defect subsystem as well as the inverse effect, namely, the variation of the defect concentration in a solid as a result of elastic strain perturbations.

NONLINEAR STATIONARY WAVES

Consider self-similar solutions of the form $u = u(\xi)$ and $n_{1j} = n_{1j}(\xi)$, where $\xi = x - vt$, describing longitudinal waves of strain and defect density propagating along the x axis with a velocity of v = const. In this case, the system of partial differential equations (1) and (2) passes into the following system of ordinary differential equations:

$$(v^2 - c_s^2)\frac{d^2 u}{d\xi^2} - \frac{\beta_N}{\rho}\frac{d^2 u}{d\xi^2}\frac{du}{d\xi} - (\alpha_1 v^2 - \alpha_2)\frac{d^4 u}{d\xi^4} = -\frac{K\Omega_j}{\rho}\frac{dn_{1j}}{d\xi}, \quad (3)$$

$$-v\frac{dn_1 j}{d\xi} + \frac{n_{1j}}{\tau_j} = q_\varepsilon\frac{du}{d\xi}. \quad (4)$$

We use the conditions

$$u_\xi(-\infty) = \varepsilon_0, \quad u_\xi(+\infty) = 0, \quad n_{1j}(\pm\infty) = 0 \quad (5)$$

as boundary conditions for Eqs. (3) and (4).

Boundary conditions (5) imply that waves propagating in a medium turn the system under consideration from a deformationless state into that with a constant deformation (ε_0). We will further restrict our consideration to a system with only one type of defects and take $n_{1j}(\xi) \equiv n_1(\xi)$, $\tau_j \equiv \tau$, and $\Omega_j \equiv \Omega$ in (3)–(5).

The solution of the nonuniform differential equation (4), in view of boundary conditions (5), has the form

$$n_1(\xi) = \int_{\xi}^{+\infty} d\xi' q(\xi') \exp\left(\frac{\xi - \xi'}{\tau v}\right), \quad (6)$$

where $q(\xi) = q_\varepsilon v^{-1} du/d\xi$.

Having eliminated the defect density, using (6), we arrive at equation

$$(v^2 - c_s^2)\frac{d^2u}{d\xi^2} - \frac{\beta_N}{\rho}\frac{d^2u}{d\xi^2}\frac{du}{d\xi} - (\alpha_1 v^2 - \alpha_2)\frac{d^4u}{d\xi^4} + \frac{K\Omega}{\rho}\frac{d}{d\xi}\int_{\xi}^{+\infty} \exp\left(\frac{\xi - \xi'}{\tau v}\right) q(\xi') d\xi' = 0 \quad (7)$$

describing the propagation of a nonlinear elastic strain wave.

Equations similar to (7) are typical for systems with strain memory (or relaxation) [1]. At $\alpha_1 = \alpha_2 = 0$ (without dispersion) and $q_\varepsilon = \beta = 0$ (without defect generation), this equation has the same form as in the case of a longitudinal wave in the free space. On the basis of Eq. (7), a thorough analysis of the strain wave propagation is possible in view of both the dispersion properties of a medium and the elastic properties of a lattice and defect subsystem. An exact analysis of this equation with arbitrary values of the parameters involved seems impossible. Further, we will consider it at small (compared to the period of the wave t_0) defect relaxation times ($\tau \ll t_0$). In this case, the integral term in (7) can be replaced by a differential one. Let us expand the function $q(\xi - z)$ by its Taylor series expansion at ξ. Retaining the first three terms in this expansion, we find

$$\frac{d}{d\xi}\int_{\xi}^{+\infty} d\xi' q(\xi') \exp\left(\frac{\xi - \xi'}{\tau v}\right) \approx q_\varepsilon\left(\tau\frac{d^2u}{d\xi^2} + \tau^2 v\frac{d^3u}{d\xi^3} + \tau^3 v^2\frac{d^4u}{d\xi^4}\right).$$

Having substituted this expression into (7), we arrive at the following equation:

$$(v^2 - \tilde{c}_s^2)\frac{d^2u}{d\xi^2} - \frac{\beta_N}{\rho}\frac{d^2u}{d\xi^2}\frac{du}{d\xi} + \frac{K\Omega q_\varepsilon \tau^2 v}{\rho}\frac{d^3u}{d\xi^3} - \left(\alpha_1 v^2 - \alpha_2 - q_\varepsilon \tau^3 v^2 \frac{K\Omega}{\rho}\right)\frac{d^4u}{d\xi^4} = 0, \quad (8)$$

where $\tilde{c}_s = c_s(1 - K\Omega q_\varepsilon \tau/\rho c_s^2)^{1/2}$ is the velocity of sound renormalized due to the defect-strain interaction.

In Eq. (8), the term with the third derivation of the displacement (the Burgers term) describes the wave energy dissipation. The appearance of this term is clearly related to the generation and recombination processes in the defect subsystem. In addition, the finiteness of the defect recombination rate (τ^{-1}) results in an additional contribution to nonlinear equation (8). This may influence the nonlinear wave properties.

Having performed single integration with respect to ξ and introduced the notation $\varepsilon = du/d\xi$, we find an equation coinciding with the first integral of the well-known stationary Korteweg–de Vries–Burgers equation [14]:

$$g\frac{d^2\varepsilon}{d\xi^2} - \delta\frac{d\varepsilon}{d\xi} + (\beta_N/\rho)\varepsilon^2 - \alpha\varepsilon = 0,$$

$$\alpha = v^2 - \tilde{c}_s^2, \quad g = \alpha_1 v^2 - \alpha_2 - K\Omega q_\varepsilon \tau^3 v^2 \rho^{-1}, \quad (9)$$

$$\delta = K\Omega q_\varepsilon \tau^2 v \rho^{-1}.$$

Here, the integration constant is equal to zero in view of the boundary conditions $du/d\xi|_{\xi \to \pm\infty} = 0$.

Equation (9) has repeatedly been considered in the literature. In particular, the characteristic features of solitary-wave (solitons) attenuation at low dissipation were studied. Shock-wave attenuation in elastic media without dissipation was considered in the framework of the Burgers equation [1, 14, 15]. Equation (9) also describes the propagation of nonlinear ion-sound waves in plasma in view of the Landau damping [16]. Equation (9), with the boundary conditions

$$\varepsilon(-\infty) = \varepsilon_0, \quad \varepsilon(+\infty) = 0 \quad (10)$$

admits a solution in the form of shock waves of low intensity (step-function solution) [14].

If the dispersion is negligible, Eq. (9) yields the stationary Burgers equation

$$\delta\frac{d\varepsilon}{d\xi} - (\beta_N/\rho)\varepsilon^2 + \alpha\varepsilon = 0,$$

having a solution in the form of shock waves with a monotonic profile,

$$\varepsilon = \frac{\varepsilon_0}{2}\left(1 - \tanh\frac{x - vt}{b}\right), \quad b = \frac{2\rho\delta}{\beta_N \varepsilon_0}.$$

In the general case, we will qualitatively determine the pattern of the solution to Eq. (9) in view of the influence of dispersion using the analysis performed in [14]. Note that an explicit analytical solution of Eq. (9) with additional restrictions on its coefficients can be found by the method described in [5].

The dependence of wave velocity v on its amplitude ε_0 is determined by the formula

$$v^2 = \tilde{c}_s^2 + \varepsilon_0 \beta_N \rho^{-1}. \quad (11)$$

From analysis of the asymptotic wave behavior, it follows that a solution satisfying boundary conditions (10) exists if the wave velocity $v > \tilde{c}_s$. Then, according

to (11), the wave excited is a tension wave ($\varepsilon_0 > 0$) for $\beta_N > 0$, and a compression wave ($\varepsilon_0 < 0$) for $\beta_N < 0$.

WAVE STRUCTURE

The structure of a nonlinear wave can be determined by studying the asymptotic behavior of the solutions of Eq. (9) subject to boundary conditions (10). Hereafter, we follow the qualitative analysis conducted in [14].

The structure of the shock wave depends on the ratio between the dispersion and dissipation parameters (g, δ) in Eq. (9). At sufficiently small values of δ, the shock wave has an oscillating structure. If the dissipation parameter exceeds a certain critical value $\delta > \delta_*$, the shock wave has a monotonous profile [14]. Critical values of the dissipation parameter δ_* corresponding to monotonous and oscillating wave profiles are determined by the formula

$$\delta_* = \sqrt{4|\alpha g|}.$$

Using (11), this equation can be represented in the form $|\varepsilon_0| = \varepsilon_*$, where the critical amplitude value is

$$\varepsilon_* = \frac{(K\Omega q_\varepsilon v\tau^2)^2}{|\beta_N|\left|\rho(\alpha_1 v^2 - \alpha_2) - K\Omega q_\varepsilon \tau^3 v^2\right|} \approx \left(\frac{K\Omega}{kT}\right)(q_0\tau\Omega).$$

Thus, the shock wave has an oscillating structure at $|\varepsilon_0| > \varepsilon_*$ and a monotonic structure at $|\varepsilon_0| < \varepsilon_*$. The critical amplitude value ε_* dividing shock waves with an oscillating structure from monotonic shock waves is determined by the elastic modulus, temperature of the medium, intensity of defect generation, their relaxation time, and dilatation volume of defects. At characteristic values of parameters (for vacancies) $K = 5 \times 10^{11}$ dyn/cm, $q_0\tau = 10^{19}$ cm^{-3}, $\beta_N = 10^{12}$ dyn/cm, $\rho = 8$ g/cm^3, and $|\Omega| = 10^{-23}$ cm^3, we find $\varepsilon_* = 4 \times 10^{-2}$.

The spatial scale of the variation of the solution to Eq. (9) evidently determines the width of a shock wave (L), i.e., the distance at which the oscillations die out [14]. An estimation yields

$$L = \frac{(4|g|/\delta)\sqrt{\varepsilon_* + |\varepsilon_0|}}{\sqrt{\varepsilon_* + |\varepsilon_0|} - \sqrt{\varepsilon_*}}. \quad (12)$$

The oscillation period (d) is found from a solution linearized in the neighborhood of the homogeneous solution $\varepsilon = \alpha\rho/\beta_N$ of Eq. (9),

$$g\frac{d^2\varepsilon}{d\xi^2} - \delta\frac{d\varepsilon}{d\xi} + \alpha\varepsilon = 0.$$

Finally, we find

$$d = (4\pi|g|/\delta)\sqrt{\frac{\varepsilon_*}{|\varepsilon_0| - \varepsilon_*}}. \quad (13)$$

According to (13), the oscillation period decreases with increasing amplitude of a nonlinear wave ε_0 and takes on the value

$$d \approx 4\pi\sqrt{\rho g/|\beta_N\varepsilon_0|}$$

in the limit $|\varepsilon_0| \gg \varepsilon_*$.

DISCUSSION

From the conditions of the existence of an oscillating shock wave ($\varepsilon_* < |\varepsilon_0|$) and smallness of its amplitude $|\varepsilon_0| \ll 1$, we find the restriction on its velocity,

$$\tilde{c}_s^2(1 + \varepsilon_*(|\beta_N|/\rho\tilde{c}_s^2)) < v^2 < \tilde{c}_s^2(1 + |\beta_N|/\rho\tilde{c}_s^2).$$

Since monotonic shock waves can appear in media with rather large values of ε_* ($\varepsilon_* > |\varepsilon_0|$), we find the following constraints on the velocities of these waves:

$$v^2 < \tilde{c}_s^2(1 + |\beta_N|/4\rho\tilde{c}_s^2).$$

In solids with negative dispersion ($g > 0$), an oscillating structure takes place before the wave front. On the contrary, in mediums with a positive dispersion ($g < 0$), the oscillating tail is behind the front.

According to (12) and (13), the parameters L and d of oscillating shock waves are determined by the dispersion parameter g. Therefore, the dispersion in a system is necessary for these waves to exist. Monotonic shock waves, in contrast to oscillating ones, may exist in dispersionless systems.

Let us discuss now the contribution of defects to the dispersion properties of a medium. The correction due to nonequilibrium defects to the dispersion parameters is of importance if $K\Omega q_\varepsilon \tau^3 v^2 \rho^{-1} > \alpha_1 v^2 - \alpha_2$.

This implies the following restriction on the defect density:

$$q_0\tau > \frac{\rho(\alpha_1 v^2 - \alpha_2)kT}{(v\tau K\Omega)^2}.$$

This condition can be satisfied for rather high defect densities ($q_0\tau \geq 10^{19}$ cm^{-3}), which are typical for powerful impulse laser exposures on most solids. However, if the linear elastic moduli for a lattice, the dilatation volume of defects, and their relaxation time are large, the corrections due to defects become substantial even at lower densities.

Thus, in a solid exposed to external energy fluxes resulting in the generation of nonequilibrium point defects, the strain wave may propagate as a shock wave of low intensity. Shock waves may have an oscillating profile as well as a monotonic one. The existence of such waves is determined by dissipation processes of the generation (recombination) of defects (rate of defect generation, recombination time), the dispersion of a medium, and the elastic properties of the lattice and defect subsystem.

The model equation describing the propagation of the nonlinear wave of elastic deformation in an elastic medium is derived in view of generation and recombination processes. Its structure is a combination of the stationary Korteweg–de Vries and Burgers equations. The quantitative estimations of contributions into linear elastic moduli and bulk dispersion due to a finite defect recombination rate are presented. The critical defect densities are found in the case when their influence on the strain wave propagation is substantial.

Note, in conclusion, that strain wave propagation is of significant interest in a medium with clusters of point defects (vacancies, interstitial clusters, etc.). A strain wave interacting with such defects may result in a local temperature increase and, hence, the strengthening of recombination processes. The latter, in turn, are accompanied by local heat generation and the deformation of the medium. Further study of the nonlinear interaction of deformation fields and temperature with structure defects (both point defects and clusters) is of interest from scientific and practical standpoints. A propagating strain wave carries information about various defects of a condensed medium that is necessary for diagnosing the defect structure of solids.

ACKNOWLEDGMENTS

The author is grateful to L.A. Shelepin and E.V. Zelenov for helpful discussion of results.

REFERENCES

1. Yu. K. Éngel'brekht and U. K. Nigul, *Nonlinear Strain Waves* (Nauka, Moscow, 1981).
2. A. M. Samsonov, G. V. Dreĭden, A. V. Porubov, and I. V. Semenova, Pis'ma Zh. Tekh. Fiz. **22** (21), 61 (1996) [Tech. Phys. Lett. **22**, 891 (1996)].
3. G. V. Dreĭden, Yu. I. Ostrovskiĭ, and A. M. Samsonov, Zh. Tekh. Fiz. **58**, 2040 (1988) [Sov. Phys. Tech. Phys. **33**, 1237 (1988)].
4. A. M. Samsonov, G. V. Dreĭden, A. V. Porubov, and I. V. Semenova, Phys. Rev. B **57**, 5778 (1998).
5. A. M. Samsonov, Appl. Anal., 85 (1995).
6. M. Toda, in *Springer Series in Solid State Sciences*, Vol. 20: *Theory of Nonlinear Lattices* (Springer-Verlag, Berlin, 1981).
7. L. M. Lyamshev, Usp. Fiz. Nauk **135**, 637 (1981) [Sov. Phys. Usp. **24**, 977 (1981)].
8. A. M. Kosevich, *Foundations of Crystal-Lattice Mechanics* (Nauka, Moscow, 1972).
9. F. Mirzoev and L. A. Shelepin, Zh. Tekh. Fiz. **71** (8), 23 (2001) [Tech. Phys. **46**, 952 (2001)].
10. A. A. Karabutov, V. T. Platonenko, O. V. Rudenko, and V. A. Chupryna, Vestn. Mosk. Univ., Ser. 3: Fiz., Astron. **25** (3), 88 (1984).
11. Yu. A. Bykovskiĭ, *Ionic and Laser Implantation of Metallic Materials* (Énergoatomizdat, Moscow, 1991).
12. F. Mirzoev, V. Ya. Panchenko, and L. A. Shelepin, Usp. Fiz. Nauk **166**, 3 (1996) [Phys. Usp. **39**, 1 (1996)].
13. A. I. Lur'e, *Nonlinear Theory of Elasticity* (Nauka, Moscow, 1980).
14. V. I. Karpman, *Non-Linear Waves in Dispersive Media* (Nauka, Moscow, 1973; Pergamon, Oxford, 1975).
15. A. I. Potapov, *Nonlinear Strain Waves in Rods and Plates* (Gorki, 1985).
16. E. N. Pelinovskiĭ, Izv. Vyssh. Uchebn. Zaved., Radiofiz. **14** (8), 67 (1971).

Translated by M. Fofanov

Technical Physics, Vol. 47, No. 10, 2002, pp. 1263–1267. Translated from Zhurnal Tekhnicheskoĭ Fiziki, Vol. 72, No. 10, 2002, pp. 58–62.

SOLID-STATE ELECTRONICS

Current–Voltage Characteristic and Parameters of the Current Filament Region of an Amorphous Gallium Telluride–Crystalline Silicon Barrier Negistor Structure

A. Čhesnys, S.-A. Karpinskas, and A. Urbelis

Gediminas Technical University, Vilnius, 2040 Lithuania

e-mail: fizkat@fm.vtu.lt

Received December 4, 2001

Abstract—The transient *I–V* characteristic of an amorphous $GaTe_3$–crystalline *n*-Si barrier negistor structure under negative differential resistance (NDR) conditions is studied. The basic parameters (cross-section radius, current density, and resistivity) of the current filament region in the amorphous layer of the structure are determined. Results obtained are compared with the associated parameters of the current filament in a C–amorphous $GaTe_3$–C reference barrier-free structure. Under NDR conditions, the conductivity of the filament region in this heterostructure is shown to be governed largely by processes occurring in the crystalline component. *© 2002 MAIK "Nauka/Interperiodica".*

INTRODUCTION

The idea of using an amorphous chalcogenide semiconductor as the emitter of a bipolar transistor [1, 2] seems to be very promising. Depending on the collector voltage to base voltage ratio, such a transistor may take either of two (weakly and strongly amplifying) states, which would greatly extend the range of its application [2]. Amorphous semiconductor–crystalline semiconductor barrier heterostructures, exhibiting an *S*-shaped *I–V* characteristic (negistor structures), are of great interest in this respect.

Negative differential resistance, which is responsible for the *S* shape of the *I–V* characteristic, is due to processes taking place in the amorphous semiconductor. In this layer, a specific high-conductivity channel normal to the current electrodes forms under conditions of electrical instability. This channel is a part of the increased current density region (current filament) in the heterostructure. The rest of this region (channel) is in the crystalline component. The important parameters of the structure, primarily its stability and service life, depend on physical processes taking place in the channel. That is why the physical situation in the channel is of great interest for both elucidating the mechanism of electrical instability and finding optimal operating conditions.

A great deal of information can certainly be derived from the electrical properties of the channel. However, they are difficult to study because of the small size of the current filament region. Moreover, the resistances of both parts of the filament (in the amorphous and crystalline layers) may be comparable. Therefore, the application of conventional techniques for investigating barrier-free negistor structures [3–5] to determine the channel parameters may introduce great errors.

The aim of this work was to take the *I–V* characteristics of the heterojunction in the current filament region and to clarify the contributions of electronic processes taking place in the amorphous and crystalline layers to the conductivity of this region. In addition, we tried to estimate channel nonthermal parameters (cross-section radius r_c, current density j_c, and resistivity ρ_c) in the amorphous semiconductor.

OBJECT OF INVESTIGATION

The object studied was an amorphous $GaTe_3$–crystalline *n*-Si barrier negistor structure. In such structures, the forward branch of the *I–V* characteristic lacks the ohmic portion up to the onset of the NDR effect (i.e., up to the conditions of electrical instability and current filamentation)[1]. Moreover, the conductivity of these structures in high electric fields is associated with the monopolar injection of charge carriers from the crystalline semiconductor to the amorphous layer (space-charge-limited current mode) [6]. The conductivity of $GaTe_3$ amorphous films in high electric fields is due to the field-enhanced thermal generation of charge carriers [7]. These heterostructures retain a sensitivity to voltage polarity, which specifies electrical instability, and conductivity asymmetry in a wide range of electrical pulse durations (including nanosecond durations) because of different conditions for charge carrier injection into the $GaTe_3$ layer in the forward and backward directions [6].

[1] In what follows, the states of the structure before and after filamentation will be called high-ohmic and low-ohmic, respectively.

1063-7842/02/4710-1263$22.00 © 2002 MAIK "Nauka/Interperiodica"

INVESTIGATION TECHNIQUES

The structures were fabricated by the discrete evaporation of a $GaTe_3$ preparation at low pressures (about 10^{-3} Pa) with the subsequent condensation of its vapors on substrates kept at temperatures between 330 and 340 K. The substrate was a film of *n*-Si with a resistivity $\rho_{Si} = 1.0\ \Omega$ cm epitaxially grown on a lower resistivity ($\rho_{Si} \approx 0.01\ \Omega$ cm) single-crystal Si wafer of the same conductivity type. Current filament parameters found on these structures were contrasted with those for C–amorphous $GaTe_3$–C barrier-free reference structures, which have symmetric *S*-shaped *I–V* characteristics. The references were fabricated on glassy carbon plates. In both structures, a pressed glassy carbon probe was used as an electrode to the amorphous layer; in the structures investigated, we also used an evaporated molybdenum film of area 10^{-5} cm^2 as a contact. The amorphous layer thickness was varied between 0.6 and 1.0 μm.

The transient *I–V* characteristics of the heterostructures were taken in the low-ohmic state (Fig. 1) with the so-called double pulse method [8]. Two rectangular voltage pulses (a long basic pulse and a short pulse of variable amplitude and polarity superimposed on the latter) were applied to the sample and to a series-connected resistor limiting the current upon switching to the low-ohmic state. The pulses of the voltage dropped across the sample and the current in the measuring circuit are schematically shown in Fig. 1. The amplitude of the former pulse (pulse *1* in Fig. 1) was large enough for electrical instability in the sample to arise, while its duration was long enough for a current filament to form and the resulting low-ohmic state to be sustained during the measurements (U_{0s} and I_{0s} are the sustaining voltage and current, respectively). The latter (measuring) pulse (pulse *3* in Fig. 1) was used to take transient *I–V* characteristics. Its duration was no more than 10^{-7} s, so that its application could not change noticeably the current filament parameters. Thus, the transient *I–V* characteristic of the negistor structure taken under the above conditions reflects adequately the behavior of the current passing through the heterojunction in the filament region.

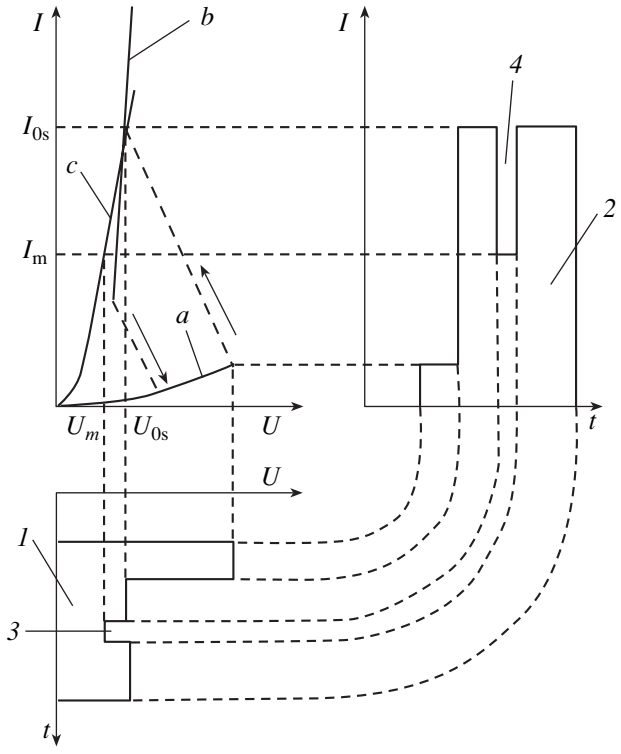

Fig. 1. (a, b) S-shaped and (c) transient *I–V* characteristics of the negistor structure and (*1–4*) electrical pulses in the measuring circuit. (*1*) Pulse of the voltage (*U*) dropped across the structure and (*2*) pulse of the current (*I*) through the structure upon switching to the low-ohmic state; (*3, 4*) measuring voltage (U_m) and current (I_m) pulses, respectively; U_{0s} and I_{0s} are the voltage and current sustaining the low-ohmic state; and *t* is time.

The radius r_c of the filament (channel) cross section in the amorphous semiconductor was calculated by the formula

$$r_c = \frac{d_{Si}}{2}\left[\left(1 + 4\frac{\rho_{Si}}{\pi d_{Si} R_{Si}}\right)^{1/2} - 1\right], \qquad (1)$$

where d_{Si} is the thickness of the epitaxial Si layer.

This formula follows from the calculation of the filament resistance R_{Si} in the epitaxial layer under the assumption that the current passing from the high-conductivity channel in the amorphous layer spreads in the crystalline semiconductor at an angle of 45° (such an assumption is well justified according to [9]). In our case, the filament in the epitaxial Si layer has the shape of a blunted cone with radii of the lower and upper bases $d_{Si} + r_c$ and r_c, respectively.

The current density j_c in the channel was evaluated from the relationship

$$j_c = \frac{I_{0s}}{\pi r_c}\left[1 + \frac{\rho_c}{\rho_{out}}\left(\frac{r_0}{r_c} - 1\right)^2\right]^{-1}, \qquad (2)$$

where ρ_{out} is the resistivity of the region outside the channel in the amorphous semiconductor and r_0 is the radius of the effective contact between the amorphous and crystalline components of the heterostructure.

In real negistor structures, the condition $\rho_{out}/\rho_c \gg r_0/r_c$ is usually valid; hence, $(\rho_c/\rho_{out})(r_0/r_c - 1)^2 \ll 1$, as evidenced by the great difference in the currents in the low-ohmic and initial high-ohmic states (the currents usually differ by several orders of magnitude [3]).

The parameters r_c and j_c in the C–amorphous $GaTe_3$–C barrier-free reference structures were found by measuring microwave noise [4, 5].

RESULTS AND DISCUSSION

The transient *I–V* characteristics of our heterostructures are asymmetric with respect to the measuring pulse polarity (Fig. 2). However, their asymmetry is somewhat weaker than the *I–V* characteristic in the high-ohmic state (Fig. 3). Unlike the high-ohmic *I–V* characteristic, the forward branch of the transient curve (the *n*-Si is negatively biased) contains an exponential portion (at low voltages) and a rectilinear portion, which is typical of the usual *I–V* characteristics for barrier structures. The slope $G = dI_m/dU_m$ (I_m and U_m are the measuring current and voltage) of the rectilinear part of the transient curve depends on the sustaining current, increasing with it. The rectilinearity of the transient curve indicates that the total resistance of the high-conductivity channel in the amorphous layer and the electrically active part of the epitaxial silicon film (its filament region) adjacent to the channel is ohmic. The variation of the slope of the transient curve with the sustaining current reflects the variation of the transverse size of the current filament in the amorphous semiconductor. As the temperature rises, the transient curve shifts toward higher currents; however, the slope of its exponential portion is virtually temperature independent in the semilogarithmic coordinates. Hence, this portion is described by the expression $I_m = I_0 \exp(U_m/U_0)$, where I_0 is a temperature-dependent preexponential and $U_0 = (0.15 \pm 0.02)$ V is close to the related parameter in the exponential voltage dependence of the barrier resistance (R_b) in the forward direction when the heterostructure is in the high-ohmic state [6].

To estimate the parameters of the high-conductivity channel, it is necessary to know the resistance R_{Si} entering into formula (1). This parameter was determined from the slope G of the rectilinear portion of the transient curve ($R_{Si} = G^{-1} - R_c$) on assumption that the channel resistance is given by the expression $R_c = U'_{0s}/I_{0s}$, where U'_{0s} is the sustaining voltage in the low-ohmic state of the C–amorphous $GaTe_3$–C barrier-free reference. This assumption relies on the fact that in the low-ohmic state, our barrier-free structure exhibits nonactivated conduction in the filament region, which appears because of electron processes like electron-phase transition [10]. Since this transition is due mainly to Joule heating, as follows from microwave noise studies [10], one may suppose that the sustaining of the low-ohmic state in the amorphous layer does not depend on a mechanism of charge carrier transfer in the high-ohmic state of the negistor structure. In other words, the mechanism of sustaining must be the same in the barrier-free reference and in the barrier structure under study. With this assumption, the parameters r_c and j_c in our heterostructures were estimated at several micrometers and 10^4 A/cm^2, respectively. For example, for the heterostructure whose *I–V* characteristic is shown in Fig. 2 (here, $d_{out} \approx 0.8$ μm) with the current sustaining the low-ohmic state being equal to 6 μA, r_c was found to be (2.7 ± 0.1) μm and j_c, $(2.6 \pm 0.2) \times 10^4$ A/cm^2. In this case, the ratio r_0/r_c is no more than 10, while the ratio ρ_{out}/ρ_c may be as high as several orders of magnitude, as judged from the difference between the currents passing through the structure in the low- and high-ohmic states at the same bias voltages. The value of ρ_c

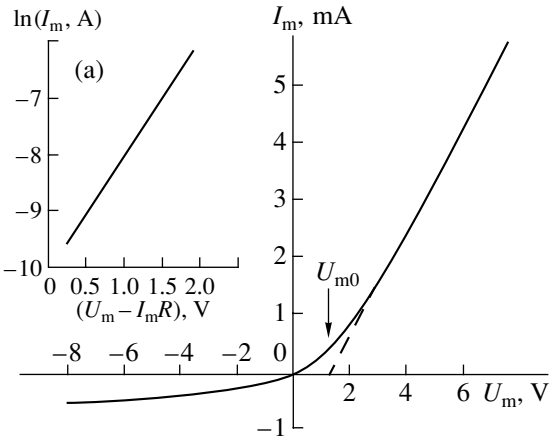

Fig. 2. Transient *I–V* characteristic of the amorphous $GaTe_3$–crystalline *n*-Si negistor heterostructure in the low-ohmic state, arising when the forward voltage is applied. The current sustaining the low-ohmic state and the duration of the low-ohmic state are, respectively, 6 μA and 140 ns. The measuring pulse duration is 20 ns. (a) Forward current vs. voltage for $U_m \le U_{m0}$.

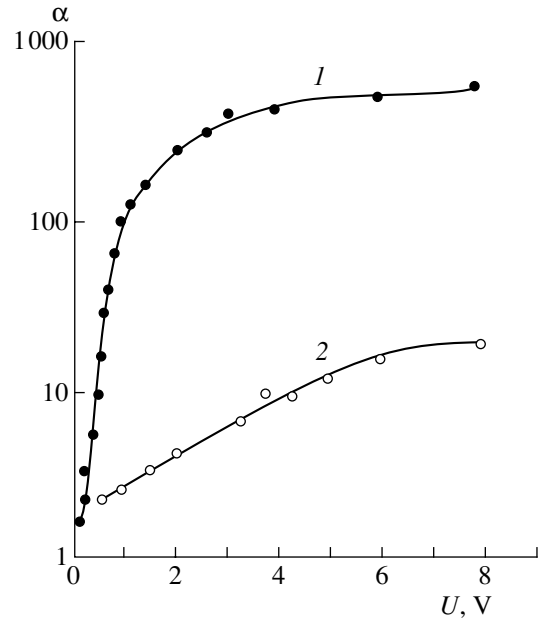

Fig. 3. Asymmetry of the conductivity of the amorphous $GaTe_3$–crystalline *n*-Si negistor structure vs. bias voltage in (*1*) the initial high-ohmic state and (*2*) the low-ohmic state. α is the forward-to-reverse current ratio at the same bias voltage. Curve *2* is calculated based on the transient characteristic in Fig. 2.

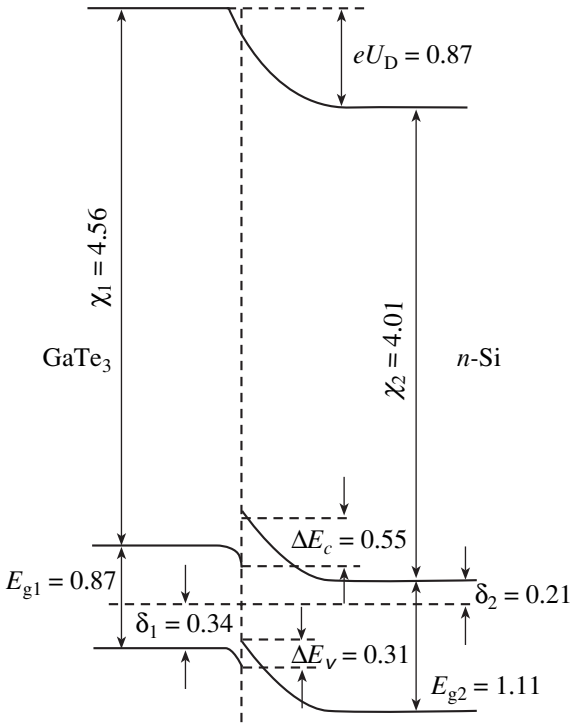

Fig. 4. Tentative energy band diagram for the heterojunction of the amorphous $GaTe_3$–crystalline n-Si negistor structure in the initial high-ohmic state. $\delta_{1(2)}$ and $\chi_{1(2)}$ are the spacings between the Fermi level and the band edge and the electron affinities of the materials, respectively; ΔE_c and ΔE_v are the band discontinuities at the heterojunction; $\Delta E_{g1(2)}$ are the energy gaps; U_D is the diffusion potential; and e is the unit charge. All parameters are given in electronvolts.

estimated with the values of r_c, j_c, and R_c obtained above was equal to (0.38 ± 0.04) Ω cm.

The values of r_c and j_c obtained in this work coincide with those for the C–amorphous $GaTe_3$–C barrier-free reference structure within the experimental error; in addition, r_c coincides with the value (0.09–0.22 Ω cm) found by studying microwave noise in similar structures [10] by order of magnitude.

The same shape of our exponential dependence $I_m = f(U_m)$ and of the dependence $R_b = f(U)$ mentioned above at low forward voltages, as well as the roughly equal values of U_0 in these dependences, allows us to argue (in view of data in [6]) that this portion of the transient characteristic describes only processes in the potential barrier still persisting in the filament region of the crystalline component. The nature of this barrier can be judged from the tentative energy band diagram of the heterostructure in the initial high-ohmic state (Fig. 4). When constructing this diagram, we assumed that the screening length and the density of states in the energy gap of amorphous $GaTe_3$ are close to those in glassy chalcogenide semiconductors by order of magnitude [11]. In our case, the uncompensated space charge must spread in the crystalline component of the heterostructure to a much greater distance than in the amorphous layer. Moreover, the diffusion potential U_D was set equal to the cutoff voltage in the *C–V* characteristic found in [6]. As follows from Fig. 4, the discontinuity in the conduction band edge of the heterostructure causes a Schottky-type spike, which governs charge carrier transfer in the structure. According to [6], charge carrier tunneling is the prevailing mechanism of current passage through the barrier at low forward voltages, the tunnel current being of a thermal nature [12].

For the spike to be retained in the energy band of the filament region after the heterostructure has been passed to the low-ohmic state (i.e., for the charge transfer mechanism to remain the same at low forward voltages in this region, as follows from the above results), the position of the Fermi level at the heterojunction in the filament region must not change drastically. Irrespective of the Fermi level position in the high-conductivity channel, such a situation may take place owing to the screening action of states on the crystalline component surface and, according to [13], is typical of the real (unprocessed) silicon surface. Impurity centers on the silicon surface may also arise during the deposition of amorphous $GaTe_3$. Furthermore, the conductivity of the channel is likely to be nonuniform (especially if currents sustaining the low-ohmic state are low) because of a temperature gradient arising when heat is removed through the contacts, including the contact to the silicon. Along with the central part of the channel with nonactivated quasi-metallic conduction, there may exist a thin (even tunnel-transparent) layer with residual conduction of semiconductor type near the silicon. This layer may fix the Fermi layer in the energy gap of $GaTe_3$. Data reported in [14] indicate that such a near-contact layer is a possibility.

The different asymmetries of the transient characteristic in the low-ohmic state and the steady-state characteristic in the high-ohmic state may be associated with different reverse current densities in these states. In barrier *p–n* structures, the reverse current is known to be related to minority carrier drift (holes in the silicon and electrons in amorphous $GaTe_3$ in our case). Since the concentration of minority carriers in the initial high-ohmic state is relatively small, the reverse current density is insignificant. After the heterostructure has been switched to the low-ohmic state, the reverse current density must increase noticeably, because the free-electron concentration in the conducting channel of the amorphous semiconductor sharply grows. Because of this effect, the heterojunction in the filament region can be considered as an analog of a metal–semiconductor Schottky barrier, while in the high-ohmic state, the heterojunction is akin to a *p–n* junction with a lightly doped *p*-region. If silicon is used as a semiconductor in these junctions, the reverse current density in the former exceeds that in the latter by several orders of

magnitude, according to [13]. This is the basic reason why the asymmetry of the filament conductivity in our heterostructure is weaker.

CONCLUSIONS

(1) Upon switching from the high- to low-ohmic state, the potential barrier in the current filament region of the amorphous $GaTe_3$–crystalline *n*-Si negistor structure persists. The conductivity of this region, which is described by the transient *I–V* characteristic in the low-ohmic state, is governed by electronic processes taking place in the silicon. The weaker asymmetry of the filament conductivity observed upon switching is explained by enhanced electron drift through the potential barrier under reverse biases.

(2) The parameters r_c, j_c, and ρ_c of the current filament (channel) in the amorphous $GaTe_3$ of our heterostructure are on the order of several micrometers, 10^4 A/cm^2, and 10^{-1} Ω cm, respectively. These values virtually coincide with those for the C–amorphous $GaTe_3$–C barrier-free reference, supporting the assumption that the origin of the high-conductivity channel in the $GaTe_3$ is independent of the processes initiating electrical instability in such structures.

ACKNOWLEDGMENTS

The authors are indebted to A.-K. Oginskis for assistance in the experiments.

REFERENCES

1. K. E. Petersen and D. Adler, IEEE Trans. Electron. Devices **ED-23**, 471 (1976).
2. D. Adler, Sci. Am. **26**, 36 (1977).
3. S. A. Kostylev and V. A. Shkut, *Electronic Switching in Amorphous Semiconductors* (Naukova Dumka, Kiev, 1978).
4. A. Česnys, A. Oginskas, K. Gaška, and V. Lisauskas, J. Non-Cryst. Solids **90**, 609 (1987).
5. USSR Inventor's Certificate No. 1278624, G01 K7/30 (1985).
6. A. Česnys, A. Oginskas, E. Butinaviciute, *et al.*, Litov. Fiz. Sb. **24** (3), 83 (1984).
7. A. Česnys, A. Oginskas, and V. Lisauskas, Litov. Fiz. Sb. **32**, 664 (1992).
8. R. W. Pryor and H. K. Henisch, J. Non-Cryst. Solids **7**, 181 (1972).
9. K. E. Petersen and D. Adler, J. Appl. Phys. **47**, 256 (1976).
10. A. Česnys and A.-K. Oginskis, Litov. Fiz. Zh. **38**, 385 (1998).
11. N. F. Mott and E. A. Davis, *Electronic Processes in Non-Crystalline Materials* (Clarendon, Oxford, 1979; Mir, Moscow, 1982).
12. B. L. Sharma and R. K. Purohit, *Semiconductor Heterojunctions* (Pergamon, Oxford, 1974; Sov. Radio, Moscow, 1979).
13. E. H. Rhoderick, *Metal–Semiconductor Contacts* (Clarendon, Oxford, 1978; Radio i Svyaz', Moscow, 1982).
14. A. Česnys and A.-K. Oginskis, Litov. Fiz. Zh. **34**, 272 (1994).

Translated by V. Isaakyan

Technical Physics, Vol. 47, No. 10, 2002, pp. 1268–1271. Translated from Zhurnal Tekhnicheskoĭ Fiziki, Vol. 72, No. 10, 2002, pp. 63–66.

SOLID-STATE ELECTRONICS

Effect of Hydrogen on the Photoelectronic Properties of GaAs/InGaAs Quantum-Well Heterostructures with an Island Palladium Layer on the Surface

I. A. Karpovich, S. V. Tikhov, E. L. Shobolov, and B. N. Zvonkov

Lobachevsky State University, Nizhni Novgorod, 603950 Russia

e-mail: fdp@phys.unn.ru

Received January 8, 2002

Abstract—The effect of hydrogen on the photoluminescence and planar conductivity of GaAs/InGaAs quantum-well heterostructures with an island Pd layer at the anodically oxidized surface was studied. Unlike continuous deposited Pd layers, island layers do not cause the formation of defects in the GaAs surface region and yet the Pd layer maintains high catalytic activity with respect to hydrogen. It is found that the thermal treatment of such a structure in a hydrogen atmosphere causes atomic-hydrogen passivation of the defects in quantum wells. Studies of the characteristics of planar photoresistors with an island Pd layer acting as hydrogen sensors show that their hydrogen detectivity is approximately two orders of magnitude higher than that of diode structures with continuous Pd layers. *© 2002 MAIK "Nauka/Interperiodica".*

INTRODUCTION

Metal–oxide–semiconductor (MOS) GaAs diode structures with Pd rectifying contacts, which possess high catalytic activity, can be used as the basis for high-sensitive fast-response hydrogen sensors [1–3]. Their sensitivity to hydrogen susceptibility increases as InGaAs quantum wells (QWs) hindering hydrogen diffusion into the bulk are inserted into the GaAs layer [4]. However, the deposition of a continuous Pd layer in the case of optimal oxide layer thickness (≈4 nm) results in defect generation in the surface GaAs region [4], which is probably caused by the chemical reaction of Pd with GaAs as well as by the pronounced lattice mismatch between Pd and GaAs (the lattice constants are 3.9 and 5.7 nm, respectively). This impairs the parameters of the gas sensors and can cause their failure.

In this paper, we report the results of studying hydrogen interaction with QW semiconductor structures, in which a continuous conducting Pd layer is replaced by a nonconducting island layer. Apart from being of interest from the standpoint of fundamental science, the study of this problem opens up prospects for the development of a new type of sensors based on the planar photoconductivity phenomena in GaAs layers. As in [4–6], to control the defect formation in the surface region of GaAs, we used the photoluminescence from QWs, which is a very sensitive indicator of the presence of defects.

EXPERIMENTAL

GaAs/InGaAs quantum well heterostructures (QWHs) were grown by metal-organic vapor phase epitaxy (MOVPE) at atmospheric pressure on semi-insulating GaAs(001) substrates. Three $In_xGa_{1-x}As$ ($x \approx 0.2$–0.28) QWs were incorporated into the surface region of the GaAs epitaxial layer. The widths of these QWs decreased with the distance from the GaAs surface and amounted in different structures to 7–12, 4–5, and 3 nm for QWs 1, 2, and 3, respectively. Both doped GaAs layers with the electron density $n_0 \approx 10^6$ cm^{-3} and undoped GaAs layers with $n_0 \approx 5 \times 10^{13}$ cm^{-3} were used in this study.

The GaAs overlayer thickness was 20 nm, the barrier layers between QWs were 30 nm thick, and the total thickness of the entire layer was ≈0.6–0.8 μm. To eliminate the interaction between Pd and Ga and the formation of a compound that is insensitive to hydrogen [7], an anodic oxide (AO) film ≈4 nm thick was grown on the GaAs overlayer through liquid-phase anodization prior to Pd deposition.

The Pd layers were deposited on the AO film using vacuum thermal evaporation. The continuous semitransparent Pd layer had a thickness $d_{Pd} \approx 5$ nm and a surface conductivity of $\approx 10^{-3}$ $\Omega^{-1}/\square$. The island layers were obtained with a nominal thickness of ≈2.5 and 1.5 nm and possessed a conductivity lower than 10^{-5} $\Omega^{-1}/\square$. The thickness of the continuous Pd and AO layers were measured to an accuracy of ≈0.3 nm by a Topometrix atomic-force microscope (AFM) using an etched or a scratched step (for AO or Pd layers, respectively). The nominal thickness of the island Pd layer was determined from the weight ratios of the evaporated charges. According to AFM studies, the conducting Pd layers with a nominal thickness of 5 nm had an average grain size of ≈200 nm, and, in the island layers

1063-7842/02/4710-1268$22.00

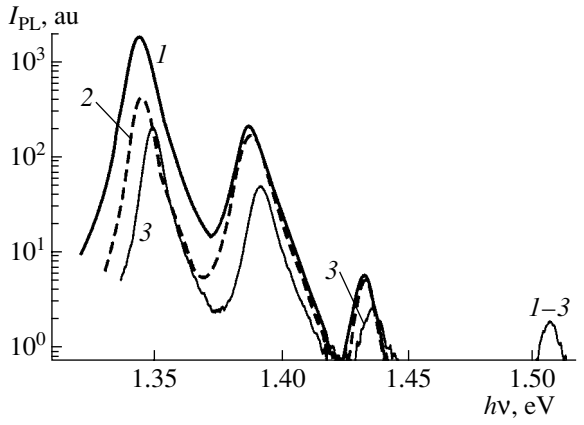

Fig. 1. Effect of the Pd electrode thickness d_{Pd} on the PL spectra. d_{Pd} = (*1*) 0, (*2*) 1.5 and 2.5, and (*3*) 5.0 nm.

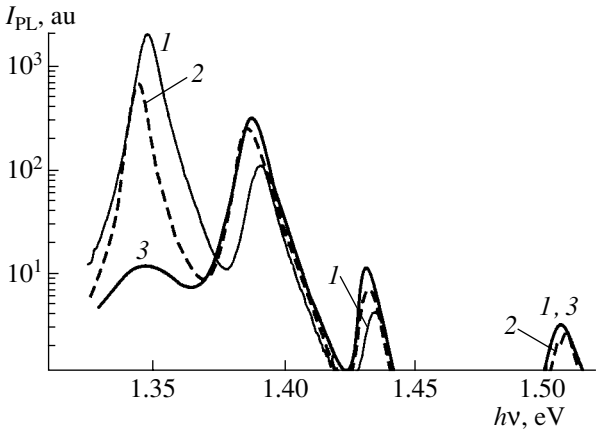

Fig. 2. Effect of thermal treatment in hydrogen ambient on the PL spectra. d_{Pd} = (*1*) 0, (*2*) 2.5, and (*3*) 5.0 nm.

with a nominal thickness of ≈2.5 nm, the average grain size was ≈50 nm.

The planar structures were fabricated by the fusion of two Sn ohmic contacts to the GaAs epitaxial layer. The area of the contacts was 1×5 mm^2, and the distance between them was ≈4–5 mm. The diode structures Pd/AO/GaAs/Sn with a continuous Pd electrode were also formed on the conducting GaAs substrate ($n_0 \approx 10^{16}$ cm^{-3}).

The influence of hydrogen exposure on the characteristics of the planar and diode structures was studied in the gas-sensor mode. At the optimal temperature of 370 K, the samples were subjected to pulses of hydrogen treatment in an air–argon flow mixture with a hydrogen concentration $P_{H_2} \approx 0.002$–0.2 vol % [2] and in the heat-treatment mode (the samples were briefly heated (for 600 s) in hydrogen at 743 K). The planar conductivity and photoconductivity (PC) under illumination with white modulated light, photoluminescence (PL), and photovoltage (in the diode structures) were investigated.

RESULTS AND DISCUSSION

1. Photoluminescense Spectra

Figure 1 presents the PL spectra of the studied samples at various thicknesses of the Pd electrode. It is evident from Fig. 1 that the PL intensity in the QW decreases after the Pd layer deposition. The decrease in the PL intensity depends on the distance of the QW from the surface and the thickness of the Pd layer and is caused by defect generation in the course of the chemical interaction of Pd with GaAs, as well as by defect penetration into the QW material [4]. The most pronounced effect is observed in the region of the first QW. It is evident that, at the nominal thicknesses of 1.5 and 2.5 nm corresponding to the discontinuous Pd layer, the defect-formation rate is substantially lower.

Figure 2 illustrates the influence of the thermal treatment in hydrogen under atmospheric pressure at 473 K for 600 s on the PL spectra of the structures with different thicknesses of the Pd electrode. After such a treatment, pronounced PL quenching (by more than two orders of magnitude) occurs in the first QW in the structures with a continuous Pd electrode, and far less quenching (approximately by a factor of 3) occurs in the structures with an island Pd layer. Simultaneously, PL amplification in the second and third QW by a factor of 2–3 is observed in both structures, which indicates that atomic hydrogen passivates the defects in these wells. The intensity of the edge PL in GaAs (1.5 eV) was almost the same in all structures.

The considerable decrease of the PL intensity in the QW closest to the surface is characteristic of hydrogenization in a hydrogen plasma and is related to the accumulation of defects formed in the course of the ion

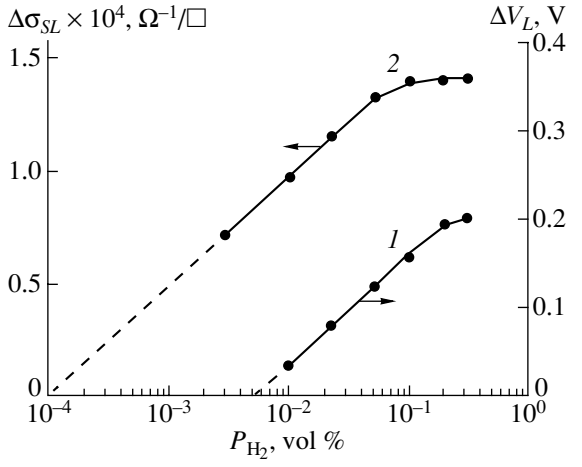

Fig. 3. Dependence of the steady-state PC response $\Delta\sigma_{SL}$ (*2*) for the planar structure ($d_{Pd} \approx 2.5$ nm) and of the barrier photovoltage ΔV_L for the diode structure (*1*) on hydrogen concentration at 370 K.

Effect of hydrogen on the planar dark conductivity and photoconductivity of the resistor structures in the gas-sensor mode

GaAs doping level, n_0, cm^{-3}	d_{Pd}, nm	$P_{H_2} = 0$		$P_{H_2} = 0.22$ vol %	
		σ_n, Ω/□	σ_L, Ω/□	σ_n, Ω/□	σ_L, Ω/□
5×10^{13}	0	5.0×10^{-6}	9.7×10^{-6}	5.0×10^{-6}	9.7×10^{-6}
	1.5	2.5×10^{-6}	2.9×10^{-6}	2.6×10^{-6}	2.4×10^{-6}
	2.5	5.5×10^{-5}	1.4×10^{-3}	5.8×10^{-5}	7.3×10^{-5}
	5.0	1.6×10^{-3}	1.2×10^{-6}	1.7×10^{-3}	5.6×10^{-7}
10^{16}	0	1.1×10^{-3}	1.6×10^{-5}	1.1×10^{-3}	1.6×10^{-5}
	1.5	1.6×10^{-3}	1.7×10^{-5}	1.7×10^{-3}	1.2×10^{-5}
	2.5	1.4×10^{-3}	8.8×10^{-6}	1.5×10^{-3}	2.2×10^{-6}
	5.0	1.5×10^{-3}	3.5×10^{-6}	1.5×10^{-3}	2.4×10^{-6}

bombardment of the surface [6]. It might be expected that this effect can be avoided if hydrogen is introduced through the Pd electrode. However, these expectations are partly realized only in the case of the island Pd layer. This result can be explained by the fact that the island Pd layer induces weaker stresses in the oxide and surface GaAs layer, which ensures the higher structural quality of these regions. The hydrogen-induced passivating effect becomes apparent only in the second and third QW, as in the case of the treatment with hydrogen plasma [6]. This fact is probably related to the higher penetrability of atomic hydrogen in comparison with the defects, which are mainly arrested by the first QW.

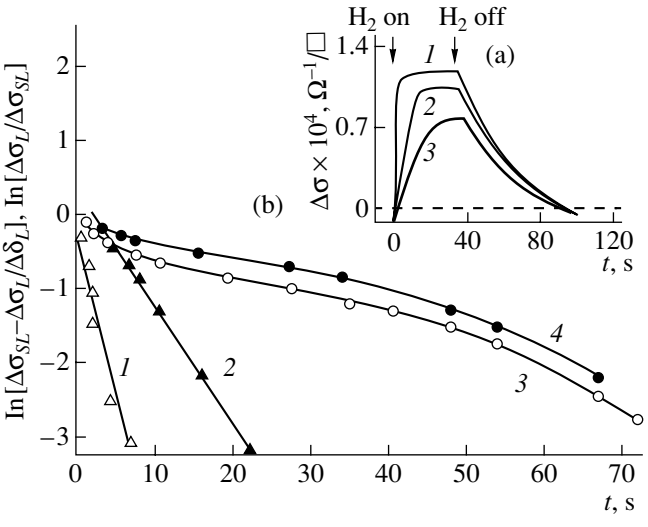

Fig. 4. (a) Kinetic curves $\Delta\sigma_L$ for a planar structure at different hydrogen concentrations: P_{H_2} = (*1*) 0.22, (*2*) 0.022, and (*3*) 0.011 vol %; T = 370 K; $d_{Pd} \approx 2.5$ nm. (b) Response to hydrogen of the planar structure plotted as $\ln[(\Delta\sigma_{SL} - \Delta\sigma_L)/\delta\sigma_{SL}]$ versus t for the rise (*1*, *2*) and as $\ln(\Delta\sigma_L/\Delta\sigma_{SL})$ versus t for the decay (*3*, *4*): P_{H_2} = (*1*) 0.088; (*2*, *4*) 0.011, and (*3*) 0.22 vol %; T = 370 K; $d_{Pd} \approx 2.5$ nm.

2. Planar Conductivity and Photoconductivity

The data for the hydrogen effect in the gas-sensor mode on the dark conductivity σ_n reduced to the surface conductivity and on the photoconductivity σ_L of the planar structures at 370 K are listed in the table.

It is obvious from the table that the hydrogen reduces the planar photoconductivity of the GaAs layers coated with the Pd layer and scarcely affects (increases only slightly) the dark conductivity. The largest relative change in photoconductivity is observed for the layers with a low density of carriers when the Pd layer thickness $d_{Pd} \approx 2.5$ nm.

The decrease in the planar PC under exposure to hydrogen is reasonably explained by the barrier mechanism of PC in GaAs layers [8]. The atomic hydrogen appearing at the Pd islands due to catalytic reaction [1] penetrates through the oxide layer to the GaAs surface and reduces the negative charge at surface states via chemisorption, which results in the reduction of the surface barrier height and barrier PC. The logarithmic dependence of the photoconductivity of the layers on the illumination intensity L ($\sigma_L \sim \log L$) is evidence in favor of the barrier mechanism [8].

3. Gas-Sensor Characteristics

Figure 3 presents the dependences of the steady-state PC response $\Delta\sigma_{SL}$ for the planar structure and those of the photovoltage ΔV_L for the diode structure on the hydrogen concentration at 370 K. At a low concentration, these dependences are logarithmic, which corresponds to the heterogeneous hydrogen adsorption [1] and is typical of gas sensors based on Schottky diodes and MOS structures. The response leveling-off as the hydrogen concentration increases is explained by the filling of the adsorption centers. The detectible threshold concentration of hydrogen obtained through the extrapolation of $\Delta\sigma_L$ and ΔV_L dependences on $\log P_{H_2}$ for a planar structure is approximately two orders of

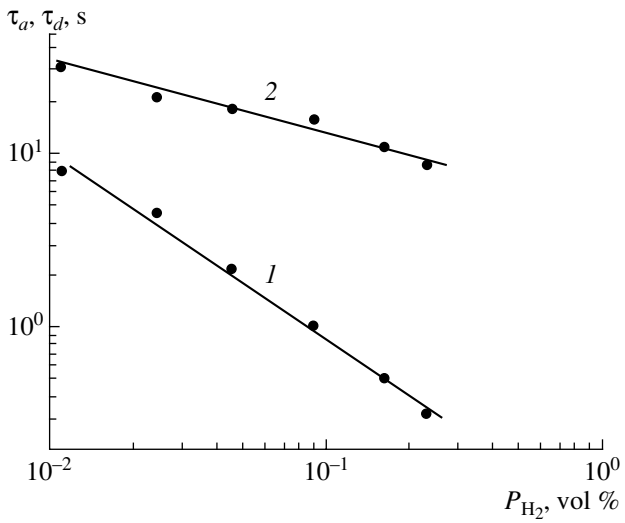

Fig. 5. Dependences of time of adsorption τ_a and desorption τ_d on P_{H_2} for planar structure: (*1*) corresponds to τ_a and (*2*) corresponds to τ_d. T = 370 K, $d_{Pd} \approx 2.5$ nm.

magnitude lower than that for a diode structure (compare curves *2* and *1*, respectively). It should be noted that this threshold value (~10^{-4} vol %) is of the same order of magnitude as for silicon diode structures [9].

The operation speed of planar structures at 370 K is characterized by the kinetic curves $\Delta\sigma_L$ measured under the pulsed exposure to hydrogen and shown in Fig. 4a. It follows from Fig. 4a that when the hydrogen flow is on, the steady-state $\Delta\sigma_{SL}$ value is attained and, when the hydrogen flow is off, the response essentially decreases to zero. Both the response rise and decay times depend on the hydrogen pressure and vary from 0.1 to 100 s, which corresponds to the characteristics of fast-response sensors [1, 2]. Analysis of the kinetic curves has shown that the response rises exponentially (Fig. 4b, curves *1*, *2*) and decays nonexponentially (Fig. 4b, curves *3*, *4*). The adsorption time τ_a (Fig. 5, curve *1*), which is determined from the response rising curve, varies in inverse proportion to hydrogen pressure and falls in the range 0.1–10 s at T = 370 K. The desorption time τ_d determined from the response decay curve at a level of 0.5 from the steady-state value has a weaker dependence on pressure ($\tau_d \sim 1/\sqrt{P_{H_2}}$).

CONCLUSION

We have shown that photoresistor GaAs/InGaAs QW heterostructures with a discontinuous Pd layer on the anodically oxidized surface are promising as hydrogen sensors. Beneath the island Pd layer, the defect-formation rate is considerably lower in such structures than that beneath a continuous Pd layer. We have demonstrated the possibility of passivating defects in a QW by incorporating atomic hydrogen through the island Pd layer into these structures.

ACKNOWLEDGMENTS

This study was supported by the Russian Ministry of Education under the program “Universities of Russia” (grant no. 015.06.01.37), by a joint program of the Russian Ministry of Education and CRDF (BRHE, REC-001), and by the Russian Foundation for Basic Research (project no. 00-02-17598).

REFERENCES

1. A. V. Evdokimov, M. I. Mushuli, A. E. Rzhanov, *et al.*, Zarubezhn. Élektron. Tekh., No. 3 (321), 3 (1988).
2. S. V. Tikhov, V. P. Lesnikov, V. V. Podol’skiĭ, *et al.*, Zh. Tekh. Fiz. **65** (11), 120 (1995) [Tech. Phys. **40**, 1154 (1995)].
3. V. I. Gaman, M. O. Duchenko, and V. M. Kanygina, Izv. Vyssh. Uchebn. Zaved., Fiz., No. 1, 69 (1998).
4. I. A. Karpovich, S. V. Tikhov, E. L. Shobolov, *et al.*, in *Proceedings of the International Conference “Fundamental Problems in Physics”* (Saratovs. Gos. Univ., Saratov, 2000), pp. 92–93.
5. I. A. Karpovich, A. V. Anshon, N. V. Baĭdus’, *et al.*, Fiz. Tekh. Poluprovodn. (St. Petersburg) **28**, 104 (1994) [Semiconductors **28**, 63 (1994)].
6. I. A. Karpovich, A. V. Anshon, and D. O. Filatov, Fiz. Tekh. Poluprovodn. (St. Petersburg) **32**, 1089 (1998) [Semiconductors **32**, 975 (1998)].
7. L. M. Krasil’nikova, I. V. Ivonin, and M. P. Yakubenya, Izv. Vyssh. Uchebn. Zaved., Ser. Fiz., No. 3, 60 (1989).
8. I. A. Karpovich, B. I. Bednyĭ, N. V. Baĭdus’, *et al.*, Fiz. Tekh. Poluprovodn. (Leningrad) **23**, 2164 (1989) [Sov. Phys. Semicond. **23**, 1340 (1989)].
9. G. G. Kovalevskaya, M. M. Meridov, E. V. Russo, *et al.*, Zh. Tekh. Fiz. **63** (2), 185 (1993) [Tech. Phys. **38**, 149 (1993)].

Translated by M. Lebedev

Technical Physics, Vol. 47, No. 10, 2002, pp. 1272–1276. Translated from Zhurnal Tekhnicheskoĭ Fiziki, Vol. 72, No. 10, 2002, pp. 67–72.

OPTICS, QUANTUM ELECTRONICS

Development of Methods for Multidimensional Measurements in the Optical Investigation of Surface

A. I. Rodionov, B. V. Zubkov, A. P. Kalinin, V. N. Lyubimov, A. F. Osipov, I. D. Rodionov, I. P. Rodionova, and I. B. Shilov

Institute for Problems in Mechanics, Russian Academy of Sciences, Moscow, 119526 Russia

e-mail: kalinin@ipmnet.ru

Received November 22, 2001; in final form, February 27, 2002

Abstract—The problems of developing methods for multidimensional (multichannel) data acquisition as applied to the optical study of the surface are considered. Unlike conventional methods of transition to multidimensional measurement, which employ mechanical scanning, the use of new-type instruments that allow for coordinate-sensitive and time measurements are discussed. Both the sensitive elements (detectors) and the instruments (hyperspectrometers) created for multidimensional coordinate–spectrum–time measurements are described. The application of hyperspectrometers makes it possible to increase manyfold the information content of measurements. The fluorescence of dye molecules deposited on the surfaces of germanium and silicon preirradiated by a laser beam is studied. The scattering spectra from these samples are examined. © *2002 MAIK "Nauka/Interperiodica".*

INTRODUCTION

When studying many physical phenomena, the transition from measurements of some property at a point of the space to multidimensional (multichannel) measurements is a challenge. An example of such a transition is the measurement of double-differential scattering cross sections (angular and energy cross sections) for molecular beams [1]. Usually, a detector with a very small aperture is used to measure the intensity of a molecular beam scattered at a certain angle and the energy of its particles [2]. The transition from one-dimensional to multidimensional measurements in this case is performed by mechanically scanning the detector over various scattering angles of the beam. The disadvantage of this approach is obvious: the use of a detector with a pointlike aperture drastically deteriorates the statistics of measurements and substantially increases the measurement time. Any mechanical scanning (especially one-dimensional scanning) makes the study of anisotropic processes difficult and imposes extremely stringent (often unachievable) requirements on the stability of the system components. Actually, an improvement of the measurement accuracy in this approach (by a decrease in the detector aperture) leads to a quadratic decrease in the counting rate and to a corresponding lengthening of the experiment time. Moreover, when using mechanical scanning, the time variation of the parameters of an experimental setup imposes strict restrictions on improving the measurement accuracy by decreasing the detector aperture. For the same reason, correlation measurements with several pointlike apertures are made difficult. Similar problems also appear in optical studies of surface, which are finding ever-widening application in micro- and nanotechnologies.

Multidimensional (multichannel) measurements of differential scattering cross sections have been touched upon in [3], where the double-differential scattering cross sections of molecular beams scattered at small angles were measured. In this work, we study the surface inhomogeneity of semiconductors by the dye probe method to elucidate the possibility of the transition from point (0D) to two-dimensional (2D) and then to multidimensional (ND) measurements. To date, studies of surface states by the molecular probe method have already become classical. Instruments for such studies are usually based on a pair of monochromators that allow one to measure the fluorescence intensity at a wavelength λ_1 for an illumination wavelength λ_2 at one point in the parameter space.

The transition from 0D to ND measurements in the space of data is usually performed by the mechanical scanning of both the sample and the settings of the monochromator. The disadvantage of this approach is the necessity of making a wealth of measurements for all parameters of interest. Moreover, mechanical scanning always implies a backlash in the motor (e.g., in changing the coordinate) or another cause of inaccuracy in positioning the point of observation. Within the time taken to go from one point to another in the coordinate or wavelength space, undetected changes in other parameters influencing experimental results may occur. Therefore, at different points, the measurements are virtually made under different conditions. Note that the noise of photosensitive devices (PSDs) used in 0D

1063-7842/02/4710-1272$22.00 © 2002 MAIK "Nauka/Interperiodica"

measurements concentrates at a point of measurement and limits the sensitivity of a technique.

We elaborate upon this classical fundamental approach by replacing mechanical scanning by the use of new-type detectors that enable coordinate-sensitive and time measurements. Such an elaboration is possible owing to modern computer facilities allowing for real-time processing of huge data arrays.

The basic aim of this work is the development of next-generation PSDs that differ from conventional single-channel PSDs in that they have 2D and time resolutions. The use of such photodevices made it possible to create so-called hyperspectrometers for multidimensional studies. According to the currently accepted terminology, hyperspectral measurements are those performed simultaneously in a range from several hundreds to a thousand spectral channels and a hyperspectrometer is a device intended for the simultaneous measurement of spectral and spatial coordinates. These devices are also called videospectrometers. Their application enables the information content of experimental data to be increased by several orders of magnitude (depending on the PSD resolution) or significantly improves the sensitivity of the measurements.

The instruments were tested by investigating the surface inhomogeneity of semiconducting germanium preirradiated by a laser beam. Samples studied were Ge wafers repeatedly ($N = 10^3$–10^5) subjected to pulsed laser radiation of duration $\tau = 0.1$–1.0 μs, absorbed energy density $Q \sim 0.1$ J/cm^2, and beam radius ≈ 25 μm. The laser irradiation was carried out so that different areas of the sample were exposed to different radiation doses. Then, the sample thus treated was coated by a monomolecular film of rhodamine-*B* dye by placing it in a solution of rhodamine in ethyl alcohol for a given time.

EXPERIMENTAL INSTRUMENTS AND MEASURING TECHNIQUES

We created two instruments with different sensitive elements (detectors). The former is a hyperspectrometer based on an image-intensifier tube (IIT) where the signal is picked up by a charge-coupled device (CCD). In essence, it is a very sensitive videospectrometer. This instrument displays 2D videoinformation: the *X* axis is the coordinate of a narrow stripe on the sample along which the radiation dose varies, the *Y* axis is the radiation wavelength λ, and the *Z* axis is the intensity specifying the spectral density. In other words, we record a set of coordinate-swept spectra.

Thus, the instrument makes it possible to perform measurements at several hundreds of thousands of points in the coordinate–wavelength space per second. Simultaneous measurement over the whole length of the sample, along which its characteristics vary, gives the exact radiation distribution undistorted by mechanical scanning. For the case when the properties of the sample vary along another axis as well, provision is made for mechanical scanning over a narrow stripe along the other coordinate of the sample. This allows us to image the whole sample in the hyperspectrum.

However, the property of signal accumulation, which is an advantage of the IIT + CCD configuration as a detector of relatively strong signals, turns out to be a disadvantage for investigating ultraweak signals and the time characteristics of the fluorescence signal.

With statistical methods, we can go beyond the dynamic range of CCDs, which does not exceed 100 for series-produced CCDs and achieves 1000 for commercially available application-specific CCDs. It can be raised by two orders of magnitude for 7 min owing to accumulation.

The second modification is a hyperspectrometer based on an original time- and position-sensitive detector (TPSD) from the Reagent Research & Development Center [4]. This device can detect individual photons, find their 2D coordinates in the detection plane, and determine the photon arrival time with an accuracy as high as 40 ps (in the most precision experiment). The design of the TPSD will be considered below.

The use of the TPSD as a sensitive element gives a new property to the hyperspectrometer on its basis, namely, the possibility of detecting weak signals against the background of stronger ones with intensities several orders of magnitude higher than those of the former, since the dynamic range of the TPSD is extremely large (1–10^6 l/s).

The TPSD-based device can serve as the videospectrometer described above and also makes it possible to gain three-parameter information. The third parameter is the time delay between the instance of the sample-illuminating pulse application and the instance of photon detection (the other two are the photon coordinates in the detection plane). Thus, the advantages of the approach using the TPSD over all other approaches to studying fluorescence are the following:

(1) It is possible to perform time measurements with a step of 10^{-11} s.

(2) The photon counting rate of the TPSD achieves 10^6 l/s.

(3) The device is almost noiseless. The noise is as low as 10^{-3} l/s at an image point (pixel), which is negligibly small in comparison with the valid information flow.

(4) The new approach allows us to measure not only the spatial dependence of the spectra for inhomogeneous samples but also to find other coordinate dependences for homogeneous samples subjected to nonuniform effects of temperature, electric and magnetic fields, deformation, as well as laser and other radiations.

The new photosensitive devices, allowing the spatial and time resolution of incident radiation, differ from conventional ones in that they have microchannel plates

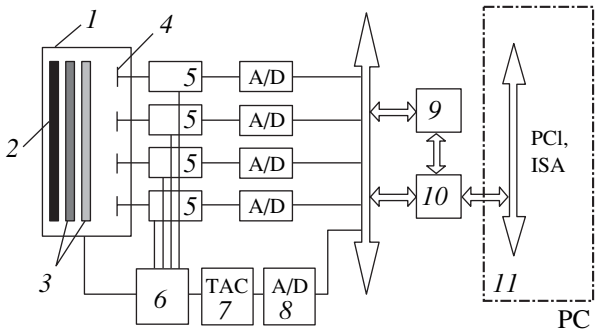

Fig. 1. Schematic diagram of the coordinate-sensitive photodetector: (*1*) metal-ceramic vacuum chamber; (*2*) photocathode; (*3*) microchannel plates (chevron); and (*4*) multianode collector. Numerical subsystems of the detector: (*5*) digital–analog processor; (*6*) time channel (electronics assigning exact arrival time to each photon); (*7*) time-to-amplitude converters; (*8*) analog-to-digital converters; (*9*) signal processor; (*10*) interface unit; and (*11*) personal computer.

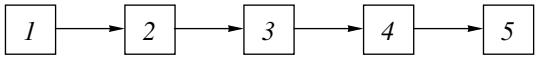

Fig. 2. Schematic diagram of the instrument: (*1*) radiation source; (*2*) fluorescence cell; (*3*) mechano-optical unit; (*4*) detector; (*5*) computer.

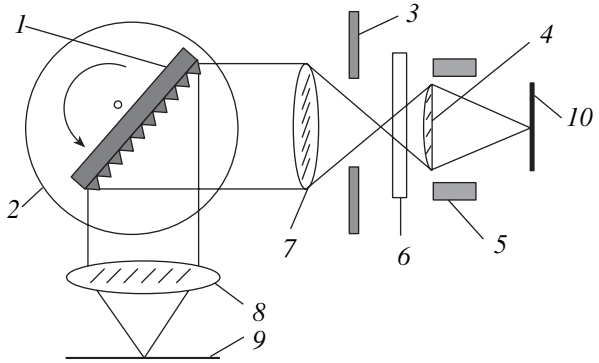

Fig. 3. Schematic diagram of the mechano-optical unit: (*1*) mirror or diffraction grating; (*2*) turntable; (*3*) adjustable slit; (*4*) entrance objective lens; (*5*) lens hood; (*6*) replaceable filters; (*7*) second objective lens; (*8*) exit objective lens; (*9*) image plane; and (*10*) sample plane.

that multiply photoelectrons and a special electron collector that determines the coordinates of individual photons at the photocathode input. The diagram of such a coordinate-sensitive photodetector, along with the analog-to-digital converter subsystems, is shown in Fig. 1. The TPSD modification described in [4] makes it possible to carry out synchronous measurements and provides a 6D data flow.

In this work, we used this approach to observe the fluorescence spectrum variation when the surface of the semiconductor is irradiated by a laser beam (the TPSD-based instrument detecting weak signals) and also to take the dispersion curve for the surface under the same laser treatment (the IIT-based setup detecting strong signals).

The schematic diagram of both the TPSD- and IIT-based hyperspectrometers is the same (they differ only in the detector they use) (Fig. 2). A 1-kW halogen lamp was used as a basic radiation source. In addition, we used a pulsed green laser with a wavelength of 532 nm, a pulse width of ≈20 ns, and a pulse-repetition rate of ≈5 kHz. We also used UV sources (a DDS-30 lamp and a sunlamp), as well as a monochromator with a calibrated broadband lamp.

A fluorescence cell represents a closed volume protected against stray light and containing a sample placed on an *x–y* table. The cell can work in two modes.

(1) The cell has two windows; one is an entrance window with a filter that transmits only the exciting component of the radiation from the source. A broad uniform beam illuminates the sample at an angle $\Theta = 45° \pm 10°$ to the sample plane.

(2) The 1-kW halogen lamp is placed near the cell. A light guide 1 cm in diameter is brought to the lamp. It sustains a peak power of up to 1 MW in a pulse and can be placed close to the emitting surface of the lamp. The diameter of individual fibers of the light guide is 5 μm. The end of the light guide is equipped with a 530-nm interference filter. The light guide is placed immediately adjacent to the sample.

With the UV radiation used for the excitation of fluorescence, the illumination may be incident perpendicularly to the sample. This is achieved with a glass plate inserted in the cell that reflects the UV radiation toward the sample by one its side and transmits visible fluorescence radiation.

The mechano-optical unit consists of the following elements (Fig. 3):

(1) An entrance objective. The sample studied is located at its front focus, and a vertical adjustable calibrated slit is located at its back focus. The slit width can be continuously adjusted from 10 μm to 0.4 mm, is placed parallel to the sample, and cuts a narrow strip (up to 10 mm wide) from the sample image along the *X* axis.

(2) Another objective lens. The calibrated adjustable slit is at its front focus, and its back focus extends to infinity. As a reflecting surface, a mirror or a diffraction grating with lines directed parallel to the entrance slit can be used. The diffraction grating decomposes the image into spectra along the axis perpendicular to the slit axis. The reflecting surface is mounted onto a rotatable platform.

(3) An exit objective lens. Its front focus extends at infinity, and the surface of the photon detector is at its back focus. The mechano-optical unit projects the image spectrum vs. the *X* coordinate along the stripe onto the surface of the detector. In this way, a continuous three-dimensional picture in the coordinates

"wavelength–coordinate of the stripe along the sample axis–radiation intensity" is recorded. We use a diffraction grating with 300 lines per 1 mm, which projects a spectral range of 0.4–0.7 μm onto the surface of the PSD. To eliminate background light, protective blackened shields were mounted. The opacity of the shields was checked by completely closing the slit and measuring the background intensity with the radiation source on and off.

The measuring technique based on the hyperspectrometer equipped with detectors built around the IIT and TPSD is described in detail elsewhere [5]. Note that calibration can be carried out by various methods using both objects with a given calibrated shape and a monochromator; the absence of background light is checked.

Below, we present several results obtained with our instrument.

EXPERIMENTAL RESULTS

The setup with the TPSD-based detector was used to measure the fluorescence hyperspectrum of rhodamine deposited on a germanium sample preirradiated by a laser beam, as was described in the Introduction. The sample was illuminated by 530-nm-wavelength radiation.

As an example, Fig. 4 shows the three-dimensional fluorescence spectrum of the Ge sample coated by rhodamine-*B*.

The hyperspectrum recorded was separated into spectra corresponding to sample regions variously treated by the laser radiation. To determine the irradiation dose, we introduced a measure *W* of sample damage that is related to the absorbed energy *Q*. Figure 5 shows the fluorescence spectra of regions exposed to different doses (*Q* in arbitrary units). From these spectra, one can gain information on the dose dependence of the fluorescence intensity maximum, FWHM, etc.

It is seen from Fig. 5 that the increase in the lasing intensity quenches the fluorescence possibly because of energy transfer to the solid [6]. We can also draw the conclusion that the FWHM of the spectra increases with irradiation intensity, which is likely to be due to the inhomogeneity of the surface and the various states of adsorbed molecules [7].

The instrument equipped with the IIT-based detector was used to take scattering spectra from Ge samples subjected to laser irradiation. For illumination, we used an incandescent lamp with the calibrated spectrum. Figure 6 shows the scattering spectra for regions of the sample variously damaged by the laser radiation.

These spectra show that the scattering intensity increases with the intensity of surface irradiation and, hence, with the concentration of surface defects. Based on the spectra recorded and knowing the lamp spectrum, we constructed dispersion curves (Fig. 7). Figure 7 demonstrates the dependence of the diffuse reflection factor on the wavelength of the incident light

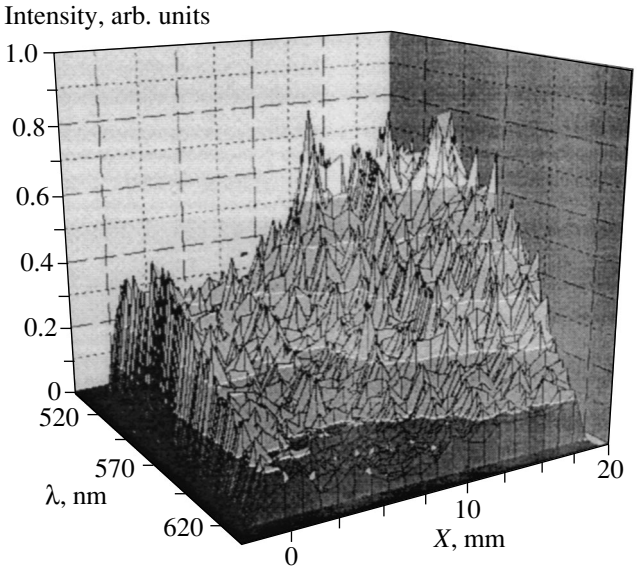

Fig. 4. Fluorescence hyperspectrum from the Ge sample coated by rhodamine-*B*. The height corresponds to the intensity.

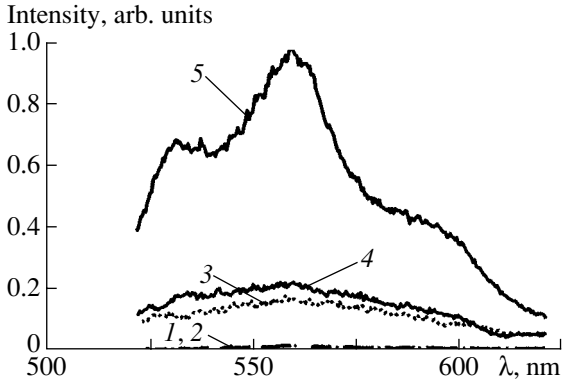

Fig. 5. Fluorescence spectra from variously irradiated regions of the germanium sample: (*1*) $W_1 = 240$; (*2*) $W_2 = 190$; (*3*) $W_3 = 115$; (*4*) $W_4 = 87$; and (*5*) $W_5 = 70$.

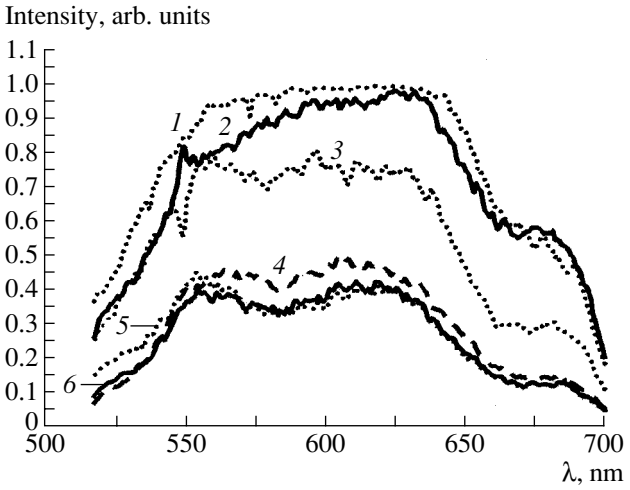

Fig. 6. Scattering spectra for variously irradiated regions of the germanium sample: (*1*) $W_1 = 240$; (*2*) $W_2 = 190$; (*3*) $W_3 = 115$; (*4*) $W_4 = 87$; (*5*) $W_5 = 70$; and (*6*) $W_6 = 0$.

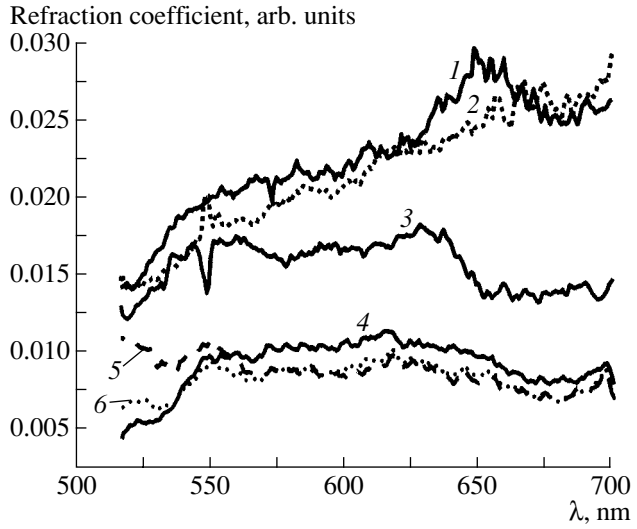

Fig. 7. Dispersion curves for variously irradiated regions of the Ge sample. For (*1*–*6*), see Fig. 6.

for regions exposed to various irradiation doses. It was found that the shape of the spectral dispersion curve strongly depends on the surface damage. Geometrically, this fact can be attributed to the formation of surface lines similar to those forming a diffraction grating. Accordingly, these lines cause interference effects that redistribute the reflection spectra.

CONCLUSION

The experimental study of the fluorescence properties of the material exhibited the possibility of multidimensional (multichannel) data acquisition.

Unique instruments for 2D hyperspectral measurements to study spatially nonuniform spectral characteristics of the surfaces were created. Their modifications employ various photonic devices.

A measuring technique that allows one to rapidly take the spectra of reflected and fluorescence radiations from a stripe separated on the sample surface and process them in selected regions was developed.

A software package for controlling the instrument and processing experimental results was devised.

The method of hyperspectral analysis was used to visualize the three-dimensional dependences of the fluorescence spectra and scattering spectra on the surface damage.

Owing to multidimensional data acquisition, the instrument and the software make it possible to greatly accelerate the measurement of the spectral characteristics of samples and gain information that is unattainable using conventional unidimensional systems.

ACKNOWLEDGMENTS

This work was supported in part by the Russian Foundation for Basic Research (projects no. 97-03-33741a and 99-02-82007).

REFERENCES

1. A. P. Kalinin, D. Yu. Dubrovitskiĭ, V. A. Morozov, *et al.*, Khim. Fiz. **19** (7), 8 (2000).
2. V. B. Leonas, Usp. Fiz. Nauk **107** (1), 29 (1972) [Sov. Phys. Usp. **15**, 266 (1972)].
3. D. Yu. Dubrovitskiĭ, A. P. Kalinin, and V. A. Morozov, Preprint No. 591, Inst. Problem Mekh. Ross. Akad. Nauk (Institute of Problems of Mechanics, Russian Academy of Sciences, Moscow, 1997).
4. I. D. Rodionov, A. I. Rodionov, and I. B. Shilov, Nucl. Instrum. Methods Phys. Res. A **471**, 239 (2001).
5. A. I. Rodionov, S. V. Vintsents, A. P. Kalinin, *et al.*, Preprint No. 685, Inst. Problem Mekh. Ross. Akad. Nauk (Institute of Problems of Mechanics, Russian Academy of Sciences, Moscow, 2001).
6. S. V. Vintsents, V. F. Kiselev, L. V. Levshin, *et al.*, Dokl. Akad. Nauk SSSR **274**, 96 (1984).
7. V. B. Zaĭtsev, Candidate's Dissertation (Moscow State Univ., Moscow, 1991).

Translated by K. Shakhlevich

Technical Physics, Vol. 47, No. 10, 2002, pp. 1277–1282. Translated from Zhurnal Tekhnicheskoĭ Fiziki, Vol. 72, No. 10, 2002, pp. 73–78.

OPTICS, QUANTUM ELECTRONICS

Laser Diagnostics of Ultrasonic Outgassing of an Insulating Liquid

Gen. M. Mikheev, Geor. M. Mikheev, E. G. Fateev, and A. Yu. Popov

Institute of Applied Mechanics, Ural Division, Russian Academy of Sciences, Izhevsk, 426000 Russia

e-mail: mikheev@udmnet.ru

Received February 13, 2002

Abstract—The efficiency of hydrogen evolution from transformer oil into a vacuum and into air under normal pressure is studied for the case when the oil is exposed to focused ultrasonic radiation. The study is performed by the method of spectroscopy of biharmonic-pumping coherent anti-Stokes Raman scattering (CARS) based on stimulated Raman scattering (SRS). Ultrasonic radiation at a frequency of 1.76 MHz is excited by a spherical piezoceramic transducer mounted on the bottom of the vessel and is focused on the surface of the oil. This causes the intense stirring of the oil with the formation of a fountain. The room-temperature diffusion coefficient of hydrogen in the transformer oil, 10^{-7} m^2/s, is found by approximating experimental data by a theoretical relationship for hydrogen evolution into air. It is shown that ultrasonic radiation with a power density of 2.2 kW/m^2 accelerates diffusion processes ten- to fifteen-fold. © *2002 MAIK "Nauka/Interperiodica".*

INTRODUCTION

It is known that gases dissolved in an insulating liquid (IL) can be extracted by evacuation into a vacuum under reduced ambient pressure [1]. Air dissolved in water is usually removed by means of thermal deaeration, where the water is heated to a temperature exceeding the boiling point corresponding to the pressure in the working zone of a deaerator [2]. Some gases can be removed from water by chemical methods. For example, the removal of carbon dioxide is accomplished by combining the gas with reagents (ammonia, an alkali, or sodium silicate) introduced into the solution [3]. It has been suggested [4] that gases may be extracted by convection arising when the liquid is irradiated by low-intensity microwaves. Finally, dissolved gases can be extracted from liquids ultrasonically [5].

Outgassing efficiency is usually estimated with chromatographic analysis. When the amount of dissolved gases in an IL is determined by direct vapor analysis with the use of a chromatograph, the gases are extracted by shaking the sample at regular intervals until thermodynamic equilibrium sets in [6]. However, the chromatographic method, based on the separation of the gas sample into components with a chromatography column [7], makes the real-time observation of liquid outgassing impossible. Therefore, an alternative method of express diagnostics of liquid ultrasonic outgassing would be of great interest.

In this work, we demonstrate that the laser spectroscopy of SRS-based CARS with biharmonic laser pumping (BLP) can be used for studying hydrogen evolution from an IL exposed to a focused ultrasonic radiation.

SRS-BASED CARS DIAGNOSTICS OF HYDROGEN EVOLUTION

CARS is a four-photon parametric process where a coherent beamed radiation with an anti-Stokes frequency $\omega_a = 2\omega_p - \omega_s$ is generated by mixing two laser beams at frequencies ω_p and ω_s in a medium with a cubic nonlinear susceptibility $\chi^{(3)}$ [8]. As applied to the diagnostics of hydrogen in a gaseous mixture, the essence of the method is as follows. A gaseous mixture is probed by biharmonic laser pumping with frequencies ω_p and ω_s roughly meeting the resonance condition

$$\omega_p - \omega_s \approx \Omega_\rho, \tag{1}$$

where Ω_ρ is the frequency of the Raman transition $Q_{01}(1)$ of hydrogen that is present in the gaseous mixture of density ρ.

The radiation intensity I_a at the frequency ω_a is given by

$$I_a \sim \left|\chi^{(3)R} + \chi^{(3)NR}\right|^2 I_p^2 I_s, \tag{2}$$

where I_p and I_s are the intensities at the frequencies ω_p and ω_s, respectively; $\chi^{(3)R} = c_{H_2}\gamma_r$ is the resonant cubic susceptibility of gas molecules; $\chi^{(3)NR} = c_{BG}\gamma_{nr}$ is the nonresonant cubic electron-related susceptibility associated largely with buffer gas molecules participating in an scattering event; γ_r and γ_{nr} are the cubic hyperpolarizabilities of hydrogen molecules and buffer gas molecules, respectively; and c_{H_2} and c_{BG} are the molecular concentrations of the hydrogen and buffer gas, respectively.

The resonant cubic susceptibility $\chi^{(3)R}$ is given by [9]

$$\chi^{(3)R} = \frac{1}{3}\Delta_k^n \frac{2\pi c_{H_2} c^4}{\pi\Gamma\omega_s^4}\frac{d\sigma}{do}\frac{\Gamma}{\Omega_\rho - (\omega_p - \omega_s) - i\Gamma}, \quad (3)$$

where Γ is the half-width of the Raman-active transition line, Δ_k^n is the difference in the level populations, and $d\sigma/do$ is the molecular cross section of spontaneous Raman scattering (SpRS) for this transition.

From (3), it follows that the value of $|\chi^{(3)R}|$ decreases noticeably if $|\Omega_\rho - (\omega_p - \omega_s)| \gg \Gamma$. This means that the intensity I_a depends mostly on scattering by an impurity being detected when condition (1) is met.

It was shown [10] that if the CARS method is applied for detecting a small amount of hydrogen (small c_{H_2}) in a gaseous mixture of constant density ρ, when condition (1) is satisfied and the nonresonant scattering by buffer gas molecules can be neglected, one can use the relationship

$$c_{H_2} = \frac{1}{b_a}\left(\frac{I_a}{I_p^2 I_s}\right)^{1/2}(\Gamma_\rho^2 + \Delta\omega_\rho^2)^{1/2}, \quad (4)$$

where b_a is a dimensional coefficient, Γ_ρ is the half-width of the hydrogen molecule transition line at a gaseous mixture density ρ, and $\Delta\omega_\rho = (\omega_p - \omega_s) - \Omega_\rho = \Omega_g - \Omega_\rho$.

In gaseous mixtures, the half-width Γ_ρ of hydrogen molecules depends on the Dicke collisional narrowing [11] and $\Delta\omega_\rho$ may vary with ρ. If, however, the density ρ is constant, the values of Γ_ρ and $\Delta\omega_\rho$ are fixed; hence, the concentration c_{H_2} can be determined by measuring the radiation intensities at the frequencies ω_a, ω_p, and ω_s. BLP simultaneously satisfying conditions (1) and $\Delta\omega_\rho$ = const can be found by applying the SRS method to compressed hydrogen, for example, with the vibrational transition $Q_{01}(1)$ [12–15]. In this case, the laser part of the equipment is greatly simplified [15].

LIQUID OUTGASSING IN THE FIELD OF FOCUSED ULTRASOUND

It is known that ultrasonic energy (momentum) losses generate so-called radiative force [16]. Due to this force, a liquid jet (fountain) may appear over the focal plane of a spherical ultrasonic vibrator, intensely stirring and thus outgassing the liquid. Moreover, with a focused ultrasonic radiation, the acoustic pressure amplitude is spatially nonuniform (gradient). In the field of such an acoustic wave, gas bubbles experience the action of the Bjerknes force [17, 18]:

$$\mathbf{F}_B = -\langle V\nabla P\rangle, \quad (5)$$

where V and P are the instantaneous values of the bubble volume and acoustic pressure, respectively, averaged over the vibration period.

Under the action of this force, the bubbles migrate toward the higher pressure zone, which is in the focal region if the ultrasonic radiation is focused [19]. Consequently, gas inclusions coming to this region under the action of the Bjerknes force will be rejected into the environment together with the fountain, and the liquid outgassing will become more vigorous. However, sufficiently intense acoustic waves may activate chemical reactions [5], such as the decomposition of the IL with the formation of hydrogen, methane, acetylene, etc. [20]. Therefore, IL outgassing *per se* should proceed at moderate ultrasonic intensities.

EXPERIMENTAL

The simplified experimental scheme is depicted in Fig. 1. Spherical piezoceramic transducer *1* is mounted on conductive support *2* with glass vessel *3*. The transducer, which is connected to rf generator *4* (~27 V, 1.76 MHz), excites acoustic vibrations in liquid *5*. The ultrasonic radiation propagating in the liquid is focused on its surface and produces fountain *6*, which disintegrates into droplets. The scheme allows for the creation of a rarefied area above the liquid with fore pump *7* before the ultrasonic radiation is generated. Valve *8* shuts off the fore pump from the rarefied area during the measurements. Hydrogen evolving from the liquid passes through tube *9* to measuring cuvette *10* with optical windows and is detected at regular intervals by the SRS–CARS method. To this end, the second harmonic of single-active-element single-frequency YAG : Nd^{3+} laser *11* [21] was used. The peak energy of a laser pulse at a wavelength of 532 nm was 40 mJ; the pulse half-width, τ_p = 7 ns; and the divergence, about 0.6 mrad. The pulse energy was varied between 15 and 20 mJ. Lens *12* (F_1 = 0.66 m) focuses the laser output on SRS cuvette *13* (L_1 = 0.86 m) containing compressed molecular hydrogen of density 2.8 Amagat. BLP arising in cuvette *13* from SRS by the vibrational transition $Q_{01}(1)$ is collimated by lens *14*, is separated from other SRS components with a set of filters *15* (*18*), and is focussed on measuring cuvette *10* (L_2 = 0.21 m) with objective lens *16* (F_2 = 0.13 m). The anti-Stokes component, which arises in cuvette *10* because of CARS, is applied to monochromator *19* through lens *17*. Then, the signal is recorded with a photoelectric multiplier and multichannel laser-pulse-recording system *20*, which is interfaced with a PC. During recording, the signal is multiply averaged. The product $I_p^2 I_s$ entering into formula (4) is measured with an additional optical branch (omitted in Fig. 1) consisting of a reference measuring cuvette with hydrogen compressed to a density of 2.8 Amagat and an additional system for recording the anti-Stokes component [10].

Unlike the chromatographic method, the approach described above is in many respects selective and provides real-time observation of the kinetics of hydrogen evolution from the liquid phase.

The ultrasonic power N introduced into the liquid was estimated using the law of conservation of energy. The work spent on overcoming surface tension forces was neglected. It was assumed that the ultrasonic energy is completely converted to the energy of the liquid jet. Then [22],

$$N = (\pi/8)\rho_{liq} d^2 (2gh)^{3/2}, \quad (6)$$

where ρ_{liq} is the density of the liquid, g is the free-fall acceleration, h is the fountain height in a vacuum (Fig. 1), and d is the mean diameter of the fountain jet.

For d = 1.5 mm, h = 0.15m, ρ_{liq} = 880 kg/m^3, we have N = 4 mW. At the focus of transducer *1*, the ultrasonic power density is 2.2 kW/m^2. Such a value does not cause the chemical decomposition of ILs [22].

We studied hydrogen desorption from hydrogen-saturated oil. Saturation was accomplished as follows. First, some amount of hydrogen was introduced into the evacuated chamber containing the oil. Then, the chamber was exposed to ultrasonic vibration for 30 min. Under the action of ultrasound, the oil was vigorously mixed with gas-phase hydrogen. Then, the ultrasound was switched off, and, after the complete vibration relaxation, the hydrogen was removed from the chamber with the fore pump switched on for a short time.

KINETICS OF HYDROGEN EVOLUTION

The kinetics of hydrogen evolution from the transformer oil is illustrated in Figs. 2 (desorption in a vacuum) and 3 (under normal pressure). In a vacuum (Fig. 2, curve *1*), the gas may be desorbed spontaneously for some time. Under these conditions, the ultrasonic vibration greatly accelerates the gas evolution (Fig. 2, curve *2*). Data points $V_{H_2}(t)$ for gas evolution in Fig. 2 are well fitted by the function

$$V_{H_2} = V_{H_2}^{(0)}[1 - \exp(-t/\tau)], \quad (7)$$

where $V_{H_2}^{(0)}$ is the initial hydrogen volume in the oil sample normalized to normal conditions and τ is the characteristic time of gas evolution.

As follows from the experiments, the ultrasonic vibration cuts the characteristic time τ 3.9 times.

Under normal pressure in air, the desorption of the hydrogen from the oil is appreciably retarded (Fig. 3, the early portion of experimental plot *1*). However, as ultrasound is switched on at $t = t_1$, the hydrogen concentration c_2 in the measuring cuvette sharply rises. If the switching delay increases to t_2, the curve $c_2(t)$ shifts to the right along the time axis (Fig. 3, experimental plot *2*). The rate of growth of $c_2(t)$ in air changes noticeably some time after ultrasound has been switched on. This is attributed to the finite time t_D of hydrogen diffusion through tube *9* to optical measuring cuvette *10* (Fig. 1). As the air pressure decreases, t_D tends to the molecule transit time through the tube.

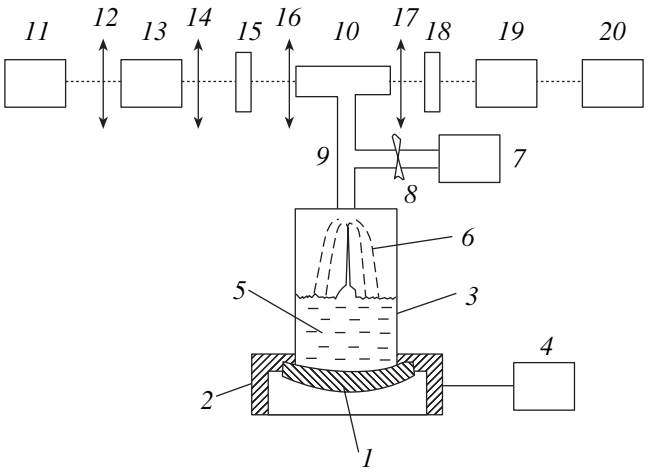

Fig. 1. Scheme of the experiment.

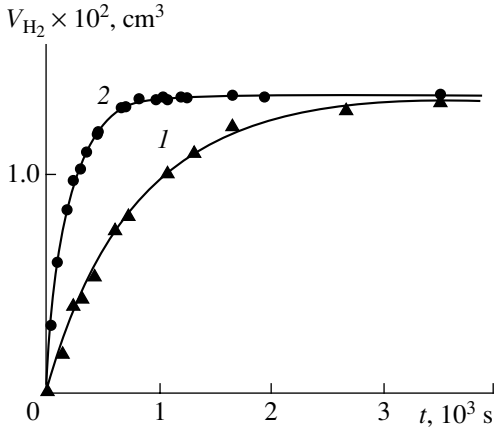

Fig. 2. Time dependence of the volume V_{H_2} of hydrogen that evolves from hydrogen-saturated GK transformer oil into the measuring cuvette (residual pressure 100 Pa): (*1*) spontaneous desorption and (*2*) ultrasonically stimulated desorption.

DIFFUSION COEFFICIENT OF HYDROGEN IN TRANSFORMER OIL

It is of interest to theoretically consider the evolution of hydrogen from the oil in order to explain the experimental dependences shown in Fig. 3. Let the total volume occupied by the vessel with the IL and by the measuring cuvette be a cylinder of cross section S (Fig. 4), with a part of the volume of height L being occupied by the liquid. Since the mean hydrogen concentration c_2 in the measuring cuvette is known from

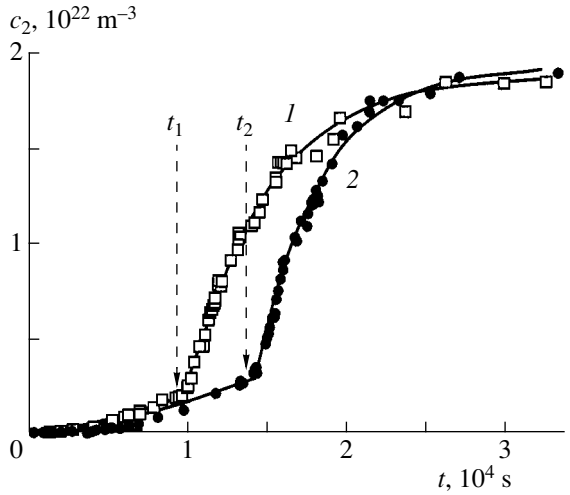

Fig. 3. Time dependence of the hydrogen concentration c_2 in the measuring cuvette when hydrogen is desorbed from the hydrogen-saturated GK transformer oil into the measuring cuvette in air under normal pressure. t_1 and t_2 are the time instants, at which the ultrasonic radiation is applied, which correspond to curves *1* and *2*, respectively, in Fig. 1. Solid lines are functions approximating data points for gas evolution.

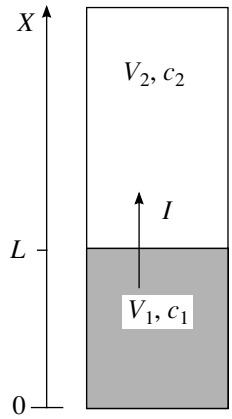

Fig. 4. Experimental geometry for the model problem.

the experiment, the diffusion coefficient of the hydrogen in the liquid will be found as follows.

Let the number of hydrogen molecules in the liquid be $N_0 = c_1(0)V_1$ at the initial time instant $t = 0$, where $c_1(0)$ is the initial hydrogen concentration in the liquid and V_1 is the volume of the liquid. According to the law of conservation, the number of gas molecules desorbed from a volume V_1, $N_1 = c_1V_1$, equals the number of molecules appearing in a volume V_2 over the liquid, $N_2 = c_2V_2$. Then, the amount of the gas in the volume V_1 at a time instant t is found from the relationship

$$c_1(t)V_1 = c_1(0)V_1 - c_2(t)V_2 \tag{8}$$

and the mean hydrogen concentration over the liquid measured in the experiment, from the formula

$$c_2(t) = [c_1(0) - c_1(t)](V_1/V_2). \tag{9}$$

The variation of the amount of gas molecules in the volume V_1 for a time dt is given by the kinetic equation

$$d[V_1c_1(t)] = -I(t)Sdt. \tag{10}$$

Here, $I(t)$ is the flow of a gas with a diffusion coefficient D_1 in the liquid through a surface area S. The flow $I(t)$ can be determined from the Fick law and is written in the form

$$\begin{aligned} I(t) &= D_1(\partial c/\partial x)_{x=L} \\ &= D_1[c_1(0,t) - c_1(L,t)]/L = D_1[c_1(t)]/L. \end{aligned} \tag{11}$$

The simplification in (11) reflects the fact that the hydrogen concentration at the bottom of the vessel differs essentially from that near the surface; that is, $c_1(0, t) \gg c_1(L, t)$. The explanation is as follows. The stirring of the liquid with dissolved hydrogen provides its uniform distribution in the volume V_1 with an average concentration $c_1(t)$. The remaining (undissolved) hydrogen over the liquid is rapidly pumped off. As a result of the latter procedure, the near-surface layer of the liquid is substantially degassed. This seems likely to be the basic reason for the relatively long time taken to set the steady-state process, as clearly seen from Fig. 3 for the two experimental dependences. Next, substituting (11) into (10) yields

$$d[c_1(t)]/dt = [-SD/V_1L]c_1(t). \tag{12}$$

A solution to this differential equation subject to the boundary condition $c_1(t)_{t=0} = c_1(0)$ has the form

$$c_1(t) = c_1(0)\exp(-t/\tau), \tag{13}$$

where

$$\tau = V_1L/SD_1 \tag{14}$$

is the relaxation time.

If an additional transfer mechanism emerges at some time instant t_1, Eq. (11) should be recast as

$$I(t) = \{D_1 + D_2\Theta(t - t_1)\}[c_1(t)]/L. \tag{15}$$

Here, D_2 is the diffusion coefficient with the additional transfer mechanism and $\Theta(t - t_1)$ is the Heaviside (switching) function:

$$\Theta(t - t_1) = \begin{cases} 0 & \text{for} \quad t < t_1 \\ 1 & \text{for} \quad t \geq t_1. \end{cases} \tag{16}$$

Then, Eq. (12) has the solution

$$c_1(t) = c_1(0)\exp[-(t/\tau_1 + (t - t_1)/\tau_2)], \tag{17}$$

where

$$\tau_1 = V_1L/SD_1, \quad \tau_2 = V_1L/[SD_2\Theta(t - t_1)]. \tag{18}$$

Eventually, we have

$$c_2(t) = c_1(0) \times [1 - \exp[-(t/\tau_1 + (t - t_1)/\tau_2)]](V_1/V_2). \quad (19)$$

Expression (19) was used for the nonlinear approximation of two sets of data points (Fig. 3) for the case when diffusion is ultrasonically accelerated at a time instant t_1.

The problem of nonlinear approximation was solved by using an algorithm for searching for the following four parameters: the diffusion coefficients D_1 and D_2 before and after switching on the ultrasonic radiation, respectively; the initial ($t = 0$) mean concentration $c_1(0)$ of the gas in the liquid; and the delay time t_1 of switching on the radiation (in order to refine the delay due to gas diffusion to the cuvette). The objective function to be minimized was the sum of the squared deviations of data points (Fig. 3) from the theoretical curve. As a result of the approximation, we also found the ratio of the diffusion coefficients before and after the radiation has been switched on. Moreover, we succeeded in finding the diffusion coefficient of hydrogen in the IL, using the known experimental geometrical values involved in the problem: $S = 5.726 \times 10^{-4}$ m^2, $L = 0.08$ m, $V_1 = 45.8 \times 10^{-6}$ m^3, and $V_2 = 85.7 \times 10^{-6}$ m^3. From the first set of data (experimental dependence *1* in Fig. 3), it follows that $D_1 = 0.96 \times 10^{-7}$ m^2/s, $D_2 = 1.4 \times 10^{-6}$ m^2/s, and $c_1(0) = 3.3 \times 10^{22}$ molecules/m^3. From the second set of data (experimental dependence *2* in Fig. 3), it follows that $D_1 = 1.1 \times 10^{-7}$ m^2/s, $D_2 = 1.1 \times 10^{-6}$ m^2/s, and $c_1(0) = 3.4 \times 10^{22}$ molecules/m^3. Note that these parameters do not depend on the gas volume over the liquid. The results obtained show that the ultrasonic vibration accelerates diffusion in the liquid ten- to fifteenfold.

Comparing the hydrogen diffusion coefficients found with known values in metals [23] and water solutions [24] indicates that the diffusion coefficients in transformer oil are two or three times higher. Since our SRS–CARS method is express, multiply averaged values of the hydrogen concentration in the measuring cuvette were determined every minute. Thus, it is hoped that our value of the diffusion coefficient of hydrogen in GK transformer oil was evaluated with a sufficiently high accuracy.

From the diffusion coefficient of hydrogen in an IL, one can estimate the lifetime of the nonequilibrium hydrogen concentration in the oil. It is known that, in high-voltage oil-filled equipment, a nonequilibrium hydrogen concentration may arise as a result of IL decomposition. Knowing the diffusion coefficient of hydrogen in oil, one can calculate the characteristic time of its spontaneous desorption from the liquid. Obviously, this time must correlate with the relaxation time for a given geometry of the liquid volume in a transformer. Let the geometrical parameters of a transformer be $S = 1$ m^2, $L = 1.2$ m, and $V_1 = 1.2$ m^3. Then, with our value of the diffusion coefficient without the ultrasonic effect, we get $\tau_1 = V_1 L/SD_1 = 1.44/10^{-7} \approx 10^7$ s or 115 days. Thus, the spontaneous relaxation of a nonequilibrium hydrogen concentration by diffusion proceeds rather slowly if convection and other desorption-promoting mechanisms are absent.

Based on our technique for measuring the diffusion coefficient of hydrogen in transformer oil, we proposed an efficient way of sampling transformer oil from high-voltage (500–700 kV) bushings for detecting oil-dissolved gases without switching-off the transformer [25].

CONCLUSION

The feasibility of a laser (SRS–CARS) method for monitoring the hydrogen content above an IL was demonstrated. It was shown that the rate of transformer oil outgassing can be substantially increased in both a vacuum and air under normal pressure by stirring the oil with focused ultrasonic radiation causing a fountain above its surface. The diffusion coefficient of hydrogen in transformer oil was determined.

ACKNOWLEDGMENTS

This work was financially supported by the Russian Foundation for Basic Research (project no. 01-02-96461).

REFERENCES

1. V. G. Arakelyan, Élektrotekhnika, No. 2, 8 (1994).
2. A. M. Bravikov, Élektr. Stn., No. 5, 25 (2001).
3. V. I. Sharapov and M. A. Sivukhina, Élektr. Stn., No. 3, 23 (2001).
4. B. G. Emets, Pis'ma Zh. Tekh. Fiz. **22** (8), 22 (1996) [Tech. Phys. Lett. **22**, 313 (1996)].
5. M. A. Margulis, *Foundations of Sound Chemistry* (Vysshaya Shkola, Moscow, 1984).
6. B. V. Ioffe, M. I. Kostkina, and A. G. Vitenberg, Zh. Prikl. Khim. **53**, 2280 (1980).
7. V. V. Brazhnikov, *Detectors for Chromatography* (Vysshaya Shkola, Moscow, 1992).
8. S. A. Akhmanov and N. I. Koroteev, *Methods of Nonlinear Optics in Spectroscopy of Light Scattering* (Nauka, Moscow, 1981).
9. A. F. Bunkin and S. G. Ivanov, Kvantovaya Élektron. (Moscow) **9**, 1821 (1982).
10. Gen. M. Mikheev, Geor. M. Mikheev, T. N. Mogileva, *et al.*, Kvantovaya Élektron. (Moscow) **32**, 39 (2002) [Quantum Electron. **32**, 39 (2002)].
11. W. K. Bischel and M. J. Dyer, Phys. Rev. A **33**, 3113 (1986).
12. P. R. Regnier and J. P. E. Taran, Appl. Phys. Lett. **23**, 240 (1973).
13. A. A. Ivanov, G. A. Polyakov, and V. B. Voronin, Izv. Akad. Nauk, Ser. Fiz. **57**, 165 (1993).

14. A. A. Ivanov, Opt. Spektrosk. **80**, 362 (1996) [Opt. Spectrosc. **80**, 318 (1996)].
15. G. M. Mikheev and T. N. Mogileva, Kvantovaya Élektron. (Moscow) **23**, 943 (1996) [Quantum Electron. **26**, 919 (1996)].
16. O. V. Rudenko, Vestn. Mosk. Univ., Ser. 3: Fiz., Astron., No. 6, 18 (1996).
17. L. A. Crum, J. Acoust. Soc. Am. **57**, 1363 (1975).
18. É. M. Agrest and G. N. Kuznetsov, Akust. Zh. **18**, 168 (1972) [Sov. Phys. Acoust. **18**, 143 (1972)].
19. T. V. Makarova and E. A. Gubernatorova, *Acoustics and Ultrasonic Technology: Republican Interdepartmental Scientific and Technical Collection* (Tekhnika, Kiev, 1991), No. 26, pp. 15–19.
20. V. G. Arakelyan, L. A. Dar'yan, and A. K. Lokhanin, Élektrichestvo, No. 5, 33 (1988).
21. G. M. Mikheev, D. I. Maleev, and T. N. Mogileva, Kvantovaya Élektron. (Moscow) **19**, 45 (1992).
22. Gen. M. Mikheev, Geor. M. Mikheev, G. P. Nekryachenko, and I. P. Gotlib, Pis'ma Zh. Tekh. Fiz. **24** (1), 79 (1998) [Tech. Phys. Lett. **24**, 36 (1998)].
23. R. M. Barrer, *Diffusion in and through Solids* (Cambridge University Press, Cambridge, 1941; Vysshaya Shkola, Moscow, 1984).
24. R. C. Reid, J. M. Prausnitz, and T. K. Sherwood, *Properties of Gases and Liquids* (McGraw-Hill, New York, 1977; Khimiya, Leningrad, 1982).
25. Geor. M. Mikheev, Gen. M. Mikheev, and V. K. Filippov, Élektr. Stn., No. 1, 39 (2001).

Translated by V. Isaakyan

Technical Physics, Vol. 47, No. 10, 2002, pp. 1283–1290. Translated from Zhurnal Tekhnicheskoĭ Fiziki, Vol. 72, No. 10, 2002, pp. 79–84.

OPTICS,
QUANTUM ELECTRONICS

Volume and Contact Photo-Emf in GaAs Adaptive Photodetectors

M. A. Bryushinin, V. V. Kulikov, and I. A. Sokolov

Ioffe Physicotechnical Institute, Russian Academy of Sciences,
Politekhnicheskaya ul. 26, St. Petersburg, 194021 Russia
e-mail: mikbr@mail.ru

Received April 9, 2002

Abstract—The generation of non-steady-state photo-emf in an adaptive photodetector made of semi-insulating GaAs is studied. Single- and double-frequency excitation modes are considered. It is found that a contact component of the photocurrent arises in the detector when the spatial frequencies of the interference pattern and phase modulation frequencies are low. The contact signal, being sensitive to a slow drift of the interference pattern, adversely affects the adaptive properties of the device. It is shown theoretically and confirmed experimentally that the contact emf signal at the frequency of basic phase modulation can effectively be suppressed by specially selecting the amplitude of additional phase modulation and the spatial frequency of the interference pattern. The spectral components of the non-steady-state emf signal are calculated for the double-frequency excitation mode. © *2002 MAIK "Nauka/Interperiodica".*

INTRODUCTION

To date, several devices for detecting optical phase-modulated signals have been developed [1, 2]. The basic difference between them is the design of the photodetector converting the variations of the interference pattern intensity to an electrical signal. The use of conventional photodiodes requires the operating point of the interferometer to be stable and the wave fronts of interfering beams to be tuned with an accuracy up to $\lambda/10$. This necessitates the introduction of extra optical and electrical components, which inevitably increases the cost of the system and makes it more difficult to use. A promising type of detector that allows one to avoid these problems is an adaptive photodetector based on the non-steady-state photo-emf effect [3].

The non-steady-state photo-emf effect [4] consists in the appearance of alternating current in a semiconductor crystal illuminated by an interference pattern of varying intensity (Fig. 1). The photocurrent is generated when the distribution of the photoconductivity and the electric field are periodically shifted relative to each other. The gratings of the conductivity and the space-charge field that emerge in the crystal because of the diffusion record mechanism [5] are dynamic. This shows up in the specific amplitude–frequency response of the non-steady-state emf: at low phase-modulation frequencies, the signal is proportional to the frequency, whereas for frequencies above the so-called cutoff frequency ω_0, the photocurrent reaches a maximum and then remains frequency-independent. Thus, an adaptive photodetector based on the non-steady-state emf effect makes it possible to effectively detect high-frequency phase-modulated optical signals and simultaneously suppress low-frequency signals due to a drift in the operating point of the interferometer, variations of the ambient temperature, and mechanical vibrations.

The adaptive properties of a photodetector employing the non-steady-state photo-emf effect are the most conspicuous in experiments on detecting the high-frequency signal in the presence of low-frequency large-amplitude jamming signals [6]. It has been found that the amplitude of the valid signal begins to decline appreciably only when the amplitude of a phase inter-

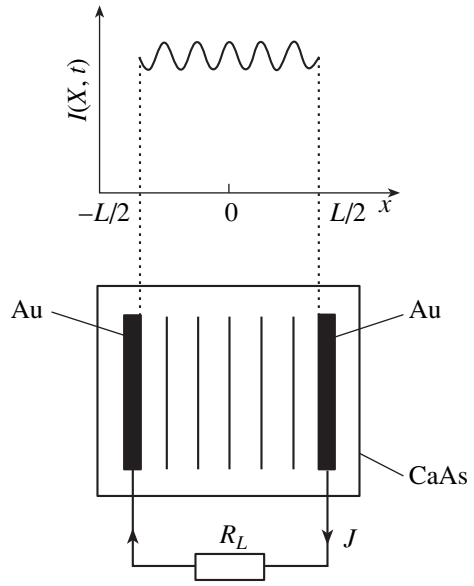

Fig. 1. Non-steady-state photo-emf excitation in a GaAs adaptive photodetector.

1063-7842/02/4710-1283$22.00

ference with a frequency Ω reaches the value of ω_0/Ω. This means that requirements imposed on the vibration isolation of the interferometer may be relatively loose if semiconductors with a high cutoff frequency are used. For example, for GaAs photodetectors with a typical cutoff frequency $\omega_0/2\pi \approx 1$ kHz and an interference frequency $\Omega/2\pi \approx 10$ Hz, the allowable interference amplitude is $\Delta \approx 100$ rad, which corresponds to the vibration amplitude of the interferometer mirrors $A = \lambda\Delta/4\pi \approx 5$ μm (at a wavelength $\lambda = 0.633$ μm).

The implementation of a photodetector with such properties needs the selection of a semiconductor that is optimal in terms of photoconductivity, carrier lifetime, mean diffusion length of carriers, etc. In addition, the fabrication of contacts with desired properties is a challenge in this case. Namely, the contacts must have a lower resistance compared with the bulk resistance of the crystal and the presence of a contact photo-emf is extremely unwanted. The low resistance of the contacts is necessary for efficient current removal into an external measuring circuit. This requirement is quite feasible, since the bulk resistance is very high when semi-insulating crystals with a large electrode spacing are used and may exceed the resistance of a rectifying contact.

The presence of the contact photo-emf adds the "photodiode" component to the total signal picked up from the photodetector. The photodiode component is sensitive to slow displacements of the interference pattern; in other words, the photodetector partially loses its adaptive properties. One way of tackling the problem [7] is to rotate the crystal through some angle so that the contacts are not parallel to interference fringes. In this case, the mean optical intensity in the near-contact regions remains nearly constant and the contact component of the current diminishes. However, such an approach is ineffective when the spatial frequencies of an interference pattern are low.

The aim of this work is the theoretical and experimental study of a non-steady-state photo-emf generated by single- and double-frequency techniques in an adaptive photodetector on semi-insulating GaAs. Emphasis is on the separation of the volume and the contact components of the signal.

THEORETICAL ANALYSIS

Our model of an adaptive photodetector built around the non-steady-state photo-emf effect is as follows. A sensor representing a photoconductor with two electrodes (Fig. 1) is illuminated by a variable (vibrating) interference pattern

$$I(x, t) = I_0\{1 + m\cos[Kx + \delta\cos(\omega t) + \Delta\cos(\Omega t) + \psi]\}. \quad (1)$$

Here, I_0 is the mean light intensity, m is the contrast, K is the spatial frequency, ψ is the initial phase of the interference pattern, δ and ω are the amplitude and frequency of basic phase modulation, and Δ and Ω are the amplitude and frequency of additional phase modulation. We will assume that

$$\omega \gg \Omega, \quad \delta \ll 1, \quad \Delta \approx 1. \quad (2)$$

This situation corresponds to the detection of a weak high-frequency signal in the presence of low-frequency high-amplitude jamming signals. Under such an illumination, a volume non-steady-state photo-emf J_V arises in the volume of the crystal and a contact (barrier-layer [8]) photo-emf, J_{C1} and J_{C2}, in the near-contact regions. Let the contacts be similar for simplicity. The bulk of the semiconductor has a resistance R, a capacitance C, and contacts R_C and C_C. The external circuit of the photodetector is terminated by a load resistance R_L. The equivalent circuit of the system is depicted in Fig. 2. The expression for the complex amplitude of the current with a frequency ω passing in the external circuit is given by

$$J^\omega = \frac{\dfrac{J_V^\omega R}{1 + i\omega RC} + \dfrac{(J_{C1}^\omega - J_{C2}^\omega)R_C}{1 + i\omega R_C C_C}}{R_L + \dfrac{R}{1 + i\omega RC} + 2\dfrac{R_C}{1 + i\omega R_C C_C}}. \quad (3)$$

Here, J_V^ω, J_{C1}^ω, and J_{C2}^ω are the complex amplitudes of the related currents. Other harmonics of the current are expressed similarly. Let the condition

$$\frac{R}{1 + i\omega RC} \gg R_L, \quad \frac{R_C}{1 + i\omega R_C C_C} \quad (4)$$

be fulfilled in a frequency range under consideration.

Then, expression (3) may be greatly simplified:

$$J^\omega = J_V^\omega + (J_{C1}^\omega - J_{C2}^\omega)\frac{R_C(1 + i\omega RC)}{R(1 + i\omega R_C C_C)}. \quad (5)$$

(1) Contact photo-emf. An expression for the contact signal $(J_{C1}^\omega - J_{C2}^\omega)$ can easily be derived under the assumption that the photocurrent is proportional to the light intensity in the near-contact region; that is, $J_{C1}(t) = \xi I(-L/2, t)$ and $J_{C2}(t) = \xi I(L/2, t)$, where L is the electrode spacing. The coefficient ξ depends on the effective surface area of the planar electrodes, light absorption coefficient, and quantum efficiency of photoconductivity [8]. In our case, we have

$$J_{C1}^\omega - J_{C2}^\omega = 4\xi I_0 m J_1(\delta) J_0(\Delta)\cos\psi\sin(KL/2). \quad (6)$$

Here, $J_n(x)$ is the nth-order Bessel function of first kind. For a harmonic at the nth side frequency, we come to a similar expression:

$$J_{C1}^{\omega + n\Omega} - J_{C2}^{\omega + n\Omega} = 4\xi I_0 m J_1(\delta) J_n(\Delta) \times \cos(\psi + n\pi/2)\sin(KL/2). \quad (7)$$

(2) Volume photo-emf. Let us derive an expression for the complex amplitude of the bulk signal at the carrier, J_V^{ω}, and side, $J_V^{\omega+n\Omega}$, frequencies. To do this, we will consider the general case of generating a non-steady-state photo-emf in an *n*-type semiconductor by an optical pattern,

$$I(x, t) = I_0\left[1 + \frac{m(t)}{2}\exp(iKx) + \frac{m^*(t)}{2}\exp(-iKx)\right]. \quad (8)$$

An expression for the photocurrent density can be written as [4]

$$J_V(t) = Se\mu n_0\frac{1}{4}[a(t)E_{SC}^*(t) + a^*(t)E_{SC}(t)]. \quad (9)$$

Here, e is the electron charge, μ and n_0 are the mobility and mean concentration of photoelectrons, $n_0a(t)$ is the complex amplitude of their space-periodic distribution, E_{SC} is the space-charge field, and S is the electrode area. Let us consider our problem assuming that the generation and recombination of charge carriers are linear, the contrast m is small, and the dark conductivity is low [5]. Also, we assume that the external and photovoltaic fields are zero. Then, the quantities $a(t)$ and $E_{SC}(t)$ are solutions to the set of linear differential equations

$$\begin{aligned}\frac{dE_{SC}}{dt} &= -\frac{1}{\tau_M}E_{SC} - \frac{iE_D}{\tau_M}a,\\ \frac{da}{dt} &= iK\mu E_{SC} - \frac{1 + K^2L_D^2}{\tau}a + \frac{m(t)}{\tau}.\end{aligned} \quad (10)$$

Here, E_D is the diffusion field, τ_M is the Maxwell relaxation time, τ is the electron lifetime in the conduction band, and L_D is the electron diffusion length. Substituting the solutions to this set into (9) yields for the photocurrent

$$J_V(t) = \frac{S\sigma_0E_D}{2\tau^2\tau_M(\lambda_1 - \lambda_2)}\mathrm{Im}\left(\int_0^{\infty} m(t-t')\exp(\lambda_1t')dt' \times \int_0^{\infty} m^*(t-t')\exp(\lambda_2t')dt'\right). \quad (11)$$

Here, λ_1 and λ_2 are the roots of the characteristic equation for set (10):

$$\lambda_{1,2} = -\frac{1}{2}\left(\frac{1}{\tau_M} + \frac{1 + K^2L_D^2}{\tau}\right) \pm \sqrt{\frac{1}{4}\left(\frac{1}{\tau_M} + \frac{1 + K^2L_D^2}{\tau}\right)^2 - \frac{1}{\tau_M\tau}}. \quad (12)$$

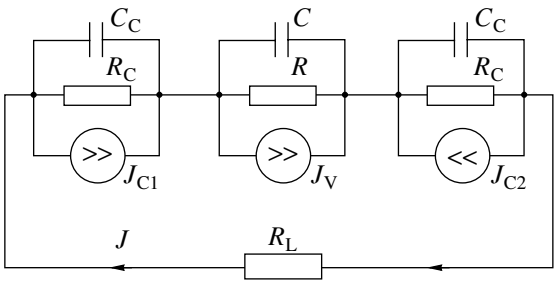

Fig. 2. Equivalent circuit of the photodetector model.

For the photoconductor of "relaxation" type ($\tau \ll \tau_M$),

$$\begin{aligned}\lambda_1 &= -\omega_0 = -\frac{1}{\tau_M(1 + K^2L_D^2)},\\ \lambda_2 &= -\omega_0' = -\frac{1 + K^2L_D^2}{\tau}.\end{aligned} \quad (13)$$

Here, we introduced the designations for the cutoff frequencies of non-steady-state photo-emf [9]. If, in addition, the quantity $m(t)$ can be represented as $m(t) = m\exp[i\varphi(t)]$ and the characteristic time of variation of this quantity far exceeds the electron lifetime τ, the expression for the photocurrent is greatly simplified:

$$J_V(t) = \frac{Sm^2\sigma_0E_D\omega_0}{2(1 + K^2L_D^2)} \times \mathrm{Im}\left(\int_0^{\infty}\exp\{-\omega_0t' + i[\varphi(t-t') - \varphi(t)]\}dt'\right). \quad (14)$$

In our problem, $\varphi(t) = \delta\cos(\omega t) + \Delta\cos(\Omega t) + \psi$. To integrate (14), one can take advantage of the expansion of the function $\exp(i\Delta\cos\Phi)$ in harmonic functions in view of approximation (2). Eventually, the following expression for the harmonic of the photocurrent at the nth side frequency was obtained:

$$J_V^{\omega+n\Omega} = \frac{Sm^2J_0(\delta)J_1(\delta)\sigma_0E_D}{1 + K^2L_D^2}\cos\frac{n\pi}{2} \times \sum_{p=-\infty}^{\infty}\frac{J_p(\Delta)J_{p-n}(\Delta)(-i\omega/\omega_0)}{(1 + ip\Omega/\omega_0)[1 + i(\omega + p\Omega)/\omega_0]}. \quad (15)$$

It is seen that the spectrum of the volume photo-emf lacks odd side frequencies. In practice, it is not necessary to integrate from $-\infty$ to ∞. Calculations show the summation from $-\Delta$ to Δ provides a required accuracy. Let $\omega \gg \Omega\Delta$. Then,

$$J_V^{\omega+n\Omega} \simeq J_{V0}^{\omega}\cos\frac{n\pi}{2}\sum_{p=-\Delta}^{\Delta}\frac{J_p(\Delta)J_{p-n}(\Delta)}{1 + ip\Omega/\omega_0}. \quad (16)$$

Here,

$$J_{V0}^{\omega} = \frac{Sm^2 J_0(\delta) J_1(\delta) \sigma_0 E_D}{1 + K^2 L_D^2} \frac{-i\omega/\omega_0}{1 + i\omega/\omega_0} \quad (17)$$

is the complex amplitude of the photocurrent in the absence of additional modulation.

For the complex amplitude of the photocurrent with a frequency ω, we have, according to (16),

$$J_V^{\omega} \simeq J_{V0}^{\omega} \left[J_0^2(\Delta) + 2 \sum_{p=1}^{\Delta} \frac{J_p^2(\Delta)}{1 + (p\Omega/\omega_0)^2} \right]. \quad (18)$$

The numerical simulation shows that for $\Omega < \omega_0$, expression (18) can be approximated by [6]

$$J_V^{\omega} \approx \frac{J_{V0}^{\omega}}{\sqrt{1 + (\Omega\Delta/\omega_0)^2}}. \quad (19)$$

For comparison, we also write the expression for the amplitudes of the photocurrent with frequencies $\omega \pm 2\Omega$:

$$J_V^{\omega \pm 2\Omega} \simeq J_{V0}^{\omega} \left[\frac{J_1^2(\Delta)}{1 \pm i\Omega/\omega_0} - \sum_{p=0}^{\Delta} \frac{2(1 \pm i\Omega/\omega_0) J_p(\Delta) J_{p+2}(\Delta)}{(1 \mp ip\Omega/\omega_0)[1 \pm i(p+2)\Omega/\omega_0]} \right]. \quad (20)$$

If $\Delta < \omega_0/\Delta$, one can expand a function like $(1 + x)^{\alpha}$ into the Taylor series and take advantage of relationships for the Bessel functions (see Appendix). Then, we arrive at the estimate

$$J_V^{\omega \pm 2\Omega} \approx J_{V0}^{\omega} \left(\frac{\Omega\Delta}{2\omega_0} \right)^2. \quad (21)$$

As follows from the above expression, the amplitude of the harmonics with the frequencies $\omega \pm 2\Omega$ is the amplitude of the signal at the carrier frequency times the factor $(\Omega\Delta/2\omega_0)^2$. Numerical calculations show that the amplitude of even harmonics with frequencies $\omega \pm 2n\Omega$ varies with harmonic number as $(\Omega\Delta/2\omega_0)^{2n}$.

(3) Comparison between volume and contact signals. Let us consider the difference between contact and volumes non-steady-state emfs. First, the amplitude of the former depends on the phase of the interference pattern ψ, while the latter does not depend on this parameter. Another specific feature of contact emf is that for those values of ψ when the amplitudes of even harmonics are zero, the amplitudes of odd harmonics reach their maxima.

One more specific feature of contact emf is its dependence on the spatial frequency of the interference pattern. When the electrode spacing covers the integer number of interference fringes ($KL = 2k\pi$, $k \in N$), the contact emf is absent; if the number of fringes is half-integer [$KL = (2k + 1)\pi$], the contact emf is maximum. In order to add a fringe into the interference pattern, it is necessary to change the angle between the beams by $\Theta' = \lambda/L$. Here, λ is the radiation wavelength; the spatial frequency is assumed to be small, $K = (2\pi/\lambda)\sin\Theta \ll 2\pi/\lambda$; and Θ is the angle between the beams. The dependence of the non-steady-state emf is much smoother: this curve shows a single peak at $K = L_D^{-1}$ [9] (in the case of bipolar photoconductivity, two peaks with a zero current in between may exist [10]).

As follows from (17), the amplitude of the non-steady-state emf tends to zero with decreasing phase modulation frequency ω. The contact emf has a nonzero limit at low frequencies [see (6)]. A possible run of the frequency characteristic of the total signal is demonstrated in Fig. 3. This curve was calculated for $S = 0.01$ mm^2, $L = 1$ mm, $m = 0.5$, $\delta = 0.1$ rad, $\Delta = 0$, $K \simeq 30$ mm^{-1}, $KL_D \ll 1$, $KL = (2k + 1)\pi$, $\omega_0/2\pi = 3$ kHz, $\xi I_0 = 0.4$ μA, $R = 10$ MΩ, $C = 1.1 \times 10^{-3}$ pF, $R_C = 100$ kΩ, and $C_C = 10$ pF. It should be noted that the parameters σ_0 (or ω_0) and R were preset independently, although they must obey the relationship $S\sigma_0 = L/R$. This is because GaAs has two cutoff frequencies [11], one of which is near 10 MHz and satisfies roughly the above relationship, while the other lies in the range 1–100 kHz and appears in the frequency response because of conductivity slow relaxation in GaAs [11, 12]. In this work, we consider only the low-frequency range; therefore, the parameters indicated were chosen independently and the quantity L/R was used instead of $S\sigma_0$ in (17).

From (6) and (17), it also follows that the amplitudes of the contact and non-steady-state emfs variously depend on the interference pattern contrast: as the contrast drops, a fraction of the contact photocurrent in the total signal rises.

Note also the great difference in the spectral compositions of the contact and volume photocurrents that is observed in the case of double-frequency excitation. In the contact signal, the amplitudes of side-frequency harmonics differ from those of input (optical) signal harmonics by K- and ψ-dependent factors. Specifically, for $\Delta = 2.405$ rad, harmonics with the frequency ω are absent in the light intensity oscillation spectrum and in the spectrum of the contact photocurrent. A similar result can be achieved by taking Δ large enough (such that $J_0(\Delta) \approx 0$); in this case, the contact emf spectrum will obviously contain a large number of harmonics. For non-steady-state volume emf, such a simple relation to the input (optical) signal is absent. With the condition $\Delta < \omega_0/\Omega$ fulfilled, the harmonic at the carrier frequency [see (19)] prevails in the signal spectrum, odd side frequencies are absent, and the even harmonic amplitudes decay rapidly as their number increases [see (21)]. Of practical interest is the case of detecting the photo-emf signal against the background of a low-frequency interference ($\Omega \ll \omega_0$). With such frequencies, the volume photocurrent spectrum remains narrow

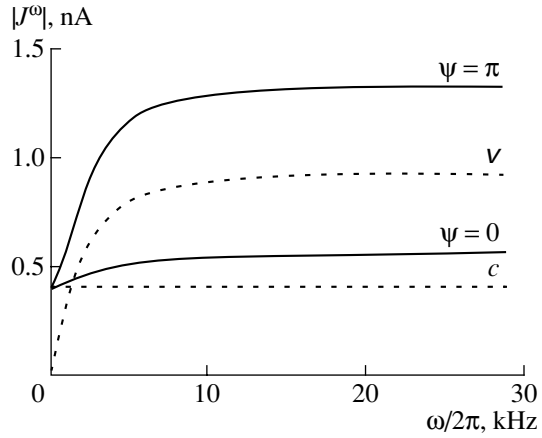

Fig. 3. Theoretical dependence of the non-steady-state photo-emf on phase modulation frequency according to (5), (6), and (17) for the phase $\psi = 0$ and π. Dotted lines stand for the volume (v) and contact (c) photocurrents.

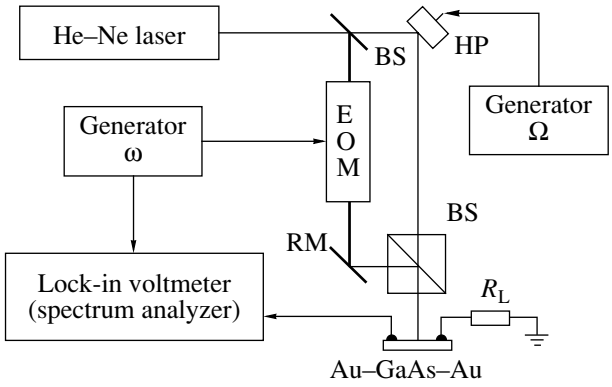

Fig. 4. Experimental setup for measuring the non-steady-state photo-emf under double-frequency excitation. BS, beam splitters; EOM, electrooptic modulator; HP, headphone with mirror; RM, rotating mirror; R_L, load resistance.

even if $\Delta > 1$. Moreover, from (18) and (19), it follows that the volume signal harmonic with the frequency ω is observed at $\Delta = 2.405$ rad.

EXPERIMENTAL SETUP

The experimental setup is shown in Fig. 4. A He–Ne laser ($\lambda = 633$ nm, $P_{out} \le 30$ mW) is used as a source of coherent radiation. The laser radiation is split into two beams, one of which is phase-modulated with an MD-102A electrooptic modulator and the other, with a TA-56m headphone with a mirror attached to its membrane. Then, the radiation is directed to the crystal surface, where a vibrating interference pattern is formed. To provide the possibility of varying (over narrow limits) the spatial frequency of the pattern, a rotating mirror is placed near the crystal (at a distance of ≈10 cm). The current in the external circuit is measured with an SK4-56 spectrum analyzer and with a Unipan-232B lock-in nanovoltmeter. To obtain a flat frequency response of the measuring circuit, a load resistance R_L is connected parallel to the photodetector.

The sample used was a semi-insulating GaAs single crystal measuring $3 \times 3 \times 0.5$ mm with gold electrodes applied to its front surface. The front and back surfaces (3×3 mm) were subjected to optical finishing. The electrodes were made of two strips spaced 1.2 mm apart. The contact was provided by means of a silver paste.

EXPERIMENTAL RESULTS

In the range of phase modulation frequencies 0.01–50 kHz, the sign of the non-steady-state emf generated in the GaAs crystal corresponded to the hole component of the current.

Figure 5 demonstrates the experimental frequency dependences of the signal picked up from the adaptive photodetector in the case of single-frequency phase modulation. These curves were obtained under the same experimental conditions in 10 min intervals. It is seen that the signal amplitude roughly doubles within several minutes. One reason for his may be the slow drift of the interferometer, which eventually shows up as a shift of the interference pattern, that is, as a slow variation of its phase in expression (1) with time: $\psi = \psi(t)$. As follows from (6), the amplitude of the contact emf also becomes a slowly varying function of time. In addition, the signal amplitude in these frequency dependences does not tend to zero at low phase modulation frequencies, as it should for the volume non-steady-state emf [see (17)]. As was noted above, such behavior can be explained if one takes into account the presence of the contact current. A similar frequency dependence of the photo-emf was observed in [11], where its specific behavior was not attributed to the presence of the contact emf.

Let us consider the transfer characteristic and the spectral composition of the signal for double-frequency excitation. The frequency dependence of the non-steady-state emf (Fig. 6) was taken with the parameters of additional phase modulation $\Omega/2\pi = 10$ Hz and $\Delta = 2.4$ rad. The passband f' of the spectrum analyzer was set equal to 3 Hz; hence, the condition $f' < \Omega/2\pi$ was fulfilled. With the passband thus selected, the signal was measured only at the frequency of basic phase modulation. Note first of all that the amplitude of the signal measured is fairly stable (within 5%). This is because the contact emf signal is suppressed: the harmonic at the carrier frequency ω is suppressed by appropriately selecting the amplitude Δ, and side frequencies are beyond the passband of the instrument. At the same time, the volume emf signal is not suppressed: for a cutoff frequency $\omega_0/2\pi \approx 1$ kHz and the selected values of Ω and Δ, the amplitude of the non-steady-state photo-emf [see (18)] should only decrease by

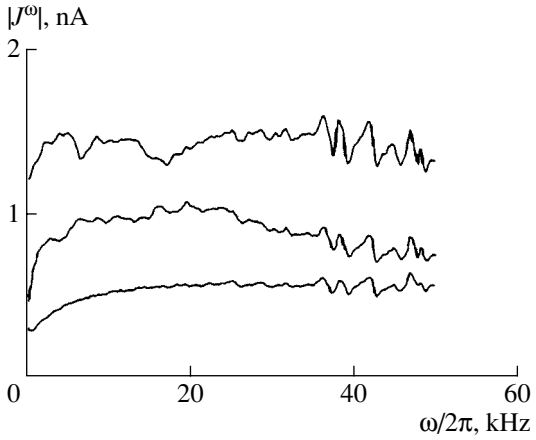

Fig. 5. Frequency responses of the non-steady-state photo-emf taken by the single-frequency technique in 10 min intervals. $P_0 = 1.1$ mW, $K = 31$ mm^{-1}, $m = 0.6$, $\delta = 0.10$ rad, and $\Delta = 0$.

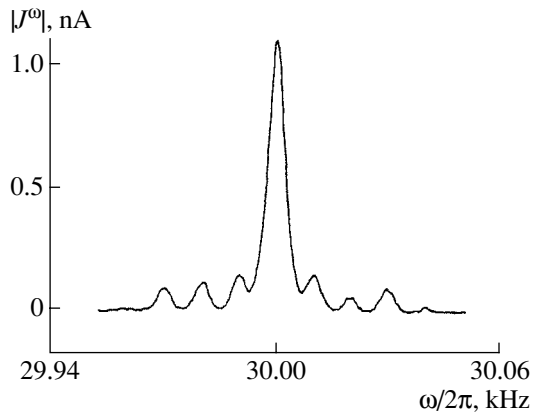

Fig. 7. Photocurrent spectrum in GaAs under double-frequency excitation. $P_0 = 1.1$ mW, $K = 31$ mm^{-1}, $m = 0.6$, $\delta = 0.13$ rad, $\omega/2\pi = 30$ kHz, $\Delta = 2.4$ rad, and $\Omega/2\pi = 10$ Hz.

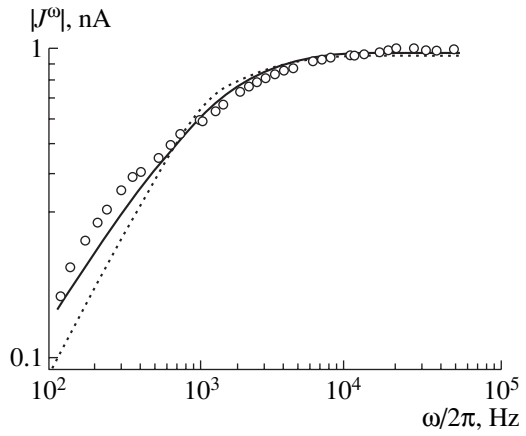

Fig. 6. Frequency responses of the non-steady-state photo-emf taken by the double-frequency technique. $P_0 = 1.1$ mW, $K = 31$ mm^{-1}, $m = 0.6$, $\delta = 0.10$ rad, $\Delta = 2.4$ rad, and $\Omega/2\pi = 10$ Hz. Data points are approximated by standard relationship (17) (dotted line) and also by relationship (22), which includes strong optical absorption in GaAs (solid curve).

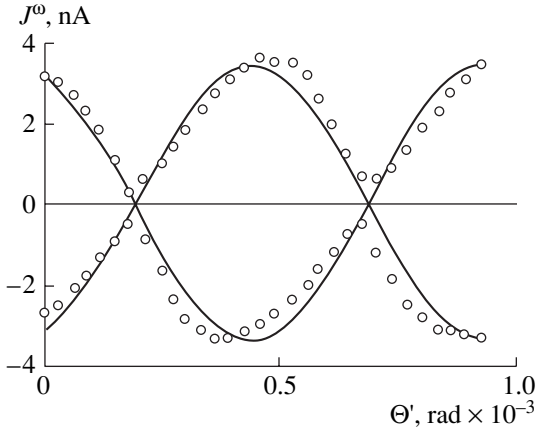

Fig. 8. Contact photocurrent vs. angle increment Θ' between the beams forming the interference pattern. $P_0 = 8.5$ mW, $m = 0.5$, $\delta = 0.14$ rad, $\omega/2\pi = 3$ Hz, and $\Delta = 0$. The spatial frequency for $\Theta' = 0$ was $K \approx 19$ mm^{-1}. Solid curve is theoretical dependence (6).

0.03%. As follows from Fig. 6, at low frequencies of phase modulation, the signal amplitude tends to zero. The aforesaid suggests that the frequency response thus measured is close to the actual frequency characteristic of the volume non-steady-state emf in GaAs crystals. Yet, the approximation of experimental data by the standard frequency dependence like (17) with $\omega_0/2\pi = 1.1$ kHz disagrees markedly with the experiment at low ω. The dependences observed can be described adequately by taking into account the specific character of the surface excitation of non-steady-state emf in semi-insulating GaAs (Fig. 6). To approximate the transfer characteristic, we used the semi-empiric expression [13]

$$J_V^{\omega}(\omega) \propto -i\frac{\omega}{\omega_0(0)}\ln\left[1 - i\frac{\omega_0(0)}{\omega}\right], \qquad (22)$$

where $\omega_0(0)$ is an adjustable parameter (the cutoff frequency on the crystal surface): $\omega_0(0)/2\pi = 2.5$ kHz.

The spectrum of the signal picked up from the photodetector for double-frequency phase modulation is shown in Fig. 7. The harmonic at the carrier frequency ω remains stable. It is easy to see three or four side-frequency harmonics in the spectrum. In addition, the spectrum contains both odd and even harmonics. Their amplitudes are comparable in height with the signal at the frequency ω and slowly vary with time. It is noteworthy that the odd harmonics are maximal when the even ones vanish and vice versa. Let us estimate the amplitudes of the volume signal at the carrier and at side frequencies for the GaAs crystal under study ($\omega_0/2\pi = 2.5$ kHz, $\Delta = 2.4$ rad, and $\Omega/2\pi = 10$ Hz). As was noted in the theoretical analysis of the effect, the

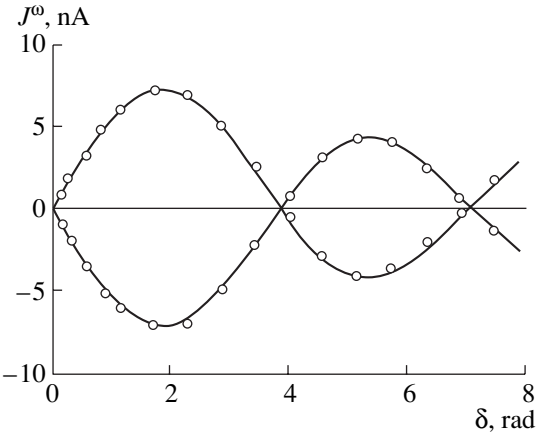

Fig. 9. Contact photo-emf vs. amplitude of phase modulation at the carrier frequency. $P_0 = 0.58$ mW, $K \approx 19$ mm^{-1}, $m = 0.5$, $\omega/2\pi = 3$ Hz, $\Delta = 0$. Solid curve is theoretical dependence (6).

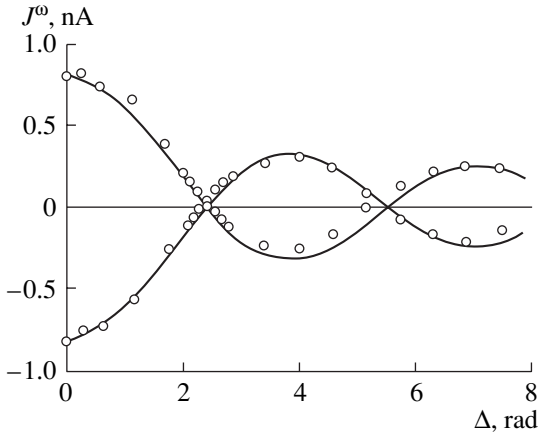

Fig. 10. Non-steady-state photocurrent vs. additional phase modulation amplitude. $P_0 = 0.58$ mW, $K \approx 19$ mm^{-1}, $m = 0.5$, $\delta = 0.13$ rad, $\omega/2\pi = 125$ Hz, and $\Omega/2\pi = 3$ Hz. Solid curve is theoretical dependence (6).

amplitudes of even harmonics of the volume photo-emf with frequencies $\omega \pm 2n\Omega$ vary with their number roughly as $(\Omega\Delta/2\omega_0)^{2n}$. Using this dependence, we find the relative amplitude of the second harmonic (2.3×10^{-5}), fourth harmonic (5.3×10^{-10}), etc. The signal-to-noise ratio was ~10^3. This means that all the side-frequency harmonics of the volume photocurrent must be below the noise level. The above features and estimates indicate the different nature of the spectral components: the harmonic at the frequency ω is the volume emf signal, while the side-frequency harmonics are the components of the contact signal.

To make sure that the signal identified as contact is in fact contact, we performed measurements at low phase-modulation frequencies ($\omega, \Omega \ll \omega_0$), where the signal of the non-steady-state emf is extremely small and can be neglected. The need for such a corroboration is associated with the fact that similar phenomena can be treated alternatively based on slowly relaxing conductivity and field gratings in a semiconductor. Figure 8 shows the dependence of the photodetector signal on the spatial frequency of the interference pattern (i.e., on the angle between the beams). In the measurements, we used the lock-in voltmeter, which can not only measure the signal but also detect the change of sign. For each K, the signal is represented by two circles that are the maximal (by magnitude) positive and negative values of the photocurrent over 10–20 min. The difference between the angles of the photocurrent maxima (minima), $\Theta' = 4.9 \times 10^{-4}$ rad, is in fairly good agreement with an angular increment necessary for a fringe offset by the electrode spacing to be added: $\Theta' = \lambda/L = 5.3 \times 10^{-4}$ rad.

We also took the dependences of the photocurrent on the amplitudes of basic and additional phase modulations (Figs. 9, 10). Associated experimental data were approximated by expression (6). From Figs. 9 and 10, one can see that the contact emf is suppressed if the amplitudes of additional phase modulation are the roots of the zeroth-order Bessel function.

CONCLUSION

The presence of the contact emf is shown to have an adverse effect on the adaptive properties of the photodetector. The problem can be resolved by decreasing the contact emf and by separating the volume and contact components. The former way can be accomplished if the spatial frequency of the interference pattern is taken such that the electrode spacing covers the integer number of fringes ($KL = 2k\pi$). The separation of the volume and contact signals can be made by introducing additional low-frequency phase modulation of amplitude $\Delta = 2.4$ rad. With such a parameter of the additional modulation, the contact photocurrent spectrum lacks the harmonic at the frequency ω of the basic phase modulation. In addition, with the condition $\Delta < \omega_0/\Omega$ satisfied, the volume signal spectrum broadens insignificantly: the amplitudes of harmonics at frequencies $\omega \pm 2n\Omega$ are roughly $(2\omega_0/\Omega\Delta)^{2n}$ times lower than the amplitude of the harmonic at the frequency ω, and harmonics at odd side frequencies are absent.

The results presented were obtained for an adaptive photodetector based on a semi-insulating GaAs single crystal and having simple electrode geometry and arrangement. The optimization of the photoelectrical properties of the contacts is a challenge and may be the subject of further investigation.

APPENDIX

Below are given several relationships for the Bessel functions of the first kind used in the theoretical analy-

sis [14]:

$$\exp(i\Delta\cos\Phi) = \sum_{p=-\infty}^{\infty} J_p(\Delta)\exp\left[ip\left(\Phi+\frac{\pi}{2}\right)\right], \quad \text{(A.1)}$$

$$J_{-n}(\Delta) = (-1)^n J_n(\Delta), \quad \text{(A.2)}$$

$$J_1^2(\Delta) = 2\sum_{p=0}^{\infty} J_p(\Delta)J_{p+2}(\Delta), \quad \text{(A.3)}$$

$$\frac{\Delta^2}{4} = J_1^2(\Delta) + 2\sum_{p=1}^{\infty} p(p+2)J_p(\Delta)J_{p+2}(\Delta). \quad \text{(A.4)}$$

ACKNOWLEDGMENTS

This work was supported by the Russian Foundation for Basic Research and the NATO grants HTEH.LG 970314 and CNS 972900.

REFERENCES

1. S. I. Stepanov, in *International Trends in Optics*, Ed. by J. W. Goodman (Academic, Boston, 1991), pp. 125–140.
2. R. J. Dewhurst and Q. Shan, Meas. Sci. Technol. **10**, R139 (1999).
3. S. I. Stepanov, I. A. Sokolov, G. S. Trofimov, *et al.*, Opt. Lett. **15**, 1239 (1990).
4. S. I. Stepanov and G. S. Trofimov, Fiz. Tverd. Tela (Leningrad) **28**, 2785 (1986) [Sov. Phys. Solid State **28**, 1559 (1986)].
5. M. P. Petrov, S. I. Stepanov, and A. V. Khomenko, *Photorefractive Crystals in Coherent Optics* (Nauka, St. Petersburg, 1992).
6. I. A. Sokolov, S. I. Stepanov, and G. S. Trofimov, Zh. Tekh. Fiz. **59** (10), 126 (1989) [Sov. Phys. Tech. Phys. **34**, 1165 (1989)].
7. G. S. Trofimov, S. I. Stepanov, M. P. Petrov, and M. V. Krasin'kova, Pis'ma Zh. Tekh. Fiz. **13**, 265 (1987) [Sov. Tech. Phys. Lett. **13**, 108 (1987)].
8. V. L. Bonch-Bruevich and S. G. Kalashnikov, *Physics of Semiconductors* (Nauka, Moscow, 1990).
9. I. A. Sokolov and S. I. Stepanov, Optik (Stuttgart) **93** (4), 175 (1993).
10. S. I. Stepanov and G. S. Trofimov, Fiz. Tverd. Tela (Leningrad) **31**, 89 (1989) [Sov. Phys. Solid State **31**, 49 (1989)].
11. N. Korneev, S. Mansurova, P. Rodriguez, and S. Stepanov, J. Opt. Soc. Am. B **14**, 396 (1997).
12. N. Korneev, S. Mansurova, and S. Stepanov, J. Appl. Phys. **78**, 2925 (1995).
13. M. A. Bryushinin, Cand. Sc. Dissertation (Ioffe Physicotechnical Inst., Russian Academy of Sciences, St. Petersburg, 2001).
14. I. S. Gradshteyn and I. M. Ryzhik, *Table of Integrals, Series, and Products* (Fizmatgiz, Moscow, 1963; Academic, New York, 1980).

Translated by V. Isaakyan

Technical Physics, Vol. 47, No. 10, 2002, pp. 1291–1298. Translated from Zhurnal Tekhnicheskoĭ Fiziki, Vol. 72, No. 10, 2002, pp. 85–94.

OPTICS, QUANTUM ELECTRONICS

Quasi-Diffraction Effects during Irradiation of Moving Surfaces. Part I

K. I. Zor'ko*, M. F. Kudoyarov*, A. V. Matyukov*, S. A. Mukhin*, and M. Ya. Patrova**

** Ioffe Physicotechnical Institute, Russian Academy of Sciences, ul. Politekhnicheskaya 26, St. Petersburg, 194021 Russia*
e-mail: mkud@cycla.ioffe.rssi.ru
*** NPF TREM Close Corporation, St. Petersburg, 194223 Russia*
Received April 4, 2002

Abstract—The formation of the radiation flux density (dose rate) distribution over a moving surface irradiated by an intensity-modulated flux through a spatially periodic structure is considered. Relationships for a number of particular cases are derived and analyzed. The irradiation process is regarded as the wave quasi-diffraction on two-dimensional slot objects. A method for converting the quasi-diffraction pattern into a one-dimensional hologram is described and the results of applying the quasi-wave approach to a description of moving films irradiated by pulsed accelerated beams are presented. © *2002 MAIK "Nauka/Interperiodica".*

INTRODUCTION

The action of various types of radiation on moving films is a rather widely used processing step. Depending on the purpose, it is required either to irradiate the object uniformly over the whole surface or to provide the required distribution of the radiation flux density (dose rate) in the direction of motion. We can particularly distinguish here technologies involving a time-periodic irradiation. A typical example of such a technology is the production of track membranes from polymer films [1–3]. If the pulsed irradiation is produced via a complex, for example, spatially periodic, aperture, typical space–time beats are observed, which lead to a number of specific features in the distribution of the radiation flux density over the film surface. We have observed these features when irradiating a moving film through periodic spatial arrays with a small effective screening cross section on a cyclotron at the Ioffe Physicotechnical Institute (Russian Academy of Sciences, St. Petersburg). Further experiments and a thorough mathematical analysis have shown that such arrays are equivalent to specific space–time filters that can make the irradiation of the object either more or less uniform. It has been shown that the mathematical formalism that describes these processes is completely the same as the formalism used to characterize the diffraction of two-dimensional waves on planar screens in the Fraunhofer approximation [4].

Based on the above similarity, this paper attempts to draw a parallel between the irradiation of a moving surface and diffraction processes. Therefore, Part I of this work mostly focuses on the derivation and discussion of the general relationships, while Part II applies the theory to a particular problem; namely, it studies the behavior of the radiation flux density distribution created by beams of pulsed particle accelerators. Part II also presents experimental results and describes how to obtain specific holograms of the diffracting structures, which may be referred to as the information holograms.

IRRADIATION OF A MOVING SURFACE THROUGH A PERIODIC SPATIAL ARRAY BY A SINUSOIDALLY MODULATED FLOW

Let the moving surface be irradiated through a regular set of identical slots that form a periodic spatial array, the slots being perpendicular to the direction of motion as shown in Fig. 1. Also, let the intensity of the irradiating flux in the plane of the screen depend only on the time, while being independent of the x coordinate. After passing through the screen, the intensity will certainly depend on x. For a sinusoid-modulated flow, this intensity can be written as

$$I(x, t) = \begin{cases} I_0 + I_m \sin(\omega t) & x = x\ id < x < l_1 + id, \\ i = 1, 2, 3, \ldots, N-1 & \\ 0 & x \neq \bar{x}, \end{cases} \quad (1)$$

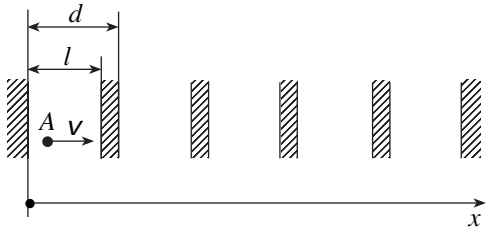

Fig. 1. Motion of the point A fixed on the irradiated surface under a periodic screen.

1063-7842/02/4710-1291$22.00 © 2002 MAIK "Nauka/Interperiodica"

where l_1 is the slot width, d is the array spacing, and N is the total number of slots.

Let point A fixed on the surface move under the array at the velocity v in the positive x direction. If the point is at $x = 0$ at the time moment $t = T$, then, after it passes under the ith slot, the dose rate in the vicinity of this point will increase by

$$\rho_i = I_0\tau_1 + I_m \int_{T+(\tau_1+\tau_2)(i-1)}^{T+(\tau_1+\tau_2)(i-1)+\tau_1} \sin(\omega t)dt = I_0\tau_1 + \frac{2I_m}{\omega}\sin\left(\frac{\omega\tau_1}{2}\right)\sin\left[\omega T + \frac{(i-1)d\omega}{v} + \frac{\omega\tau_1}{2}\right], \quad (2)$$

where $\tau_1 = l_1/v$ and $\tau_2 = (d - l_1)/v$.

After passing all the N slots, the total dose rate at point A will be

$$\rho_\Sigma = \sum_{i=1}^{N}\rho_i = NI_0\tau_1 + \frac{2I_m}{\omega}\sin\left(\frac{\omega\tau_1}{2}\right) \times \sum_{i=1}^{N}\sin\left[\omega T + \frac{(i-1)d\omega}{v} + \frac{\omega\tau_1}{2}\right] = NI_0\frac{l_1}{v} + \frac{2I_m}{\omega}\sin\left(\frac{\omega l_1}{2v}\right)\frac{\sin\left(\frac{Nd\omega}{2v}\right)}{\sin\left(\frac{d\omega}{2v}\right)}\sin\left[\omega T + \frac{(N-1)d\omega}{2v} + \frac{\omega\tau_1}{2}\right]. \quad (3)$$

The first term on the right-hand side of expression (3) is a constant component of the dose rate ρ_0, which is independent of T. The second term is a variable component ρ_a of the dose rate, its last factor alone being dependent on time T. The remaining T-independent factors determine the amplitude of the variable component.

Let us write the ratio of variable and constant dose rate components and use the change of variables $T = t - (\tau_1 + \tau_2)(N - 1) - \tau_1$, which introduces a common time variable in formulas for the flux intensity and dose rate. Physically, this change of variables simply means that any change in the dose rate observed at the trailing edge of the last slot must start immediately after the intensity of the irradiating flux starts changing:

$$A(t) = \frac{\rho_a}{\rho_0} = A_\rho\sin\left[\omega t - \frac{(N-1)d\omega}{2v} - \frac{\omega\tau_1}{2}\right], \quad (4)$$

where

$$A_\rho = \frac{I_m}{NI_0}\frac{\sin\xi}{\xi} - \frac{\sin(Na\xi)}{\sin(a\xi)}, \quad \xi = \frac{\omega l_1}{2v}, \quad a = \frac{d}{l_1}. \quad (4a)$$

In terms of the coordinate x' connected to the surface being irradiated, for constant ω and v, the dose rate variation in the direction of motion can be written as

$$A(x') = A_\rho\sin\left(\frac{x'-x}{v}\omega\right), \quad (5)$$

where A_ρ is given by (4a) and x is the origin of the of x' axis.

The expressions obtained above show that, when a moving surface is irradiated by a sinusoid-modulated beam through a uniform array of slots in a screen (Fig. 1), the dose rate also varies sinusoidally in the direction of motion with a period of $\lambda = v/f$, where $f = \omega/2\pi$ is the modulation frequency of the radiation intensity. In accordance with its physical meaning, coefficient A_ρ can be called the spatial modulation index of the dose rate in the x' coordinate, and $A_T = I_m/I_0$ can be called the temporal intensity modulation index of the irradiating flux.

It can easily be seen that, accurate to within the interpretation of quantities involved, the function $A_\rho(\xi)$ coincides with the expression that describes diffraction of a plane electromagnetic wave on a periodic array of slots in a screen in the Fraunhofer approximation [4]. In particular, for $N = 1$, expressions (4) and (4a) reduce to expressions (6) and (6a) which describe the Fraunhofer diffraction by a single slot of width l_1:

$$A_1(t) = A_{\rho 1}\sin\left(\omega t - \frac{\omega\tau}{2}\right), \quad (6)$$

$$A_{\rho 1} = \frac{I_m}{I_0}\frac{\sin\xi}{\xi}, \quad (6a)$$

where $\tau = l_1/v$ and $\xi = \omega l_1/2v$.

In the above expressions, changing the sign of amplitude A_ρ at certain discrete ξ means that a jumplike phase change by π occurs at these points in the modulating function. The function $|A_\rho(\xi)|$ is the sequence of alternating main and side lobes that is well known from diffraction spectroscopy. At the points where the phase changes abruptly, $A_\rho(\xi) = 0$. This means that, by appropriately choosing the frequency-to-velocity ratio, the moving surface can be irradiated quite uniformly at the variable intensity of the irradiating flow. Conversely, a periodic array with a very small screening cross section (highly transparent) introduced in the irradiating aperture can significantly increase the nonuniformity of the illumination under certain conditions. As an example, consider the case of a large number N and $(\alpha - 1) \ll 1$. Such an array can be created by introducing a uniform mesh of thin filaments across the working aperture that are perpendicular to the x' axis. Clearly, the transparency of this array will be proportional to $1/a$, i.e., will be close to unity. In this case, increasing ξ gradually shifts the main maximums of the factor $\sin(Na\xi)/\sin(a\xi)$ in expression (4) relative to the min-

ima (zeros) of the factor $\sin\xi/\xi$. The phase of the shift $\Delta\xi_m$,

$$\Delta\xi_m = \pi m\frac{a-1}{a}. \quad (7)$$

increases linearly with the order m of the spectrum. By expanding the function $\sin\xi$ in a power series about $\xi_i = \pi i$ and truncating it beyond the linear term, it can be shown that, with an allowance for (7) and with small m meeting the condition

$$\Delta\xi_m \ll \frac{\pi}{2}, \quad (8)$$

the function $A_\rho(\xi)$ has the same value independent of m at the locations $\xi_m = \pi m/a$ of the main maxima.

In order to compare the values of $|A_\rho|$ and $|A_{\rho 1}|$, it is convenient to consider these quantities as functions of the frequency ω rather than of the generalized variable ξ. Figure 2a is a plot of the function $|A_{\rho 1}(\omega)|$ for a single wide slot; Fig. 2b plots the function $|A_\rho(\omega)|$ for the same slot with a mesh of 19 thin filaments. The total area of the filaments accounts for 5% of the aperture area. The transmission coefficient of this mesh is $K_p = 1/a = 0.95$. As can be seen from the figures, when condition (8) is met, the function $|A_\rho(\omega)|$ has almost equal values at locations of its main maxima, which are significantly higher than $|A_{\rho 1}(\omega)|$ at these points. Thus, an additional thin uniform mesh with a high transmission introduced into the aperture increases the modulation index of the irradiation intensity at particular discrete frequencies ω in the resonance manner.

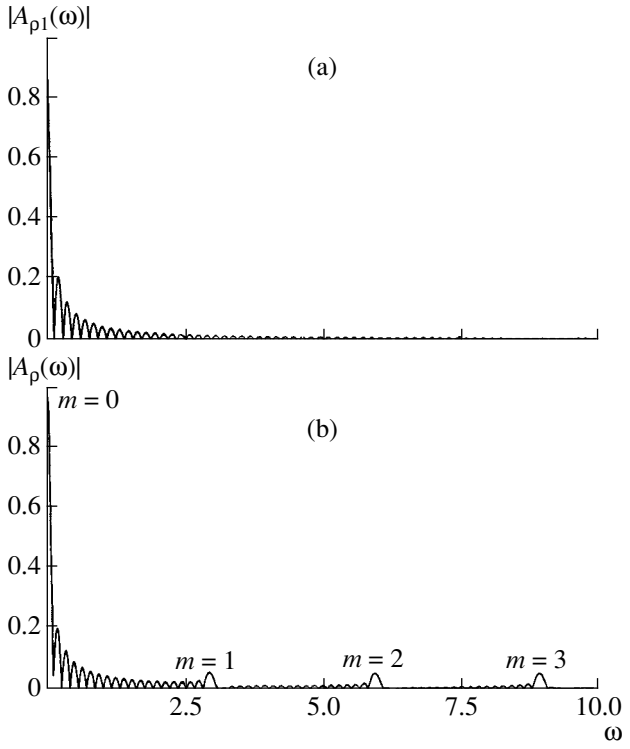

Fig. 2. Function $|A_{\rho 1}(\omega)|$ for (a) a single slot and (b) the same slot with a periodic mesh at $N = 20$ and $K_p = 1/\alpha = 0.95$.

IRRADIATION THROUGH A SINGLE SLOT BY A PULSED FLUX

The irradiation of moving targets on charged particle accelerators is very often performed with pulsed sources. Therefore, an analysis of the spatial dose density distribution for such an irradiation has a real practical significance. It is reasonable to consider the problem for a single slot separately from the general case.

Let a moving surface be irradiated by a sinusoidally time-modulated flux through a single slot of width l_1. The dose rate $A_1(t)$ at the point $x = l_1$ will be described by expressions (6) and (6a), in which a change in the sign of the intensity means a phase change by π. In accordance with formula (2), the constant component $I_0\tau_1$ of the resultant dose rate is independent of the frequency ω and the integral operator is a linear functional transformation. Therefore, to within a constant dimensional factor, the function $A_{\rho 1} = A_{\rho 1}(\omega)$ can be regarded as an amplitude-versus-frequency response of a certain linear circuit to the harmonic component of the source radiation applied to its input, the corresponding harmonic dose rate component being observed at its output. In accordance with formula (6), the phase-versus-frequency response of this circuit is $\varphi(\omega) = -\omega\tau/2$. Hence, the following expression can be written for the complex transfer function $\dot{K}(\omega)$ of this circuit [5, 6]:

$$\dot{K}(\omega) = C\frac{\sin\frac{\omega\tau}{2}}{\frac{\omega\tau}{2}}\exp\left(-j\frac{\omega\tau}{2}\right), \quad (9)$$

where C is the dimensional constant.

The pulsed response $h'(t)$ of the linear circuit is defined as the inverse Fourier transform of $\dot{K}(\omega)$. In this case,

$$h'(t) = \frac{1}{2\pi}\int_{-\infty}^{\infty}\dot{K}(\omega)\exp(j\omega t)dt = \frac{C}{2\pi}\int_{-\infty}^{\infty}\frac{\sin\frac{\omega\tau}{2}}{\frac{\omega\tau}{2}} \times \exp\left[j\omega\left(t-\frac{\tau}{2}\right)\right]d\omega = \begin{cases}0 & t<0\\ \frac{C}{\tau} & 0\le t\le\tau\\ 0 & t>\tau.\end{cases} \quad (10)$$

Since $h'(t) = 0$ for $t < 0$, the system can be realized [5, 6], which could be expected because our calculations did not involve any simplifying assumptions that could lead to an unfeasible system.

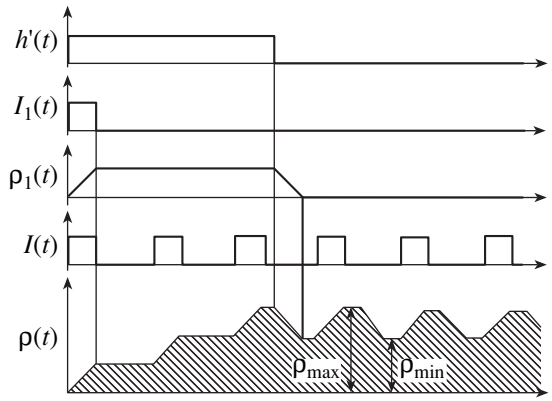

Fig. 3. Time patterns illustrating the formation of the dose rate $\rho(t)$ distribution under a periodic pulsed action.

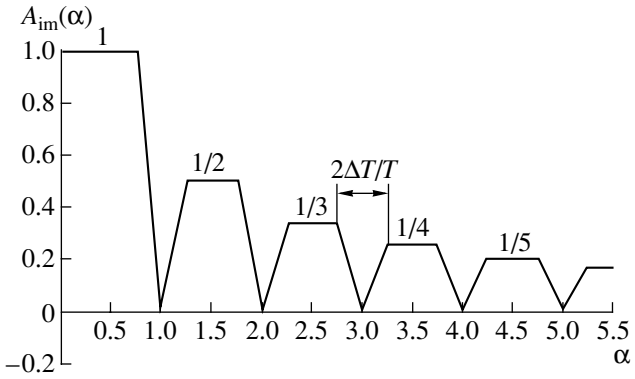

Fig. 4. Modulation index of pulsed dose rate versus parameter $\alpha = \tau/T_0$ for $\Theta = T_0/\Delta T = 3$.

Let a periodic sequence of rectangular pulses of the length ΔT and pulse repetition interval T_0 be applied to the system $\dot{K}(\omega)$ (Fig. 3). The response of the system to this sequence, which determines the dose rate created by the pulsed source, can be written as [5]

$$\rho(t) = \sum_{i=1}^{\infty} \rho_1(t - [i-1]T), \qquad (11)$$

where

$$\rho_1(t) = \int_0^t h'(t-t')I_1(t')dt',$$

$$I_1(t) = \begin{cases} 0 & t < 0,\ t > \Delta T \\ I_m & 0 \le t \le \Delta T, \end{cases}$$

and $h'(t)$ is given by expression (10).

Figure 3 plots the function $\rho(t)$ at $\alpha = \tau/T_0 = 2.5$ and $\Theta = T_0/\Delta T = 3$. Figure 3 also shows the input pulse sequence $I(t)$, pulsed response $h'(t)$, and response $\rho_1(t)$ to a single pulse. As can be seen from the figure, the transient has a finite duration and the dose rate distribution comes at $t > \tau$ to its periodic steady state $\rho(t)$, which has a typical trapezoidal shape. Note that the slope in the corresponding intervals depends for $v =$ const on the radiation intensity I_m only and is independent of T_0, ΔT, and τ.

Consider the index of pulsed dose rate modulation

$$A_{im} = \frac{\rho_{\max} - \rho_{\min}}{\rho_{\max}}. \qquad (12)$$

Figure 4 is a plot of A_{im} versus parameter $\alpha = \tau/T_0$, which clearly shows that, in the course of the pulsed irradiation of a moving surface through a single slot, the irradiation dose becomes distributed more uniformly as the number of pulses that arrive over time τ increases. Also, if the irradiation time is a multiple of the pulse repetition interval, then $A_{im}(\alpha) = 0$ and the irradiation is completely uniform. However, when the pulses are short ($\Theta \gg 1$), this condition is satisfied to a sufficient accuracy only in very small intervals of α. Conversely, if it is necessary to obtain the deepest modulation of the dose rate, the condition $\tau < T_0 - \Delta T$ should be met.

IRRADIATION BY A PULSED FLUX THROUGH A PERIODIC SPATIAL ARRAY

In the previous section, we used the dose rate distribution on the moving surface to perform the time-domain analysis [4–6]. However, when the slot screen represents a sufficiently long periodic structure (Fig. 1), then, according to (4a), the index of modulation depends on the frequency as the Fraunhofer diffraction function, i.e., has the form of a sequence of resonance peaks. If we analyze this case as above in terms of the linear circuit theory, the results are the clearest in the time domain [6].

Following the procedure used in the previous section and taking into account Eqs. (4) and (4a), we can write the complex transfer function $\dot{K}_N(\omega)$ for the linear system that models the process of irradiation under the action of the time-harmonic component of the flux intensity as

$$\dot{K}_N(\omega) = C_N \frac{\sin\dfrac{\omega\tau_1}{2}}{\dfrac{\omega\tau_1}{2}} \frac{\sin\dfrac{N\omega(\tau_1+\tau_2)}{2}}{\sin\dfrac{\omega(\tau_1+\tau_2)}{2}} \times \exp\left[-j\omega\frac{(N-1)(\tau_1+\tau_2)+\tau_1}{2}\right], \qquad (13)$$

where $\tau_1 = l_1/v$ and $\tau_2 = (d - l_1)/v$.

Let an infinite periodic sequence of rectangular pulses $f(t)$ of the length ΔT and amplitude $\alpha_{\max}$ arrive at the input of system (13) with the pulse repetition inter-

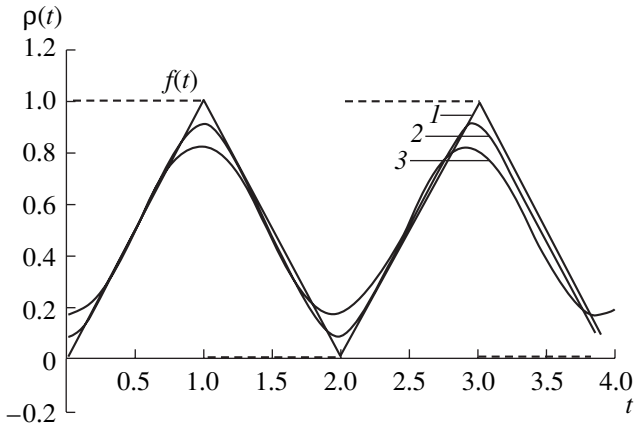

Fig. 5. Function $\rho(t)$ at $C_N = \alpha_{max} = \tau_1 = \tau_2 = 1$, $N = 10$, and $\omega = 2\pi/T_0 = (1)\ \pi$, $(2)\ \pi + \pi/60$, and $(3)\ \pi + \pi/30$.

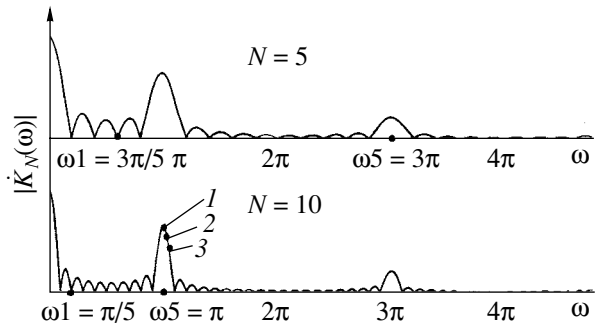

Fig. 6. Magnitude of the transfer function $\dot{K}_N$ versus frequency ω at $C_N = \alpha_{max} = \tau_1 = \tau_2 = 1$, $\Delta T/T_0 = 0.5$, and $N = 5$ and 10.

val T_0. This sequence can be represented as the Fourier series [4, 5]

$$f(t) = \sum_{k=-\infty}^{\infty} b_k \exp(jk\omega t) = \frac{\Delta T \alpha_{max}}{T_0 \pi} \sum_{k=-\infty}^{\infty} \times \frac{\sin\dfrac{k\pi\Delta T}{T_0}}{\dfrac{k\Delta T}{T_0}} \exp(jk\omega t). \quad (14)$$

Since system (13) is linear, its response to action (14) is a superposition of responses to each harmonic component of the series. If our interest is in the intensity of this response irrespective of an arbitrary phase shift, the exponential factor in (13) can be dropped. Then, the time variation of the dose rate at the output of the aperture can be expressed as

$$\rho(t) = \sum_{k=-\infty}^{\infty} \dot{K}_N(k\omega) b_k \exp(jk\omega t) = C'_N \sum_{k=-\infty}^{\infty} \frac{\sin\dfrac{k\omega\tau_1}{2} \sin\dfrac{k\omega N(\tau_1+\tau_2)}{2} \sin\dfrac{k\pi\Delta T}{T_0}}{k^2\omega \sin\dfrac{k\omega(\tau_1+\tau_2)}{2}} \exp(jk\omega t), \quad (15)$$

where

$$C'_N = \frac{2C_N\alpha_{max}}{\pi\tau_1}.$$

Figure 5 shows the waveform of the source sequence of the irradiating pulses $f(t)$ and the respective irradiation intensity $\rho(t)$ obtained from (15) for several frequencies $\omega = 2\pi/T_0$ at $C_N = \alpha_{max} = \tau_1 = \tau_2 = 1$, $\Delta T/T_0 = 0.5$, and $N = 10$. These frequencies are indicated by dots on the amplitude-versus-frequency response (Fig. 6). As can be seen from the plots, when the fundamental frequency of the sequence is tuned to the maximum corresponding to $m = 1$, all higher harmonics reside at the odd main maxima of the function $\dot{K}_N(\omega)$, which provides their maximum transmission through the linear system and, as a consequence, the deepest modulation of the output dose rate distribution. At $\omega = (2\pi + 2\pi/N)T_0 = \pi + \pi/30$, the alternating component of the dose rate has the smoothest, nearly sinusoidal, waveform, the contribution of higher order harmonics decreasing with increasing total slot number N. In this case, a sort of space–time filtering is observed, which creates the sinusoid-modulated dose rate $\rho(t)$ for any periodic source function $I(t)$ that contains only odd harmonics.

The resonance properties of the transfer function (13) enable the device to operate at the harmonics of the source radiation $I(t)$. This means that the relationship between the fundamental frequency $\omega = 2\pi/T_0$, velocity of the irradiated surface v, and number of slots N can always be chosen such that the frequency of the alternating component of the function $\rho(t)$ will be equal to $k_1\omega$, where k_1 is the frequency multiplication factor. A particular multiplication factor can be implemented in different ways. Figure 6 plots the magnitude of the function $\dot{K}(\omega)$ for $N = 5$ and 10. If the frequency ω of the fundamental harmonic of the source function is such as shown in the plots, all harmonics will be in both cases suppressed in the output spectrum except for those with indexes $5(2i - 1)$, where $i = 1, 2, 3, \ldots$. These harmonics can be regarded as odd harmonics of the new fundamental frequency $\omega_5 = 5\omega$. It can easily be seen that their amplitudes and phases are related as those for the harmonics of $\rho(t)$ when its fundamental frequency is tuned to the main quasi-diffraction maximum ($m = 1$). Thus, in both cases, the frequency of the alternating component of $\rho(t)$ is multiplied by a factor of $k_1 = 5$, the shape of the component remaining the same. The maximum of the intensity modulation index is attained if

and only if the frequency of the first harmonic being selected coincides with the main maximum at $m = 1$. In our example, this occurs at $N = 10$ (Fig. 6).

IRRADIATION OF A MOVING SURFACE BY A TIME-MODULATED FLUX AS A QUASI-DIFFRACTION PROCESS

We have already noted above that an analogy exists between the process of irradiation of a moving surface and wave diffraction. At first sight, this analogy may seem to go no further than the formal resemblance of expression (4a) and the function that describes the Fraunhofer diffraction by a one-dimensional planar slot screen [4], because the nature of both processes is completely different. However, a technique exists that can be used to refer the spatial modulation index of the dose rate $A_p(x)$ of a moving surface to the results of diffraction on more complex two-dimensional objects. We will consider here the simplest example of such a two-dimensional object, while limiting our analysis of more complex cases to the formulation of general statements.

Consider a planar slot screen $B'B''$ inclined by an angle α_0 to the observation plane $A'A''$ (Fig. 7). Let a plane electromagnetic wave be normally incident on the screen and the conditions

$$\lambda = \frac{2\pi c}{\omega} \ll l_1 \ll Z \tag{16}$$

be met, where λ is the wavelength, c is the velocity of light, l_1 is the slot width, and Z is the distance between the lower edge of the slot and the observation plane.

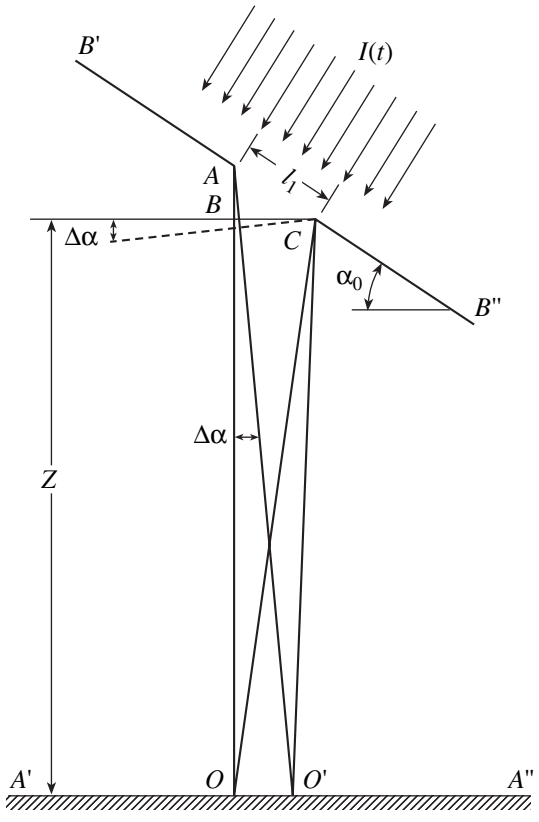

Fig. 7. Illustration of the Fraunhofer diffraction on an inclined slot screen.

According to the Huygens–Fresnel principle [4], the points of the wave front that lie in the plane of the slot are the sources of the secondary spherical waves. Let us find phases of the secondary waves that propagate in directions AO and CO (Fig. 7). If the angle α_0 is chosen so that $l_1 \sin\alpha_0 = i\lambda$, where i is an integer, then the phases of the corresponding waves at the points B and C will be equal. The interval BC, which is parallel to $A'A''$, will accommodate exactly i spatial periods $\lambda_\varphi = \lambda/\tan\alpha_0$ of the phase wave that travels rightward with the phase velocity $v_\varphi = c/\tan\alpha_0$. It is clear that, in this case, the secondary waves will completely compensate each other at the observation point O at any time moment.

Let us change the observation angle by small value $\Delta\alpha \ll \alpha_0$ by moving the observation point from O to O'. It can easily be shown that, as a result, a path length difference will appear between the secondary waves propagating in the directions AO' and CO', which can approximately be written as

$$\begin{aligned} \Delta l &= l_1 \cos\alpha_0 \sin\Delta\alpha - l_1 \sin\alpha_0 \sin^2\Delta\alpha \\ &\approx l_1 \cos\alpha_0 \Delta\alpha - l_1 \sin\alpha_0 \Delta\alpha^2. \end{aligned} \tag{17}$$

This approximation is only valid for small $\Delta\alpha$, i.e., when the Fraunhofer condition is met. At large inclination angles α_0, a negative term proportional to squared $\Delta\alpha$ appears on the right-hand side of (17), which stretches the diffraction pattern as the observation point moves rightward on the $A'A''$ plane. This distortion of the diffraction pattern with respect to the diffraction pattern produced by the plane-parallel screen occurs because the planar slot, being turned by an angle $\alpha_0 \neq 0$, is seen from the observation region as a two-dimensional object rather than as a one-dimensional object. Each point of its surface is now characterized by two coordinates x and z and the nonlinear dependence $\Delta l(\Delta\alpha)$ mentioned above is an indirect consequence of this fact.

Let us find the electric field (or magnetic field) distribution in the plane $A'A''$ with respect to the observation angle $\Delta\alpha$. Let the angle α_0 be chosen so that

$$n_1 = \frac{l_1 \sin\alpha_0}{\lambda} \gg 1. \tag{18}$$

At $\Delta\alpha = 0$, condition (18) means that n_1 spatial periods of the wave traveling horizontally are present on the interval BC, which corresponds to the initial phase parameter of the Fraunhofer diffraction pattern equal to

$\alpha_0 = 2\pi n_1 = 2\pi l_1 \sin\alpha_0/\lambda$. As the observation angle $\Delta\alpha$ increases, the path length difference Δl also grows, which increases the phase parameter by $\Delta l/\lambda$. The field intensity $E(\alpha_0, \Delta\alpha)$ will then be distributed along the $A'A''$ direction by the Fraunhofer law

$$E(\alpha_0, \Delta\alpha) = C_0 \frac{\sin\left(\alpha_0 + \frac{\Delta l}{\lambda}\right)}{\alpha_0 + \frac{\Delta l}{\lambda}}$$

$$= C_0 \frac{\sin\left[\frac{2\pi l_1}{\lambda}(\sin\alpha_0 + \Delta\alpha\cos\alpha_0 - \Delta\alpha^2\sin\alpha_0)\right]}{\frac{2\pi L_1}{\lambda}(\sin\alpha_0 + \Delta\alpha\cos\alpha_0 - \Delta\alpha^2\sin\alpha_0)} \quad (19)$$

$$= C_0 \frac{\sin(b_0 + b_1 D\alpha - b_2\Delta\alpha^2)}{b_0 + b_1\Delta\alpha - b_2\Delta\alpha^2},$$

where $b_0 = b_2 = 2\pi l_1 \sin\alpha_0/\lambda$, $b_1 = 2\pi l_1 \cos\alpha_0/\lambda$, and C_0 is the proportionality coefficient.

Expression (19) is valid when $\Delta\alpha \ll 1$ and, at $\alpha_0 = 0$, goes over to the expression that describes diffraction on a straight slot in a planar screen.

Let us turn again to the analysis of irradiation of the moving surface by a sinusoid-modulated flow assuming that parameter ξ in (6a) varies adiabatically with time as

$$\xi(t) = b_0' - b_1' t - b_2' t^2. \quad (20)$$

The adiabatic variation complies with the condition $|[\xi(t) - \xi(t+\tau)]/\xi(t)| \ll 1$. If the velocity of the surface is constant, $v = \text{const}$, this variation can be related to a change in the frequency ω. Formally, the adiabaticity of the process will be manifested in that the expression (6a) for $A_{\rho 1}(t)$ remains valid and the time dependence is conveyed only through the time dependence of parameter ξ. Hence, we can write

$$A_{\rho 1}(\xi(t)) = \bar{A}_{\rho 1}(t) = C\frac{\sin(b_0' + b_1' t - b_2' t^2)}{b_0' + b_1' t - b_2' t^2}$$

$$= C\frac{\sin\left(b_0' + \frac{b_1'}{v}x' - \frac{b_2'}{v}x'^2\right)}{b_0' + \frac{b_1'}{v}x' - \frac{b_2'}{v}x'^2} = \bar{\bar{A}}_{\rho 1}(x'). \quad (21)$$

In the last equality, we have changed to the spatial coordinate x' under the assumption that $x' = 0$ at $t = 0$.

Expressions (19) and (20) have an identical form. This means that, if the coefficients are chosen appropriately, the distribution of the alternating component of the irradiation intensity in the x' coordinate on the surface will exactly reproduce the diffraction pattern for a single slot rotated by the angle α_0 with respect to the observation plane. The maximum x' that complies with the Fraunhofer conditions can easily be found from the corresponding expressions for the coefficients b_i and b_i'.

In the general case, it can easily be shown that, at fixed v and l_1, slowly varying functions $I_m(t)$ and $\omega(t)$ can always be chosen for an arbitrary two-dimensional object such that, if the intensity of the irradiating flow varies as

$$I(t) = I_0 + I_m(t)\sin[\omega(t)t], \quad (22)$$

the modulation index of the dose rate will be distributed in the x' coordinate as the wave diffracted on this object. Also, it is not necessary to stay within the Fraunhofer approximation, because the above technique can be used to synthesize the diffraction pattern in an arbitrary range of the observation angle.

Let us return to the Fraunhofer diffraction on a periodic spatial array parallel to the observation plane. As we noted above, the diffraction pattern is described in this case by a function similar to (4a). This is due to the fact that, in the one-dimensional case, the two-dimensional Fourier transform, which follows from the electromagnetic theory and is used in the Fraunhofer diffraction theory, coincides with integral transformation (2) to within a constant factor. Therefore, if the moving surface is irradiated by a sinusoid-modulated flux through a one-dimensional slot screen of any configuration, the distribution $A_\rho(\xi)$ observed will always correspond to the Fraunhofer diffraction pattern for an object of the same configuration. Based on this analogy, we may consider variation of the modulation index of the dose rate as a function of the frequency ω and the irradiated surface velocity v as being due to the action of a certain quasi-wave process evolving according to the wave equation in an artificially introduced two-dimensional metric space. Unfortunately, it seems impossible to uniquely define this space. Moreover, it can be shown that any admissible definition of this space prevents defining a metric such that nontrivial invariant transformations would have physical meaning. Nevertheless, applying the term "quasi-diffraction process" to refer to the irradiation of the moving surface is quite justified in our opinion for the following reasons.

First, using this term implies that the commonly accepted and convenient terminology of diffraction spectroscopy is automatically extended to the field of our interest.

Second, using a coherent reference radiation, a real hologram of the slot configuration can be obtained on a moving surface, which can (at least in principle) be used to reconstruct the image of this configuration with the help of the inverse wave process. Of course, this reconstruction is only possible by methods of computer optics [7], but the existence of such a possibility alone suggests that the processes studied in this paper are closely connected to the wave processes.

A technique for creating the above hologram will be described in the second part of the paper.

REFERENCES

1. A. A. Nechaev, V. V. Berezkin, A. I. Vilenskiĭ, *et al.*, Membrany, No. 6, 17 (2002).
2. M. F. Kudoyarov, A. V. Matyukov, and S. A. Mukhin, in *"Membrane-98": Abstracts of Papers, Moscow, 1988*, p. 123.
3. K. I. Zor'ko, M. F. Kudoyarov, A. V. Matyukov, *et al.*, Preprint No. 1743, FTI im. A.F. Ioffe RAN (Ioffe Physicotechnical Institute, Russian Academy of Sciences, St. Petersburg, 2000).
4. Fr. T. S. Yu, *Introduction to Diffraction, Information Processing, and Holography* (MIT Press, Cambridge, 1973).
5. G. V. Zeveke, P. A. Ionkin, A. V. Netushil, *et al.*, *Foundations of Circuit Theory* (Moscow, 1975).
6. W. McC. Siebert, *Circuits, Signals, and Systems* (MIT Press, Cambridge, 1984), Part II.
7. A. V. Goncharskiĭ, V. V. Popov, and V. V. Stepanov, *Introduction to the Computer Optics* (Moscow, 1991).

Translated by A. Khzmalyan

Technical Physics, Vol. 47, No. 10, 2002, pp. 1299–1305. Translated from Zhurnal Tekhnicheskoĭ Fiziki, Vol. 72, No. 10, 2002, pp. 95–102.

OPTICS, QUANTUM ELECTRONICS

Efficiency of Optical-to-Acoustic Energy Conversion upon the Interaction of a Pulsed Laser Radiation with a Liquid: I. Calculation of the Efficiency upon Acoustooptic Interaction

G. V. Ostrovskaya

Ioffe Physicotechnical Institute, Russian Academy of Sciences, Politekhnicheskaya ul. 26, St. Petersburg, 194021 Russia

Received April 10, 2002

Abstract—Relationships for the efficiency of conversion of laser radiation energy to acoustic energy for the acoustooptic (thermal) mechanism of interaction are derived. The cases of short and long laser pulses interacting with the rigid and free boundaries of a heavily absorbing liquid are considered. The efficiency is numerically calculated for the situation when the radiation of a transverse-excitation atmospheric (TEA) CO_2 laser interacts with water with regard for the temperature variation of the volume thermal expansion coefficient of the latter.

INTRODUCTION

Pioneering investigations into laser radiation–liquid interaction date back to the 1960s–1970s. To date, a variety of both theoretical and experimental studies on this subject have been published, including monographs [1, 2] and reviews [3–8] with extensive references therein.

The interaction of laser radiation with liquids depends considerably both on the radiation parameters (energy E_L, laser pulse width τ_L, focusing conditions) and on the properties of the liquid (especially on its absorption coefficient α at a radiation wavelength).

Depending on the energy density absorbed in the surface layer of the liquid, the following mechanisms behind the generation of acoustic and shock waves in the liquid are possible:

(1) For heavily absorbing liquids and low absorbed energy densities, when the temperature of the surface layer is below the boiling point, acoustic waves are generated basically by the acoustooptic (or thermal) mechanism, i.e., are due to thermoelastic stresses arising because of the nonuniform heating of the liquid.

(2) If the absorbed energy exceeds the energy of evaporation, the evaporative mechanism comes into play. In this case, acoustic waves are generated by a recoil momentum arising upon liquid evaporation.

(3) With still higher laser radiation power densities, flash evaporation takes place and the liquid surface or the air–stream mixture over the surface breaks down, causing shock waves in both the liquid and air.

(4) In liquids transparent to laser radiation, volume dielectric breakdown may occur in the liquid if the laser radiation intensity exceeds some threshold value (breakdown threshold).

All the above mechanisms have been considered more or less rigorously in [1–8]. Experimental studies performed with hydrophones and piezoelectric sensors [6, 9, 10], as well as by optical methods [11–13], in a wide range of laser radiation energy densities (covering different interaction mechanisms) show that the measured amplitudes and shapes of the acoustic pulses are in fairly good qualitative and quantitative agreement with theoretical predictions. In the experiments, the highest shock pressures generated upon flash evaporation and dielectric breakdown on the surface reached hundreds and even thousands of atmospheres [10, 13]. This means that associated techniques may find wide application in medical, environmental, and technological problems, as well as in the laboratory simulation of hydrodynamic processes accompanying actual underwater explosions.

However, in applications using acoustic and shock waves generated upon laser radiation–liquid interaction, one should take into account not only the parameters of the waves generated but also the lasing-to-acoustic energy conversion efficiency.

Earlier, the conversion efficiency upon the interaction of laser radiation with liquids was discussed in [2, 5, 8]. In this work, we derive relationships for estimating the energy conversion efficiency η for the acoustooptic mechanism of interaction between pulsed laser radiation and liquids. The efficiency is theoretically calculated for the specific case of interaction between the radiation of a CO_2 laser and water with regard for the temperature dependence of the volume thermal expansion coefficient of the latter.

1063-7842/02/4710-1299$22.00

BASIC RELATIONSHIPS FOR CALCULATING THE CONVERSION EFFICIENCY UPON ACOUSTOOPTIC INTERACTION

The conversion efficiency is defined as the ratio of the energy E_{ac} transferred by a pulsed acoustic (or shock) wave to the energy of laser radiation incident on the liquid surface:

$$\eta = E_{ac}/E_L, \tag{1}$$

where

$$E_{ac} = \int_S \varepsilon_{ac} dS,$$

ε_{ac} is the acoustic energy density passing through the wave front, and S is the surface area of the wave front.

In turn, ε_{ac} can be calculated by the formula

$$\varepsilon_{ac} = \frac{1}{\rho_0 c_0} \int_{-\infty}^{+\infty} [P(t)]^2 dt, \tag{2}$$

where ρ_0 is the initial density of the medium, c_0 is the velocity of sound in the medium, and P is the excess pressure in an acoustic pulse over the initial pressure P_0.

In view of (2), (1) can be recast as

$$\eta = \frac{1}{\rho_0 c_0 E_L} \int_S \left\{ \int_{-\infty}^{+\infty} [P(t)]^2 dt \right\} dS. \tag{3}$$

This relationship can be used in calculating the efficiency for various mechanisms of optical-to-acoustic energy conversion provided that the time profile of the acoustic pulse is known over the entire wave front surface.

When calculating the efficiency in terms of the thermal mechanism, we will take advantage of theoretical relationships for the pressure pulse profile given in [2]. The case under study will be strong absorption, which takes place when the radiation of a CO_2 laser interacts with water. The criterion for strong absorption is $a\alpha \gg 1$, where α is the absorption coefficient (for water, $\alpha = 800$ cm^{-1} at a wavelength of 10.6 μm) and a is the radius of the radiation spot on the liquid surface. In this case, the zone of energy evolution represents a thin disk adjacent to the liquid surface.

The interaction character and the energy conversion efficiency depend considerably on the laser pulse width τ_L and properties of the interface between the absorbing liquid and transparent medium. The interface is considered to be rigid if the acoustic impedance ratio $N = \rho_0 c_0/\rho_{tr} c_{tr}$ for the liquid and transparent medium is much less than unity. This is the case for a liquid–solid interface. For a free interface, such as the air–water interface, the situation is reverse: $N \gg 1$.

SHORT PULSE

If the laser pulse duration is much less than the time it takes for an acoustic wave to travel the distance α^{-1} (short pulse), the pressure pulse profile is given by [2]

$$P_r(\tau) = (\alpha c_0^2 \beta \varepsilon_L / 2c_p) \exp(-\alpha c_0 |\tau|) \tag{4}$$

for a rigid interface and

$$P_f(\tau) = (\alpha c_0^2 \beta \varepsilon_L / 2c_p) \exp(-\alpha c_0 |\tau|) \operatorname{sgn} \tau \tag{5}$$

for the free surface of the liquid. Here, ε_L is the density of the laser radiation energy on the surface, β is the thermal expansion coefficient of the liquid, c_0 is the velocity of sound in the liquid, c_p is the specific heat at a constant pressure of the liquid, $\tau = z - tc_0$, z is the coordinate normal to the surface and directed inward to the liquid, t is the time counted from the instant of optical pulse incidence on the surface.

At relatively small distances from the surfaces, when diffraction can be neglected (for $z \ll L_{DF} = a^2/2c_0\tau_L$, where L_{DF} is the diffraction length), the acoustic pulse front is flat and the pressure distribution over the front is the same as the energy density distribution over the focal spot. Let us put for simplicity that the energy density within the spot of radius a is constant, $\varepsilon_L = E_L/\pi a^2$, and the surface area of the wave front equals that of the focal spot ($S = \pi a^2$). Then, Eq. (3) can be rearranged to the form

$$\eta = \frac{1}{\rho_0 c_0 \varepsilon_L} \int_{-\infty}^{+\infty} [P(t)]^2 dt. \tag{6}$$

Substituting (4) or (5) into (6) and taking the integral yields

$$\eta = \frac{c_0^2 \beta^2 \alpha \varepsilon_L}{4\rho_0 c_p^2} = k_0 \varepsilon_L, \tag{7}$$

where the coefficient $k_0 = (c_0^2 \beta^2 \alpha)/(4\rho_0 c_p^2)$ depends only on the liquid parameters. Specifically, for water at room temperature, $k_0 \approx 10^{-3}$ cm^2/J (in calculations, the values of the parameters were the following: $c_0 = 1.5 \times 10^5$ cm/s, $\beta = 2 \times 10^{-4}$ deg^{-1}, and $c_p = 4.17$ J/(g deg)). Note that (7) coincides with the formula for the efficiency of the thermal mechanism in the linear mode [2, 5, 8]. Since the integrand in (6) is the acoustic pressure squared, the conversion efficiency for the rigid and free interfaces turns out to be the same.

As follows from (7), the conversion efficiency for the thermal mechanism is proportional to ε_L. However, the possibility of increasing η within the thermal mechanism by raising the energy density is limited by the transition to the evaporative mechanism at $\varepsilon_L > \varepsilon_{ev} \approx 1.5$ J/cm^2.

Thus, the maximal efficiency of light-to-sound conversion by the thermal mechanism is no more than sev-

eral fractions of a percent. To attain such a value, the laser pulse duration τ_L must be much less than the time $(\alpha c_0)^{-1}$, which corresponds to $\tau_L \ll 8 \times 10^{-9}$ s.

LONG PULSE AND RIGID INTERFACE

The pulse duration for a typical TEA CO_2 laser far exceeds the time $(\alpha c_0)^{-1}$. The waveform of pulses from the CO_2 laser used in our experiments is depicted in Fig. 1. The pulse consists of a relatively sharp front peak with a half-width $\Delta t_1 \approx 100$ ns and an extended tail ($\Delta t_2 \approx 3$ μs). Thus, the relationship $\alpha c_0 \tau_L \gg 1$ for a long pulse is fulfilled for the whole duration of the pulse and even for its front edge.

For a long pulse and a rigid interface, the time profile of the pressure pulse coincides with that of the laser pulse [2]:

$$P_r(t) = \frac{c_0 \beta I_0}{c_p} f(t). \quad (8)$$

Here, I_0 is the peak intensity (power density) and $f(t)$ is the time evolution of the laser pulse. The quantity I_0 is obviously related to the energy density ε_L as

$$\varepsilon_L = I_0 \int_0^\infty f(t)dt = I_0 t_{eff}, \quad (9)$$

where t_{eff} has the dimension of time and represents the area under the curve $f(t)$.

Substituting (8) into (6) yields the conversion efficiency for a long pulse and a rigid interface:

$$\eta_r = \frac{c_0 \beta^2 I_0}{\rho_0 c_p^2 t_{eff}} \int_0^\infty f^2(t)dt = \frac{4 k_0 \varepsilon_L t_1}{c_0 \alpha t_{eff}^2}, \quad (10)$$

where

$$t_1 = \int_0^\infty f^2(t)dt.$$

To calculate t_{eff} and t_1, we represent the actual function $f(t)$ as the sum of two functions $f_1(t)$ and $f_2(t)$ describing, respectively, the front peak and the tail of the pulse (Fig. 1b). The former can be conveniently taken in the form

$$f_1(t) = A \sin^2(\pi t/2\Delta t_1) + B \cos^2(\pi t/2\Delta t_1), \quad (11)$$

where $A = 1$ at $0 < t < 2\Delta t_1$ and $A = 0$ beyond this interval, while $B = B_0$ at $\Delta t_1 < t < 2\Delta t_1$ and $B = 0$ beyond this interval.

The coefficient B_0 characterizes the relative intensity of the tail and front peak and depends essentially on the composition of the lasing medium of the CO_2 laser. For the pulse shown in Fig. 1a, $B_0 \cong 0.3$.

The tail in the interval $2\Delta t_1 < t < \Delta t_2$, where Δt_2 is the full width of the pulse, is approximated by a straight line given by

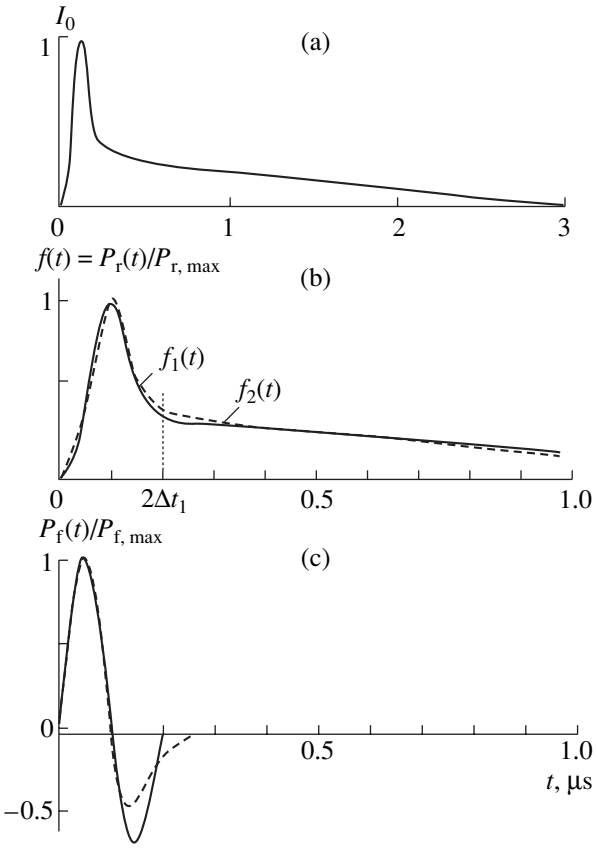

Fig. 1. (a) Waveform of a typical TEA CO_2 laser pulse. (b) Laser pulse profile $f(t)$; dashed curve, actual CO_2 laser pulse; solid curve, its approximation by the sum of functions $f_1(t)$ and $f_2(t)$. (c) Time evolution of the thermoacoustic pulse $P_f(t)$ found by differentiating $f(t)$ with respect to time (dashed curve, actual laser pulse; solid curve, its approximation).

$$f_2(t) = B_0 \frac{(\Delta t_2 - t)}{(\Delta t_2 - 2\Delta t_1)}. \quad (12)$$

Then, for t_{eff}, we have

$$t_{eff} = \int_0^{2\Delta t_1} f_1(t)dt + \int_{2\Delta t_1}^{\Delta t_2} f_2(t)dt = \Delta t_1 \left(1 + \frac{B_0}{2}\right) + \frac{B_0}{2}(\Delta t_2 - 2\Delta t_1). \quad (13)$$

Let us put $\Delta t_1 = 100$ ns and $\Delta t_2 \gg 3$ μs, which corresponds to the pulse in Fig. 1a; then, $t_{eff} \cong 5.3 \times 10^{-7}$ s.

The value of t_1 can be found as

$$t_1 = \int_0^{2\Delta t_1} f_1^2(t)dt + \int_{2\Delta t_1}^{\Delta t_2} f_2^2(t)dt.$$

Integrating yields

$$t_1 = \frac{3}{4}\Delta t_1\left(1 + \frac{1}{3}B_0 - \frac{1}{2}B_0^2\right) + \frac{B_0^2}{3}(\Delta t_2 - 2\Delta t_1).$$

For the values of B_0, Δt_1, and Δt_2 adopted earlier, $t_1 \cong 1.6 \times 10^{-7}$ s.

Substituting t_1 and t_{eff} found previously into (10), we arrive at a computing formula for η_r:

$$\eta_r \approx 1.9 \times 10^{-5}\varepsilon_L \ (\text{J/cm}^2). \quad (14)$$

Thus, in the case of a long pulse and a rigid interface, the optical-to-acoustic energy conversion efficiency is roughly 50 times lower than for a short pulse. At $\varepsilon_L \approx 1.5$ J/cm^2, the conversion efficiency $\eta_r \approx 2.8 \times 10^{-5}$.

LONG PULSE AND FREE SURFACE

In this case, the conversion efficiency is still lower. According to [2], when long laser pulses interact with the free surface, the pressure pulse profile varies as the derivative of the laser pulse:

$$P_f(t) = \frac{1}{\alpha c_0}\frac{dP_r(t)}{dt} = \frac{\beta I_0}{\alpha c_p}\frac{df(t)}{dt}. \quad (15)$$

The waveform of the pressure pulse is depicted in Fig. 1c, where the dashed curve was obtained by differentiating the actual pulse of the CO_2 laser (Fig. 1a) and the continuous curve was found by approximating the function $f(t)$ as before. The pulse generated at the free surface is seen to consist of two, positive and negative, parts, i.e., is bipolar.

Substituting (15) into (6) yields

$$\eta_f = \frac{\beta^2\varepsilon_L}{\rho_0 c_0 \alpha^2 c_p^2 t_{\text{eff}}^2}\int_0^\infty\left[\frac{df(t)}{dt}\right]^2 dt = \frac{4k_0\Phi_t\varepsilon_L}{\alpha^3 c_0^3 t_{\text{eff}}^2}, \quad (16)$$

where

$$\Phi_t = \int_0^\infty\left[\frac{df(t)}{dt}\right]^2 dt. \quad (17)$$

To calculate Φ_t, we use above approximations (11) and (12). Then, in the interval $0 < t < \Delta t_1$, we have

$$\frac{df(t)}{dt} = \frac{\pi}{2\Delta t_1}\sin\frac{\pi t}{\Delta t_1}.$$

For $\Delta t_1 < t < 2\Delta t_1$,

$$\frac{df(t)}{dt} = (1 - B_0)\frac{\pi}{2\Delta t_1}\sin\frac{\pi t}{\Delta t_1},$$

for the tail ($2\Delta t_1 < t < \Delta t_2$),

$$\left(\frac{df(t)}{dt}\right)_{\text{tail}} = -\frac{B_0}{(\Delta t_2 - 2\Delta t_1)}.$$

It is easy to check that $(df/dt)_{\text{tail}}$ is roughly two orders of magnitude less than df/dt in the extrema of the acoustic pulse. Therefore, we can ignore the pulse tail when calculating the efficiency by formula (16), which involves df/dt squared. Integrating (17) with the values of df/dt for the front edge of the pulse, we find that

$$\Phi_t = \frac{\pi^2}{4\Delta t_1}(1 - B_0 + 0.5b_0^2) \approx \frac{1.8}{\Delta t_1}.$$

Substituting Φ_t into Eq. (16), we obtain the computing formula for the conversion efficiency in the interaction of a long pulse with the free liquid surface:

$$\eta_f = \frac{\pi^2(1 - B_0 + 0.5B_0)k_0\Phi_t\varepsilon_L}{\alpha^3 c_0^3 t_{\text{eff}}^2\Delta t_1} \approx 1.5 \times 10^{-7}\varepsilon_L, \quad (18)$$

where ε_L is given in J/cm^2.

For $\varepsilon_L \approx \varepsilon_{ev}$, the conversion efficiency is $\eta_f \approx 2.5 \times 10^{-7}$.

TAKING INTO ACCOUNT THE TEMPERATURE DEPENDENCE OF THE VOLUME EXPANSION COEFFICIENT

All the above calculations of the conversion efficiency were performed in the linear approximation, i.e., under the assumption that the liquid parameters remain constant during the action of a laser pulse. Actually, many of the parameters entering into the formulas derived depend on temperature to some extent or other, which varies when the surface layer is heated by laser radiation. The volume thermal expansion coefficient β depends on temperature to the greatest extent (Fig. 2). The thermal nonlinearity related to the temperature dependence of β was taken into account in [15, 16]. In these works, the effect of the nonlinearity on the shape of the pressure pulse near the liquid surface and in the far zone, respectively, was considered (see also [1, 2]).

We ignore the effect of heat conduction and assume that the dependence $\beta(T)$ is linear:

$$\beta(T) = \beta(T_0) + \left(\frac{d\beta}{dT}\right)_{T_0} T', \quad (19)$$

where T_0 is the initial temperature of the liquid and T' is its variation due to radiation absorption. We also assume that T' varies across the layer as

$$T' = \frac{\alpha\varepsilon_L}{\rho_0 c_P}e^{-\alpha z}. \quad (20)$$

Then, it is easy to find the time profile of the pressure pulse with regard for thermal nonlinearity [2]

when the short pulse acts on the rigid and free surface:

$$P_r(\tau) = (\alpha c_0^2 \beta \varepsilon_L / 2c_p) \times [\exp(-\alpha c_0|\tau|) + N\varepsilon_L \exp(-2\alpha c_0|\tau|)], \quad (21)$$

$$P_f(\tau) = (\alpha c_0^2 \beta \varepsilon_L / 2c_p) \times [\exp(-\alpha c_0|\tau|) + N\varepsilon_L \exp(-2\alpha c_0|\tau|)]\operatorname{sgn}\tau. \quad (22)$$

Here,

$$N = \left(\frac{\alpha}{\rho_0 c_p \beta(T_0)}\right)\left(\frac{d\beta}{dT}\right)_{T_0} \quad (23)$$

is a nonlinear parameter.

Putting $T_0 = 20°C$, $\beta = 2 \times 10^{-4}$ deg^{-1}, and $(d\beta/dt) = 7.2 \times 10^{-6}$ deg^{-2}, we find $N \cong 7$ cm^2/J.

Substituting (21) or (22) into (6) and integrating yields the conversion efficiency for the short pulse in view of thermal nonlinearity:

$$\eta = k_0 \varepsilon_L \left(1 + \frac{4}{3} N\varepsilon_L + \frac{1}{2} N^2 \varepsilon_L^2\right). \quad (24)$$

For the long pulse acting on the liquid surface, the surface temperature grows in time proportionally to the absorbed energy:

$$T(t) = T_0 + \frac{\alpha I_0}{\rho_0 c_p}\int_0^t f(\tau)d\tau = T_0 + \frac{\alpha \varepsilon_L}{\rho_0 c_p t_{eff}}\int_0^t f(\tau)d\tau. \quad (25)$$

Accordingly, β increases as

$$\beta(t) = \beta(T_0)\left[1 + \frac{N\varepsilon_L}{t_{eff}}\int_0^t f(\tau)d\tau\right]. \quad (26)$$

The variation of the surface temperature and thermal expansion coefficient calculated by formulas (25) and (26) with a CO_2 laser pulse approximated as above is shown in Figs. 3a and 3b for various values of ε_L.

Substituting $\beta(t)$ for β in (8), we come to the shape of a pressure pulse generated by the action of the long pulse on the rigid interface in view of thermal nonlinearity:

$$P_r(t) = \frac{c_0 \beta(T_0)\varepsilon_L}{c_p t_{eff}} f(t)\left[1 + \frac{N\varepsilon_L}{t_{eff}}\int_0^t f(\tau)d\tau\right]. \quad (27)$$

The time profile of a pressure pulse generated on the free surface can be found by differentiating (27) with respect to time:

$$P_f(t) = \frac{1}{\alpha c_0}\frac{dP_r(t)}{dt} = \frac{\beta_0 \varepsilon_L}{\alpha c_p t_{eff}} \times \left[\frac{df(t)}{dt}\left(1 + N\frac{\varepsilon_L}{t_{eff}}\int_0^t f(\tau)d\tau\right) + N\frac{\varepsilon_L}{t_{eff}} f^2(t)\right]. \quad (28)$$

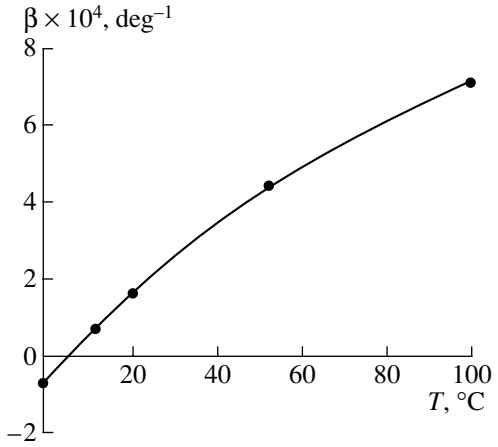

Fig. 2. Temperature dependence of the volume expansion coefficient β for water [14].

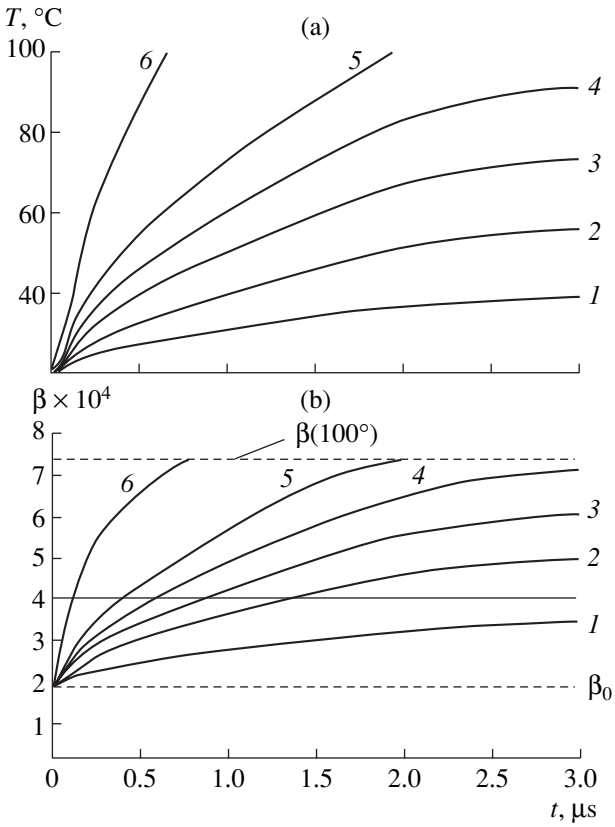

Fig. 3. Variation of the (a) surface temperature and (b) volume thermal expansion coefficient of water during the action of a CO_2 laser pulse. ε_L = 0.1 (*1*), 0.2 (*2*), 0.3 (*3*), 0.4 (*4*), 0.5 (*5*), and 1.0 (*6*) J/cm^2.

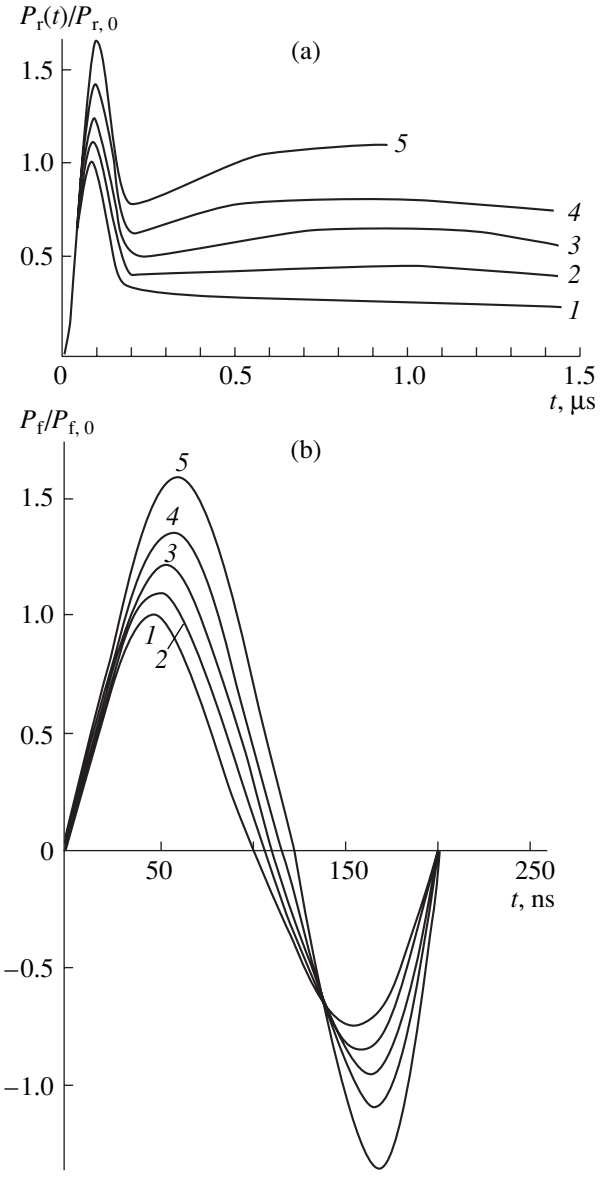

Fig. 4. Time profiles of the pressure pulses generated by the CO_2 laser pulse on (a) rigid and (b) free water surfaces (*1*) with and (*2*) without considering thermal nonlinearity. ε_L = 0.2 (*2*), 0.4 (*3*), 0.6 (*4*), and 1.0 (*5*) J/cm^2.

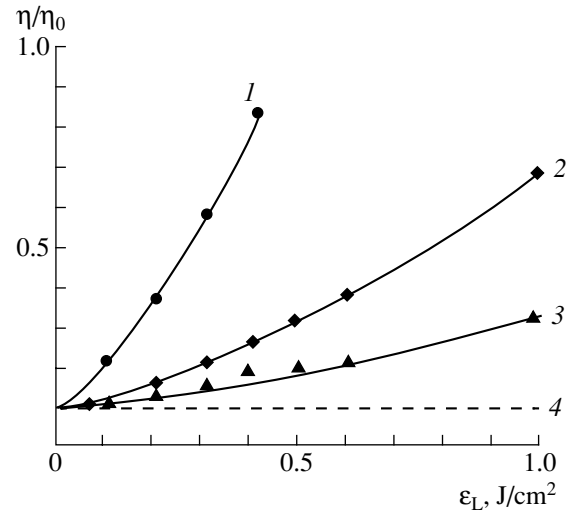

Fig. 5. Effect of thermal nonlinearity in the conversion efficiency for different interaction conditions: (*1*) short pulse, (*2*) long pulse and rigid interface, (*3*) long pulse and free surface, and (*4*) with no regard for nonlinearity.

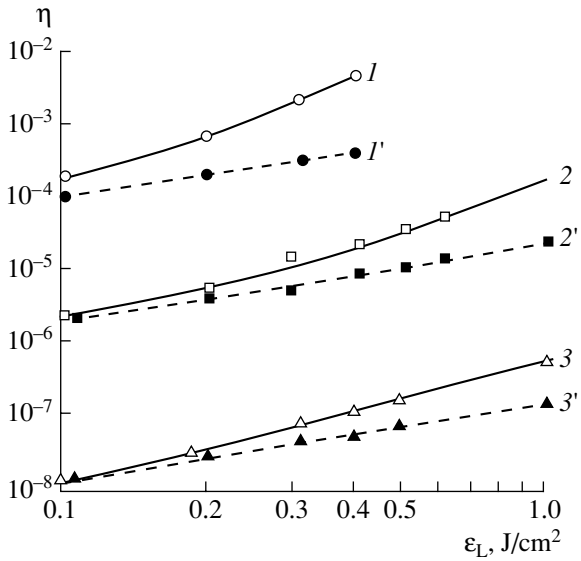

Fig. 6. Absolute values of the efficiency for different interaction conditions: (*1*) short pulse, (*2*) long pulse and rigid interface, (*3*) long pulse and free surface; (*1*–*3*) with regard for nonlinearity and (*1*'–*3*') with no regard for nonlinearity.

Formula (28) can be rearranged to the form

$$\frac{P_f(t)}{P_{f,0}} = \frac{df(t)}{df}\left(\frac{df}{dt}\right)^{-1}_{max} + qF(t), \qquad (29)$$

where $(df/dt)_{max} = \pi/2\Delta t_1$ is the maximum value of df/dt in the linear mode,

$$q = \frac{N\varepsilon_L}{t_{eff}}\left(\frac{df}{dt}\right)^{-1}_{max}$$

is the dimensional parameter characterizing the degree of nonlinearity, and

$$F(t) = \frac{df(t)}{dt}\int_0^t f(\tau)d\tau + f^2(t)$$

is a dimensional function of time.

Results of calculations of the functions $P_r(t)$ and $P_f(t)$ by formulas (27)–(29) including thermal nonlinearity are presented in Figs. 4a and 4b. Here, $f(t)$ was approximated by (11) and (12).

The pressure time profiles thus found were used to estimate the efficiency of laser energy conversion in view of thermal nonlinearity by formula (6). Figure 5 shows the numerical calculations of η_r and η_f (curves *2*, *3*) normalized to the associated values of the efficiency calculated by formulas (14) and (18) with no regard for thermal nonlinearity. Curve *1* in Fig. 5 shows the quantity $\eta/k_0\varepsilon_L$ calculated by formula (24). Dashed line *4* corresponds to the linear approximation ($N = 0$).

The calculations of η by formula (24) was performed for ε_L varying within the interval 0–0.4 J/cm^2, since at larger ε_L, the surface temperature calculated by formula (20) at $z = 0$ exceeds 100°C. Such a situation means that the evaporative mechanism of acoustic wave generation comes into play. The values of η_r and η_f were calculated in a wider range of ε_L, since, for a long pulse, evaporation lags behind the pulse application and the acoustooptic and evaporative pressure pulses are time-separated. In addition, experiments show that the evaporative pulse appears at an energy density $\varepsilon_L \approx 1.5$ J/cm^2, i.e., much greater than 0.4 J/cm^2. This is likely to be associated with the effect of heat conduction at long laser pulses.

The results obtained in this work are generalized in Fig. 6, where the absolute values of the conversion are plotted against ε_L for different interaction conditions with and without regard for thermal nonlinearity. As follows from Fig. 6, the efficiency of laser-to-acoustic energy conversion for the long pulse and rigid interface (curves *2*, *2*') is roughly two orders of magnitude less than for the short pulse (curves *1, 1*'), while for the long pulse and free surface (curves *3, 3*'), the efficiency is less by an additional two orders of magnitude.

The effect of thermal nonlinearity decreases in the same sequence. For the short pulse at $\varepsilon = 0.4$ J/cm^2, the nonlinearity raises the efficiency by one order of magnitude; for the long pulse at the same energy density, the efficiency grows by a factor of 2.5 in the case of a rigid interface and only by a factor of 1.5 if the interface is free. As ε_L rises, the slope of the curves $\eta(\varepsilon_L)$ increases from unity (linear mode) to two (quadratic dependence).

Thus, our calculations shows that for a CO_2 laser radiation energy density of about 1 J/cm^2 or higher, the nonlinearity caused by the temperature dependence of the volume thermal expansion coefficient considerably influences the parameters of the acoustic pulse generated and the efficiency of laser-to-acoustic energy conversion.

In the next work, we will report experimental measurements of acoustic-to-optic conversion efficiency by the method of holographic interferometry.

ACKNOWLEDGMENTS

This work was supported by the Federal Program of Leading Schools of Thought (grant no. 00-15-96771 from the Russian Foundation for Basic Research; the school of thought headed by Academician Yu.N. Denisyuk).

REFERENCES

1. L. M. Lyamshev, *Laser Thermooptical Sound Excitation* (Nauka, Moscow, 1989).
2. V. É. Gusev and A. A. Karabutov, *Laser Optoacoustics* (Nauka, Moscow, 1991).
3. F. V. Bunkin and V. M. Komissarov, Akust. Zh. **19**, 305 (1973) [Sov. Phys. Acoust. **19**, 203 (1973)].
4. F. V. Bunkin and M. I. Tribel'skiĭ, Usp. Fiz. Nauk **130** (2), 103 (1980) [Sov. Phys. Usp. **23**, 105 (1980)].
5. L. M. Lyamshev, Usp. Fiz. Nauk **135**, 637 (1981) [Sov. Phys. Usp. **24**, 977 (1981)].
6. B. S. Maccabee, in *Transaction of Ultrasonic Symposium, IEEE, 1987*, p. 1101.
7. G. V. Ostrovskaya and E. N. Shedova, Preprint No. 1723, FTI im. A.F. Ioffe RAN (Ioffe Physicotechnical Institute, Russian Academy of Sciences, St. Petersburg, 1999).
8. L. M. Lyamshev and K. A. Naugol'nykh, Akust. Zh. **27**, 641 (1981) [Sov. Phys. Acoust. **27**, 357 (1981)].
9. P. Giovanneschi, D. Dufresne, J. P. Caresso, and Ph. Bournet, Appl. Phys. Lett. **36**, 882 (1980).
10. A. F. Vitshas, V. V. Grigor'ev, V. V. Korneev, *et al.*, Pis'ma Zh. Tekh. Fiz. **9**, 1442 (1983) [Sov. Tech. Phys. Lett. **9**, 620 (1983)].
11. I. I. Komissarova, G. V. Ostrovskaya, V. N. Filippov, and E. N. Shedova, Zh. Tekh. Fiz. **62** (2), 34 (1992) [Sov. Phys. Tech. Phys. **37**, 130 (1992)].
12. I. I. Komissarova, G. V. Ostrovskaya, V. N. Filippov, and E. N. Shedova, Zh. Tekh. Fiz. **67** (2), 138 (1997) [Tech. Phys. **42**, 247 (1997)].
13. G. V. Ostrovskaya and E. N. Shedova, Izv. Akad. Nauk, Ser. Fiz. **61**, 1342 (1997).
14. *Tables of Physical Quantities*, Ed. by I. K. Kikoin (Atomizdat, Moscow, 1976).
15. L. V. Burmistrov, A. A. Karabutov, O. V. Rudenko, and E. B. Cherepetskaya, Akust. Zh. **25**, 616 (1979) [Sov. Phys. Acoust. **25**, 348 (1979)].
16. T. A. Dudina, S. V. Egerev, L. M. Lyamshev, and K. A. Naugol'nykh, Akust. Zh. **25**, 622 (1979) [Sov. Phys. Acoust. **25**, 353 (1979)].

Translated by V. Isaakyan

Technical Physics, Vol. 47, No. 10, 2002, pp. 1306–1309. Translated from Zhurnal Tekhnicheskoĭ Fiziki, Vol. 72, No. 10, 2002, pp. 103–106.

OPTICS, QUANTUM ELECTRONICS

On the Possibility of Monitoring Mechanical Displacements by Using Laser Beams of Different Wavelengths

R. S. Asatryan, G. S. Karayan, A. A. Makaryan, and Yu. S. Chilingaryan

Yerevan State University, ul. A. Manukyana 1, Yerevan, 375049 Armenia

e-mail: amakar@www.physdep.r.am

Received July 16, 2001; in final form, February 14, 2002

Abstract—The use of spatially aligned laser beams of two or more different wavelengths from various spectral ranges is proposed to determine the microscopic displacements for different temperature profiles in the medium where the beams propagate. For certain temperature gradients, numerical simulations are performed. © *2002 MAIK "Nauka/Interperiodica".*

For the most part, present-day experiments require information about the mutual disposition of all subsystems in a complex measuring system. The accuracy and reliability of experimental data can be considerably improved through the simultaneous use of a number of independent measurement methods including optical ones. The advantages offered by the latter are a wide variety of thoroughly studied sources and detectors of light, as well as a deep insight into the physical mechanisms behind the propagation of light in various media. The main limitation of the methods used for a given experiment is imposed by the accuracy required when taking into account the smallness of distances to be measured (from several to hundreds of microns), the quasi-continuous mode of measurements (the entire measuring cycle and the processing of data take $\tau_m \approx$ 1 s), and the computerization of measurements.

An example of such a problem is the measurements of vertical shifts of probe-carrying large-diameter radial blocks in the ALICE experiment [1], where not only the measured quantity is random, but the environmental parameters are random as well. The most important of these is the state of the air (temperature inhomogeneities, contaminations, humidity, pressure, etc.). This study considers the possibility offered by optical means to perform measurements in these conditions.

Let a number of identical semitransparent photodetectors be located in a vertical plane in the path of a laser beam, each being rigidly linked to one module of the measuring system. When the beam passes through a stationary uniform medium, variations in the position of each module are measured in real time (within the interval of $\sim 3 \times 10^{-s}$ s) with a certain accuracy. A computer procedure based on statistical averaging over the coordinate of the centroid of the beam yields results with a micron accuracy [2]. Let us denote this quantity for the ith module by a_{0i}.

If a dispersion of the irregular type appears in the medium, the beam shifts additionally and the measured quantities a_i include not only the mechanical displacements of detectors a_{0i} but can be expressed as a sum

$$a_i = a_{0i} + \delta a_i, \tag{1}$$

where δa_i are unknown random quantities that characterize the displacement of the beam from its initial direction for the ith detector.

Assuming that the time of measurement of τ_m is shorter than the time of change τ_g in the dispersion term δa_i and using the formal procedure mentioned above, it is possible to eliminate the additional term δa_i from the system of expressions of type (1). One of the simplest ways to realize this is to employ laser beams of different frequencies, since the refractive index of the kth beam is defined by its wavelength λ_k. Then, Eq. (1) is replaced by the system of equations

$$a_{ik} = a_{0i} + \delta a_{ik}. \tag{2}$$

Here, the subscript k indicates the number of the beam or the number of the wavelength and i denotes the number of the photodetector (in what follows, the subscript i will be omitted unless it is necessary to avoid misunderstanding). The number of different wavelengths to be used in an experiment depends on the particular character of the origination of dispersion in the medium. We assume that the dispersion originates from the temperature nonuniformities. In this case, the refractive index $n(\lambda, T)$ may be described by the empirical formula [3, 4]

$$n(\lambda, T) = 1 + 10^{-4}\left[\frac{77.6p}{T} + \frac{5.84 \times 10^{11} p}{T\lambda^2} - 0.06 p_{\text{W.V.}}\right], \tag{3}$$

1063-7842/02/4710-1306$22.00

where λ is the wavelength expressed in meters, p is the atmospheric pressure ($p_0 = 1.013 \times 10^5$ Pa), and $p_{w.v.}$ is the partial pressure of the water vapor ($p_{w.v.} \approx 1500$–2000 Pa).

For the wavelengths in the optical range, the contribution of the last term is negligibly small and can be ignored. In this case, the refractive index

$$N_\lambda(T) = (n(\lambda, T) - 1) \times 10^4 \quad (4)$$

can be calculated by the multiplicative formula

$$N_\lambda(T) = \frac{p}{T}\left(77.6 - \frac{5.84 \times 10^{11}}{\lambda^2}\right) \equiv f(T)\varphi(\lambda). \quad (5)$$

Relationships (2) and (5) make it possible, by carrying out measurements at two different frequencies, to exclude the $\delta a_k(\lambda, t)$ term from system (2) and to determine a_0. If the refractive index $n(\lambda, T)$ is known, the determination of $\delta a_k(\lambda, T)$ within the approximation of geometrical optics is generally reduced to solving the eikonal equation. However, this problem may be appreciably simplified when certain special models are considered.

A MODEL OF A VERTICAL MOMOGENEOUS LAYER

Let a vertical band of heated air be limited by parallel planes and have a width d. The volume inside this band is characterized by a uniform distribution of temperature T, which exceeds the environmental temperature T_0 (Fig. 1). Because of a change in the refractive index, the initial beam, which is incident at an angle α_0 to the point (y_0, z_0) at the interface, leaves this region at the same angle α_0 at the point $(y, z_0 + d)$ with a certain deviation Δy with respect to the incident beam:

$$\Delta y(\lambda) = d\left(\frac{n_0 \sin\alpha_0}{\sqrt{n^2(\lambda) - n^2 \sin\alpha_0}} - \tan\alpha_0\right). \quad (6)$$

The dispersion-induced deviation of two beams with wavelengths λ_1 and λ_2 from each other is expressed as

$$\Delta(\lambda_1\lambda_2) = d\sin\alpha_0\left(\frac{n_{01}}{\sqrt{n^2(\lambda_1, T) - n_{01}^2 \sin^2\alpha_0}} - \frac{n_{02}}{\sqrt{n^2(\lambda_2, T) - n_{02}^2 \sin^2\alpha_0}}\right), \quad (7)$$

where $n_{01} \equiv n(\lambda_1, T_0)$ and $n_{02} \equiv n(\lambda_2, T_0)$.

Within the technique proposed in [2], the detectors may be used to determine the displacement of a beam by a layer with a thickness $d \cong 5m$ at a temperature difference $\Delta T = 15$ K or $d \approx 3m$ at $\Delta T = 25$ K (see Table 1).

The use of the two-beam method in this case allows the estimation of the air-layer thickness d via the direct measurement of a_1 and a_2 taking into account (7) and the condition $\Delta(\lambda_1, \lambda_2) = a_1 - a_2 = \delta a_1 - \delta a_2$.

The use of three beams within this approximation makes it also possible to determine the preheated region temperature T if the environmental temperature T_0 is known.

A MODEL OF THE VERTICAL GRADIENT OF TEMPERATURE

Let an infinite layer of heated air occupy the interval $[0, d]$ and have a constant temperature gradient g_z in the $0z$ direction. Dividing the length $[0, d]$ into uniform layers of thickness dz and assuming a constant refractive index n_i in the range $[z_i, z_i + dz]$, we have

$$n_0 \sin\alpha_0 = n_i(z_i, y_i)\sin\beta_i(z_i, y_i), \quad dz = \cot\beta dy. \quad (8)$$

The system of Eqs. (8) enables one to determine both the direction of the beam coming out of the layer and the deviation from the direction of incidence. Choosing the origin of coordinates at the point where the beam enters the layer and restricting ourselves to a linear approximation, we obtain $n(T, \lambda)$ in the form

$$n(T(y), \lambda) = \bar{n} + \left.\frac{\partial n}{\partial T}\right|_{(0,0)} \frac{dT}{dy} = \bar{n} - \frac{f(0,0)\varphi_\lambda g_y y}{T} - \frac{f(0,0)\varphi_\lambda g_z z}{T}, \quad (9)$$

where $\bar{n} = 1 + f[T(0, 0)]\varphi(\lambda)$ is the refractive index in the first layer with a width dz.

In line with the model of the vertical gradient of temperature, one must substitute $g_y = 0$ in (9). Then, the "trajectory" of the beam in the yOz plane can be

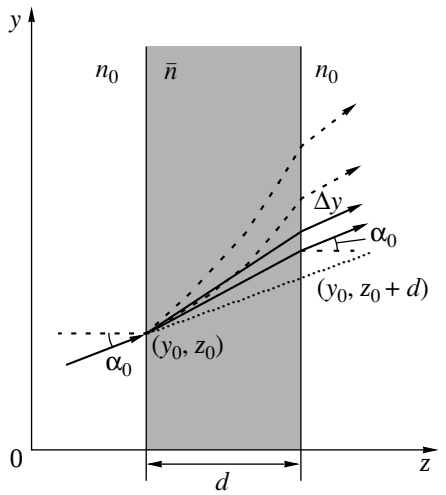

Fig. 1. The trajectories of two beams with different wavelengths (dashed line) in the presence and (solid line) in the absence of a temperature gradient.

Table 1. The dispersion-induced deviation of beams with different wavelengths in the model of vertical uniform layer of preheated air

d, (m)	ΔT = 5 K		ΔT = 15 K		ΔT = 25 K	
	$\Delta(\lambda_1, \lambda_2)$ (μm)	$\Delta(\lambda_1, \lambda_3)$ (μm)	$\Delta(\lambda_1, \lambda_2)$ (μm)	$\Delta(\lambda_1, \lambda_3)$ (μm)	$\Delta(\lambda_1, \lambda_2)$ (μm)	$\Delta(\lambda_1, \lambda_3)$ (μm)
1	0.37	0.48	1.05	1.4	1.71	2.26
2	0.54	0.72	1.59	2.1	2.56	3.39
3	0.73	0.96	2.12	2.8	3.42	4.52
4	0.91	1.2	2.65	3.5	4.27	5.65
5	1.1	1.45	3.17	4.2	5.13	6.77

Note: Hereafter, the results of numerical simulations are presented for beams with wavelengths $\lambda_1 = 0.25 \times 10^{-6}$ m, $\lambda_2 = 0.45 \times 10^{-6}$ m, and $\lambda_3 = 0.85 \times 10^{-6}$ m.

Table 2. The dispersion-induced deviations of beams with different wavelengths in the model of vertical gradient of temperature

d, (m)	g_z = 50 K/m		g_z = 100 K/m		g_z = 500 K/m	
	$\Delta(\lambda_1, \lambda_2)$ (μm)	$\Delta(\lambda_1, \lambda_3)$ (μm)	$\Delta(\lambda_1, \lambda_2)$ (μm)	$\Delta(\lambda_1, \lambda_3)$ (μm)	$\Delta(\lambda_1, \lambda_2)$ (μm)	$\Delta(\lambda_1, \lambda_3)$ (μm)
1	3.95	5.22	7.54	9.96	36.29	47.95
2	8.62	11.39	16.7	22.06	81.44	107.6
3	15.08	19.93	29.44	38.9	144.65	191.11
4	23.34	30.84	45.78	60.49	225.95	298.52
5	33.39	44.12	65.72	86.83	325.39	429.89

determined as

$$y = \frac{c_0 T^2 10^4}{p_0 \varphi_\lambda g_z} \times \left[\operatorname{arccosh}\frac{\bar{n}}{c_0} - \operatorname{arccosh}\frac{\bar{n} - \dfrac{10^{-4} p_0 \varphi_\lambda g_z}{T} z}{c_0} \right], \quad (10)$$

where $c_0 \equiv n_0 \sin\alpha_0$.

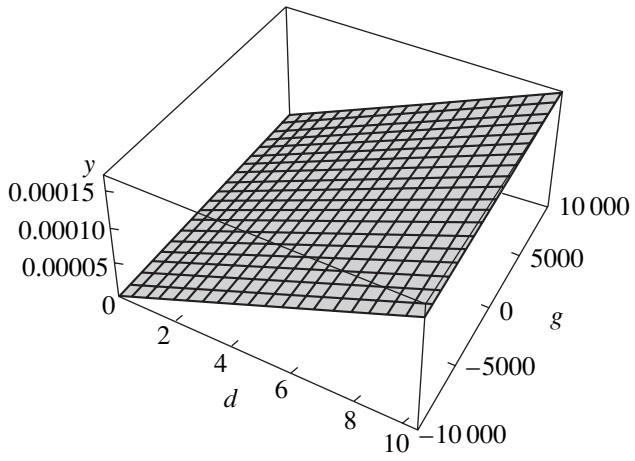

Fig. 2. Beam shift as a function of the heated-air-layer thickness and the vertical gradient of temperature.

Table 2 presents the numerically calculated deviations of three beams with different wavelengths from each other at different temperature gradients.

Measurements performed using three different wavelengths allow the determination of two unknown characteristics of the heated air (for example, the gradient g_z and $f[T(0, 0)]$ with d and p_0 given). Figure 2 illustrates the beam shift as a function of the air-layer thickness and the vertical gradient of temperature.

A MODEL OF THE HORIZONTAL GRADIENT OF TEMPERATURE

This model deals with the case where the temperature field varies uniformly along the $0Y$ direction. Within this model, the horizontal layer of air within the range $[y_i, y_i + dy]$ can be characterized by a constant refractive index n_i. Then, the system of equations (8) appears in the following form:

$$n_0 \cos\alpha_0 = n_i(z_i, y_i) \sin\beta_i(z_i, y_i), \quad dz = \cot\beta dy. \quad (8')$$

The refractive index can be found by taking into account that the gradient along the $0Z$ direction in expression (9) is zero and

$$n(y, \lambda) = \bar{n} - \frac{f(0, 0)\varphi_\lambda g_y y}{T}. \quad (9')$$

Table 3. The dispersion-induced deviations of beams with different wavelengths for different horizontal gradients of temperature

d, (m)	g_y = 50 K/m		g_y = 100 K/m		g_y = 500 K/m	
	$\Delta(\lambda_1, \lambda_2)$ (μm)	$\Delta(\lambda_1, \lambda_3)$ (μm)	$\Delta(\lambda_1, \lambda_2)$ (μm)	$\Delta(\lambda_1, \lambda_3)$ (μm)	$\Delta(\lambda_1, \lambda_2)$ (μm)	$\Delta(\lambda_1, \lambda_3)$ (μm)
1	215.71	284.17	30.87	40.9	8.13	10.74
2	498.78	658.57	80.52	106.38	29.24	38.63
3	903.14	1192.19	153.11	202.27	61.75	81.59
4	1430.89	1888.4	248.73	328.57	105.68	139.62
5	2084.78	2750.68	367.49	485.43	161.05	212.76

The solution of the system (8'), (9') is similar to (10) but with the coordinates x and y being interchanged. For numerical simulations, one may use a simpler expression obtained from this solution by retaining the first and second terms in the expansion in the arcsine function:

$$z = \frac{y}{\left(\frac{\bar{n}^2}{c^2} - 1\right)} + \frac{\frac{\bar{n}}{c}}{2\left(\frac{\bar{n}^2}{c^2} - 1\right)^{3/2}} \frac{p_0 10^{-4} \varphi_\lambda g_y}{cT^2} y^2, \qquad (10')$$

where $c_0 \equiv n_0 \cos\alpha_0$.

Table 3 presents the numerically calculated deviations of the beams from each other, and Fig. 3 shows the beam shift as a function of the air-layer thickness and the horizontal gradient of temperature.

The method proposed above for detectors with a given accuracy [2, 5, 6] may turn out to be effective for either large temperature gradients along the heated air layers of small thicknesses or for large dispersion regions with small temperature gradients.

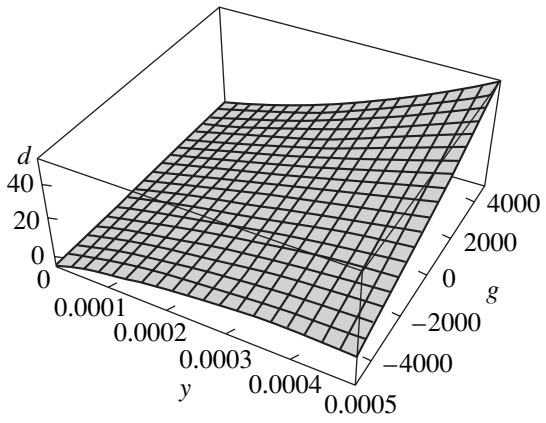

Fig. 3. Beam shift as a function of the heated-air-layer thickness and the horizontal gradient of temperature.

To apply our method when a minimal value of the measured displacement is specified requires new methods for data acquisition that have a certain predetermined accuracy.

In conclusion, it should be noted that the multibeam method of measuring relative displacements may find a wide range of applications, for example, in the fields of meteorological, seismological, and technological studies.

ACKNOWLEDGMENTS

This study was supported by an INTAS-CERN program, grant no. 99-00118.

REFERENCES

1. ALICE Experiment. CERN/LHCC 95-71. LHCC/P3 (1995).
2. V. D. Danielyan and V. H. Margaryan, *Reflected Light Monitor for Molty-Point Position Measurements*, ALICE/99-27. Internal Note/DIM (1999).
3. A. A. Grigoryan and A. A. Teymurazyan, *Light Ray Displacements Due to Air Temperature Gradient*, ALICE/2000-13. Internal Note/DIM (2000).
4. B. Edlen, J. Opt. Soc. Am. **43**, 339 (1953).
5. A. S. Gurvich *et al.*, *Laser Emission in Turbulent Atmosphere* (Nauka, Moscow, 1976).
6. S. Grigoryan, H. Gulkanyan, and H. Karayan, *Exploiting Light Beams of Different Wavelength in the Optical Monitoring Systems*, ALICE/2000-xx. Internal Note/DIM (2000).

Translated by A. Sidorova

Technical Physics, Vol. 47, No. 10, 2002, pp. 1310–1315. Translated from Zhurnal Tekhnicheskoĭ Fiziki, Vol. 72, No. 10, 2002, pp. 107–113.

**SURFACES,
ELECTRON AND ION EMISSION**

Promising Variants of Single Crystal Tungsten Electrodes for High-Performance Thermionic Converters

V. P. Kobyakov

Institute of Structural Macrokinetics and Materials Science Problems, Russian Academy of Sciences, Chernogolovka, Moscow oblast, 142432 Russia

Received July 19, 2001; in final form, January 29, 2002

Abstract—New variants of tubular single crystal tungsten electrodes with an electron work function of 5.3–5.7 eV are considered. An appreciable increase in the work function is achieved due to special technologies ensuring the "monofaceting" of a cylindrical electrode surface and doping of the vapor-phase-grown epitaxial tungsten with oxygen. © *2002 MAIK "Nauka/Interperiodica".*

INTRODUCTION

Methods for producing crystallographically oriented tungsten electrodes have been developed during the second half of the last century in connection with the problem of obtaining effective high-temperature emission electrodes, in particular, for thermionic converters (TCs). The most close-packed tungsten face (110) is of most interest for use in modern TCs with an easily ionized additive of cesium in the interelectrode gap, because this face provides the maximum coverage of tungsten surface during high-temperature adsorption of cesium. To achieve this purpose, different approaches were used in the USSR and in the West. The use of tungsten electrodes in the form of single crystal tubes [1] became a basic R&D concept for the main scientific centers engaged in thermoemission investigations in the USSR. The main advantages of this approach are the greatly improved stability of the electrode and TC characteristics as well as the possibility of solving the problem of fuel component diffusion through the emitter cladding of TCs. An alternative concept has been adopted and, apparently, still exists in Western countries [2, 3]. This approach is based on using tubular electrodes with an external coating of polycrystalline "chloride" tungsten with an axial ⟨110⟩ texture. These electrodes are commonly referred to as duplex electrodes since they contain an inner layer of the "fluoride" tungsten with an axial ⟨100⟩ texture formed on a textureless polycrystalline molybdenum substrate. The growth techniques used in both cases employ vapor phase epitaxy. According to one method, tungsten is deposited from a chloride medium (the Western technology, unlike the "transport" process developed in the USSR, employed a chloride medium flow through a reactor in which tungsten is deposited); alternatively, the deposition proceeds from a fluoride medium. Apparently, the choice of "duplex" technology was caused by economic reasons only because the cost of single crystal refractory metals was much higher in Western countries than in the USSR. As to the emission properties, both concepts of tungsten electrodes (cf. Fig. 1a for USSR and Fig. 1b for USA and other countries) in the original variants were almost the same. In both cases, the electron work function of the cylindrical electrodes was about 4.9–5.0 eV [2–4].

The much greater high-temperature strength of single crystal tungsten cladding in comparison with polycrystalline (including textured) electrodes was unexpectedly found [5], but this fact is not discussed here in detail. The paper focuses on the prospects for improving the emission properties of tungsten electrodes for TCs. In this respect, the characteristics of polycrystalline textured tungsten electrodes have hardly changed over the last 50 years, while the emission and adsorption properties of single crystal tungsten electrodes have greatly increased.

EXPERIMENTAL

In the most general case, a polyface tube with a [111] axial orientation and, hence, with six [110] poles emerging at a lateral cylindrical surface (Fig. 1a) can be considered as the base variant of a single crystal tungsten electrode for TCs. The term "polyface lateral surface of a single crystal tube" means that, depending on the axial crystallographic orientation of the tube, one or another set of poles (repeating a certain number of times) emerges at this surface to form a crystallographic belt. For bcc lattices, the aforementioned axial orientation is known to be preferred since it features a maximum possible number of poles with the most favorable orientation [110] emerging at the lateral surface. As was mentioned above, the effective work function of such a tube is 4.9–5.0 eV. Numerous and various attempts to increase the area occupied by (110) facets on the lateral surface of a polyface tube (for example, by etching) were of limited success, the more so as the thermal stability of such faceted surfaces was insufficient. In this connection, our investigations were

1063-7842/02/4710-1310$22.00

mainly focused on finding technological solutions ensuring the obtaining of single crystal tungsten electrodes possessing a much higher electron work function. This was achieved either by forming single-face tubes with (110) orientation at any point of the lateral surface (Figs. 1c–1e) or by doping tungsten with active microadditives that will be discussed below.

Two technological methods were developed in order to manufacture single-face tubular electrodes. One of these employs the chemical (chloride) vapor-phase epitaxial deposition of tungsten onto a cylindrical molybdenum substrate with [111] axial orientation, whereby the growing layer is self-faceted by (110) planes (Figs. 1c and 2). This technology is based on a chemical transport reaction whose main stages are separated in space inside a crystallizer reactor [6]. The thermal dissociation of chloride and tungsten deposition proceed on a heated substrate at temperatures 1700–1800 K according to the reaction

$$WCl_6 = W\downarrow + 3Cl_2\uparrow.$$

The reaction of chloride synthesis with its subsequent sublimation takes place in a tungsten supply unit operating at temperatures 1100–1300 K:

$$W + 3Cl_2 = WCl_6\uparrow.$$

When an epitaxial tungsten layer was grown, the molybdenum substrate was etched-off. The tungsten electrodes obtained using this technology had a hexahedral outer surface with smoothed edges and a round cylindrical inner surface.

Alternatively, a single-face electrode with inner and outer cylindrical surfaces was produced by bending (through winding on a mandrel) a single crystal ribbon with (110) orientation, followed by electron-beam welding of workpieces along a helical line (Figs. 1c, 3). This technique not only ensured the total exposure of the most effective face (110) on the lateral surface, but produced substructural hardening of this surface as well. This method was developed in collaboration with V.A. Kononenko and A.I. Dekhtyar (Institute of Metal Physics, National Academy of Sciences of Ukraine).

This paper gives a brief description of all the aforementioned promising technologies and presents the main results of investigations of the impurity composition (ion microprobe, Auger spectroscopy) and of the effective thermoemission work function of the samples. The thermoemission measurements were carried out by the method of total current using a setup described in [7]. The measurement error is indicated in one of the temperature dependences presented and considered in the next section.

RESULTS AND DISCUSSION

All variants based on chemical vapor deposition technology were realized using an apparatus designed at the Sukhumi Physicotechnical Institute in collaboration with the Department of Physical Metallurgy of the Moscow Engineering Physics Institute (MEPI). The contribution of the author was in designing an all-metal crystallizer reactor for tungsten deposition from a chloride vapor phase [8, 9]. The technique of epitaxial "chloride" tungsten deposition onto tubular single crystal molybdenum substrates was developed in parallel with similar works at the MEPI and the Scientific Research Institute of the Luch Corporation. However, MEPI and Luch [10–12] obtained tungsten single crystals faceted by planes (211). Previously [13], we showed that there are methods allowing one to change the indices of habit planes and to grow crystals faceted by planes (110) with acceptable rates (up to 0.1 mg/cm^2 s). One method consists in doping deposited tungsten with oxygen microadditives. In this case, we obtained hexahedral single crystal tubes (Figs. 1c, 2) with (110) face orientation. A minimum thickness of the tungsten layer in the cross-section was 1–2 mm. When layers of such a thickness were deposited, the substrate orientation was found to be retained in the regimes of vapor phase deposition ensuring spatially matched orienting effects of the substrate (epitaxial growth) and of the crystallization process (texture formation) [14]. The study of microstructure by optical and electron microscopy [15] showed that, when the spatial matching conditions are observed, the quality of orientation of a deposited layer is not deteriorated but even tends to increase with thickness. A dislocation ensemble in epitaxial tungsten

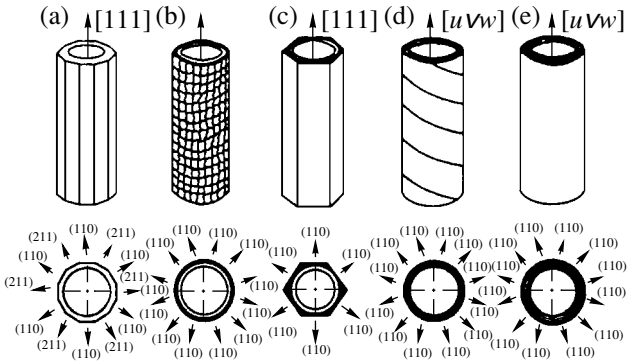

Fig. 1. Main variants of tubular tungsten electrodes for TCs representing (a, c, d, e) single crystal concept (USSR, Russia) and (b) "duplex" texture concept (USA, Western Europe): (a) polyface electrode with ⟨111⟩ axial orientation of "chloride" epitaxial tungsten; (b) polycrystalline electrode comprising the first layer of "fluoride" vapor phase grown tungsten with (100) texture and the outer layer of "chloride" vapor phase grown tungsten with (110) texture; (c) single-face oxygenated "chloride" epitaxial tungsten self-faceted by six (110) planes; (d) single-face (110) cylindrical electrode with substructural hardening, fabricated from undoped tungsten by crucibleless electron beam zone melting under "deformation" technology; (e) case (d) modified by "chloride" epitaxial layer of oxygenated tungsten. Top view: blackened regions—"chloride" layer; open circular regions—molybdenum substrate; dashed regions—polygonized substructural hardened layer.

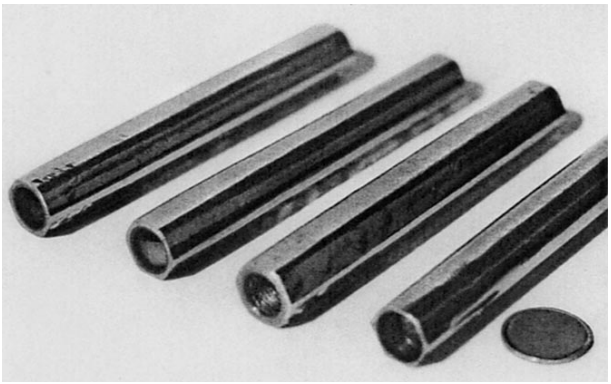

Fig. 2. single-face electrodes of oxygenated "chloride" epitaxial tungsten self-faceted by six planes (110).

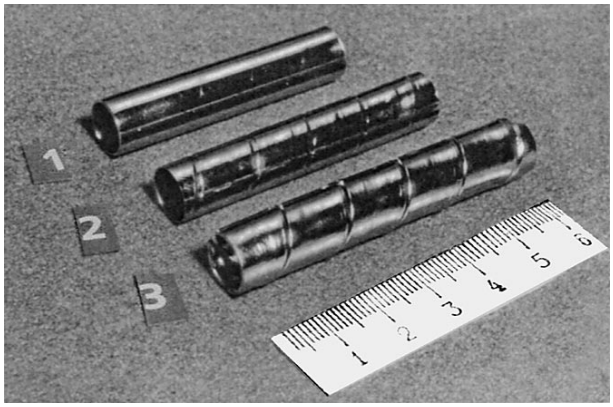

Fig. 3. single-face (110) cylindrical electrodes with substructural hardening of undoped tungsten obtained by crucibleless electron beam zone melting in different stages of "deformation" technology: (*1*) after winding the ribbon on a mandrel; (*2*) after electron beam welding with a helical weld; (*3*) after mechanical polishing and electropolishing.

appeared spontaneously as a result of the formation of misfit dislocations, which compensated the misfit in lattice parameters of the substrate and the deposit. The density of dislocations estimated from etch pits averaged about 10^8 cm^{-2}.

The investigations of such electrodes using an ion microprobe (Cameca IMS-3F) showed [16] that, in the absence of specially introduced oxygen, the total content of impurities in the material did not exceed 10^{-2} wt %. The content of interstitial impurities (C, N, O) is about 10^{-5}–10^{-4} wt %, the concentration of regular contaminants (Na, Mg, Al, Si, K, Ca) is 10^{-4}–10^{-3} wt %, and the content of elements representing the material of apparatus (Ti, Cr, Fe, Cu) is 10^{-6}–10^{-5} wt %. The molybdenum concentration is about 10^{-2} wt %. This technological impurity is unavoidable in "chloride" tungsten deposited onto a molybdenum substrate. However, it is known [17] that the presence of even a few percents of molybdenum on tungsten surface does not change the work function. From this standpoint, the investigated tungsten was rather pure material with respect to all groups of the impurities. This fact was confirmed by the thermoemission measurements of the effective work function of (110) faces for the hexahedral single crystal electrodes, which amounted on average to 5.2–5.3 eV.

When a dozed oxygen additive was introduced into the gas phase during the epitaxial crystallization of tungsten, the oxygen concentration increased in a solid deposit as well. The oxygen content could be varied within a rather wide range (10^{-5}–10^{-2} wt %). The oxygen concentrations in epitaxial tungsten determined by the ion microprobe and by the method of fast neutron activation coincided satisfactorily. Indeed, the oxygen concentration measured by the ion microprobe in the sample investigated in [16] was about 1.0×10^{-3} wt %, while the neutron activation analysis showed 1.7×10^{-3} wt %. The tungsten with increased oxygen content is referred to as oxygenated tungsten. As will be shown below, oxygenated epitaxial tungsten exhibits a sharp change in the emission properties.

It was shown [5] that, under conditions of the high-temperature creep (T = 1870 K, σ = 10 MPa, τ = 1000 h) the dimensional stability of oxygenated epitaxial tungsten tubes is characterized by a creep rate which, in our case, falls within 10^{-9}–10^{-8} s^{-1}. Such a level of the creep straining rate is more typical of the "chloride" epitaxial tungsten deposited on single crystal molybdenum. In [5], these rather low creep rates (much lower than those observed in polycrystalline tungsten) were explained by substructural hardening of the material as a result of polygonization of the tungsten substructure. The polygonized substructure was formed spontaneously during the epitaxial growth of tungsten on molybdenum due to the generation of misfit dislocations at the deposit–substrate interface.

In the "deformation" technique, single-face (110) electrodes were obtained by helical winding a single crystal tungsten ribbon with orientation (110) under conditions of pure bending at a temperature of about 1000 K (Figs. 1d, 3). The initial unstrained tungsten ribbon was obtained by cutting (along the corresponding axis) single crystal ingots oriented in a certain manner. The ingots were produced by crucibleless electron beam zone melting. The regimes of electron beam welding of the workpieces along a helical line and subsequent heat treatment ensured a single crystal structure of the weld material. X-ray diffraction studies showed that electrodes fabricated by this technology are characterized by an orientation close to (110) at any point of the external cylindrical surface, with a disorientation of the neighboring regions within 20–30 angle minutes. The cross section of subgrains in tungsten did not exceed 100 μm and the dislocation density was 10^9–10^{10} cm^{-2}.

After appropriate heat treatments, a polygonized substructure of dislocations of the same sense was formed in the bending strained tungsten that provided substructural hardening of the material. As to the con-

centration of impurities, the material was almost identical to that of the "chloride" tungsten electrodes (without additionally introduced oxygen) considered above, except for a molybdenum impurity, which was almost absent here. However, the effective work function of such welded electrodes was not higher than 5.0 eV. This can be probably explained by the appreciable density of structural defects formed in the material as a result of deformation and polygonization processes in various stages of the manufacture of cylindrical single-face electrodes. It might seem that such a work function may restrict the potential of "deformation" technology to manufacture cylindrical single-face electrodes. However, the increased dislocation density, which is responsible for the lower work function [18], simultaneously accounts for the increasing adsorption ability of the material surface. This is also valid for the adsorption of cesium vapor present in the interelectrode gap of modern TCs. On the other hand, such single-face electrodes offer a decisive advantage because of their long-term stability under creep conditions. The test results obtained in the Scientific Research Institute of the Luch Corporation (P.V. Zubarev and N.G. Tachkova) are worth mentioning here. The long-term (700 h) creep tests of such electrodes were carried out at a temperature of 2070 K under conditions of internal inert gas pressure equivalent to a tangential bulging load of 10 MPa. The tests showed quite small initial deformation (less than 0.1%) and a low rate of the steady-state creep (1.2×10^{-9} s^{-1}). The tests carried out at the Institute of Metal Physics of the National Academy of Sciences of Ukraine [5] at the same values of temperature and bulging pressure (the latter was produced by multipoint mechanical loading) during 2000 h showed an initial deformation of 0.2–0.3% and the lowest rate of the steady-state creep (10^{-11}–10^{-10} s^{-1}).

Let us consider the problem of doping single crystal tungsten with an active oxygen microadditive. Of course, the impossibility of oxygen dissolution in the ideal tungsten single crystal due to the specific configuration of its valence electron shells [16] is a well-known fact. In real tungsten, the presence of structural defects accounts for a small equilibrium solubility of oxygen (0.005 wt % at 1973 K [19]). However, as mentioned above, we revealed the essentially higher solubility of oxygen in "chloride" epitaxial tungsten when studying the effect of impurities on the work function of single crystal tungsten [16, 20, 21].

The results of investigations of the (110) surface of oxygenated "chloride" epitaxial tungsten using the high-temperature Auger electron spectroscopy are shown in Fig. 4. The complete removal of carbon from the tungsten surface heated to 1300 K (i.e., a kind of the sample self-cleaning from carbon) is a rather unexpected effect because it seems absolutely improbable for ordinary tungsten. A broad minimum on the oxygen profile (curve *2*) in this temperature interval is probably related to the fact that oxygen emerging at the surface

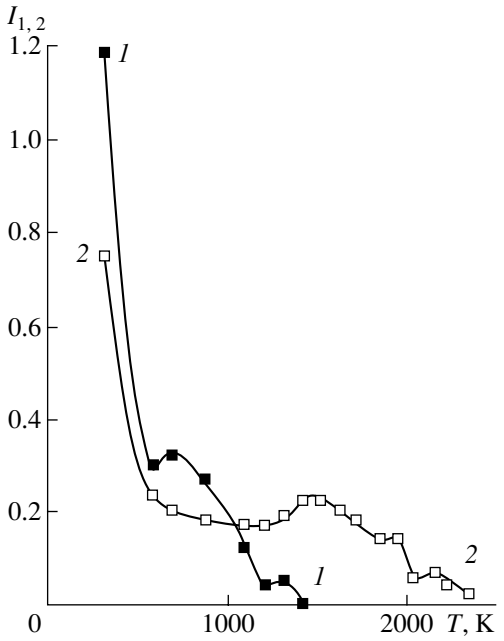

Fig. 4. Temperature dependence of the normalized Auger signal amplitude for carbon I_1 (*1*) and oxygen I_2 (*2*) on the (110) face surface of oxygenated "chloride" epitaxial tungsten (normalized to the tungsten peak at 169 eV).

is consumed to form carbon oxide. From this it follows that the surface of oxygenated tungsten studied in our experiments did not contain carbon but oxygen was present. This conclusion is valid for the temperature range where the work function measurements, both presented above and considered below, were carried out. The oxygen peak amplitude gradually decreases when the temperature rises above 1300 K (see Fig. 4), but up to 2273 K a considerable part of the crystal surface remains coated by a monolayer of oxygen.

A correlation between the oxygen impurity content and thermoemission work function was established in [16, 20, 21]. We proposed a physical model explaining the possible incorporation of oxygen atoms into the tungsten lattice during the "chloride" chemical vapor deposition process in the case when the vapor phase contains a certain amount of oxygen. This model is based on the assumption about the reconstructive formation of surface tungsten suboxide at the crystallization front of a growing face, with layer-by-layer "immuring" of oxygen in the volume of the growing crystal. Tungsten crystals grown under such conditions possess a significantly increased work function. The effective work function of the (110) face for such tungsten varies from the tabulated value of 5.3 up to 5.7 eV, depending on the oxygen content. This considerable oxygen-induced effect is best characterized by the temperature dependences (polytherms) of the work function (see, for example, Fig. 5). For single crystal tungsten with an oxygen content above $> 5 \times 10^{-4}$ wt %, the work function sharply increases with temperature. The

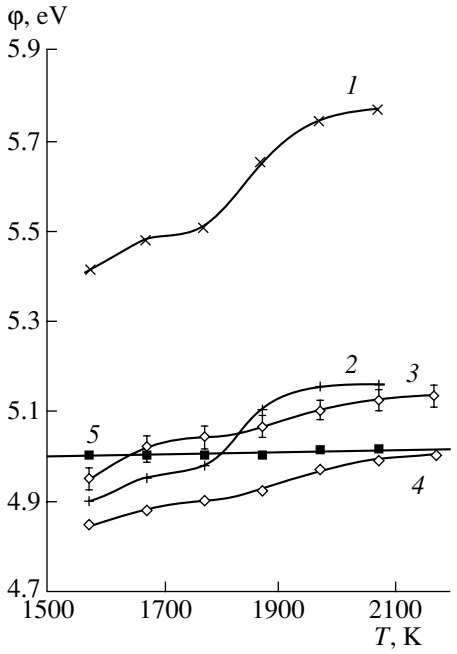

Fig. 5. Work function polytherms of oxygenated "chloride" tungsten self-faceted by six planes (110): (*1*) after growth; (*2*) after turning up to a cylindrical surface and electropolishing; (*3*, *4*) similar samples not finally faceted by (110) planes (with a polyface lateral surface); (*5*) cylindrical substructural hardened sample of undoped tungsten obtained by crucibleless electron beam zone melting ("deformation" technology). Oxygen content in the samples (wt %): (*1*) 2.3×10^{-2}; (*3*) 1.7×10^{-2}; (*4*) 4.6×10^{-3}; (*5*) 6.7×10^{-5}.

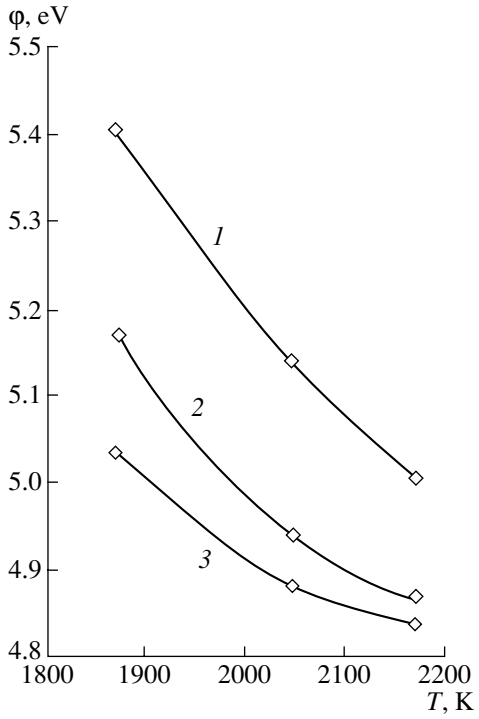

Fig. 6. Work function polytherms of (110) face for a tungsten sample cut from a single crystal ingot grown by crucibleless electron beam zone melting at different partial oxygen pressures from "external" source: (*1*) 10^{-4}; (*2*) 10^{-5}; (*3*) 10^{-6} Pa (data from [22]).

presence of two, usually sloped, plateaus on this dependence is a typical feature. The first plateau is observed in the temperature interval 1700–1900 K and the second, at temperatures above 2000 K. The temperature dependences of the work function for oxygen-free tungsten differ sharply from the ones described. Usual linear temperature dependences with a very slight increase in the work function in the temperature range from 1500 to 2500 K (Fig. 5) are registered if the measurements are carried out in sufficiently high vacuum. This behavior was repeatedly confirmed, including the experiments with vapor-phase-grown tungsten [16]. It is interesting to note that, when the work function measurements for oxygen-free tungsten were carried out at various small oxygen partial pressures sufficient to form a fraction of a monolayer on the tungsten surface, we observed a pattern (Fig. 6) opposite to that typical of oxygenated tungsten (Fig. 5). It is clear from Fig. 6 that, at the beginning of the temperature interval studied, there is a maximum and very significant oxygen effect and, as the temperature increases, the work function sharply decreases due to intensification of oxygen desorption from the tungsten surface.

Thus, we can conclude that a considerable growth in the work function of the tungsten electrode with increasing temperature is typical only of the oxygenated tungsten obtained by the chloride vapor-phase technique. According to the above, oxygen desorption from the tungsten volume is a thermally activated process and this very circumstance determines the temperature dependence of the work function of oxygenated tungsten. Leaving the crystal volume, oxygen forms different states on the tungsten surface, depending on the temperature. According to [20, 23], a low-temperature branch of the work function polytherm (up to a temperature of about 1800 K) is determined by the presence of tungsten suboxide W_3O (which is thermally stable at these temperatures) on the tungsten surface. A high-temperature branch (>2100 K) is determined by the dynamic processes which ensure the presence of physically adsorbed oxygen on tungsten with the surface coverages of up to several tenths of a monolayer, depending on the real surface structure.

CONCLUSION

In summary, two promising variants of tubular single crystal tungsten electrodes for high-performance TCs are proposed. One of these is based on chloride vapor phase technology and, hence, represents single-face electrodes of oxygenated epitaxial tungsten with outer hexahedral and inner cylindrical surfaces. At the

usual working temperatures of TCs, the electrode material has a work function of 5.6–5.7 eV and a high-temperature creep rate not exceeding 10^{-8} s^{-1}. Such electrodes can be used for designing thermoemission units of hexahedral geometry, which ensure their closest packing in a converter. Upon appropriate modification, these electrodes can be used in cylindrical modules too.

Another variant is based on the "deformation" technology using single crystal ingots of undoped tungsten obtained by crucibleless electron beam zone melting. Both inner and outer surfaces of the tubular electrodes manufactured according to this technique are cylindrical. The electrode material has a work function of 5.0 eV; under typical working conditions of TCs, the dimensional stability of the material is characterized by a high-temperature creep rate of 10^{-9} s^{-1} according to one test method and 10^{-11} s^{-1} according to another method.

Finally, a combination of the two variants considered above can be offered as the third version (Fig. 1e). In this case, a single-face tube of the variant in Fig. 1c serves as a high-strength substrate for depositing a layer of chloride vapor grown oxygenated epitaxial tungsten with a high work function. In so doing, as was shown earlier [24], a hardened substrate substructure is inherited by the epitaxial layer.

ACKNOWLEDGMENTS

The author would like to thank "vapor phase craft master" N.I. Kushchenko (Sukhumi Physicotechnical Institute) and A.I. Dekhtyar (Institute of Metal Physics, Kiev). The paper is devoted to the blessed memory of V.A. Kononenko for many years of fruitful creative cooperation.

REFERENCES

1. Yu. V. Nikolaev, in *Proceedings of the Conference "Nuclear Power Engineering in Space"* (NPO "Luch," Podol'sk, 1993), p. 5.
2. P. Batzies, P. Schroder-Bado, and G. Wahl, BBC-Nachr., Nos. 1–2, 31 (1972).
3. L. Yang, R. G. Hudson, H. Johnson, *et al.*, in *Proceedings of the 3rd International Conference on Thermionic Electrical Power Generation, Julich, 1972*, p. E-32.
4. D. V. Karetnikov, V. A. Koryukin, and V. P. Obrezumov, *High-Purity and Single Crystalline Metallic Materials* (Nauka, Moscow, 1987), pp. 154–158.
5. A. I. Dekhtyar and V. P. Kobyakov, At. Énerg. **79** (1), 13 (1995).
6. V. S. Emel'yanov, A. I. Evstyukhin, and V. A. Shulov, *Theory of Production Processes of Pure Metals, Alloys, and Intermetallides* (Énergoatomizdat, Moscow, 1983).
7. V. P. Kobyakov, Metally, No. 1, 82 (2000).
8. V. P. Kobyakov, Vysokochist. Veshchestva, No. 6, 45 (1994).
9. V. P. Kobyakov, Vysokochist. Veshchestva, No. 3, 101 (1995).
10. V. S. Emel'yanov, A. I. Evstyukhin, A. I. Shulepov, *et al.*, *Molybdenum in Nuclear Power Engineering* (Atomizdat, Moscow, 1977).
11. A. I. Evstyukhin, I. I. Gavrilov, V. N. Yal'tsev, *et al.*, *Rare Metals and Alloys with Single Crystal Structure* (Nauka, Moscow, 1981), pp. 36–41.
12. V. P. Smirnov, Yu. I. Sidorov, and V. P. Yanchur, Poverkhnost, No. 4, 123 (1986).
13. V. P. Kobyakov, Kristallografiya **41**, 552 (1996) [Crystallogr. Rep. **41**, 523 (1996)].
14. A. A. Babad-Zakhryapin and G. D. Kuznetsov, *Textured High-Temperature Coatings* (Atomizdat, Moscow, 1980).
15. V. P. Kobyakov, Kristallografiya **41**, 1093 (1996) [Crystallogr. Rep. **41**, 1040 (1996)].
16. V. P. Kobyakov and S. A. Zaslavskiĭ, Vysokochist. Veshchestva, No. 5, 75 (1989).
17. G. Wahl and J. Demny, in *IEEE Conference Record of 1970 Thermionic Conversion Specialist Conference: Papers Presented at the 9th Annual Conference, Miami Beach, 1970* (IEEE, New York, 1970), No. 4, p. 95.
18. É. F. Chaĭkovskiĭ and A. A. Taran, Pis'ma Zh. Tekh. Fiz. **5**, 920 (1979) [Sov. Tech. Phys. Lett. **5**, 381 (1979)].
19. R. P. Elliott, *Constitution of Binary Alloys* (McGraw-Hill, New York, 1965; Metallurgiya, Moscow, 1970), Vol. 2.
20. V. P. Kobyakov, Zh. Tekh. Fiz. **66** (7), 161 (1996) [Tech. Phys. **41**, 722 (1996)].
21. V. P. Kobyakov, Zh. Tekh. Fiz. **66** (7), 169 (1996) [Tech. Phys. **41**, 726 (1996)].
22. D. Lieb and F. Rufeh, in *IEEE Conference Record of 1970 Thermionic Conversion Specialist Conference: Papers Presented at the 9th Annual Conference, Miami Beach, 1970* (IEEE, New York, 1970), No. 4, p. 741.
23. B. M. Zykov, V. P. Kobyakov, and Yu. I. Nardaya, Vysokochist. Veshchestva, No. 1, 71 (1991).
24. V. P. Kobyakov, V. A. Kononenko, and A. I. Dekhtyar, Dokl. Akad. Nauk SSSR **294**, 856 (1987) [Sov. Phys. Dokl. **32**, 503 (1987)].

Translated by M. Astrov

Technical Physics, Vol. 47, No. 10, 2002, pp. 1316–1320. Translated from Zhurnal Tekhnicheskoĭ Fiziki, Vol. 72, No. 10, 2002, pp. 114–118.

EXPERIMENTAL INSTRUMENTS AND TECHNIQUES

Universal SAW Gas Sensor

R. G. Kryshtal, A. P. Kundin, A. V. Medved, and V. V. Shemet

Institute of Radio Engineering and Electronics (Fryazino Branch), Russian Academy of Sciences, pl. Vvedenskogo 1, Fryazino, Moscow oblast, 141190 Russia

e-mail: avm@ms.ire.rssi.ru

Received November 6, 2001

Abstract—A new principle of designing a SAW gas sensor is described. This sensor, being essentially of sorption type, also offers properties of thermometric SAW sensors. The basic idea here is that heat fluxes propagate between the SAW substrate and the working surface of the temperature-regulating system with some delay. A sensor based on this principle can detect not only the vapors of volatile substances but also gases by their thermal properties, retaining high temperature stability and speed of response unlike conventional SAW thermometric sensors. The design of this sensor built around a $LiNbO_3$ SAW delay line is described, and experiments on detecting a household propane–butane mixture with this sensor are reported. In particular, the responses of the sensor are measured at different gas-flow rates, two different SAW substrate temperatures, and two propane–butane concentrations. Ways of improving the sensor's performance are discussed. © *2002 MAIK "Nauka/Interperiodica".*

INTRODUCTION

It is well known that most SAW devices are very sensitive to the surface condition of the SAW substrate along which the waves propagate. The adsorption of molecules from the gaseous phase on the working surface of a delay line or a resonator changes SAW propagation parameters. This, in turn, changes the phase of the device's output signal (in passive delay lines) or its frequency (in oscillators built around resonators and delay lines). This factor underlies the operation of SAW gas sensors, which were first so named in [1]. To provide a chemical selectivity, a thin layer of a special material offering an increased absorptivity with respect to particular compounds is applied to the working surface of the substrate. Due to their unique properties, such SAW gas sensors are finding increasing use, including in the sensor arrays of modern gas analyzers of the electronic nose type [2]. However, the best reproducibility, time stability, and sometimes sensitivity are demonstrated by SAW sensors without a sensitive coating [3]. Of course, sensors without a sensitive coating are not selective and can only detect the vapors of volatiles that are readily adsorbed on the working surface kept at a temperature lower than that of the vapor of a substance being detected. Nevertheless, "uncoated" sensors are successfully used in many modern high-speed portable devices for detecting and identifying volatiles, including toxic agents, explosives, and narcotics, which may be present in the environment in very small amounts [3, 4]. These devices separate chemical mixtures into their constituents with the help of chromatographic columns. For rapid identification, well-known algorithms similar to those used in analyzers of the electronic nose type with the arrays of selective sensors can be employed [2].

SAW sensors without sensitive coatings are used together with chromatographic columns, which may be universal, capable of separating not only the vapors of volatiles but also mixtures containing permanent and combustible gases. Therefore, it would be desirable to have a universal SAW gas sensor that would detect as many vapors and gases as possible. There exist uncoated SAW sensors that can detect gases and vapors of a variety of substances. These are SAW thermometric gas sensors [5, 6].

SAW thermometric sensors operate as follows. An SAW delay line or an SAW resonator on a heated substrate (steady heat source) is placed into a chamber where a carrier gas flows about the substrate with a constant rate. The heat source with the SAW device is mounted in the chamber so that the chamber walls and the source exchange heat largely through the gas filling the chamber. The temperature of the chamber walls and that of the gas injected must be different from the source temperature (usually, much lower) and kept constant. The source temperature thus depends on the properties (thermal conductivity and specific heat) and flow rate of the gas injected into the chamber. The greater the properties of the gas to be detected differ from those of the carrier gas and the greater the wall and gas temperature differs from the initial heat source temperature, the greater is the change in the source temperature when the gas to be detected is injected into the chamber, i.e., the higher is the device's sensitivity. The heat source is usually a resistance-type heater connected to a regulated power supply. An SAW device here serves as a temperature-sensitive element; therefore, its substrate material must be very sensitive to temperature variations (at least quartz must be excluded). SAW thermometric sensors currently available [6] cannot how-

1063-7842/02/4710-1316$22.00

ever detect the vapors of volatiles and are exceeded by sorption SAW sensors in speed of response and in reproducibility of results.

To achieve the maximum possible thermal stability of sorption SAW sensors, their substrates are often made of thermally stable quartz cuts and precision temperature regulators built around Peltier thermoelectric elements are used [4, 7]. Therefore, such sensors cannot detect gases by their thermal properties.

This paper describes an SAW gas sensor that, being in essence a sorption sensor, also offers some properties of an SAW thermometric sensor [6]. In other words, we propose a sensor that is capable of detecting not only the vapors of volatiles but also gases by their thermal properties. Unlike conventional SAW thermometric sensors, our sensor provides high thermal stability and speed of response. We describe a sensor built around a $LiNbO_3$ delay line and report test results by an example of detecting a household propane–butane mixture. In particular, the sensor's responses as a function of the SAW substrate temperature, temperature and flow rate of the gas mixture, and propane–butane concentration in the carrier gas were measured.

THERMOSTABILIZATION OF AN SAW SENSOR

To gain greater insight into the design and operating principle of the universal SAW sensor proposed, consider the thermostabilization of an SAW device in modern sorption SAW sensors. Figure 1 illustrates the typical position of an SAW device in the measuring chamber of modern sorption SAW sensors. The sensitive SAW device (an SAW waveguide delay line on a 128°*Y*–*X* $LiNbO_3$ substrate with a center frequency of 486 MHz [7]) is mounted directly on the working surface of a Peltier thermoelectric element (TEE). In our experiment, the SAW device was fixed to the TEE by the heat-conducting paste that is commonly used in fabricating electronic equipment. The TEE working surface also supports a thermally sensitive resistor to measure its temperature. The TEE with the SAW device is placed into the measuring chamber, which has connectors for coupling the delay line with the high-frequency measuring circuits and for connecting the TEE with the thermally sensitive resistor to feed circuits and circuits for computer temperature control. The chamber is also provided with inlet and outlet pipe connections for gas delivery and removal. Commercial one-stage TEEs with a standard control circuit that were used in our experiments kept the SAW device temperature in the range 4–60°C within ±0.003°C for no less than 10 min and within ±0.01°C for 10 h with the ambient temperature varying from 20 to 30°C. To study the dynamics of SAW device thermostabilization, a continuous sinusoidal signal was applied to the input interdigital transducer of the delay line at its center frequency, and variations in the phase of the signal at the output interdigital

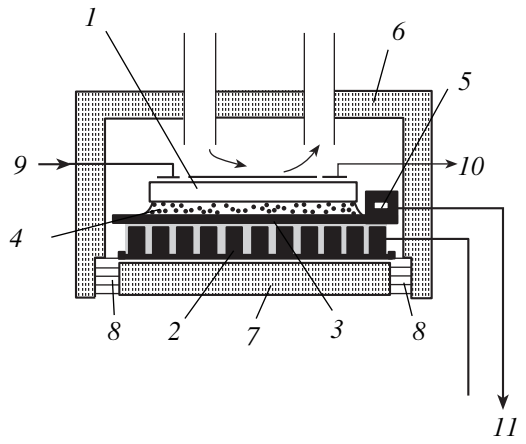

Fig. 1. SAW device in the measurement chamber: (*1*) SAW delay line; (*2*) thermoelectric element; (*3*) working surface of the thermoelectric element; (*4*) heat-conducting paste; (*5*) thermally sensitive resistor; (*6*) chamber lid with inlet and outlet pipe connections, microwave contacts, and electrical contacts; (*7*) base of the chamber; (*8*) sealing heat-insulating gasket; (*9*) microwave input; (*10*) microwave output; and (*11*) to the temperature-control unit.

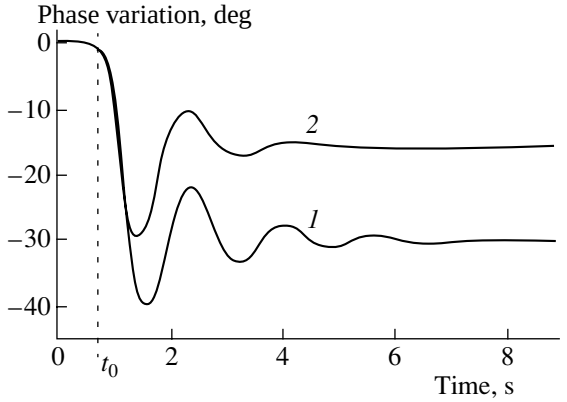

Fig. 2. Phase variation in the signal derived from the output interdigital transducer at a given change in the TEE working surface temperature. t_0 is the instant of temperature change.

transducer due to a stepwise change in the temperature of the TEE working surface were measured. Figure 2 plots the time variation of the output phase when the TEE working surface temperature changes by 1°C from 57.3 to 58.3°C (curve *1*) and by 0.5°C from 9.9 to 10.4°C (curve *2*) with the maximum rate attainable for the control system used. The measurements were made for several flow rates of the carrier gas (chromatographic nitrogen) passing through the measuring chamber. The chamber and the inlet metallic capillary tube were placed into a thermostat kept at a temperature of 30 ± 0.1°C. The results of measurement depended on the flow rate only slightly. As follows from Fig. 2, our temperature-regulating system sets the steady-state value of the temperature of the given 128°*Y*–*X* $LiNbO_3$ SAW substrate measuring 9 × 4 × 0.5 mm approxi-

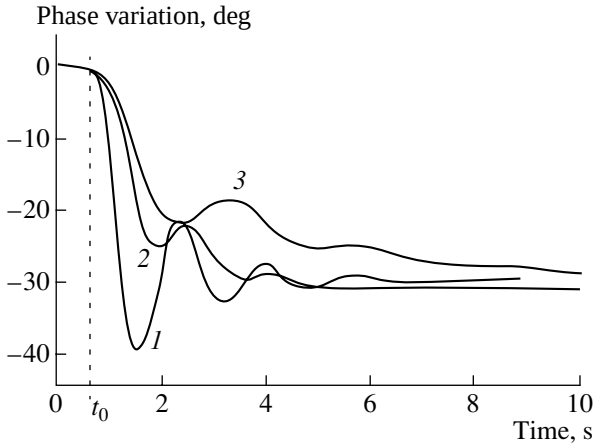

Fig. 3. Phase variation in the output signal when the TEE working surface temperature changes by 1°C from 57.3 to 58.3°C: (*1*) no spacers, (*2*) one glass spacer, and (*3*) two glass spacers between the SAW substrate and the TEE. t_0 is the instant of temperature change.

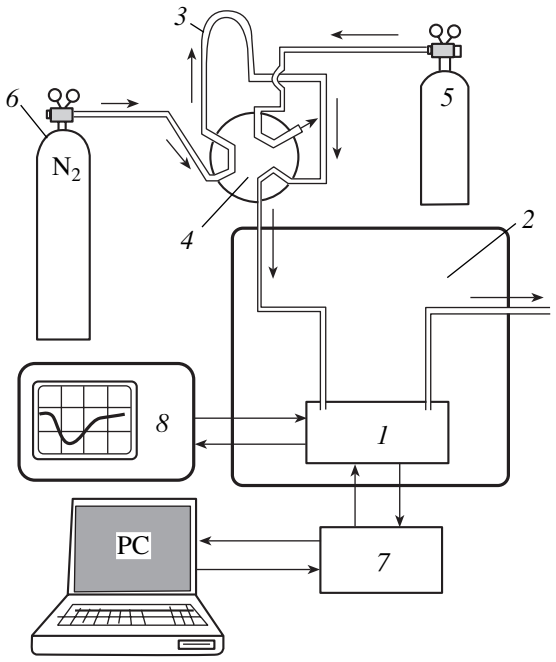

Fig. 4. Experimental setup for measuring the response of the SAW sensor (the phase of the delay line output versus time) to gaseous substances: (*1*) measuring chamber with the SAW sensor and the TEE; (*2*) thermostat; (*3*) calibrated gas-extracting tube; (*4*) six-way valve; (*5*) cylinder with the gas under study; (*6*) cylinder with the carrier gas; (*7*) electronic temperature-control unit; and (*8*) phase meter measuring the phase shift of the microwave signal passed through the SAW delay line.

mately in 5 s when a temperature jump is 1°C, the temperature change being the most rapid within the first second after the jump. The equilibrium phase change as a result of the 1°C temperature change was 30.3°C, which is in good agreement with the value calculated for the SAW substrate material and delay line employed [7]. It can be expected that the time it takes for the SAW substrate temperature to return to the initial value (thermostabilization) after applying an external thermal effect to the substrate will be roughly the same. Such an external thermal effect may be exerted by the gas injected into the measuring chamber if its parameters are different from those of the carrier gas.

At reasonable gas flow rates in the measuring chamber and temperature difference between the SAW substrate and the gas injected, this external action will not noticeably change the SAW substrate temperature even for a very short time of observation, because the temperature-regulating system has time to compensate for this difference. Thus, such a sorption SAW sensor can hardly detect gases by their thermal properties even if its SAW substrate is made from a material of poor thermal stability. Our experiments corroborated this supposition. In all our attempts to detect the propane–butane mixture, the response of the sensor was no higher than 0.5° for all possible combinations of the experimental parameters.

In our opinion, it would be possible to detect gases by their thermal properties if the temperature-regulating system actuates with some delay. Apparently, a delay can be introduced electronically by appropriately modifying the temperature-control unit. Alternatively, one may provide a delay for the heat flux between the TEE working surface and the SAW substrate. We chose the second approach. One or several thin (0.25-mm-thick) glass plates were placed between the SAW substrate and the TEE working surface and adhered to the TEE surface, the SAW substrate, and together by the heat-conducting paste. The free part of the TEE surface (not occupied by the SAW substrate) and the thermally sensitive resistor were covered by a heat-insulating material. Under the same conditions as in the previous experiment, we measured the phase variations of the output signal of the output interdigital transducer when the temperature of the TEE working surface changes stepwise by 1°C from 57.3 to 58.3°C. The results are shown in Fig. 3. It is seen that with the spacers, the SAW substrate steady-state temperature does set in more slowly and that the process is the slower, the greater the number of spacers placed between the substrate and the TEE working surface.

EXPERIMENTAL DETECTION OF THE PROPANE–BUTANE MIXTURE

The experimental setup used to measure the response of the SAW sensor (the phase shift of the delay line output versus time) is shown in Fig. 4. The measuring chamber (of volume ≈2 cm^3) with the SAW sensor and the metallic inlet capillary were placed into the thermostat at a temperature of 30 ± 1°C kept within ±0.1°C for several hours. The gas under test was dosed out with a calibrated 4-cm^3 U-shaped tube, which could

be connected to a cylinder with this gas and to the carrier gas pipeline with a standard six-way dosage valve as is usually done in gas chromatographs. In one position of the valve, the U-shaped tube is connected to the cylinder and the gas under test flows through the tube, while the carrier gas is injected into the measuring chamber, bypassing the tube. In another position of the valve (shown in Fig. 4), the U-shaped tube bridges the gap in the carrier gas pipeline, so that the carrier gas displaces the gas under test from the tube to the measuring chamber.

As we noted above, with the SAW substrate placed directly on the TEE working surface, the response of our SAW sensor to the propane–butane mixture proved to be too weak. Figure 5 shows the responses of the same sensor with glass spacers inserted between the SAW substrate and the TEE and the household propane–butane mixture injected into the measuring chamber. It can be seen that the glass spacers do increase appreciably the sensor's response.

The phase change sign in the output signal is positive when the SAW substrate temperature is higher than the temperature of the injected gas (chamber walls) and negative otherwise. This means (cf. the phase change sign upon heating the SAW substrate in Figs. 2 and 3) that the gas under test cools the SAW substrate in the former case and heats it in the latter. Since the thermal conductivity of the carrier gas (nitrogen), 2.4×10^{-4} W/(m K), is higher than that of the propane–butane mixture, 1.43×10^{-4} W/(m K), the SAW substrate temperature could be expected to increase in the former case and decrease in the latter. Since we did not observe such an effect experimentally, the major contribution to the response is apparently made by the difference in the specific heats of nitrogen, 1.04 kJ/(kg K), and the propane–butane mixture, 1.46 kJ/(kg K).

As was expected, the response depended significantly on the difference between the injected gas temperature and the specified temperature of the TEE working surface and also on the gas flow rate. As the temperature difference decreases, the response declines proportionally and changes sign when the sign of the temperature difference changes.

The responses of the sensor to the propane–butane mixture at different flow rates are plotted in Fig. 6. The response to the 5 vol % propane–butane + 95 vol % nitrogen mixture at a gas flow rate of 70 cm^3/min, SAW substrate temperature of 58°C, and gas temperature of 30°C was 2.5°, which is quite a measurable value (in our experiments, the minimal phase change measured reliably was 0.2°).

Upon detecting the vapors of several alcohols and water by the sensor with the glass spacers inserted between the TEE working surface and the SAW substrate and with the substrate temperature below the injected gas temperature, the responses were close to those obtained in [7], where a similar SAW sensor with an ordinary temperature-regulating system and without the glass spacers was used.

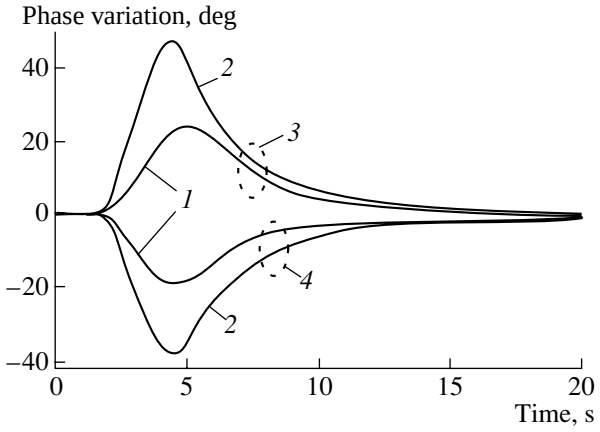

Fig. 5. Responses of the SAW sensor with (*1*) one and (*2*) two 250-μm-thick glass spacers placed between the SAW substrate and the TEE to the 100% propane–butane mixture injected into the measuring chamber at SAW substrate temperatures of (*3*) 58.3 and (*4*) 4°C. The injected gas (chamber wall) temperature is 30°C; the gas flow rate is 70 cm^3/min.

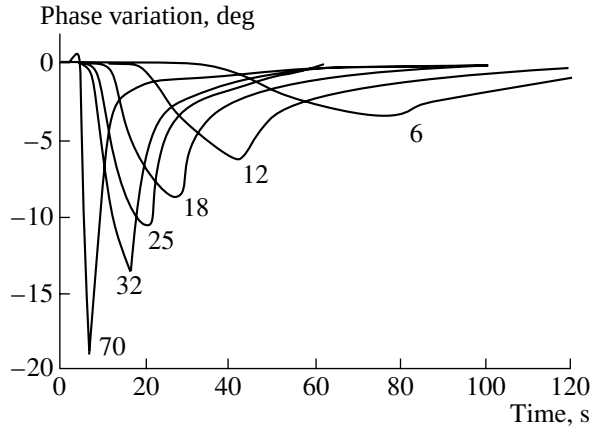

Fig. 6. Responses of the sensor with one glass spacer between the SAW substrate and the TEE to the propane–butane mixture. The gas temperature is 30°C; that of the SAW substrate, 4°C. Numbers by the curves indicate the gas flow rate in cm^3/min.

CONCLUSION

Thus, we described the physical principle accounting for the operation of a SAW sensor capable of detecting the vapors of volatiles, as well as gases, without changing its design or operating mode. The efficiency of the sensor was demonstrated experimentally. The sensor offers a high speed of response and temperature stability, which are typical of sorption SAW sensors.

The results of our experiments should not be regarded as ultimately achievable. To create a usable

device, it is necessary to optimize its design and operating modes. In fact, the response of the sensor is proportional to the difference between the temperatures of the SAW substrate and measuring chamber walls. In our experiments, this difference was about 30°C at most. The materials used in our sensor and TEE can withstand temperatures of up to 120°C. Therefore, the temperature difference can easily be increased by a factor of 3 to 3.5. Also, we did not optimize the thickness and material of the spacers between the SAW substrate and the TEE. It is also possible to reduce the volume of the measuring chamber, in which the SAW device is mounted, by a factor of 2 to 3. This will also increase the speed and magnitude of the response. The optimum choice of the carrier gas could provide a greater difference between the specific heats of the carrier gas and the gas to be detected and thus improve the parameters of the sensor. Note that all the above ways for improving the sensor's characteristics in detecting gases by their thermal properties will also improve its characteristics in detecting the vapors of volatiles.

REFERENCES

1. H. Wohltjen and R. E. Dessy, Anal. Chem. **51**, 1458 (1979).
2. H. T. Nagle, R. Gutierrez-Osuna, and S. S. Schiffman, IEEE Spectr. **35** (9), 22 (1998).
3. G. W. Watson, W. Horton, and E. J. Staples, in *Proceedings of Ultrasonic Symposium, 1991*, p. 305.
4. E. J. Staples, in *Proceedings of IEEE Ultrasonic Symposium, 1999*, p. 417.
5. D. Hauden, IEEE Trans. Ultrason. Ferroelectr. Freq. Control **34**, 253 (1987).
6. V. I. Anisimkin, S. A. Maksimov, M. Penza, and L. Vasanelli, Zh. Tekh. Fiz. **67** (5), 119 (1997) [Tech. Phys. **42**, 564 (1997)].
7. Yu. V. Gulyaev, V. E. Zemlyakov, R. G. Kryshtal, *et al.*, Akust. Zh. **47**, 39 (2001) [Acoust. Phys. **47**, 42 (2001)].

Translated by A. Khzmalyan

Technical Physics, Vol. 47, No. 10, 2002, pp. 1321–1325. Translated from Zhurnal Tekhnicheskoĭ Fiziki, Vol. 72, No. 10, 2002, pp. 119–123.

BRIEF COMMUNICATIONS

Mirror-Type Mass Analyzer with Cylindrical Poles

L. P. Ovsyannikova and T. Ya. Fishkova

Ioffe Physicotechnical Institute, Russian Academy of Sciences, Politekhnicheskaya ul. 26, St. Petersburg, 194021 Russia

e-mail: L.Ovsyannikova@pop.ioffe.rssi.ru

Received January 28, 2002

Abstract—A static mass analyzer of charged particles operating under a nonuniform magnetic field is suggested. An expression for the magnetic potential distribution is obtained in explicit form. From this expression, formulas for the basic parameters in the dispersion plane are derived for first-order angular focusing. Conditions for space focusing are found when a source and a detector are beyond the magnetic field region. Operating conditions where the trajectory exhibits three turns (in other words, charged particles travel a longer distance in the field) are established. The extended trajectory causes a considerable increase in the mass linear dispersion. © *2002 MAIK "Nauka/Interperiodica".*

Static uniform magnetic fields are of frequent use in mass analyzers of ion beams. The linear dispersion depends on the radius of curvature of the beam; therefore, the provision of a high resolution implies an increase in the overall dimensions of the instrument. Moreover, in uniform fields, angular focusing in the direction normal to the dispersion plane is absent. These disadvantages have given impetus to the development of instruments operating with nonuniform magnetic fields [1].

We suggest a mass analyzer the design of which is shown in Fig. 1. It represents a cylinder made of a magnetic material and cut along the generatrix into four identical closely spaced parts. Two of them are magnet poles with screens in between. The beam is introduced and extracted through channels cut in one of the screens.

In the 2D approximation, the scalar magnetic potential distribution along the longitudinal axis z of the system is given by

$$\omega(x, y) = W/\pi\{\arctan[\sqrt{2}(1 - x + y)/(2x - x^2 - y^2)] - \arctan[\sqrt{2}(1 - x - y)/(2x - x^2 - y^2)]\}. \quad (1)$$

Hereafter, the coordinates, as well as all geometrical parameters, are expressed through the radius r of the cylindrical poles. The lines of force for such a field are depicted in Fig. 1.

Consider the motion of a charged particle beam in the midplane $x0z$ of the magnet, which is the plane of dispersion (Fig. 2). Singly integrating the projection of the equation of motion onto this plane and equating the resulting variation of the longitudinal velocity to the velocity found from the energy law, we arrive at an expression for the beam trajectory inclination in the field:

$$(x')^2 = [1 - P^2(x)]/P^2(x), \quad (2)$$

where

$$P(x) = \cos\vartheta + \sigma\ln\{[x^2(\sqrt{2} + 1) + \sqrt{2}(1 - x)]/[x^2(\sqrt{2} - 1) + \sqrt{2}(1 - x)]\}/(2\sqrt{2}).$$

Here, ϑ is the trajectory inclination at the entrance to the field,

$$\sigma = (KW)/(rc)\sqrt{-e/2m\Phi} \quad (3)$$

is the magnetic force, $K = 2\sqrt{2}/\pi$ is the coefficient at

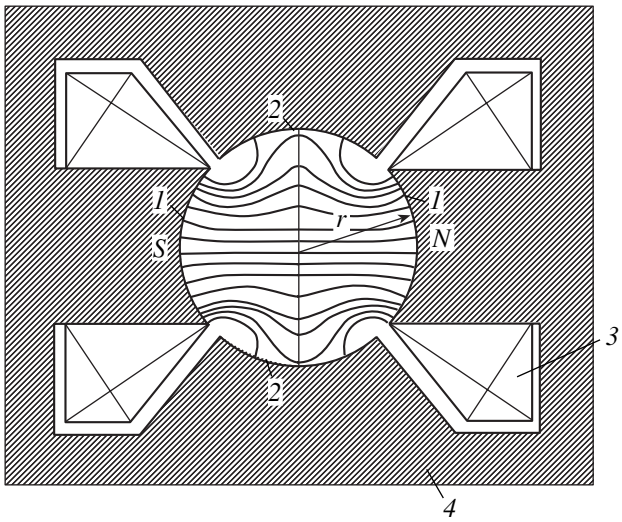

Fig. 1. Cross section of a mass analyzer with cylindrical poles and the pattern of magnetic lines of force: (*1*) pole pieces of magnet, (*2*) screens, (*3*) exciting coils, and (*4*) magnet yoke.

1063-7842/02/4710-1321$22.00 © 2002 MAIK "Nauka/Interperiodica"

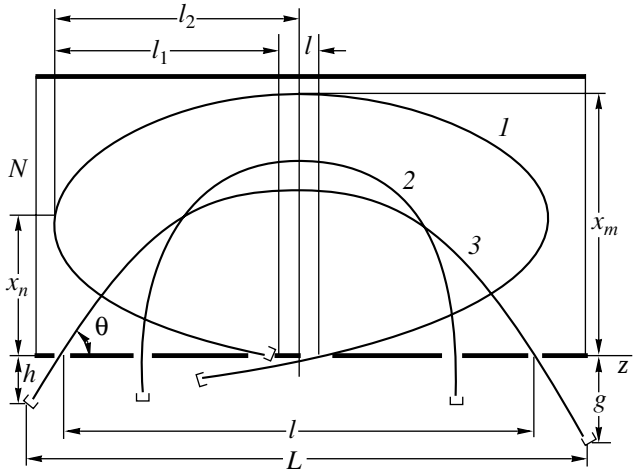

Fig. 2. Central trajectories of the beam under mirror operating conditions at entrance angles Θ > 90° (*1*), = 90° (*2*), and < 90° (*3*).

the higher harmonic (in the expansion of scalar magnetic potential (1)), m and e are the particle mass and charge, c is the speed of light, and Φ is the accelerating potential.

From (2), at $x' = 0$ one can determine the maximal coordinate through which the axis of mirror symmetry passes inside the field; at $x' = \infty$, the coordinate of a trajectory turn when the entrance angle of the beam $\vartheta > 90°$. These coordinates are written as

$$x_{m,n} = (1 - \sqrt{2\sqrt{2}\coth\mu - 3})/[\sqrt{2}(\sqrt{2} - \coth\mu)]. \quad (4)$$

To the maximal coordinate x_m, there corresponds $\mu_m = \sqrt{2}(1 - \cos\vartheta)/\sigma$; to the turning point, $x_n - \mu_n = -\sqrt{2}\cos\vartheta/\sigma$.

Let us determine the base of the mass analyzer (the spacing between the source and detector) $L = l + \lambda\cot\Theta$, where Θ is the entrance inclination of the beam central trajectory, l is the distance between the entrance and exit points of this trajectory, and $\lambda = h + g$ is the total distance by which the source and detector are offset from the field. For particles leaving a point source at angles ±α to the central trajectory, the distance between the points of entrance to and exit from the field is

$$Z = l(\alpha) + \lambda\cot(\Theta \pm \alpha) = L + C_1\alpha + C_2\alpha^2 + \ldots,$$

where the coefficients of first- and second-order aberrations in the dispersion plane are, respectively, $C_1 = \partial Z/\partial\alpha|_{\alpha=0}$ and $C_2 = 1/2\partial^2 Z/\partial\alpha^2|_{\alpha=0}$.

The value of $l(\alpha)$ is found by integrating (2) from the entrance point $x = 0$ to the maximal coordinate x_m with subsequent doubling of the result in view of the mirror symmetry of the trajectory:

$$l(\alpha) = 2\int_0^{x_m} P(x)/[1 - P^2(x)]^{1/2}dx. \quad (5)$$

From expressions (2), (4), and (5), it follows that the integrand in the upper limit tends to infinity, which can be eliminated by integrating by parts. In this case, however, infinity arises in the lower limit; therefore, integral (5) has to be split into two. Under three-turn conditions (taking place at entrance angles >90°), for which the charge particle trajectory in the field lengthens significantly (trajectory *1* in Fig. 2) and, consequently, the mass dispersion increases, it would be appropriate to take the following two sections of the trajectory: (1) from the entrance to the field to the first turn of the trajectory and (2) from the first turn to the second one. Then, the entrance–exit distance is $l(\alpha) = 2[l_1(\alpha) + l_2(\alpha)]$. Now, the length of the first section of the trajectory $l_1(\alpha)$ along the z axis is expressed through integral (5) as before, but the upper limit of integration is replaced by x_n. The value of $l_1(\alpha)$ is always negative, because the particles move in opposition to the positive direction of the longitudinal axis.

After integration by parts, the length of the trajectory in the second section is written as

$$l_2(\alpha) = \left\{u(x_n) + 2\int_{x_n}^{x_m}(x-1)\{2/[x^2(2-x)^2] - 1\}\right. \times [1 - P^2(x)]^{1/2}dx\left.\right\}/\sigma, \quad (6)$$

where $u(x) = [x^4 + 2(1-x)(1-x+2x^2)]/[x(2-x)]$ and $u(x_n)$ is the value of this function at the point of the first turn.

First-order focusing with respect to the beam angle takes place if the total source–field and detector–field distance is given by $\lambda = \sin^2\Theta\partial l(a)/\partial\alpha$. For three-turn conditions, this means that

$$\lambda = 2\sin^3\Theta\left\{-\int_0^{x_n}[1 - P^2(x)]^{-3/2}dx + 1/\sigma^2[u(x_n)(du/dx)]x_n + \int_{x_n}^{x_m}[(du/dx)^2 + ud^2u/dx^2][1 - P^2(x)]^{1/2}dx\right\}. \quad (7)$$

Hereafter, the coordinates x_m and x_n refer to the central trajectory of the beam. With condition (7) met, the expansion of the pattern is defined primarily by second-order aberrations. For three-turn operating conditions, we have

$$C_2 = 3\lambda\cos\Theta/(2\sin^3\Theta) + \sin^2\Theta\left\{G/\sigma + 3\int_0^{x_n} P(x)[1-P^2(x)]^{-5/2}dx + \sigma^{-3}\{u(x_n)[(du/dx)^2 + ud^2u/dx^2](x_n) + \int_{x_n}^{x_m}[(du/dx)^3 + 4udu/dxd^2u/dx^2 + u^2d^3u/dx^3][1-P^2(x)]^{1/2}dx\}\right\}, \quad (8)$$

where

$$G = \frac{1-\sqrt{2}\coth\mu_n + (2\sqrt{2}\coth\mu_n - 3)^{1/2}}{\sinh^2\mu_n(\sqrt{2}-\coth\mu_n)^2(2\sqrt{2}\coth\mu_n - 3)^{1/2}}. \quad (9)$$

The coefficient of mass dispersion at the exit from the field (which depends on the trajectory of particles with different masses and equal energies) is given by

$$D_m = (dl/dm)m = -0.5\sigma(\partial l/\partial\sigma). \quad (10)$$

In view of formulas (5)–(7), expression (10) can be rearranged for three-turn conditions with first-order angular focusing as follows:

$$D_m = 1 - \lambda\cos\Theta/(2\sin^3\Theta) - u(x_n)/\sigma - \int_0^{x_n} P(x)[3-2P^2(x)][1-P^2(x)]^{-3/2}dx + \sigma^{-2}\int_{x_n}^{x_m} P(x)[1-P^2(x)][(du/dx)^2 + ud^2u/dx^2]dx. \quad (11)$$

For single-turn conditions, which take place when the magnetic force is low ($\sigma \le 1$) and entrance angles $\Theta \le 90°$, the interval of integration in finding l, λ, C_2, and D_m is also split into two but arbitrary parts to remove infinity. In this way, we derived formulas for finding all basic parameters in the dispersion plane of the mass analyzer at small entrance angles (omitted to save room).

By way of example, Fig. 2 shows the beam central trajectory that experiences a 180° deflection ($\Theta = 90°$) for a magnetic force $\sigma = 1$ (curve *2*), as well as the central trajectory with entrance and exit angles $\Theta = 60°$ for $\sigma = 0.6$ (curve *3*). In Fig. 3, a number of operating conditions for the mass analyzer with single-turn trajectories are presented. These conditions are selected so that first-order focusing takes place with the source and detector placed outside the field. Generally speaking, second-order focusing is also possible but only inside the field ($\lambda < 0$), which is intolerable for applications. It should be noted that the mass dispersion is small under appropriate single-turn operating conditions. It grows (Fig. 3) when the entrance angle approaches its maximum value for a specific magnetic force. However, the aberrations increase significantly in this case.

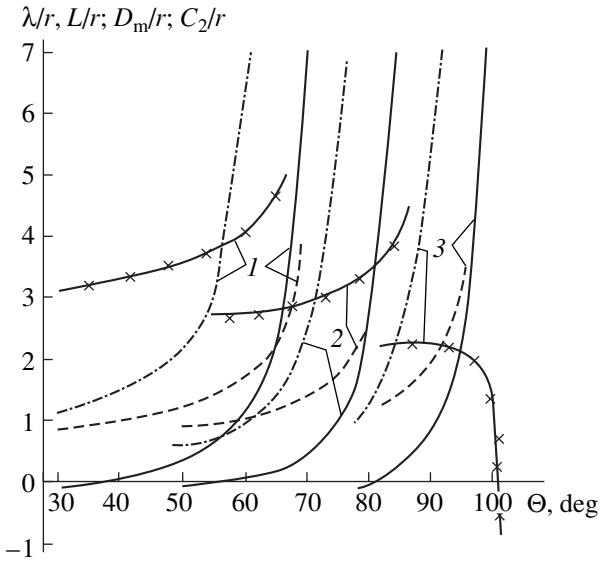

Fig. 3. Mass analyzer parameters in the dispersion plane for the single-turn trajectory. Solid curves refer to the total source–field and detector–field distance; crossed curves, to the analyzer base; dashed curves, to the mass dispersion; and dash-and-dot curves, to the second-order aberration coefficient. The magnetic force σ = 0.6 (*1*), 0.8 (*2*), and 1.0 (*3*).

The dispersion can be increased under three-turn operating conditions. The parameters for such conditions in the presence of first-order focusing that were calculated by formulas (5)–(11) are shown in Fig. 4. At a constant magnetic force, the range of entrance angles where focusing takes place beyond the magnetic field does not exceed 10°. As the force grows, the entrance angle increases and reaches its maximal value at σ = 1.6. In this case, both the mass dispersion and the coefficient of second-order aberration increase. The latter exceeds, as a rule, the dispersion coefficient; therefore, the specific dispersion, which is responsible for the resolution, is low. Yet, there exists a narrow magnetic-force range ($1.5 \le \sigma < 1.6$) where the coefficients roughly equal each other and even $D_m > C_2$ at $\sigma = 1.6$. These conditions are the most favorable for attaining a high resolution; therefore, the corresponding basic parameters are given in the table, where all linear dimensions are expressed through the radius of aperture r of the magnet. It should be noted that the negative

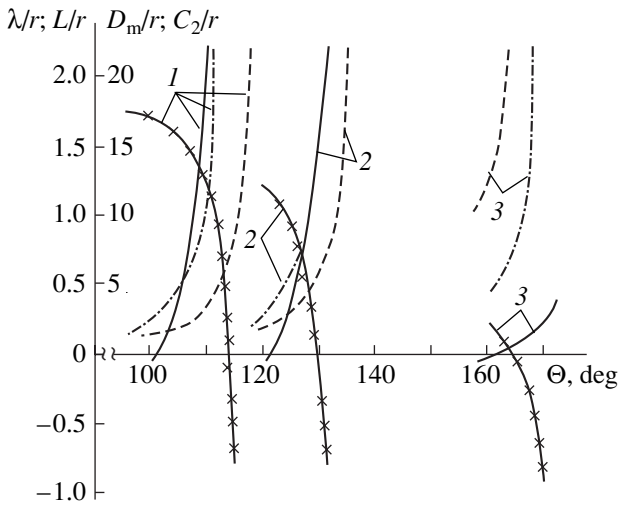

Fig. 4. Mass analyzer parameters in the dispersion plane for the three-turn trajectory. Designations are the same as in Fig. 3. The magnetic force σ = 1.2 (*1*), 1.4 (*2*), and 1.6 (*3*).

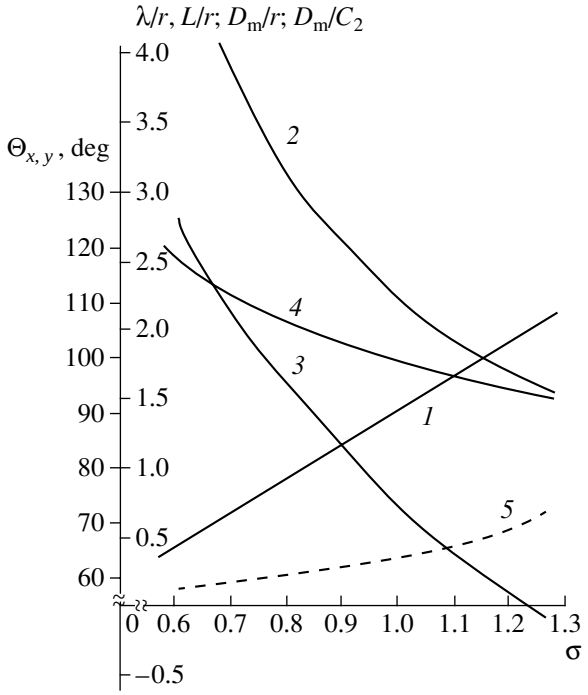

Fig. 5. Mass analyzer parameters under the space focusing conditions: (*1*) entrance angle for the beam central trajectory, (*2*) analyzer base, (*3*) total source–field and detector–field distance, (*4*) mass dispersion, and (*5*) ratio of dispersion to second-order aberration coefficient.

value of the base L of the mass analyzer means that the detector is placed on the left of the source, since the reference point is at the entrance to the instrument (trajectory *1* in Fig. 2).

Since the magnetic field is nonuniform, magnetic forces act on the beam in all directions. To find spatial focusing, one must solve the differential equation of motion in vector form projected onto the Cartesian coordinates. Since such equations are not integrated, we will solve it numerically under the initial conditions

$$x_0 = 0, \quad y_0 = h\tan\gamma/\sin\Theta, \quad v_{x0} = v_0\sin\Theta\cos\gamma,$$
$$v_{y0} = v_0\sin\gamma, \quad v_{z0} = v_0\cos\Theta\cos\gamma. \qquad (12)$$

Here, $v_0 = \sqrt{-2e\Phi/m}$ is the total velocity of the particle, Θ is the angle between the particle velocity projection onto the dispersion plane and the vertical plane (i.e., the entrance inclination of the beam central trajectory), and γ is the angle between the direction of the total velocity vector and the plane of dispersion. Note that $x' \longrightarrow \infty$ either at the entrance and the exit or at the points of the first and second turn if $\Theta \geq 90°$. Therefore, when finding the spatial focusing conditions, one should solve equations of motion where differentiation is performed with respect to time. In this case, at the source position, which is found from the condition for first-order focusing in the dispersion plane [see formula (7)], the expansion of the pattern in the normal direction is $y_i = g\tan\gamma_i/\sin\Theta_i - y_l$, where y_l, γ_i, and Θ_i are the coordinate and the angles of inclination at the exit from the field.

First-order spatial focusing occurs at an entrance angle of the central trajectory Θ_{xy} such that the expansion of the pattern in two mutually orthogonal planes is zero in the first approximation. Figure 5 plots these angles and other parameters vs. magnetic force for such conditions. As the force grows, the spatial focusing angle rises linearly, while the other parameters decline. It is noteworthy that the ratio of the linear dispersion to the second-order aberration coefficient (curve *5* in Fig. 5), which is responsible for the resolution of the mass spectrometer, increases with force. At σ = 1.23, spatial focusing is observed at the edge of the field (λ = 0). As the force grows further, focusing occurs inside the field, which is inappropriate as regards the arrangement of the charged particle source and the detector. The provision of space focusing outside the field is an advantage of the mass analyzer.

Let us demonstrate the potentialities of the mass analyzer suggested with the separation of CO (m = 27.995) and N_2 (m = 28.006) ions. This requires the resolution at the half-height of a mass spectrum line to be equal to R = 5000.

The conditions for space focusing with the source and the detector outside the field (Fig. 4) provide a mass resolution $R = 10^2$–10^3 for a luminosity of (0.01–0.03)% of 4π. A higher resolution can be attained by using three-turn operating conditions with large entrance angles (see the table). As follows from the table, the mass dispersion grows with the entrance angle for a given force. The aberrations, however, also grow. Conditions with $D_m/C_2 > 1$ are optimum. They provide a resolution $R \cong 10^4$.

Table

σ	Θ, deg	First turn		Second turn		λ	L	C_2	D_m	D_m/C_2
		x_n	$-z_n$	x_m	$z_m = l/2$					
1.50	138	0.871	0.555	1.640	0.411	0.244	0.551	6.166	4.227	0.685
	140	0.887	0.595	1.673	0.425	0.464	0.297	8.793	5.380	0.655
	145	0.923	0.706	1.765	0.535	1.569	–1.169	34.97	12.46	0.356
1.52	140	0.880	0.591	1.640	0.363	0.115	0.588	5.215	4.157	0.797
	145	0.915	0.701	1.719	0.405	0.639	–0.103	13.20	7.875	0.597
	147	0.928	0.749	1.755	0.451	1.020	–0.670	23.35	11.15	0.478
1.54	145	0.908	0.696	1.681	0.318	0.189	0.366	6.523	5.627	0.863
	150	0.939	0.821	1.762	0.385	0.742	–0.516	19.76	11.78	0.596
	152	0.950	0.876	1.800	0.456	1.209	–1.362	41.52	18.10	0.436
1.56	152	0.943	0.870	1.747	0.283	0.342	–0.076	11.11	10.07	0.906
	154	0.953	0.928	1.780	0.321	0.548	–0.454	18.89	14.18	0.751
	156	0.962	0.991	1.816	0.389	0.888	–1.216	40.01	21.93	0.548
1.58	157	0.959	1.017	1.774	0.201	0.203	–0.077	10.15	13.16	1.296
	160	0.972	1.125	1.821	0.260	0.417	–0.625	24.00	23.02	0.959
	162	0.979	1.205	1.857	0.351	0.698	–1.446	61.53	38.88	0.632
1.60	165	0.980	1.335	1.826	0.057	0.037	–0.023	7.115	24.25	3.408
	167	0.986	1.442	1.852	0.074	0.072	–0.165	10.91	35.63	3.266
	170	0.992	1.639	1.896	0.147	0.151	–0.563	38.09	78.18	2.053

Thus, in our example, $R = 5000$ can be provided in a number of operating modes. Their selection depends on the design (geometry) of the instrument. If, for example, the radius of the cylindrical poles is $r = 25$ mm and the width of the entrance and exit slits is $s = 50$ μm, the linear mass dispersion must equal $D = 20r = 500$ mm. In this case, the trajectory is a loop whose longitudinal extension is no more than $3r = 75$ mm. At the same time, a resolution $R = 5000$ in a 90° sector mass spectrometer with a uniform field and with the same slit sizes is provided if the radius of curvature of the trajectory is 500 mm; in other words, the overall dimensions of the magnet and the instrument are much greater.

To conclude, we note that with a certain potential difference applied to the screens (in essence, only one shield should be biased, since the other, through which the beam is injected, is grounded), spatially coincident mutually perpendicular magnetic and electric fields arise, which are known to provide achromatism conditions. In this way, velocity focusing can be accomplished without complicating the design.

REFERENCES

1. V. M. Kel'man, I. V. Rodnikova, and L. M. Sekunova, *Static Mass Spectrometers* (Nauka, Alma-Ata, 1985).

Translated by V. Isaakyan

Technical Physics, Vol. 47, No. 10, 2002, pp. 1326–1329. Translated from Zhurnal Tekhnicheskoĭ Fiziki, Vol. 72, No. 10, 2002, pp. 124–127.

BRIEF COMMUNICATIONS

Rapid Formation of an Electron Beam in a Magnetron Gun with a Secondary-Emission Metallic Cathode

Yu. Ya. Volkolupov, A. N. Dovbnya, V. V. Zakutin, M. A. Krasnogolovets, N. G. Reshetnyak, and V. P. Romas'ko

Uskoritel' Research Complex, National Research Center, Kharkov Institute of Physics and Technology, Kharkov, 61108 Ukraine

Received February 26, 2001; in final form, March 13, 2002

Abstract—The initial stage of forming the electron sheath and electron beam generation in magnetron guns for the case when the secondary emission process is triggered by nanosecond pulses is considered. In the guns with small transverse sizes, tubular electron beams with an outer diameter of 4–6 mm and a current of 1–2 A are produced at a cathode voltage of 5–10 kV. It is shown that the formation of the electron cloud and beam current pulse front for a time of ≥2 ns is a possibility. © *2002 MAIK "Nauka/Interperiodica".*

INTRODUCTION

In recent years, cold-cathode electron sources operating under secondary emission conditions in crossed electric and magnetic fields have become the subject of great interest [1–5]. Such sources offer a number of advantages (long service time, high current density, simple design, etc.), making it possible to use magnetron guns with cold secondary-emission cathodes in accelerators and high-power long-lived microwave sources [5], as well as in high-speed high-voltage equipment [6]. The electron beam in these sources is produced as follows. At the trailing edge of a cathode voltage pulse, primary electrons (due to field emission or external injection), returning by the action of the magnetic field, bombard the cathode surface. When moving along cycloidal trajectories toward the cathode, the electrons gain an energy proportional to the change in the electric field during their transit. Under certain conditions, i.e., when the energy of the incident electrons becomes large enough for the secondary emission coefficient to exceed unity, the process of secondary emission starts and the subsequent avalanche-type multiplication of the electron concentration results in the formation of an electron sheath from which electrons are extracted to generate a beam. In this work, we determine the time it takes for the space charge of the electron sheath to form and study the temporal stability of beam generation in magnetron guns for pulse fall times of 2–10 ns.

EXPERIMENTAL SETUP AND INVESTIGATION TECHNIQUES

The design of the setup used in our experiments is depicted in Fig. 1. A magnetron gun made of stainless steel with copper cathode *5* and 120-mm-long stainless steel anode *6* is placed in vacuum chamber *3*, which is evacuated to a pressure of $\approx 10^{-6}$ torr. An axial magnetic field in the gun is produced by solenoid *4*. A negative voltage pulse U_c (of amplitude 4–100 kV, width 2–10 μs, and repetition rate 10–50 Hz) is applied from modulator *1* to the cathode *5* of the magnetron gun. The anode *6* of the gun is grounded through resistor R_3 or is connected to generator *2*. A decaying electric field is generated in two ways. In the first case, modulator *1* generates a rectangular pulse and the process of sec-

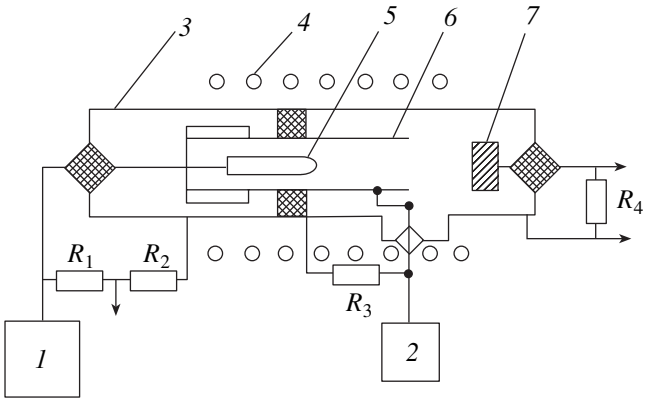

Fig. 1. Design of the experimental setup.

1063-7842/02/4710-1326$22.00 © 2002 MAIK "Nauka/Interperiodica"

ondary emission multiplication takes place during the trailing edge of the voltage pulse (of duration 2–40 ns, amplitude 3.5 kV on a load of 50 Ω, and rise and fall times *1* ns) applied from generator *2* to anode *6*. In the second case, the process of secondary emission multiplication is accomplished by producing an overshoot (of duration ≈0.6 μs) in the voltage pulse from modulator *1* [5] (with generator *2* switched off). This makes it possible to perform experiments with a rise time from 2 to 600 ns and a steepness of the voltage pulse edge from 20 to 1200 kV/μs. The beam current and sizes are measured at distances of up to 180 mm from the anode plane. The current was measured with Faraday cup *7*, which has the form of a ≈40-cm-long coaxial line, and the resistor R_4 (with the resistance equal to the wave impedance of the line, 18 Ω); the cathode voltage, with the R_1R_2 divider; and the beam sizes, from a spot on X-ray film and on molybdenum foil.

When triggering secondary emission by nanosecond pulses from generator *2*, one must take into account that transmitting circuits distort their waveforms. In our setup, the pulse-transmitting circuitry involves the coax, high-voltage insulator, vacuum transmission line, and anode mount. To determine the actual shape of the pulse, we measured its parameters in the space between the anode and the cathode. Figure 2 shows pulse waveforms obtained in two cases. In the former case, the duration of the generator pulse was ≈2 ns; in the latter, ≈6 ns. The signals were recorded by an I2-7 oscilloscope (of passband ≈3000 MHz). It is seen that the shape of the short pulse remains nearly unchanged and its fall time is ≈2 ns, while the long pulse is distorted with its fall time increased to ≈11 ns.

In our experiments, explosive electron emission was absent. This was checked by applying a voltage pulse of amplitude 70 kV to the cathode of the gun. Under these conditions (in the absence of the magnetic field), the cathode current was absent and a fall on the top of the cathode voltage pulse (characteristic of explosive emission) was not observed. (Under explosive emission, the anode–cathode gap is short-circuited by a metal plasma, the resistance of the gap approaches zero, the current is defined by the voltage supply power, and the cathode–anode voltage is also close to zero.)

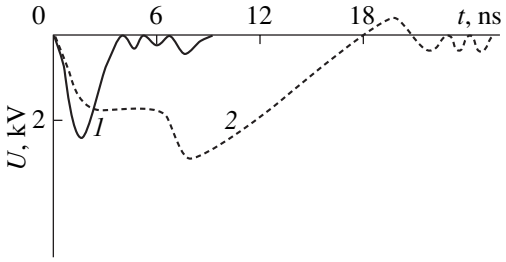

Fig. 2. Triggering pulse waveforms in the cathode–anode gap. Pulse duration is (*1*) 2 and (*2*) 11 ns.

RESULTS AND DISCUSSION

The beam generation was studied at different parameters of the pulse triggering secondary emission multiplication.

In experiments with a pulse fall time of ≈0.6 μs and a pulse edge steepness of 20–50 kV/μs (second approach), the processes of secondary emission multiplication and beam generation started within 100–500 ns (depending on experimental conditions) after the beginning of voltage pulse fall. With such a small steepness, the number of primary electrons must be significant, because few of them gain the energy sufficient for secondary emission multiplication. As a result, the accumulation of secondary electrons takes considerable time and is of a statistical nature with a time spread of several tens of nanosecond. Therefore, the resulting current pulse is temporally unstable and beam particles have an energy spread. Note also that the rise time of the current pulse also depends on the fall time of the triggering pulse; accordingly, it was on the order of tens of nanoseconds in our experiments.

To improve temporal stability, cut the current pulse rise time, and diminish the energy spread in the beam, one must increase the steepness of the triggering pulse and decrease its duration.

With this in mind, the process of secondary emission multiplication was triggered by pulses of nanosecond fall time according to the first approach (Fig. 2). In these experiments, an electron beam appeared within 1.5–2.0 ns in the first case and within ≈10 ns after the beginning of pulse fall in the second case. The occurrence of the beam was detected by a decrease in the

Table

Gun no.	d_c, mm	D_a, mm	U_c, kV	I, A	H, Oe	U, kV	τ, ns
1	2	7	6	1.4	3000	2.4	2
2	2	10	5.5	1	2200	4	12
3	2	10	7.3	1.6	2400	3	11
4	3	14	7.6	2	1400	3	14

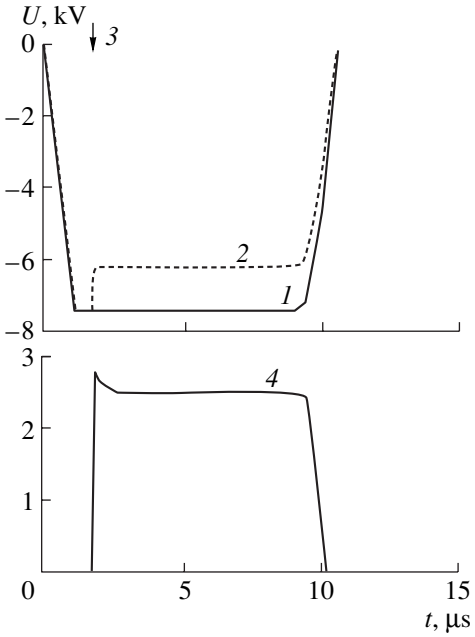

Fig. 3. (*4*) Waveforms of beam current pulses at the Faraday cup and those of voltage pulses in the (*1*) absence and (*2*) presence of the beam. Arrow *3* indicates the instant of triggering pulse application.

cathode voltage pulse amplitude because of loading by the beam. Figure 3 shows typical waveforms of cathode voltage pulses and beam current from the Faraday cup in a magnetron gun with a cathode diameter of 2 mm and an anode diameter of 10 mm. In this case, the time instability of current pulse beginning is within the triggering pulse fall time and reaches tens of nanoseconds.

The results of the investigation are summarized in the table, where d_c and D_a are the diameters of the cathode and anode of the gun, U_c is the cathode voltage, I is the beam current, U and τ are the amplitude and fall time of the triggering pulse, and H is the magnetic field. The cathode voltage amplitude was varied so as to prevent the breakdown of the anode–cathode gap (the maximal amplitude was varied between 15 and 25 kV according to the gun design). The table also lists minimal voltage amplitudes at which secondary emission multiplication and, hence, beam generation still take place. These values are of interest for applications such as low-voltage electron sources for microwave devices. For copper cathodes, the energy of primary cathode-bombarding electrons should lie between 0.4 and 0.6 keV. With such energies, the coefficient of secondary emission reaches the maximum and secondary emission multiplication proceeds very intensely. In this case, the primary electron energy is ≈10% of the electron energy at the output of the gun. This is of interest for studying the formation and stability of the electron sheath, as well as of an electron beam with a substantial energy spread.

The study of beam generation vs. steepness of the pulse trailing edge showed that this dependence has a threshold. As follows from the table, the triggering of magnetron gun 1 and beam generation take place at trailing edge steepnesses of more than 1000 kV/μs, while magnetron gun 2 is triggered at steepnesses of more than 300 kV/μs. Similar results were obtained for magnetron guns 3 and 4. For the beam generation to be stable at nanosecond triggering times, the steepness of the trailing edge must be significantly larger than for fall times within 0.4–0.6 μs.

When the gun is triggered by a voltage pulse with a nanosecond fall, the energy spectrum of the beam is improved because of a decrease in the number of high-energy electrons generated at the trailing edge of the pulse and also because of a decrease in their energy spread owing to the small amplitude of the pulse.

Our experimental results are in fairly good agreement with the numerical simulation of electron sheath formation in crossed fields. It was shown in our previous work [5], as well as in [7, 8], that during the triggering pulse fall time, electrons can gain enough energy to initiate secondary emission multiplication within 1–2 ns. With such a rapid voltage fall, the number of primary electrons is small; however, owing to the large steepness of the voltage pulse trailing edge, they can gain an energy at which the secondary emission coefficient exceeds unity and secondary emission multiplication proceeds at a considerable rate.

The measurement of the transverse size of the beams showed that their cross sections are rings with a uniform azimuth intensity distribution. Their inner diameters were roughly equal to the cathode diameter, and the “thickness” of the beams was found to be 1 or 2 mm. For example, the beam in magnetron gun 2 had outer and inner diameters of 4 and 2 mm at a distance of 130 mm from the anode plane. In gun 4, the respective sizes of the beam were ≈6 and ≈2.5 mm at a distance of 55 mm from the anode plane.

CONCLUSION

Our experiments show that the formation of a space charge cloud and the generation of an electron beam in a magnetron gun with a secondary emission cathode may take place within ≈2 ns. This allows for the generation of beam current pulses with nanosecond rise times and the synchronization of beam current pulses with a nanosecond accuracy. At cathode voltages of 5 to 10 kV and magnetic fields between 1900 and 3000 Oe, tubular electron beams with a current of 1–2 A and an outer diameter of 4–6 mm were produced.

REFERENCES

1. J. F. Skowron, Proc. IEEE **61**, 69 (1973).

2. S. A. Cherenshchikov, Élektron. Tekh., Ser. 1, No. 6, 20 (1973).
3. V. V. Zakutin, A. N. Dovbnya, N. G. Reshetnyak, *et al.*, in *Proceedings of the 1997 PAC, Vancouver, 1997*, Ed. by M. Comyn, M. K. Craddok, M. Reiser, and J. Thomson, Vol. 3, p. 2820.
4. Y. M. Saveliev, W. Sibbett, and D. M. Parkes, Phys. Plasmas **4**, 2319 (1997).
5. Yu. A. Volkolupov, A. N. Dovbnya, V. V. Zakutin, *et al.*, Zh. Tekh. Fiz. **71** (2), 98 (2001) [Tech. Phys. **46**, 227 (2001)].
6. A. I. Vishnevskiĭ, A. I. Soldatenko, and A. I. Shendakov, Izv. Vyssh. Uchebn. Zaved., Radioélektron. **11**, 555 (1968).
7. A. V. Agafonov, V. P. Tarakanov, and V. M. Fedorov, Vopr. At. Nauki Tekh., Ser. Yad.-Fiz. Issled. **1** (2–3), 134 (1997).
8. A. V. Agafonov, V. P. Tarakanov, and V. M. Fedorov, Vopr. At. Nauki Tekh., Ser. Yad.-Fiz. Issled., No. 4, 11 (1999).

Translated by V. Isaakyan

Technical Physics, Vol. 47, No. 10, 2002, pp. 1330–1332. Translated from Zhurnal Tekhnicheskoĭ Fiziki, Vol. 72, No. 10, 2002, pp. 128–130.

BRIEF COMMUNICATIONS

Statistical Model of Internal Scattering of Vibrational Energy in Composites

V. M. Arzhavitin

Kharkov Institute of Physics and Technology, National Scientific Center, Akademicheskaya ul. 1, Kharkov, 61108 Ukraine

e-mail: vasil@kipt.kharkov.ua(TO:AR)

Received October 5, 2001; in final form, February 20, 2002

Abstract—An analytical temperature dependence of the internal friction $Q^{-1}(T)$ for composite materials is derived. It is shown that the hysteresis behavior of the $Q^{-1}(T)$ curve observed in temperature cycling experiments with some composites may be a result of plastic strain clustering in the matrix. © *2002 MAIK "Nauka/Interperiodica".*

Plastic strain localized in microvolumes is a basic factor responsible for the internal scattering of the vibrational energy in structurally inhomogeneous materials. This factor is of special importance in heterostructures and composites with constituents greatly differing in mechanical properties. Earlier, it was shown [1–3] that temperature cycling (heating/cooling) applied to several composites grown by the oriented crystallization method causes hysteresis in the temperature dependence of the internal friction $Q^{-1}(T)$, which is absent in homogeneous materials. At a certain cooling temperature, tensile thermal stresses due to a difference between the thermal expansion coefficients of the constituents reach values close to the macroscopic yield strength $\sigma_{0.2}$ of the matrix. Naturally, plastic deformation in the matrix is accompanied by heat evolution, of which internal friction is a measure. However, no cases of the analytical description of $Q^{-1}(T)$ have come to our notice so far. The purpose of this work is to quantitatively describe hysteresis in $Q^{-1}(T)$ curves observed in experiments with composites using general ideas of continuum mechanics.

Consider composites consisting of elastic fibers and a plastic matrix. In this case, the matrix is the first to yield upon stressing the composite. Therefore, the dissipative power of such composites is defined by the matrix properties. To simplify the mathematics, we assume that the value of Q^{-1} is measured for longitudinal, rather than flexural, rectangular vibrations of frequency f. When thermal stresses are imposed on cyclic stressing, the matrix experiences the combined effect of asymmetrically varying stresses having the temperature and temporal components:

$$\sigma = \sigma_m \pm \sigma_0 \varphi(t), \tag{1}$$

where σ_m is the thermal stress in the matrix, σ_0 is the amplitude of variable stresses in a cycle, and $\varphi(t)$ is a periodical (not necessarily harmonic) function of time: $-1 \le \varphi(t) \le 1$.

We will proceed from the known Davidenkov concept on the statistical (nonuniform) distribution of mechanical stresses σ over grains [4], assuming that deformation is perfectly plasto-elastic (that is, without hardening). This assumption relieves us of having to formulate the matrix yield law. The yield strength of grains is assumed to be the same and equal to $\sigma_{0.2}$. Let local stresses plastically strain a matrix grain by $d\varepsilon$. The associated work of deformation is

$$dU = bV\sigma_{0.2}d\varepsilon,$$

where b is a proportionality coefficient (no more than unity) that depends on the grain size, orientation, and location and V is the grain volume.

Accordingly, the work of plastic deformation per unit matrix volume within the period of vibration is given by

$$\Delta U = bVNn\sigma_{0.2}\Delta\varepsilon.$$

Here, $\Delta\varepsilon = \oint d\varepsilon$ is the plastic strain of a grain within the vibration period, $n = N_p/N$ is the fraction of plastically strained grains in a unit matrix volume under an average macrostress σ_{av} in the matrix (not in a grain!), N_p is the concentration of plastically strained grains in the matrix, and N is the total concentration of grains in the matrix. Since the product VN is the volume occupied by grains in a unit matrix volume ($VN \approx 1$),

$$\Delta U = bn\sigma_{0.2}\Delta\varepsilon. \tag{2}$$

The expression for $n(\sigma_{av})$ for the horizontal cycle of vibration was derived in [4]:

$$n(\sigma_{av}) = \int_{\sigma_{0.2}}^{\infty} p(\sigma)d\sigma = B\left(\frac{\sigma_{av}}{\sigma_{0.2}}\right)^m, \quad (3)$$

where $p(\sigma)$ is the Gaussian distribution of stresses σ over grains and B and m are constants depending on the variance of the distribution curve $p(\sigma)$.

Expression (3) is valid when σ_{av} is large compared with the center-of-gravity value $\bar{\sigma}$ of the distribution $p(\sigma)$.

The plastic strain of a matrix grain within a vibration cycle is given by

$$\Delta\varepsilon = \oint d\varepsilon = \int_0^{1/2f} d\varepsilon.$$

Here, integration is over the positive half-period of vibration $\tau/2 = 1/(2f)$ (not over the complete period τ), because the strain within the negative half-period is elastic and does not contribute to heat evolution. When analyzing plastic strains induced by thermal stresses in composites, one should first of all take into account the matrix creep [5]. The time dependence of the plastic strain ε including the secondary creep is [6] $\varepsilon = \dot{\varepsilon}_s t + \varepsilon^0$, where $\dot{\varepsilon}_s$ is the rate of secondary creep. Here, ε^0 involves the elastic part of the strain and a jump of the plastic strain at the instant the stress is applied ("instantaneous" creep). In copper, this expression is applicable to the temperature range $(0.4–0.7)T_M$ (where T_M is the melting point of copper on the absolute temperature scale), which is important from the engineering viewpoint [7]. The rate of plastic strain is defined by the Arrhenius law $\dot{\varepsilon}_s = \dot{\varepsilon}_0 \exp(-H_0/kT)$. Here, H_0 is the energy of activation of deformation, k is the Boltzmann constant, and the preexponential $\dot{\varepsilon}_0$ depends on temperature only slightly. Then,

$$\Delta\varepsilon = \frac{\dot{\varepsilon}_0 \exp(-H_0/kT)}{2f}. \quad (4)$$

The internal friction is most frequently described by the relationship $Q^{-1} = \Delta U/2\pi U$, where U is the total energy of elastic strain per unit volume of the material. As applied to cycle (1), $U = \sigma_{av}^2/2E_m$, where E_m is the elastic modulus of the matrix. Thus, in view of (2)–(4), the expression for internal friction takes the form

$$Q^{-1} = \frac{bBE_m\dot{\varepsilon}_0}{2\pi f}\frac{\sigma_{av}^{m-2}}{\sigma_{0.2}^{m-1}}\exp(-H_0/kT). \quad (5)$$

Now, let us calculate tensile thermal stresses arising in the matrix upon cooling the Cu–1.3 wt % Cr eutectic composite from 978 K. The copper matrix can be considered perfectly plastic, since copper has a very low yield strength. In the elastic approximation, internal stresses appearing in the matrix when the temperature changes by ΔT are given by [8, 9]

$$\sigma_m = \frac{V_f E_f E_m \Delta\alpha\Delta T}{V_m E_m + V_f E_f},$$

where V_m and V_f are the volume fractions of the matrix and fibers, E_m and E_f are their elastic modulus, and $\Delta\alpha = (\alpha_m - \alpha_f) > 0$ is the difference between their thermal expansion coefficients.

For fiber composites, it is assumed that thermal stress vectors are aligned with fibers and are constant over the matrix cross sections. Data for the temperature dependences of E_m, E_f, α_m, α_f and the yield strength of copper $\sigma_{0.2}$ were taken from references books [10, 11]. Figure 1 shows the temperature dependences of thermal stresses in the matrix and of its yield strength.

The internal friction in the Cu–1.3 wt% Cr eutectics was calculated by formula (5) with $m = 4$. Diffusion creep in copper is initiated at temperatures above $0.8T_M = 1069$ K. At lower temperatures, dislocation cross slip seems to be the most probable mechanism of creep in pure copper. This mechanism of dislocation straining does not require diffusion. However, it needs thermal activation, because some energy must be spent to unpin dislocations from impurities and allow them to move to another slip plane [7, 12]. Therefore, in the calculations, the dislocation–impurity binding energy was set equal to $H_0 = 0.15$ eV, which is typical of copper at $T > 273$ K [13]. Let in the first approximation average, σ_{av}, and thermal, σ_m, stresses in the matrix be the same by order of magnitude: $\sigma_{av} \approx \sigma_m$. Experimental data [2, 3] and calculated results are demonstrated in Fig. 2. It is seen that the mechanism of microplastic losses considered in the paper does provide a peak of $Q^{-1}(T)$ on cooling the composites. The discrepancy between the temperature peaks $Q^{-1}(T)$ found experimentally and analytically may be associated with the fact that the

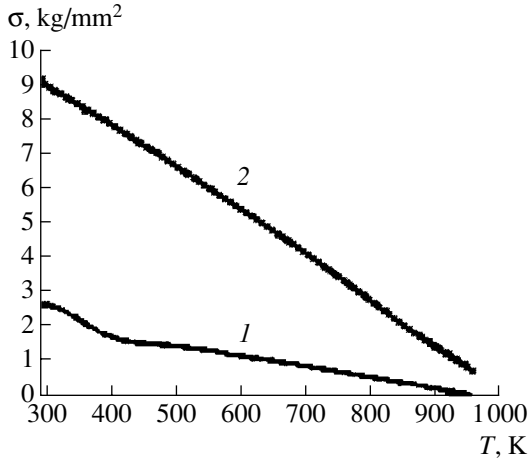

Fig. 1. (*1*) Thermal stresses in the matrix of cooled Cu–1.3 wt % Cr eutectics and (*2*) the yield strength of the matrix.

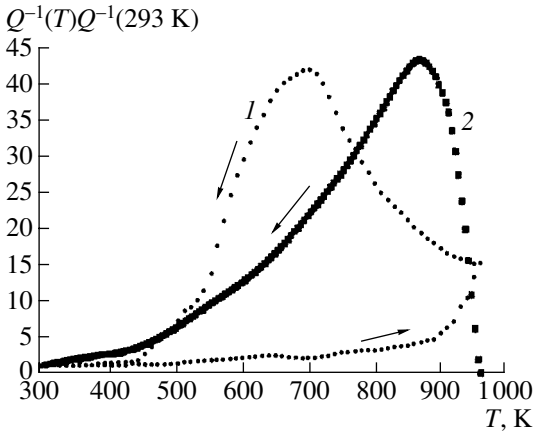

Fig. 2. Internal friction $Q^{-1}(T)$ of the Cu–1.3 wt % Cr eutectics: (*1*) experimental data and (*2*) calculated results for the cooled eutectics.

Cu–1.3 wt% Cr eutectics were prepared from high-purity electrolytically refined metals in alundum crucibles in the argon atmosphere, while the reference data used refer to other sorts of the metals.

Thus, a peak in the $Q^{-1}(T)$ curve for cooled composites may appear even if thermal stresses σ_m do not reach the yield strength $\sigma_{0.2}$ (Fig. 1). The reason for such "extreme" behavior of $Q^{-1}(T)$ is the clustering (statistical distribution) of the plastic strain over the matrix and in the relationship between the statistical average stresses $\sigma_{av} \sim \sigma_m$ and $\sigma_{0.2}$. The internal friction (at $m = 4$) of the cooled composite grows quadratically with σ_{av} and simultaneously decreases cubically with increasing $\sigma_{0.2}$.

Upon constructing a more consistent theory of plastic losses in composites, one should also take into account the localization of thermal stresses at interfaces. From general thermodynamic considerations, it follows that internal stresses decrease as $1/r$, where r is the distance to the interface [14]. The variation of the shape of the $Q^{-1}(T)$ curve with the dispersity of cooled Cu–1.3 wt% Cr eutectics [1] favors the aforesaid. If heating changes to cooling and vice versa in temperature cycling at a sufficient rate, the plastic deformation of the matrix near the interface comes before fiber fragmentation; hence, the method of low-frequency internal friction is undoubtedly a promising tool for studying the strength of composite materials.

REFERENCES

1. V. M. Arzhavitin, B. I. Shapoval, V. Ya. Sverdlov, and A. S. Tortika, Vopr. At. Nauki Tekh., Ser. Yad.-Fiz. Issled., No. 3 (3), 66 (1989).
2. V. M. Arzhavitin and V. Ya. Sverdlov, Zh. Tekh. Fiz. **68** (11), 114 (1998) [Tech. Phys. **43**, 1376 (1998)].
3. V. M. Arzhavitin, V. Ya. Sverdlov, A. S. Tortika, and B. I. Shapoval, Vopr. At. Nauki Tekh., Ser. Vakuum, Chist. Mater., Sverkhprovodn., No. 1 (9), 57 (1999).
4. V. T. Troshchenko, Fiz. Tverd. Tela (Leningrad) **2**, 1060 (1960) [Sov. Phys. Solid State **2**, 958 (1960)].
5. G. Garmong, Metall. Trans. **8**, 2183 (1974).
6. J. Cadek, *Crepp in Metallic Materials* (Elsevier, Amsterdam, 1988; Mir, Moscow, 1987).
7. T. Ekobori, *Scientific Principles of Strength and Destruction of Materials* (Naukova Dumka, Kiev, 1978).
8. A. V. Bobylev, *Mechanical and Technological Properties of Metals: A Handbook* (Metallurgiya, Moscow, 1980).
9. L. V. Tikhonov, V. A. Kononenko, G. I. Prokopenko, and V. A. Rafalovskiĭ, *Structure and Properties of Metals and Alloys (Mechanical Properties of Metals and Alloys)* (Naukova Dumka, Kiev, 1986).
10. A. I. Somov and M. A. Tikhonovskiĭ, *Eutectic Compositions* (Metallurgiya, Moscow, 1975).
11. K. I. Portnoĭ, B. N. Babich, and I. A. Svetlov, *Composite Materials on Nickel Base* (Metallurgiya, Moscow, 1979).
12. H. G. van Bueren, *Imperfections in Crystals* (North-Holland, Amsterdam, 1961; Inostrannaya Literatura, Moscow, 1962).
13. R. Honeycombe, *The Plastical Deformation of Metals* (Cambridge, 1968; Mir, Moscow, 1972).
14. N. G. Kolbasnikov and I. Yu. Trifonova, Metally, No. 2, 62 (1996).

Translated by V. Isaakyan

Technical Physics, Vol. 47, No. 10, 2002, pp. 1333–1336. Translated from Zhurnal Tekhnicheskoĭ Fiziki, Vol. 72, No. 10, 2002, pp. 131–133.

BRIEF COMMUNICATIONS

Diffusion of As Ions and Self-Diffusion in Silicon during Implantation

K. D. Demakov, V. A. Starostin, and S. G. Shemardov

Russian Research Centre Kurchatov Institute, pl. Kurchatova 1, Moscow, 123182 Russia

e-mail: vastarostin@mail.ru

Received October 19, 2001; in final form, April 5, 2002

Abstract—Experimental concentration profiles of As ions in a silicon substrate at temperatures of 20, 600, and 1050°C and ion current of 40 μA/cm^2, as well as at 1050°C and 10 μA/cm^2, are presented. On the basis of our and previously published experimental data, the process of radiation-stimulated ionic diffusion and self-diffusion in silicon is simulated. A number of interesting dependences, which are discussed in the conclusion of this study, are obtained. © *2002 MAIK "Nauka/Interperiodica".*

INTRODUCTION

The investigation of the behavior of different impurity ions implanted into semiconductor materials as functions of current density, ambient temperature, exposure time, ion energy, and the chemical properties of interacting substances is of great theoretical and practical importance. In this study, we investigate the implantation of 40-keV As ions into a silicon substrate in a wide temperature range.

EXPERIMENTAL

In our experiments, silicon substrates were irradiated using an ILU-3 accelerator [1]. For heating the substrates in the course of irradiation, a special high-temperature ion collector was developed. As a substrate material, we used single-crystalline silicon. The implantation was performed with 40-keV As ions at a dose of 2×10^{17} ion/cm^2. The distribution of implanted atoms with depth was analyzed using X-ray diffraction with layer-by-layer etching. The main irradiation parameters are listed in Table 1. The measured concentration profiles are shown in Figs. 1 and 2. It can be seen that, even for room-temperature irradiation, the profile contains a deep-lying maximum.

THEORY

In order to explain the impurity drift into the bulk, which strongly exceeds the ion range, we applied the modified Beloshitskiĭ model [2] described previously in [3]. In addition to diffusion transport, it is assumed that impurity capture by vacancies also takes place. Note that a purely diffusion equation in the presence of a source does not have a solution with a maximum located at a greater distance from the surface than the ion range. The key feature of the model consists in its nonequilibrium—diffusion occurs against a background of intense production and annihilation of defects. These processes are described by the following

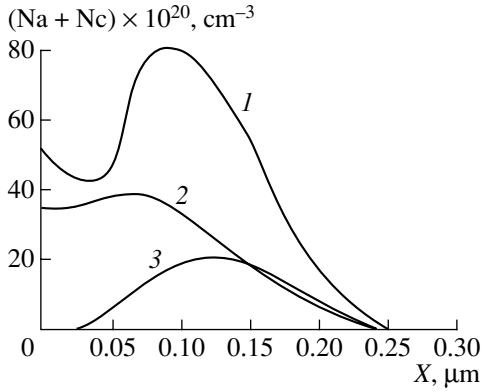

Fig. 1. Experimental concentration profiles of As in silicon at temperatures of (*1*) 20, (*2*) 600, and (*3*) 1050°C (40 μA/cm^2).

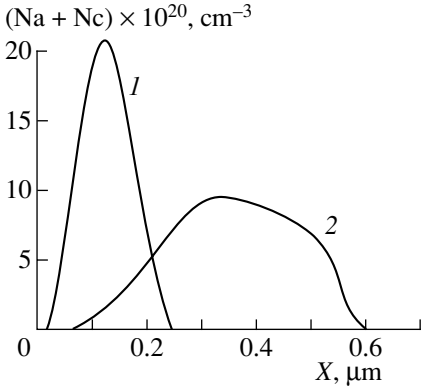

Fig. 2. Experimental concentration profiles of As in silicon for the currents (*1*) 40 and (*2*) 10 μA/cm^2 (1050°C).

1063-7842/02/4710-1333$22.00

Table 1. Basic experimental parameters of the implantation of As ions with an energy of 40 keV and a dose as high as 2×10^{17} ion/cm^2

Number	T, °C	j_0, μA/cm^2	$\mathcal{D}_{\exp}$, ion/cm$^2 \times 10^6$	$V_{b\,\exp}$, cm/s $\times 10^{-10}$	$t_{\max}$, s
1	1050	10	3.101	1.940	3200
2	1050	40	2.472	6.184	800
3	600	40	11.210	28.048	800
4	20	40	5.661	14.164	800

Table 2. Calculated diffusion coefficients and enthalpies

Number	D_a, cm^2/s $\times 10^{-11}$	D_{dv}, cm^2/s $\times 10^{-11}$	H_{dv}, cal/mol	T_{eff}, °K
1	0.169	0.204	64610	1326
2	0.540	0.0633	68151	1335
3	0.007	0.0463	47157	913
4	0.499	0.0127	31937	589

system of coupled equations:

$$\partial n_a/\partial t = D_a \partial^2 n_a/\partial x^2 - n_a n_v k_{\text{cap}} + n_c n_d k_{\text{act}} + j_0 \exp(-(R_p - x + x_0)^2/2\Delta R_p^2)/\sqrt{2}\pi\Delta R_p, \quad (1)$$

$$\partial n_c/\partial t = n_a n_v k_{\text{cap}} - n_c n_d k_{\text{act}}, \quad (2)$$

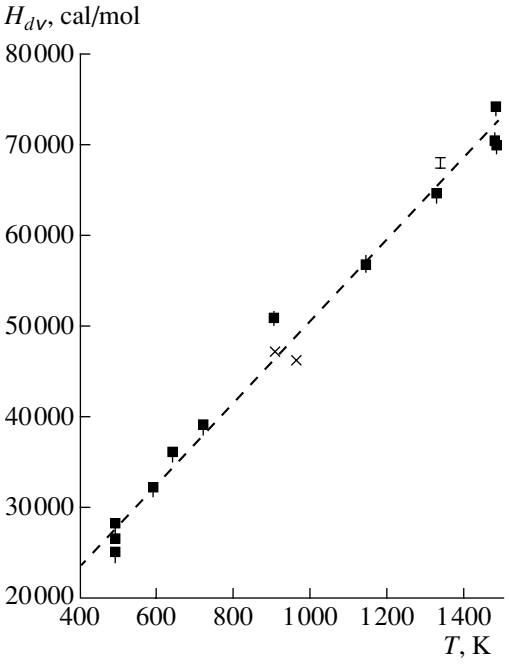

Fig. 3. Temperature dependence of the enthalpy of defect migration in silicon on the basis of the data from Tables 2 and 4.

$$\partial n_d/\partial t = D_{dv}\partial^2 n_d/\partial x^2 - n_c n_d k_{\text{act}} - n_v n_d k_{\text{ann}} + j_0 N \sigma_d \Theta(R_p - x + x_0), \quad (3)$$

$$\partial n_v/\partial t = D_{dv}\partial^2 n_v/\partial x^2 - n_a n_v k_{\text{cap}} - n_v n_d k_{\text{ann}} + j_0 N \sigma_d \Theta(R_p - x + x_0), \quad (4)$$

$$X_0 = -v_b t, \quad N = 5.04 \times 10^{22}\ \text{cm}^{-3}, \quad \sigma_d = 3.52 \times 10^{-16}\ \text{cm}^2.$$

Here, $\Theta(x)$ is the unit step; N is the density of the silicon nuclei; σ_d is the approximate cross section of the defect formation; R_p and ΔR_p are the ion range and its standard deviation, respectively; and D_a, D_{dv}, k_{cap}, k_{act}, and k_{ann} are the free parameters of the model, which have the evident physical meaning of the impurity diffusion coefficient, the diffusion coefficient of the defect–vacancy pairs, the rate of the quasi-chemical reactions responsible for the impurity capture by the vacancies, the activation rate of the impurities by the interstitial atoms, and the rate of the mutual annihilation of the vacancies and interstitial atoms, respectively.

Based on the experimental data, the boundary condition for the impurity was taken to be equal to zero, which can be interpreted as its escape to the sample surface. For the interstitial atoms and vacancies, a condition was used such that the flux of the interstitial atoms would lead to the motion of the material boundary with a velocity of v_b (the problem of Stefan type). The initial conditions and the boundary conditions at the other boundary were taken also to be equal to zero. Under the above conditions, the system of Eqs. (1–4) was solved

Table 3. Calculated rates of the quasi-chemical reactions

Number	k_{cap}, $cm^3/s \times 10^{-23}$	k_{act}, $cm^3/s \times 10^{-23}$	k_{ann}, $cm^3/s \times 10^{-23}$
1	2.355	7.421	2.609
2	0.889	8.321	5.795
3	0.943	15.60	5.763
4	0.929	8.260	5.855

Table 4. Calculated enthalpies for the other experiments

Ion	T, °C	j_0, μA/cm^2	E, keV	T_{eff}, K	H_{dv}, cal/mol	Reference
Yb	20	10	70	488	27 811*	[5, 6]
					26 877	
					24 697	
Na	365	0.3	7	638	35 845	[7]
As	20	150	25	722	38 703	[8]
Tm	500	30	150	906	50 900	[9]
C	20	300	40	961	46 377*	[2, 10]
					46 931	
					47 058	
As	850	40	40	1143	57 164	[12]
Tl	1200	40	20	1478	70 591	[3]
As	1200	40	40	1482	74 154	[11]
Tl	1200	100	20	1484	70 064	[4]

* For pure silicon (further growth in the impurity concentration).

numerically using a computer and the finite-difference scheme. The values of the free parameters in our model were fitted by the least-squares method in such a way that they corresponded as close as possible to the experimental profiles.

CONCLUSION

The results of the calculations are listed in Tables 2 and 3. In Table 2, in addition, the enthalpies of defect migrations (evaluated by the Arrhenius equation) and the effective temperatures of the surface layer (with allowance made for the beam-induced heating) are also presented. In Table 4, the data from our additional calculations of the enthalpy of silicon self-diffusion are listed. Figure 3 shows the temperature dependence of the enthalpy of the defect migration, which was obtained using the data from Tables 2 and 4.

As can be seen from Fig. 2, in contrast to our results obtained for the implantation of Tl ions into silicon [3, 4], the profile strongly depends on the As ion current.

From Table 4, one can see the dose dependences of the enthalpy of defect migrations for the impurity ions of carbon and ytterbium in silicon, which are of opposite character. Note that the ytterbium ions migrate to the surface, whereas the carbon ions migrate into the bulk of a sample.

ACKNOWLEDGMENTS

We are grateful to P.A. Aleksandrov for his formulation of the problems for our experimental and theoretical groups and to O.L. Golovina for measurements of concentration profiles. We thank E.K. Baranova, V.L. Litvinov, and V.V Budaragin for helpful comments and their participation in discussions of the results.

REFERENCES

1. V. M. Gusev, N. P. Busharov, S. M. Naftulin, and A. M. Pronichev, Prib. Tekh. Éksp., No. 4, 19 (1969).

2. V. A. Starostin, Fiz. Khim. Obrab. Mater., No. 5, 104 (1999).
3. P. A. Aleksandrov, E. K. Baranova, V. V. Beloshitsky, *et al.*, Radiat. Eff. **88**, 249 (1986).
4. K. D. Demakov, private communication.
5. V. A. Starostin, in *Proceedings of the XV International Conference "Interaction of Ions with Surface," Zvenigorod, 2001*, Vol. 2, p. 201.
6. D. É. Nazyrov, S. A. Goncharov, and A. V. Suvorov, Pis'ma Zh. Tekh. Fiz. **26** (8), 24 (2000) [Tech. Phys. Lett. **26**, 326 (2000)].
7. J. O. McCaldin and A. E. Widmer, Proc. IEEE **52**, 301 (1964).
8. F. Uesugi, Y. Kikuchi, K. Watanabe, and I. Hashimoto, Phys. Status Solidi A **177**, 331 (2000).
9. J. F. Gibbons, J. L. Moll, and N. I. Meyer, Nucl. Instrum. Methods **38**, 165 (1965).
10. P. A. Aleksandrov, E. K. Baranov, K. D. Demakov, *et al.*, Fiz. Tekh. Poluprovodn. (Leningrad) **21**, 920 (1987) [Sov. Phys. Semicond. **21**, 561 (1987)].
11. E. K. Baranova, private communication.
12. K. D. Demakov and V. A. Starostin, Zh. Tekh. Fiz. **71** (4), 128 (2001) [Tech. Phys. **46**, 490 (2001)].

Translated by Yu. Vishnyakov

Technical Physics, Vol. 47, No. 10, 2002, pp. 1337–1340. Translated from Zhurnal Tekhnicheskoĭ Fiziki, Vol. 72, No. 10, 2002, pp. 134–137.

BRIEF COMMUNICATIONS

Structure of Fullerene-Containing Soot at Different Formation Stages of Arc Discharge Vaporization of Graphite

O. P. Gorelik*, G. A. Dyuzhev, D. V. Novikov***, V. M. Oĭchenko**, and A. A. Sitnikova****

** FOMA Company, Houston, USA*

*** Ioffe Physicotechnical Institute, Russian Academy of Sciences, St. Petersburg, 194021 Russia*

e-mail: dgan@hm.csa.ru

**** Bonch-Bruevich State University of Telecommunications, St. Petersburg, 191186 Russia*

Received December 29, 2001

Abstract—Electron microscopy is used in a study of nanoclusters of the carbon soot deposited on a probe in different areas of arc discharge during graphite vaporization under conditions favorable for fullerene synthesis. It is found that the spatial network of soot nanoclusters consists of alternating regions of higher density or associates of carbon particles. Two types of nanoclusters have been identified with the correlation radii of the associates equal to 0.6–0.8 and 1.6–2.2 nm, respectively. Type I nanoclusters are dominant in the soot microparticles, and their structure shows practically no variations with increasing separation r of the soot collector from the discharge axis over the range of distances studied, r = 1–9 cm. The effective radius R_0 of the "elementary" particles making up the associates in the soot nanoclusters of Type I calculated with the use of scaling relationships is 0.15–0.17 nm and is close to the gas-kinetic radius of carbon atoms. Type II nanoclusters have been identified in soot collected at $r > 3$ cm. Values of R_0 calculated in this case are 0.6–0.9 nm and decrease with increasing r, which indicates the presence of fullerene molecules in these nanocluster associates.

INTRODUCTION

In [1], the structure of carbon soot produced by arc discharge vaporization under conditions favorable for synthesis of fullerenes was studied. It has been shown that the soot is characterized with a multilevel structure depending on the scale under study. Elementary particles in the soot are either fullerenes or carbon particles of a size on the order of fullerene dimensions ("failed" fullerenes). These elementary particles aggregate into associates, forming a spatial network of fractal nanoclusters 30–80 nm in size. The nanoclusters combine into aggregates which, in turn, are constituent parts of the soot microparticles. The soot studied in [1] was collected from the walls of a reactor (90 mm in diameter), so these results could not provide an answer as to at what distance from the discharge particular species of carbon particles were formed.

In [2], the deposition of carbon onto metallic probes placed in the path of the gas-plasma jet exiting the interelectrode gap of an arc discharge was studied. The results obtained in [2] were analyzed in [3] using a simple gas-dynamic model of the jet and a fairly general model of the cluster size distribution. It was shown that carbon chains and rings transform into fullerenes at a distance of $r > 3$ cm from the axis and the number of particles S in an associate exceeds unity at $r > 4$ cm.

The purpose of this work is to verify the conclusions made in [3] by directly studying the soot structure at different distances from the arc axis.

EXPERIMENTAL

The arc discharge burned between graphite electrodes 6 mm in diameter in a vacuum chamber 180 mm in diameter. The arc parameters were as follows: current, 80 A; helium pressure, 70 torr; interelectrode gap, 3–4 mm. Around the arc discharge at various distances from its axis, water-cooled copper wires 1.5 mm in diameter were arranged. Soot deposited on the wires was collected and analyzed.

The morphology of the soot particles was studied under a Philips electron microscope at an accelerating voltage of 100 kV. The samples were prepared by ultrasonic dispersing and placed on a specially prepared film substrate of amorphous carbon supported by copper netting.

Computer processing of the micrographs was carried out at a magnification of 5×10^6 using a cluster grid model [4] and following a procedure described in [1]. A plane square grid with a distance between sites of r = 0.2 nm was superimposed on the images. The image area scanned was about 5×10^3 nm^2. For each soot sample, no less than ten images were analyzed.

1063-7842/02/4710-1337$22.00

For quantitative characterization of the spatial distribution of nanocluster density, a lattice density radial distribution function $g(R)$ and dependence of an average lattice density $\rho_\Pi(R)$ on a scale value R [1] was used. The fractal dimension of nanoclusters D was determined by the slope of the $\rho_\Pi(R)$ curve in logarithmic coordinates.

In calculating the effective radius R_0 of the elementary particles making up the associates in nanoclusters and the average number S of particles in an associate, we used relationships obtained in [1]:

$$R_0 = \left(\frac{2}{\pi}\rho_\Pi L\xi^{1-D}\right)^{1/(2-D)}, \quad (1)$$

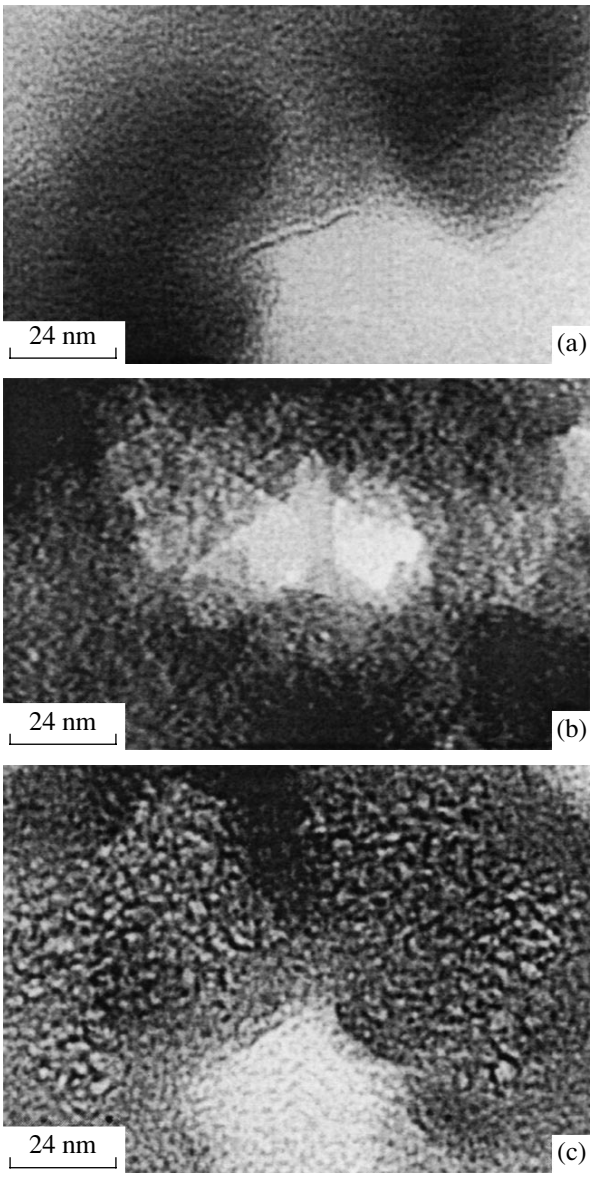

Fig. 1. Electron micrographs of nanoclusters from fullerene-containing soot collected at different distances r from the discharge axis. r = 3 (a); 4 (b); and 5 cm (c).

$$S = \omega(\xi/R_0)^D, \quad (2)$$

where L is the period of spatial alternation of the associates in a nanocluster; ξ is the average correlation radius of an associate; ρ_Π is the degree of a nanocluster being filled with associates at $R = \xi$; D is the fractal dimension of a nanocluster; and ω is the associate density (for random packing of hard spheres $\omega = 0.637$ [5]).

RESULTS AND DISCUSSION

Figure 1 shows electron micrographs of soot nanoclusters collected at different distances r from the discharge axis. It is seen that the carbon nanoclusters of the soot have a reticular internal structure arising from spatial alteration of regions of different density. These regions can be related to associates of carbon particles.

Over distances r between 1 and 3 cm, the structure of nanoclusters remains nearly the same (Fig. 1a) and can be represented by a radial density distribution function $g(R)$, shown in Fig. 2. The position of the first minimum of the $g(R)$ function corresponds to the value of the associate correlation function ξ (ξ = 0.6 nm), and the position of the next maximum corresponds to the period of spatial alternation of associates in a nanocluster L (L = 0.93 nm).

With increasing scale R, the average density of nanoclusters $\rho_\Pi(R)$ decreases as $\rho_\Pi(R) \sim R^{D-2}$, and because in logarithmic coordinates the function $\rho_\Pi(R)$ is a straight line (Fig. 3), the nanoclusters in the soot can be characterized as a fractal structure of dimension $D \approx 1.7$. Transition to the uniform continuous network of a percolation cluster ($D \approx 2$) corresponds to the kink point in the dependence of $\ln\rho_\Pi$ on $\ln R$ and occurs over a scale close to the value of correlation radius ξ.

At $r \le 3$ cm, the effective radius R_0 of elementary particles making up associates in a soot nanocluster calculated with the use of scaling relationships (1) and (2) is equal to 0.15 nm, which is close to the gas-kinetic radius of a carbon atom.

At $r \ge 4$ cm, the soot, in addition to the above, contained fractal nanoclusters of different type (Fig. 1b, 1c), with larger associates of carbon particles corresponding to ξ = 1.6–2.2 nm. The content of such nanoclusters in soot increases with increasing r.

Figure 4 shows curves of the density distribution function $g(R)$ in type II soot nanoclusters for various distances r, and Fig. 5 shows corresponding dependences of the lattice density ρ_Π on the chosen scale. Structural parameters of the nanoclusters are given in the table. The same table cites values of the fullerene content in soot α and capture parameter ε of carbon particles by a cylindrical probe [2] measured under identical experimental conditions.

The effective radius R_0 of the elementary particles calculated for such nanoclusters is 0.5–0.9 nm (see table), which is substantially greater than the gas-

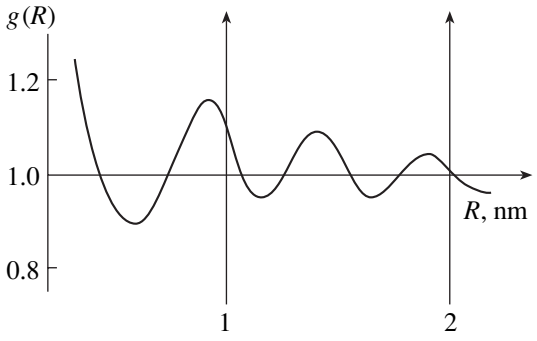

Fig. 2. Density distribution function $g(R)$ in typical nanoclusters of carbon soot.

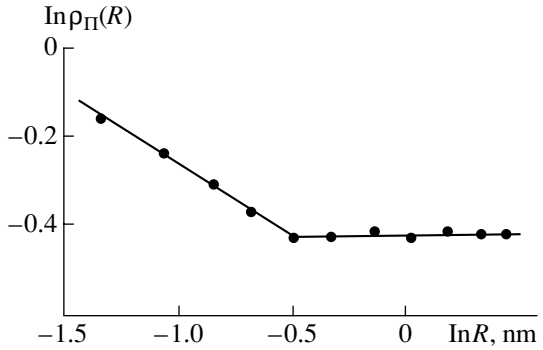

Fig. 3. Dependence on the scaling radius of the lattice density ρ_Π in typical nanoclusters of carbon soot.

kinetic radius of carbon atoms and corresponds to the characteristic size of fullerenes and more intricately structured carbon clusters. This fact suggests that the fullerene associates are formed in the soot at $r > 3$ cm. Qualitatively, this is in good agreement with the results of calculations in [3], assuming that at $r > 4$ cm the gas-plasma jet contains carbon chains, rings, and fullerenes, but no associates ($S < 1$).

Analysis of the obtained experimental data showed the following:

1. In nanoclusters from soot collected at $r < 4$ cm, the elementary particles are carbon atoms and no fullerene associates are present inside the nanocluster. It is quite possible that under these conditions nanoclusters and their aggregates form, instead of within the gas-plasma jet, at the surface of the soot collector or in the near-surface thermal layer.

2. Formation of an increasingly higher density of fullerene associates ρ_Π takes place over a rather small distance (r = 3–5 cm). At $r > 5$ cm, the lattice density ρ_Π of the nanoclusters is only slightly dependent on r.

3. Away from the arc axis, the radius of elementary particles R_0 in the fullerene associates decreases and their number in an associate increases.

4. The fractal dimension of fullerene nanoclusters increases somewhat with r and, at the reactor wall, is close to $D \approx 1.8$, the value corresponding to the aggregation mechanism of the associates of elementary particles. This is higher than the value of $D = 1.6$ given in [1]. The cause of the discrepancy is the fact that in [1] the entire soot was analyzed, collected from the walls of a pilot installation with an arc chamber of smaller diameter (90 mm).

5. Conclusions drawn from the analysis of electron microscopy data are in good agreement with measured values of α and ε. The fullerene content in the soot α increases up to $r = 4$ cm and then varies insignificantly, in agreement with the results in [6], where α was determined by spectrometric methods. The capture parameter ε is more than unity at $r > 4$ cm. This value of r can be related to carbon chains, rings, and fullerenes [2, 3].

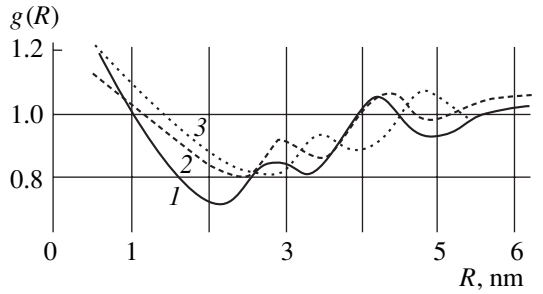

Fig. 4. Density distribution function $g(R)$ for associates of fullerene-like particles in nanoclusters of soot collected at distances of 4 (*1*), 5 (*2*), and 9 cm (*3*) from the discharge axis.

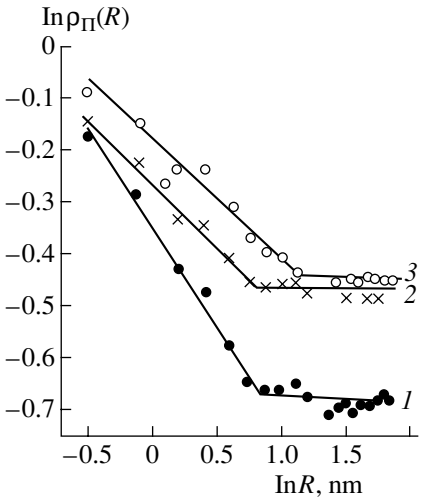

Fig. 5. Dependence of the lattice density ρ_Π of soot nanoclusters containing fullerene associates on the scaling radius for r = 4 (*1*), 5 (*2*), and 9 cm (*3*).

At $r > 4$ cm, $\varepsilon < 1$, which corresponds to fullerene associates.

The results of this study suggest that microparticles, aggregates, and nanoclusters of fullerene soot are formed at the soot collector surface, while associates

Structural parameters of soot nanoclusters containing associates of fullerene-like particles

r, cm	$\rho_{\Pi} \pm 10\%$	ξ, nm	L, nm	$D \pm 0.03$	R_0, nm	S	α, %	ε
2	–	–	–	–	–	–	0.05	4.35
3	–	–	–	–	–	–	6.7	1.40
4	0.52	1.8	4.2	1.62	0.9	2.4	10.2	0.63
5	0.62	2.2	4.2	1.76	0.7	4.8	11.0	0.83
6	0.62	2.6	4.5	1.73	0.6	8.0	–	–
9	0.63	2.8	5.0	1.77	0.6	9.7	11.0	–

consisting of fullerenes and fullerene-like carbon particles are formed in the arc chamber volume. If this is indeed the case, then it appears possible to control the structure and, consequently, the properties of fullerene soot.

ACKNOWLEDGMENTS

This study was carried out in the framework of the Russian program "Fullerenes and Atomic Clusters" and was supported in part by the Russian Foundation for Basic Research (project no. 00-02-16928).

REFERENCES

1. O. P. Gorelik, G. A. Dyuzhev, D. V. Novikov, *et al.*, Zh. Tekh. Fiz. **70** (11), 118 (2000) [Tech. Phys. **45**, 1489 (2000)].
2. D. V. Afanas'ev, G. A. Dyuzhev, and A. A. Kruglikov, Zh. Tekh. Fiz. **71** (5), 134 (2001) [Tech. Phys. **46**, 638 (2001)].
3. N. I. Alekseev, F. Chibante, and G. A. Dyuzhev, Zh. Tekh. Fiz. **71** (6), 122 (2001) [Tech. Phys. **46**, 761 (2001)].
4. J. Feder, *Fractals* (Plenum, New York, 1988; Mir, Moscow, 1991).
5. J. M. Ziman, *Models of Disorder: The Theoretical Physics of Homogeneously Disordered Systems* (Cambridge Univ. Press, Cambridge, 1979; Mir, Moscow, 1982).
6. G. A. Dyuzhev and V. I. Karataev, Fiz. Tverd. Tela (St. Petersburg) **36**, 2795 (1994) [Phys. Solid State **36**, 1528 (1994)].

Translated by B. Kalinin

Technical Physics, Vol. 47, No. 10, 2002, pp. 1341–1344. Translated from Zhurnal Tekhnicheskoĭ Fiziki, Vol. 72, No. 10, 2002, pp. 138–142.

BRIEF COMMUNICATIONS

Repetitive Low-Pressure Volume Discharge Induced by Attachment Instability in an Ar/Cl_2 Mixture

A. K. Shuaibov

Uzhhorod National University, Uzhhorod, 88000 Ukraine

e-mail: ishev@univ.uzhgorod.ua

Received March 19, 2002

Abstract—Ignition conditions and the characteristics of a repetitive volume discharge with a spherical anode and plane cathode are investigated. The discharge was ignited in Ar/Cl_2 mixtures ($P \le 2.0$ kPa) used in excimer halogen lamps operating on the ArCl (B–X) 175-nm, $Cl_2(D'$–$A')$ 257-nm, and Cl_2^{**} 195- to 200-nm molecular bands. At an interelectrode distance of 3 cm and a dc anode voltage of $U_{ch} \le 1$ kV, a stable repetitive pulsed discharge with a repetition rate of 1–50 kHz was ignited in chlorine or (0.1–2.0)/(0.04–0.12)-kPa Ar/Cl_2 mixtures. The development of attachment instability in the discharge plasma, in which the processes of the formation, decay, and diffusion of the Cl_2^- and Cl^- negative ions play an important role, leads to the formation of a solitary pearlike plasma domain with an average diameter of 0.2–3.5 cm. © *2002 MAIK "Nauka/Interperiodica".*

It is shown that the plasma of a volume discharge ignited in an Ar/Cl_2 mixtute can serve as an active medium for low-pressure excimer halogen lamps emitting in the spectral range 180–270 nm. These repetitive pulsed lamps do not require a pulsed power supply based on capacitive or inductive energy storage banks with conventional switches (spark gaps, thyratrons, etc.), which significantly expands the range of their possible applications. The pressure and composition of an Ar/Cl_2 mixture and the average discharge current were optimized to attain the maximum radiation intensity in the ArCl and Cl_2^{**} molecular bands. The effect of the working mixture composition on the ignition conditions and emission spectra of the volume discharge plasma is investigated.

1. Glow discharges ignited in low-pressure ($P \le$ 2 kPa) Ar(Kr, Xe)/Cl_2 mixtures in long glass tubes of various size and design are widely used in UV–VUV excimer lamps [1–5]. Their design is much simpler than that of lamps with microwave [6] or plasmadynamic [7, 8] pumping, and they are capable of generating cw UV–VUV emission. The interelectrode voltage in such a lamp attains 5–10 kV, which requires forced cooling of the electrodes and the discharge tube already at discharge currents of $I_{ch} \ge 20$–30 mA. Besides lamps with a cylindrical glow region (the positive column plasma of a dc glow discharge), the development of planar lamps with electrode systems not confined by dielectric walls is of great interest. In [9], a dc-excited low-pressure planar lamp operating on XeCl* molecular emission (λ = 236/308 nm) was first created and studied. A solid cathode–grid anode system with an interelectrode distance of 3 cm filled with Xe/Cl_2(HCl) gas mixtures at pressures of $P \le 2.0$ kPa was used. It was shown that the radiant efficiency of this lamp into the 4π solid angle exceeded 4% and the dc voltage at the anode was ≤1.0 kV. Most attention was paid to studying the spatial structure of the discharge plasma, whereas the time behavior of the discharge parameters and plasma emission was not investigated.

In such gas media, the formation of a volume discharge is affected by electron attachment and detachment, the diffusion of negative ions, and the onset of attachment instability [10–12]; all this impedes the operation of a steady-state glow discharge and the development of cw low-pressure excimer halogen lamps.

This paper is aimed at studying the characteristics of a dc-excited volume discharge in Ar/Cl_2 mixtures at short interelectrode distances.

2. In the experiments, we studied the spatial structure and the averaged current–voltage characteristics of the discharge, the plasma emission spectrum in the range 130–350 nm, and the waveforms of the discharge current and the integral emission intensity in the spectral range 200–700 nm, as well as the emission intensity in the maximums of the ArCl and Cl_2 molecular bands as functions of the average discharge current.

The electrode system consisting of a spherical anode and plane cathode was placed in a 10-l-volume metal discharge chamber, which was hermetically connected via an LiF window to a Seya–Namioka vacuum monochromator with a spectral resolution of 0.7 nm. An FEU-142 photomultiplier with an LiF window was used as a radiation detector in this vacuum spectrome-

1063-7842/02/4710-1341$22.00

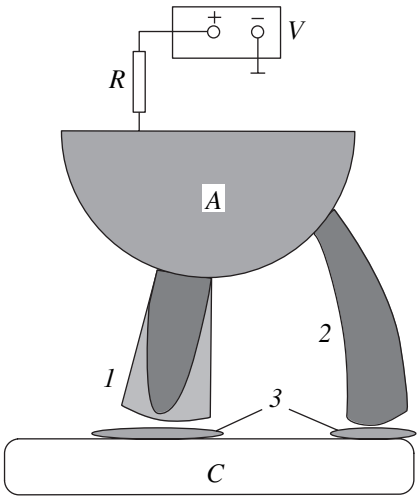

Fig. 1. Schematic of the discharge facility and the shape of the discharge plasma in the (*1*) 2.00/0.12-kPa and (*2*) 1.33/1.2-kPa Ar/Cl_2 mixtures: (*A*) anode, (*C*) cathode, (*V*) high-voltage dc power supply, and (*3*) negative cathode glow.

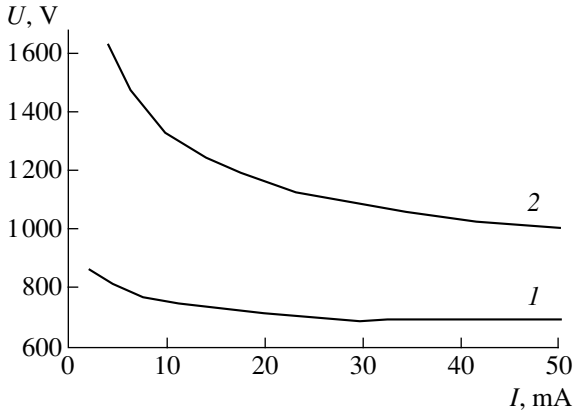

Fig. 2. Static current–voltage characteristics of a volume discharge in the (*1*) 1.33/0.12- and (*2*) 1.33/1.20-kPa Ar/Cl_2 mixtures.

ter. In the range 165–350 nm, the spectrometer was calibrated with the help of the continuum of molecular hydrogen, and, in the range 130–165 nm, the spectral sensitivity curve was extrapolated by using the data obtained for $\lambda \geq 165$ nm. Behind a quartz window located opposite the LiF window, a Foton photomultiplier (with an operating range of 200–700 nm) connected to an C1-99 oscilloscope was installed. The time resolution of the pulse recording system was 10 ns. The electrode system consisted of a massive 7-cm-diameter anode and 9-cm-diameter cathode made of duralumin and set at a distance of 3 cm from the anode (Fig. 1). The radius of curvature of the anode working surface was 3 cm, and the cathode was plane. A dc voltage ($U_{ch} \leq 1$ kV) was applied to the anode through a 10-kΩ ballast resistor *R*. The average discharge current and the gas mixture pressure varied in the ranges 2–50 mA and 40–2000 Pa, respectively.

3. A schematic of the electrode system and the characteristic shape of the Ar/Cl_2 discharge plasma are shown in Fig. 1. In low-pressure mixtures with a minimal chlorine content, a conical plasma formation was observed. It was adjacent to the central region of the anode working surface and had a clear spherical border near the cathode surface. Near the anode, the plasma diameter attained 1.0–1.5 cm, whereas near the cathode, it was 1.5–2.0 times larger. In the middle of the plasma formation, there was a brighter core, which also had a spherical border at the cathode side. The increase in the gas pressure and chlorine content led to a shift of the plasma toward the anode periphery and a decrease in the plasma diameter near the anode and cathode to 0.2 and 0.5 cm, respectively. In all the experiments, we observed a dark space, whose size increased from 0.5 to 5.0 mm with increasing pressure of the Ar/Cl_2 mixture and, especially, chlorine content in it. The diameter of the negative glow was 1.3–1.5 times the diameter of the cathode part of the plasma formation. This kind of solitary plasma formation in an electronegative gas media is called the plasma domain, or autosoliton [13, 14].

4. The static current–voltage characteristics of discharges in Ar/Cl_2 mixtures at a fixed argon pressure and at minimum and maximum chlorine partial pressures (0.12 and 1.2 kPa) are shown in Fig. 2. As in a dc longitudinal discharge in an Ar/Cl_2 mixture [4], the subnormal (at $I_{ch} \leq 20$ mA) and normal (at higher discharge currents) stages of the discharge operation can be distinguished in the averaged current–voltage characteristics of a repetitive pulsed volume discharge. The increase in the chlorine partial pressure by one order of magnitude leads to a significant increase in the discharge voltage (Fig. 2) and an increase in the electric power of a volume discharge by a factor of 1.5–2.0.

5. The emission spectra from a volume discharge are shown in Fig. 3. The plasma emission intensity in the range $\lambda \geq 400$ nm was no higher than 5–10% of the emission intensity in the UV–VUV spectral region; this was verified in a particular experiment on recording integral discharge emission with a photomultiplier and a light filter. It is seen in Fig. 3 that the autosoliton plasma is a selective source of radiation in the range 170–270 nm. The spectra are similar to those obtained from the plasma of a longitudinal glow discharge in an Ar/Cl_2 mixture [4, 15]. The ArCl (*B*–*X*) 175-nm, Cl_2^{**} 200-nm, and Cl_2 (*D*'–*A*') 257-nm molecular bands are the main constituents of the emission spectra. The spectra in Fig. 3 were corrected for the relative spectral sensitivity of the vacuum spectrometer. At low argon and chlorine partial pressures (Fig. 3a), the molecular emission spectrum consists of well-resolved vibronic bands of molecular chlorine [16]. The results of the present measurements are in excellent agreement with our previous results on the interpretation of the emission spectra from the low-temperature plasma of a transverse

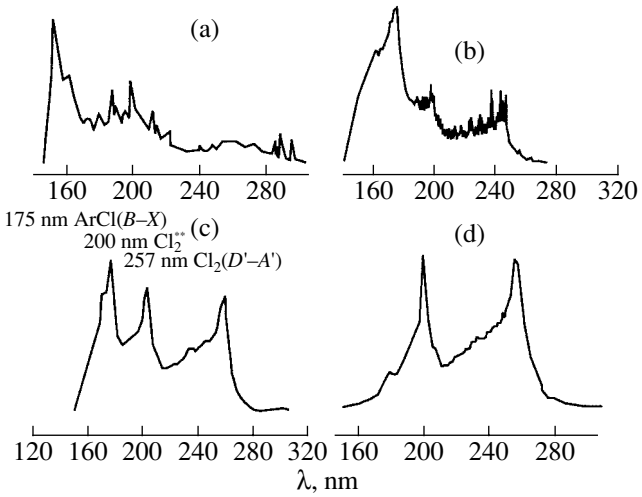

Fig. 3. Emission spectra from a volume discharge in the (a) 0.20/0.12-kPa, (b) 1.33/0.12-kPa, (c) 1.33/0.27-kPa, and (d) 1.33/1.20-kPa Ar/Cl_2 mixtures.

volume discharge in chlorine [17]. Here, ArCl molecules do not form and the 175-nm band is absent in the emission spectrum. The increase in the argon partial pressure to 1.33 kPa (Fig. 3b) leads to a significant increase in the intensity of the chlorine emission bands and the appearance of the ArCl (*B*–*X*) 175-nm band. The emission bands of molecular chlorine are distinctly structured. The efficiency of the production of ArCl molecules depends strongly on $P(\mathrm{Ar})$, because these molecules are formed only in a relatively narrow range of argon partial pressures (0.8–1.33 kPa). The increase in the chlorine partial pressure to 0.28 kPa (Fig. 3c) leads to an even higher increase in the emission intensities of all the chlorine and argon chloride molecular bands. This mixture was nearly optimum to attain the maximum intensity of the integral UV–VUV plasma emission. A further increase in $P(Cl_2)$ to 1.2 kPa results in a slight decrease in the chlorine emission intensity and strong quenching of the ArCl(*B*) molecules.

6. One of the main indicators of the onset of attachment instability in a low-temperature plasma of electronegative gases is the time modulation of both the discharge current and plasma emission [11]. It is seen in Fig. 4 that the volume discharge in a low-pressure Ar/Cl_2 mixture runs in a repetitive pulsed mode. The pulse repetition rate depends on the pressure and composition of the working mixture and the average discharge current and varies in the range 1–50 kHz. The pulse repetition rate usually increases with the average discharge current. The characteristic waveforms (mostly, those with the maximum amplitude of the parameter in question) of the discharge current and the integral plasma emission intensity are shown in Fig. 4. We usually observed the formation of autosolitons within the broad range of the amplitude values of the discharge current and photocurrent: I, $J_F = (0.3\text{–}0.9)I^{\max}$, $J_F^{\max}$. The durations of the discharge current and plasma

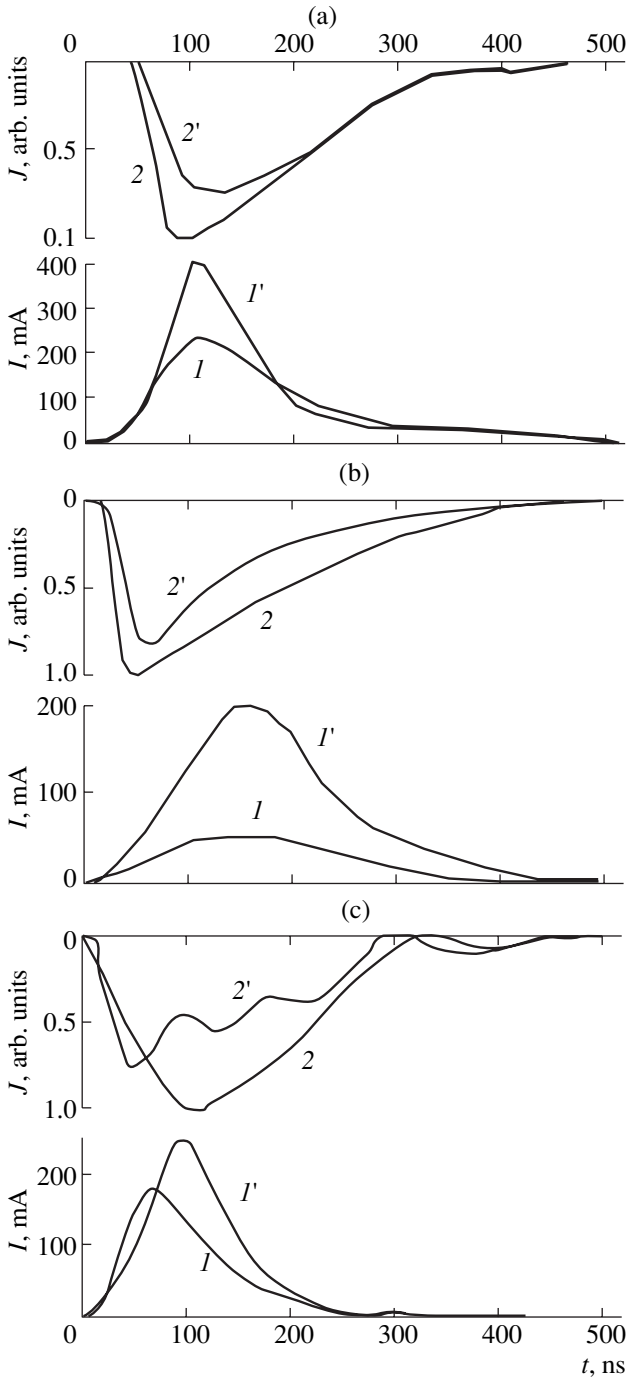

Fig. 4. Waveforms of (*1*, *1*') the discharge current and (*2*, *2*') integral emission from the discharge in the (a) 0.20/0.12-kPa, (b) 1.33/0.12-kPa, and (c) 1.33/1.20-kPa Ar/Cl_2 mixtures for average discharge currents of (*1*, *2*) 10 and (*1*', *2*') 30 mA.

emission pulses were in the range 100–200 ns. For a discharge in a low-pressure Ar/Cl_2 mixture with a low chlorine content (Fig. 4a), plasma autosolitons were formed and, consequently, plasma emission was generated near the instant when the discharge current was maximum. For all the mixture compositions, the

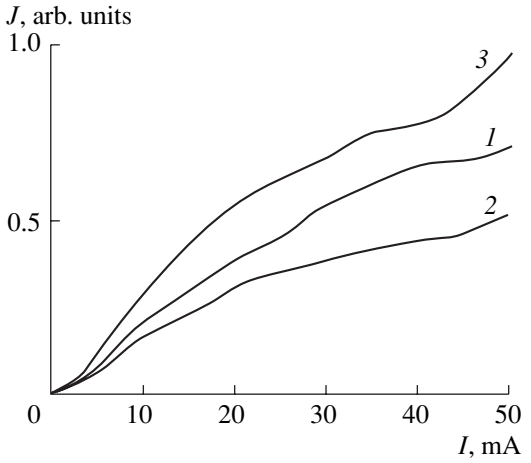

Fig. 5. Maximum emission intensity of the (*1*) ArCl (*B*–*X*) 175-nm, (*2*) Cl_2^{**} 200-nm, and (*3*) $Cl_2(D'–A')$ 257-nm molecular bands vs. average discharge current in the 1.33/0.12-kPa Ar/Cl_2 mixture.

increase in the average current from 10 to 30 mA resulted in an increase in the current amplitude and a decrease in the integral intensity of plasma emission. The increase in the argon partial pressure (Fig. 4b) led to the lengthening of the current pulse and halving of its amplitude, whereas the duration of the emission pulse increased by 20–30%. The main maximum of the emission pulse with a short rise time occurred at the current pulse leading edge. At $P(\mathrm{Ar}) = 1.33$ kPa, the increase in the chlorine partial pressure (Fig. 4) led to the shortening of the current pulse to 100 ns and an increase in its amplitude, especially at $I_{ch} \le 10$ mA. In this case, the plasma emission intensity decreased by a factor of 2.5 and three peaks arose in the waveform of the plasma emission pulse with a total duration of 450 ns. At $I_{ch} \ge 30$ mA, plasma emission was generated near the leading edge of the discharge current pulse; at low average discharge currents, the emission pulse shifted toward the peak of the current pulse.

7. The maximum emission intensities of the ArCl and Cl_2 molecular bands increased with the average discharge current, which was related to the increase in the current pulse amplitude by a factor of 1.3–3.0 and, to a large extent, to the increase in the pulse repetition rate (Fig. 5). The increase in the chlorine partial pressure from 0.12 to 1.2 kPa increased the emission intensity of the chlorine bands by 1.5–2.0 times; however, this also led to the strong quenching of ArCl (*B*) excimer molecules; consequently, the 175-nm emission band did not contribute to the integral UV plasma emission.

8. Thus, the study of a dc-excited low-pressure volume discharge in Ar/Cl_2 mixtures in an electrode system with a short interelectrode gap ($d \le 3$ cm) and with no confining dielectric walls has shown that such a volume discharge runs only in the repetitive pulsed mode ($f = 1$–50 kHz). This makes it possible to create a repetitive low-pressure excimer halogen lamp operating in the spectral range 170–270 nm. The creation of such lamps operating in a cw mode is not feasible because of the onset of attachment instability. A particular experiment performed with a volume discharge in a Xe/Cl_2 mixture at a total pressure of $P \le 1.0$ kPa has shown that, in this case, it is also impossible to achieve entirely cw emission; however, there exists a cw component of both the discharge current and plasma emission, whose magnitude depends strongly on the total pressure and composition of the working mixture, as well as on the average discharge current. The (1.0–1.5)/(0.2–0.3)-kPa Ar/Cl_2 mixtures are shown to be optimum for attaining the maximum intensity of UV–VUV emission with a pulse duration of $\tau = 100$–300 ns.

REFERENCES

1. A. P. Golovitskiĭ, Pis'ma Zh. Tekh. Fiz. **18** (8), 73 (1992) [Sov. Tech. Phys. Lett. **18**, 269 (1992)].
2. A. N. Panchenko, V. S. Skakun, É. A. Sosnin, *et al.*, Pis'ma Zh. Tekh. Fiz. **21** (20), 77 (1995) [Tech. Phys. Lett. **21**, 851 (1995)].
3. M. I. Lomaev, A. N. Panchenko, and É. A. Sosnin, Zh. Tekh. Fiz. **68** (2), 64 (1998) [Tech. Phys. **43**, 192 (1998)].
4. A. K. Shuaibov, A. I. Dashchenko, and I. V. Shevera, Kvantovaya Élektron. (Moscow) **31**, 371 (2001).
5. A. K. Shuaibov, A. I. Dashchenko, and I. V. Shevera, Zh. Tekh. Fiz. **71** (8), 121 (2001) [Tech. Phys. **46**, 1049 (2001)].
6. H. Kumagai and M. A. Obara, Jpn. J. Appl. Phys. **28**, 2228 (1989).
7. V. S. Rogulich, V. P. Starodub, and V. S. Shevera, Opt. Spektrosk. **69**, 756 (1990) [Opt. Spectrosc. **69**, 450 (1990)].
8. A. A. Alekhin, V. A. Barinov, Yu. V. Geras'ko, *et al.*, Zh. Tekh. Fiz. **65** (5), 9 (1995) [Tech. Phys. **40**, 409 (1995)].
9. É. A. Sosnin and V. F. Tarasenko, Zh. Tekh. Fiz. **67** (12), 43 (1997) [Tech. Phys. **42**, 1411 (1997)].
10. Yu. S. Akishev, A. L. Napartovich, and S. V. Pashkin, Fiz. Plazmy **4**, 152 (1978) [Sov. J. Plasma Phys. **4**, 86 (1978)].
11. V. L. Aleksandrov, I. V. Kochetov, D. A. Mazalov, and A. P. Napartovich, Fiz. Plazmy **18**, 1468 (1992) [Sov. J. Plasma Phys. **18**, 758 (1992)].
12. A. L. Vykharev, O. A. Ivanov, L. S. Ivanova, *et al.*, Zh. Tekh. Fiz. **59** (1), 40 (1989) [Sov. Phys. Tech. Phys. **34**, 22 (1989)].
13. V. L. Aleksandrov and A. P. Napartovich, Usp. Fiz. Nauk **163** (3), 1 (1993) [Phys. Usp. **36**, 107 (1993)].
14. V. S. Golubev and S. V. Pashkin, *Elevated-Pressure Glow Discharge* (Nauka, Moscow, 1990).
15. A. K. Shuaibov, L. L. Shimon, A. I. Dashchenko, and I. V. Shevera, J. Phys. Stud. **5** (2), 131 (2001).
16. A. K. Shuaibov, L. L. Shimon, A. I. Dashchenko, and I. V. Shevera, Pis'ma Zh. Tekh. Fiz. **27** (9), 8 (2001) [Tech. Phys. Lett. **27**, 354 (2001)].
17. A. K. Shuaibov, Zh. Tekh. Fiz. **70** (10), 117 (2000) [Tech. Phys. **45**, 1346 (2000)].

Translated by N. Ustinovskiĭ